Scaling relationships of global river deltas

Octria Adi Prasojo

BSc, INSTITUT TEKNOLOGI BANDUNG

MSc, INSTITUTE FRANÇAIS DU PÉTROLE

SUBMITTED IN FULFILMENT OF THE REQUIREMENTS FOR THE DEGREE OF

Doctor of Philosophy

SCHOOL OF GEOGRAPHICAL AND EARTH SCIENCES

COLLEGE OF SCIENCE AND ENGINEERING

UNIVERSITY OF GLASGOW

AUGUST 2022

Abstract

River deltas are home for ~300 million people worldwide and are hotspots for biodiversity. In recent decades, river deltas have been facing growing stressors due to dams and reservoirs, sand mining and sea-level rise, putting the human and natural systems that rely on river deltas at considerable risk to land subsidence, inland and coastal flooding, and other socially impactful geomorphological changes. The geomorphic response of river deltas to these growing stressors depends on the geomorphic controls on delta morphology and their scaling relationships. However, our current understanding of delta's geomorphic response to these forcing is limited to local cases, fragmented physical and numerical delta experiments, and simplified global models. In this thesis, I explore the possibility of adopting scaling relationships originally developed for quantitative watershed analysis of fluvial systems to river delta systems to understand deltas' morphodynamic response towards these stressors. Chapter 1 introduces the challenges faced by modern and ancient river deltas along with the scaling relationship theory. Chapter 2 details the methods used in this thesis, including modern delta observation, numerical modelling and characterisation of ancient delta deposits. Chapter 3 introduces a novel globally consistent scaling from 114 modern river deltas using satellite imageries observation, solving previously debated avulsion scaling. I found that slope break and avulsion location scale consistently, opens potential insights into how delta naturally respond to the growing stressors and how the avulsion mobility is closely tied with slope break, that are imperative for understanding delta flood risk. Chapter 4 investigates the role of the novel scaling found in Chapter 3 in controlling avulsion-bifurcation timescale and interaction in river deltas using numerical model. Avulsion is primarily controlled by delta topset slope, in which it occurs simultaneously with bifurcation process. In Chapter 5, novel palaeodischarge estimation models are proposed by correlating water discharge with delta channel widths and catchment areas from modern global deltas by adopting hydraulic geometry concept. These simple and rock-record focused correlations produce palaeodischarge estimates within the same order of magnitude as the palaeodischarge derived from existing, more complex approaches. In Chapter 6, I reclassified palaeodischarge models built in Chapter 5 based on the marine influence that affects the hydraulic geometry assumption used in earlier models. By establishing more detailed scaling relationships, I found that estimating discharge using hydraulic geometry concept is only applicable for river- and wave-dominated deltas, but not for tide-dominated deltas. Finally, Chapter 7 synthesises the previous chapters and proposes further works.

Acknowledgements

I vividly remember how I first came to Glasgow, 25th of March 2019, to start my PhD journey. With no luck in finding accommodation, one Indonesian guy who I have never met before offered his room for a week. I believe without him, Wayan Agus Purnomo, I could not start my PhD conveniently. Just like I thank Wayan, I dedicate this section to thank everyone whom I owe my gratitude to, who have given me life-changing experiences whilst I was working in Glasgow, or remotely in Indonesia or the USA.

The first and foremost, the greatest of all, the almighty God. Who let everything both good and bad happened in my life, who has flawlessly designed my life and my PhD. Without his grace, I would not be able to come out alive from my terrible bike accident on the 11th of July 2021. I will always remember that day you saved me, who left me with only scars and one month hospitalisation period. Yet you still save my brain that is very crucial for my PhD. After just 3 months of regular visit to the local GP and physiotherapist, you let me walk and even run again. And now, you let me finish the PhD with a life-changing experience that made me more mature as a human.

For my supervisors: Prof Trevor Hoey who patiently taught me since day one, who always ignites interesting intellectual discussion, who has grown the curiosity in me to keep pursuing and developing this knowledge. I specifically thank Dr Amanda Owen for giving me the opportunity to undertake fieldwork to some fabulous outcrops in the East coast of Scotland, along with the opportunity to be a graduate teaching assistant (GTA) and to be an undergraduate supervisor, in which I have learnt and been inspired a lot by you. I also thank Prof Richard Williams who trusted me to be a research assistant in his valuable Philippine catchment project, during which I learned enormous lessons on how to deal with hydro-morphodynamic modelling on Delft3D and HEC-RAS. I should also thank Dr Christina Persano and others who gave me an opportunity to be a GTA and for being really welcoming colleagues in the School. I thank Prof Chris Paola and Dr Kimberly Hill for the meaningful discussion and inspiration while observing flume tank experiments in St. Anthony Falls Laboratory. My co-author, Anna van Yperen and her supervisor, Dr Ivar Midtkandal to whom I owe meaningful discussion to develop ideas for our paper written as Chapter 6 in this dissertation. I thank all the lectures involved in assessing my progressions every year and all the administrative staff in the School of Geographical and Earth Sciences.

Many thanks to all my GES colleagues in my previous 414 room that include Cameron Floyd, Kwetishe Danjuma, Ellen, Pierre, Sammy, Faisal, and Juan. Without them, my life in GES would be not as exciting as when I am with them. I should also thank Kelly James and Marli de Jongh who asked me to move in to their quiet 208 room. Working in that small room together with them had been very productive, yet so fun. I should also thank my colleagues working in East Quadrangle office that include Dr Laura Quick who has always been supportive and encouraging me to apply for a fellowship/postdoctoral, Pamela Tolentino and Richard Boothroyd for helping my morphodynamic modelling of the Philippines catchment project, for a crash course on HEC-RAS and afternoon walks, Andri, Eilidh, Qing who I owe their hospitalities.

I thank my Indonesian friends in Glasgow who were very supportive with my work, very amiable while serving very good Indonesian cuisines everytime I come visit them. Because of them, who are Bernadetta Meika, Anggo Marantika, Tara Nursalim, Yodefia Rahmad, Cici, Derryl Reminton, Wicak, Felix, Satya Arry, Alvin Waracha, Scherzo, Kevin, Puti and some others that I cannot mention one by one, my life in Glasgow would not have been fun without all the laughs, moments and times we shared together.

It is now my turn to show my gratitude for my amazing parents who are always available every Sunday afternoon for a long story video calls to just talk about my PhD. I could not thank them enough for all their effort since I was born, putting me in very good Catholic schools and the most prestigious university in Indonesia. This degree is for you, Mom and Dad.

During this long 3.5 years PhD journey, I always have someone next to me. Who has always been encouraging, been a good listener and the best life-partner, my fiancée Filia Stephanie. I do remember the day we got the announcement that I got the scholarship to leave for the UK soon. I remember how complicated and difficult it was to absorb and to accept the fact that we will be in a long-distance relationship, and I am sorry for that. Thank you for your willingness and your patience to accompany me throughout this rough patch. You do know I cannot thank you enough in this very short paragraph.

I am also grateful to the scholarship provided by the Indonesian Endowment Fund for Education (LPDP), the Global Landscape and Climate Change research grant and the mobility funding from the College of Science and Engineering, University of Glasgow to

support my travel to St. Anthony Falls Laboratory in the USA to learn about physical modelling and to have enjoyable discussion with Prof Chris Paola. I also thank International Association of Sedimentologists for supporting my BSRG conference at Royal Holloway in 2019. I should also personally thank Prof Richard Williams who provided me with internal funding from the University of Glasgow to get a Delft3D training from the Deltares that is imperative for my study and my future career.

Octria Adi Prasojo

August 2022, Glasgow

Author's declaration

Thesis presented here is the result of my original work, except where materials from other sources (e.g. publicly-available global dataset and figures) have been properly cited. I should acknowledge that this thesis has not been submitted for any degree at the University of Glasgow or other institutions.

The chapter 3, 4, 5, and 6 in this thesis are presented as an 'Alternative Format Thesis'. The guideline of 'Alternative Format Thesis' derived from the University Code of Practice has been followed accordingly; hence the much of the texts, figures, and tables presented in the Chapter 3, 4, 5 and 6 are identical to the published or submitted versions. Parts of the supplementary materials from those papers (e.g. supplementary figures/texts/tables) have been moved into the body of these chapters to provide easier readability of the thesis.

Main texts, figures and tables from the Chapter 3 are reformatted version of materials appearing in Prasojo, O. A., Hoey, T. B., Owen, A., & Williams, R. D, 2022, Slope break and avulsion locations scale consistently in global deltas, Geophysical Research Letters, 49, e2021GL093656, https://doi.org/10.1029/2021GL093656. Overall texts, figures and tables in Chapter 4 are from a manuscript submitted to Journal of Geophysical Research: Earth Surface. The Chapter 5 texts, figures and tables are reformatted version of a manuscript under review in Sedimentology, while the overall texts, figures and tables in Chapter 6 are from a manuscript submitted to Journal of Sedimentary Research.

Octria Adi Prasojo

August 2022, Glasgow

Data availability

The thesis presented here uses the global river discharge dataset from The Global Runoff Data Centre (GRDC) 56068 Koblenz, Germany that can be accessed through (https://www.bafg.de/GRDC/EN/02_srvcs/21_tmsrs/210_prtl/prtl_node.html). Data produced by this thesis have been made publicly online. Chapter 3 dataset as mentioned in Table S3.1 are available in https://doi.org/10.6084/m9.figshare.16429998.v1, Chapter 5 dataset are available in https://doi.org/10.6084/m9.figshare.19574938.v2 and Chapter 6 dataset as mentioned in Table S6.2 are also available in https://doi.org/10.6084/m9.figshare.19964549.v4.

Notation

The following symbols are used in this thesis

A	$[L^2]$	catchment area
a, b, c, f, k, m,n,r $\gamma, \beta, \Psi, \varsigma$	[-]	constants
B	[-]	bootstrap repetition number
B_a	[L]	lobe width of each avulsion
B_b	[L]	channel width upstream of the bifurcation
B_c	[L]	channel width at avulsion node
C_f	[-]	bed friction coefficient, Chezy friction coefficient
D	[L]	delta lobe progradation distance
d	[L]	channel depth
D_{50}	[L]	50% sieve diameter of sediment materials
f_a	$[T^{-1}]$	avulsion frequency
g	$[LT^{-2}]$	gravitational acceleration
Gd	[-]	elevation gradient
H	[L]	aggradation thickness necessary for avulsion
h	[L]	flow depth
H^*	[-]	avulsion threshold
H_b	[L]	near shore water depth
h_c	[L]	characteristic or bankfull flow depth
L	[L]	river distance along the longest distributary channel
l	[L]	horizontal length used in calculating Gd
L_a	[L]	avulsion length
L_b	[L]	backwater length
L_D	[L]	distributary channel length in between bifurcated point
L_s	[L]	slope break length
L_v	[L]	valley-exit-to-shoreline distance
N	[-]	number of samples
p	[-]	statistical significance value
Q	$[L^3T^{-1}]$	discharge
Q_b	$[L^3T^{-1}]$	bankfull discharge
Q_c	$[L^3T^{-1}]$	characteristic discharge
Q_s	$[L^3T^{-1}]$	sediment load
Q_2	$[L^3T^{-1}]$	2-year recurrence interval flood
R	$[ML^3]$	submerged grain density
Rd	$[L^{-1}]$	relative steepness
S	[-]	slope, palaeoslope
S_{topset}	[-]	delta topset slope
s	[L]	river distance from the delta apex to the shoreline
Sm	[-]	smoothness level used in lowess regression
S_{w^*}	[-]	standard error of dimensionless channel width
T	[Θ]	temperature
T_a	[T]	avulsion timescale
T_b	[T]	bifurcation timescale
u, V	$[LT^{-1}]$	velocity
v_p	$[LT^{-1}]$	delta progradation rate

w	[L]	channel width
w^*	[-]	dimensionless channel width
$W_{av,}\ W_a$	[L]	channel width measured at avulsion node
W_b	[L]	bankfull channel width
W_{med}	[L]	median channel width
z	[L]	sea-level rise
α	[-]	dimensionless constant
Δ	[L]	mean bedform height
λ	[L]	bedform wavelength
λ_p	[-]	sediment porosity
τ^*_{b50}	[-]	dimensionless bankfull bed shear stress for D_{50} grain size

List of Figures

List of Tables

Contents

Chapter 1 - Introduction

Etymologically, the word ‘delta’ comes from the common triangle shape of this landform, firstly recognised from the Nile delta’s triangular ‘island’. Contrary to popular belief, Herodotus did not coin the term delta since the Oxford English Dictionary showed the first appearance of the word delta came from the English historian, Edward Gibbon, in the late-eighteenth century (Celoria, 2015). However, there may well be earlier uses of delta in other languages that were not recorded in the literature. From a geological perspective, a river delta is defined as the sediment body accumulated beyond the lateral shoreline as the product of material delivered by a river system to a water body that can be either seawater or a lake. River deltas are built by repeating lobe deposition (Edmonds and Slingerland, 2007; Edmonds et al., 2011). When a river system containing water and sediment meets a relatively static water body, the decrease in longitudinal slope caused by the resulting backwater will reduce the river transport capacity. Sediment will consequently be deposited under water, producing a lobe-shaped mouth bar deposit. The deposition of this sediment body will then trigger the river flow to split into two (i.e. bifurcation) once the deposited sediment reaches a critical height of ~0.4 of the total water depth (Edmonds and Slingerland, 2007). The river bifurcation will continue to cause sediment deposition at this site until the mouth bar emerges subaerially, initiating the formation of a delta plain. Further offshore, sediment deposition then continues, leading to a repeating pattern of mouth bar deposition. This repeating cycle of mouth bar formation and channel bifurcation produces a delta plain containing a network of distributary channels with an overall triangular shape. Examples of deltas with such a triangular shape include the Nile, Niger and Mahakam deltas. All deltas would have this triangular shape if there were no other influences (e.g. waves, tides, sea-level change, changing sediment load) on this repeated process. However, not all rivers discharging into a relatively static water body build deltas into the water body since deposition is subject to sediment availability and marine forcing that may transport the sediments deposited in the water body away from the river mouth (Nienhuis et al., 2020).

River deltas are hotspots for human populations, biodiversity and ecosystems that are experiencing growing stressors like dams (Wang et al., 2008; Yang et al., 2011; Li et al., 2017), reservoirs and channel diversions (Aslan et al., 2005; Wang et al., 2008), sand mining (Brunier et al., 2014; Hackney et al., 2020), sea-level rise (Turner et al., 2017; Chadwick et al., 2020; Edmonds et al., 2020) and increasing human populations (Vörösmarty et al., 2000;

Szabo et al., 2016). Together, these lead to decreasing sediment loads of rivers, subsidence and intense coastal flooding due to relative sea-level rise (SLR), putting human populations and ecosystems relying on river deltas at considerable risk (Ericson et al., 2006; Syvitski and Saito, 2007; Loucks, 2019; Hackney et al., 2020). These growing pressures force millions of people to migrate from the Ganges-Brahmaputra-Meghna delta annually, disproportionately impact poorer people especially in developing economies (Edmonds et al., 2020) and, for example, only leave a small fraction of the Mississippi Delta being sustainable, along with other socially impactful geomorphological changes (Blum and Roberts, 2009; Nienhuis et al., 2015, 2018a; Chamberlain et al., 2018). As the home to half a billion people, river deltas are dynamic landscapes that continuously change, demanding human society to continuously adapt to mitigate its exposure to natural disaster.

In the ancient system, river deltas have been found as prolific water, hydrogen and hydrocarbon reservoirs. As the focal point of sediment deposition, river deltas preserve relatively thick sand bodies that produce prolific reservoirs in the subsurface (Bhattacharya and Tye, 2004; Zhu et al., 2012; Eide et al., 2016; Rossi and Steel, 2016). As an important sink within the source-to-sink framework, river deltas also contain crucial information for decoding climatic signals in the rock record, by preserving sediment and precipitates from dissolved constituents that have passed through a connected suite of geomorphic settings. However, the lack of quantitative rock-record-focused methodology to decode climate signals from deltaic deposits motivates this study. Quantifying the water discharge transported through a delta system in a deep geological time has always been challenged by the limited exposure of deltaic outcrop or subsurface data. Also, the currently available methods for discharge estimation are more suitable for fluvial systems that have unidirectional river flow, than for river deltas that have bidirectional and backwater-influenced flows. Moreover, the currently available methodology uses parameters that are challenging to extract from the rock record (Holbrook and Wanas, 2014) or are climate-specific (Syvitski and Milliman, 2007; Nyberg et al., 2021). This study aims to fill this gap by creating a methodology to decode palaeodischarge from deltaic deposits that is not climate-limited and that is rock-record-focused.

In the following sections of this chapter, the challenges of understanding scaling relationships, in which geomorphic response of modern and ancient global river deltas depend on them, are discussed in more detail.

1.1. Challenges in modern river deltas

Avulsion is the sudden shift in the course of a single river channel that may typically occur on a delta every 10^1-10^3 years (Slingerland and Smith, 2004; Jerolmack, 2009). Avulsions have caused some of the deadliest floods in human history due to unexpected floods occurring inland in areas often not mapped as at risk (Slingerland and Smith, 2004; Sinha, 2009; Kidder and Liu, 2017; Chadwick et al., 2020). Given the challenges faced by global river deltas, understanding the physical phenomena of channel avulsions is critical yet remains mechanically less well understood than other mechanisms of landform change in river deltas.

Geomorphologically, avulsions in river deltas have been considered to have a direct scaling relationship with backwater length, the length along which there is a marine influence on the delta plain (Paola and Mohrig, 1996; Parker, 2004; Chatanantavet et al., 2012). The scaling relationship between avulsion and backwater length has been found to be consistent in a small number of natural deltas and a physical model (Ganti et al., 2016a, 2016b; Moodie et al., 2019; Li et al., 2022a). However, another study has found that avulsion scales more strongly with the valley exit point instead of the backwater length; note that this study has a larger sample size (Hartley et al., 2017). Another study from the Yellow river delta (Ganti et al., 2014) also found that the more active avulsions in its delta plain are clustered downstream and exhibit a direct relationship with backwater lengths. However, in the further upstream area of the delta, avulsion occurs consistently at the same location due to its relationship with bedslope change at the valley exit site, supporting Hartley et al's (2017) finding. The fragmented understanding of the avulsion scaling relationship requires a more comprehensive dataset to achieve a complete view of how avulsion scales and works in natural river deltas.

1.2. Challenges in ancient river deltas

In decoding the climate forcing that occurred in ancient river deltas, palaeohydrology has served as a helpful tool for sedimentologists. Palaeohydrology is the study of constructing hydrology from deposits (Leopold and Miller, 1954; Baker et al., 2022). The constructed hydrology is helpful in reconstructing climatic events, such as changing discharge, precipitation, or temperature, from the rock record. Along with its ability to reconstruct the hydrology of the ancient system, palaeohydrological methods can also be used to estimate

the sediment load entering a delta that may assist in predicting reservoir volume and palaeogeography.

Unfortunately, palaeohydrological reconstruction of river deltas usually adopts methods developed from fluvial systems, even though fluvial and river delta systems have distinct geomorphic processes (Brewer et al., 2020). In fluvial systems, water flow is unidirectional. This assumption is only partially true in river deltas that are directly influenced by marine forcing. In river deltas, the downstream end of the system has a direct contact with marine processes such as backwater, waves, tides, longshore currents and/or sea-level rise that influence the unidirectionality of water flow in parts of the system. An example of this is the influence of tides on river deltas that lead to stabilising and widening of delta distributary channels (Plink-Björklund, 2012; van Cappelle et al., 2016; Hoitink et al., 2017; Lentsch et al., 2018). Thus, adopting palaeohydrological reconstruction from rivers for river deltas may lead to under- or over-estimation of palaeohydrological parameters. Consequently, there is a need to establish a new palaeohydrology tool specific for river deltas.

1.3. Scaling relationships in river deltas

A scaling relationship for geomorphic units was originally derived from dimensional analysis and geometrical similarity concepts proposed by Strahler (1957). Assuming similarity between systems of various sizes, all dimensionally equivalent parameters (e.g. width, length, relief, basin area) of different sizes of river basins are postulated to be in a fixed ratio. Conversely, the non-dimensional parameters (e.g. bifurcation angle, stream junction angle, ground slope angle) will have consistent values if the ratio of dimensionally equivalent parameters is the same.

Strahler's (1957) original concept has been developed into a set of diverse scaling relationships that have been applied across sedimentary environments. It has also influenced a mix of empirical observations. In its contribution to palaeohydrology, several types of scaling relationships can be identified, including empirical-based scaling (e.g. BQART (Syvitski and Milliman, 2007), hydraulic geometry (Leopold and Maddock, 1953), downstream hydraulic geometry of tidally influenced river deltas (Sassi et al., 2012)), sedimentary characteristic-based scaling (e.g. Fulcrum (Holbrook and Wanas, 2014), regional hydraulic geometry scaling (Davidson and North, 2009)), and geomorphic scaling (e.g. bifurcation length-channel width scaling (Edmonds and Slingerland, 2007), avulsion-

backwater length scaling (Chatanantavet et al., 2012; Ganti et al., 2016a), avulsion-delta apex length (Hartley et al., 2017)), and other scaling relationships such as 2D analysis of clinoforms and clinothems sedimentation rates (Fig. 1).

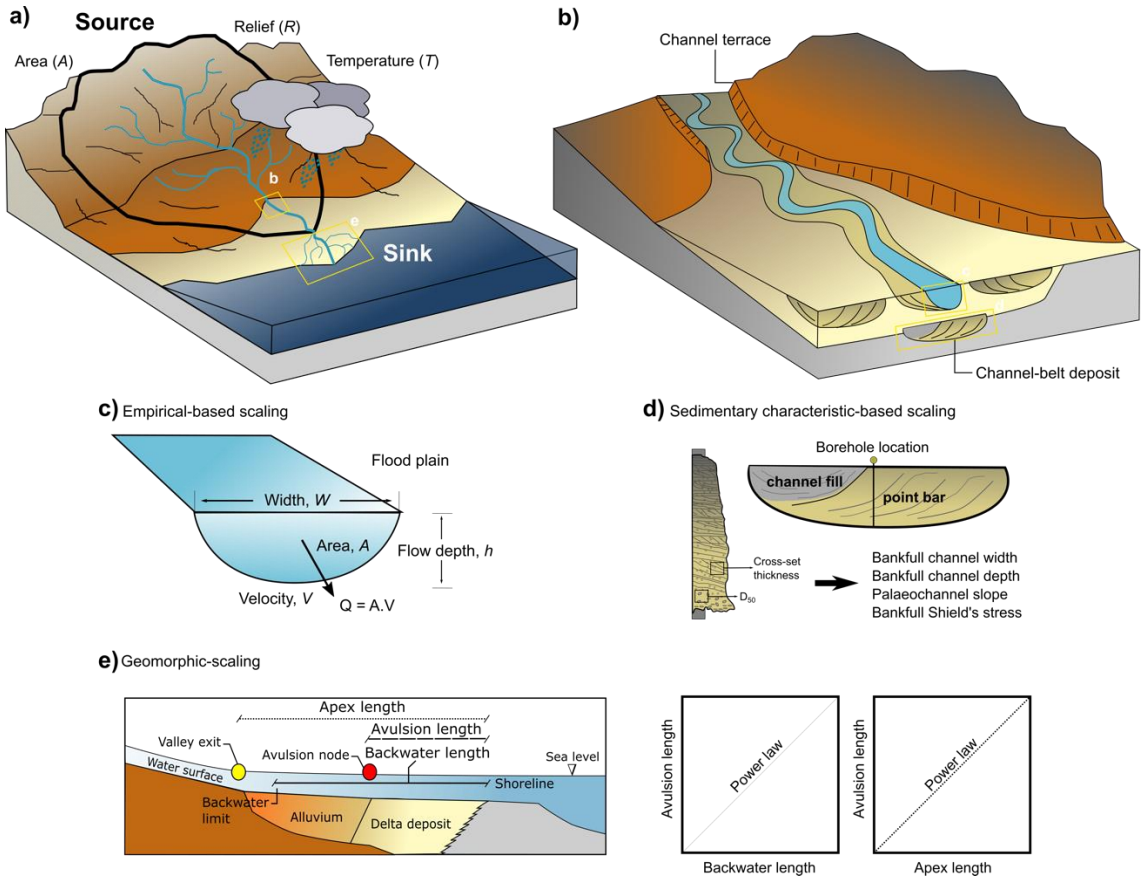

Figure 1.1 Schematic diagrams showing different classifications of scaling relationships. a) Source-to-sink diagram with notation of parameters being used in BQART model. Boxes in the diagram refer to more detailed picture shown in b) and e). b) River channel coming into an unconfined valley along with the channel-belt deposit produced underneath the surface. Inset boxes represent scaling explained in c) and sedimentary characteristic-based scaling in d). e) Geomorphic scaling produced by measuring the geomorphic elements of river deltas (e.g. backwater, apex, avulsion length) that commonly form power-law relationships.

The most recent empirical-based scaling is the 'BQART' model in which utilises catchment-scale parameters. Using global relationship between discharge *Q* and drainage area *A*, Syvitski and Milliman (2007) showed that *B* (human factor such as glacier erosion, trapping efficiency of lakes and man-made reservoirs), *R* (basin relief), *T* (temperature), also scale with sediment flux (*Qs)*, hence it is called the 'BQART' model. However, this model is quite challenging to be applied to the rock record due its parameters that can often be partially constrained. For example, estimating palaeotemperature, *T* requires palaeosols/mineralogy/biomes of flora and fauna combined with plate tectonic reconstructions that cumulatively adds uncertainty in relying to this model.

One of the most used scaling approaches is hydraulic geometry; a set of observationally derived, although theoretically justified (Ferguson, 1986), power law relationships produced to account for the inevitable consequence of channel size adjusting to the volume of water being conveyed. Leopold and Maddock's (1953) findings on the strong log-log trends relating water discharge to channel width, depth and velocity of numerous rivers in the western United States have been considered as the basis of the on-going studies of hydraulic geometry (Gleason, 2015a). Hydraulic geometry focuses on direct scaling relationships between the hydraulic properties of a river and its geometry (Fig. 1.2). When a river is at a low stage, the width of the river will be relatively smaller than when the river is at its high stage as the river discharge is a function of the channel width (Eq. 1.1), channel depth (h) and velocity (u) (Fig. 1.2; Eq. 1.1-1.3 (Leopold and Maddock, 1953). Since discharge (Q) is also directly related to the size of the catchment area contributing to the river system (A) (Eq. 1.4), channel width (w) also scales with catchment area (A).

$$w = aQ^b \tag{1.1}$$

$$h = cQ^f \tag{1.2}$$

$$u = kQ^m \tag{1.3}$$

$$A = \gamma Q^\beta \tag{1.4}$$

with the coefficients (a, c, k, γ) and exponents (b, f, m, β) derived empirically from repeat measurements (Leopold & Maddock, 1953). From the continuity equation $Q = W.h.u$, it follows that $a.c.k = (b+f+m) = 1$. The values of b, f and m are constrained by the hydraulics of water flow (Ferguson, 1986).

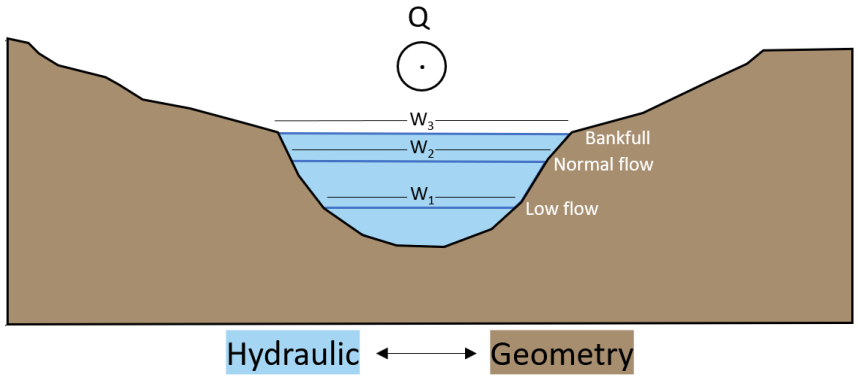

Figure 1.2 Schematic diagram showing the cross section of a river with different flow stages. Q represents river discharge; w represents the river width with notation number represents different flow stages.

Sedimentary characteristic-based scaling relationships (i.e. Fulcrum method; Holbrook and Wanas, 2014) estimate channel dimensions and palaeohydrology from sedimentary

characteristics found in the rock record. Fulcrum method assumes dynamic equilibrium between volume of sediment transported through a trunk channel with the eroded and deposited sediment upstream and downstream of a trunk channel. Bankfull flow depths are measured from the thickness of fully preserved fining-upward facies successions or from average thickness of dune-scale cross-sets. While the bankfull widths are estimated from the empirical relationship or from point bars (Bhattacharya et al., 2016; Brewer et al., 2020). The sedimentary characteristics (e.g. grain size, sorting, bedforms) are used to quantify the bed shear stress and to infer flow regimes and consequently the palaeoslope. Integrating the bankfull depth, width, and bed shear stress, bankfull discharge could then be estimated using a suspended sediment transport equation (e.g. van Rijn (1984)). Similarly, regional hydraulic geometry curves (Davidson and North, 2009) estimate bankfull channel depth and width from the thickness of palaeochannel fill and point bars measurement, respectively. Afterwards, bankfull discharge is estimated through estimating the catchment area (A) from the bankfull flow depth (h_c) due to $h_c = nA^r$ and $Q = \Psi A^\varsigma$ direct scaling relationships.

Geomorphic scaling in river deltas has been considered as the crucial factor in defining the location of delta avulsions and how delta lobes grow through time (Chatanantavet et al., 2012; Ganti et al., 2016a) due to the empirical finding of avulsion-backwater length scaling from 15 natural deltas. However, Hartley et al. (2017) argued that an avulsion node, that they referred to as the delta apex, is primarily controlled by processes at the valley mouth where unconfined deposition commences. The position of the valley mouth coincides with the location of a longitudinal slope break that triggers the onset of delta construction in an unconfined setting, due to sediment transport capacity being reduced downstream from this location to the shoreline. Thus, there should be spatial correlation between valley mouth locations and avulsion node positions. However, valley mouth location is not necessarily the upstream limit of the coastal backwater length, the length of which depends directly on sea-level and inversely on bed slope. Hence, for deltas in equilibrium with external controls, Hartley et al.'s (2017) results suggest 1:1 scaling relationships between both the avulsion (L_a) and slope break (L_s) lengths measured from the shoreline and the valley-exit-to-shoreline distance (L_v).

In mitigating the challenges of understanding geomorphic response of modern and ancient river deltas, scaling relationships have been considered as one of the most useful approaches to understanding complex hydrographic patterns (Seekell et al., 2021). Despite numerous applications in river systems, to date very few river delta studies have benefited from this

scaling relationship concept (Sassi et al., 2012; Edmonds & Slingerland, 2007), despite its potential effectiveness in predicting a system's growth. Adopting empirical-based scaling concepts to river deltas should, however, maintain assumptions associated with the hydraulic geometry concept, namely rectangular channel cross section and is in a dynamic equilibrium state. Directly adopting the hydraulic geometry concept from river systems for deltas is not straightforward due to the different geomorphic processes that occur in river deltas, as explained above.

In a river delta, hydraulic geometry relationships may not be as straightforward as in a fluvial system because of these two factors: distributary/multiple channels pattern and flow bidirectionality. Multiple channels on delta plain parallelly transport water and sediment downstream. From the continuity equation, the total discharge of a channel feeding into a delta plain should be equal to the sum of discharges of each individual distributary channel (Fig. 1.3). Due to the interaction of a river delta with a standing body of water, there is a backwater influence that create morphological complications in applying hydraulic geometry concept to a river delta (Fig. 1.3). In this backwater-influenced region, downslope discharge may not be perfectly correlated with the hydraulic geometry like in a fluvial system.

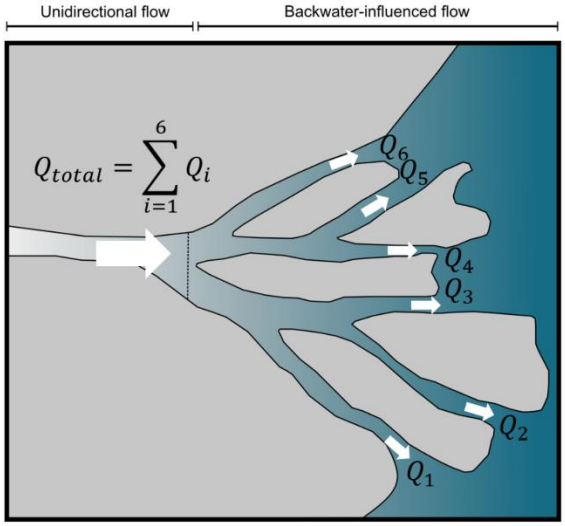

Figure 1.3 Schematic diagram of discharge partition in a river delta.

1.4. Aims and research questions

The aim of this thesis is to achieve a globally consistent scaling relationship between avulsion and backwater length, discharge-catchment area and discharge-distributary channel

width and investigate its implication for the modern and ancient deltaic deposits. In detail, the research questions (RQ) to be addressed in this thesis are:

RQ1. *Can a globally consistent avulsion-backwater length scaling relationship be derived for river deltas?*

RQ2. *What are the implications of the scaling relationships found from modern river deltas for our understanding of the growth and internal dynamics of river deltas?*

RQ3. *To what extent is the scaling relationship found from the modern river deltas applicable to deltaic deposits?*

To address these questions, morphometric parameters were collected from 114 modern river deltas distributed across five climate regions. The scaling relationships found from the modern river deltas are then tested to the rock record by compiling the palaeodischarge values from three Cretaceous deltaic deposits.

1.5. Thesis structure

The goal of this thesis is to fill the gap in our existing knowledge about morphometric scaling relationships in river deltas, from both modern and ancient systems. Morphometric variables were measured to build scaling relationships that could progress the debate about backwater-avulsion length or slope-break-avulsion length by using a large global dataset. Based on the findings from modern deltas, a suite of numerical model scenarios to understand the scaling relationships found from the modern system is built. The mechanics of avulsions and bifurcations on river deltas affected by this scaling relationship is investigated in this thesis. I tested the discharge-channel width and discharge-catchment area scaling relationships which I found in the modern river deltas to the rock record by comparing the palaeodischarge estimated using my scaling relationships to the palaeodischarge estimated from the Fulcrum method. This rock-record focused approach aims to produce a practical method for palaeodischarge estimation from the rock record, to complement previous approaches such as BQART and Fulcrum. After a methodological overview, the thesis is structured as the compilation of the manuscripts submitted or published in scientific journals that answer each research question proposed earlier.

Chapter 3 addresses research question (RQ) 1, to investigate the consistency of the backwater-avulsion length scaling relationship using a large global river delta dataset. Chapter 4 discusses the implications of the findings of globally consistent scaling relationship from Chapter 3 for understanding of how river deltas grow and autogenically interact (RQ2). From a compilation of distributary channel widths, delta catchment areas and river discharges from modern deltas, novel channel width-discharge and catchment area-discharge scaling relationships are developed specifically for river deltas in Chapter 5, along with discussion of their implications for understanding ancient deltaic deposits (RQ3). Chapter 6 discusses the limitations and practical sampling criteria deriving from the findings in Chapter 5 to other delta types such as wave- and tide-dominated deltas (RQ3). Afterwards, findings from each chapter are synthesised in Chapter 7 along with an assessment of their contribution, evaluation and suggestions for further work.

In chapter 3, avulsion lengths from global river deltas are found to consistently scale with slope break lengths measured from the delta shoreline. Other scaling relationships are determined that are consistent with previous findings of Hartley et al. (2017) and Ganti et al. (2016). However, the slope break-avulsion length scaling relationships preside over the previously found scaling relationships in all climate settings and all valley types. This finding in Chapter 3 opens the opportunity to explore alternative hypotheses for the controls on delta development. Along with the possible processes that produce these scaling relationships, a framework is proposed for understanding delta lobe building by dividing a delta into bedslope- and backwater-mediated zones. The proposed framework allows potential insights into how delta systems will respond to changing boundary conditions. This framework also contributes to our understanding of the location of avulsion nodes in a delta system that has potential significance for the large populations that live on the world's delta plains.

Chapter 4 focuses on the influence of slope break-avulsion length scaling relationships in the mechanics of avulsion and bifurcation in river deltas. A suite of morphodynamic numerical experiments was undertaken using scenarios that had various slopes upstream of the delta plain that cover the magnitude of natural river delta slopes. The numerical models allow calculation of avulsion and bifurcation timescales during the growth of a delta. The experiments used a static water level boundary condition to isolate the allogenic sea-level forcing that acts on river deltas. By eliminating this allogenic forcing, the model results produce a novel understanding of autogenically-controlled avulsion and bifurcation. From

the numerical model, delta topset slope serves as the first-order control of autogenic avulsion. Furthermore, by correlating the delta topset slope and avulsion timescale from the model with that in natural deltas, consistent agreement is found, justifying the reliability of the model built in this study.

Chapter 5 moves the focus from the modern system and numerical modelling to deltaic deposits. From the compilation of distributary channel widths, delta catchment area and river discharges from modern systems, novel channel width-discharge and catchment area-discharge scaling relationships are calculated specifically for river deltas. These scaling relationships were determined for individual climatic regions and were applied to examples of deltaic deposits from the rock record to estimate palaeodischarges of these deltaic deposits. By comparing these results with previous palaeodischarge estimates using the Fulcrum method, the scaling relationships proposed here produce the same order of magnitude of estimated palaeodischarge but based on significantly fewer input parameters that need to be estimated from the rock record. These rock-record focused scaling relationships will benefit sedimentologists working on decoding palaeodischarge values from ancient delta deposits.

In Chapter 6, the assumptions used in building scaling relationships in river deltas that are based on the hydraulic geometry concept are considered. The assumption of unidirectional flow needs the scaling relationships from Chapter 5 to be sub-divided to take account of the marine influence that can reduce the dominance of the unidirectional river current. Hence, distributary channels measured along the delta plain are divided into ‘upstream’ and ‘downstream’ parts for each river-, wave- and tide-dominated delta to establish more detailed scaling relationships based on the influence of marine forcing reflected in the distributary channel width patterns. The calculation of discharge/palaeodischarge of a river delta could benefit from applying the hydraulic geometry concept for river- and wave-dominated deltas, but not for tide-dominated deltas since there is no statistically significant discharge-channel width relationship found in tide-dominated deltas.

Chapter 7 summarises the findings presented in Chapters 3 to 6 and then syntheses the overall contribution of this study to the scientific community working with the rock record, numerical models, or modern river deltas. The study is then evaluated and suggestions for further work are presented.

Chapter 2 – Methods

Investigations conducted to understand river delta morphodynamics can use data from three different approaches: modern 'natural' river deltas, synthetic river deltas produced by numerical or laboratory simulation model, and deposits of ancient river deltas. Even though each of the following chapters has associated methods presented, Chapter 2 contextualises methods for the whole thesis. The chapter is presented based on these three perspectives of river deltas, with the section on synthetic river deltas coming from numerical simulation. From the modern deltas, the next sub-section 'Modern river deltas observation' is linked to Chapters 3, 5 and 6, to answer the first research question about the consistency of backwater-avulsion length scaling relationship and the third research question about the extent of the scaling relationship found from the modern river deltas applicable to deltaic deposits. I give an overview of satellite imagery that was used to observe modern river deltas and the morphometric measurements I acquired. Afterwards, the following sub-section 'Synthetic river delta observation' is linked to Chapter 4. It answers the second research question about the implications of the scaling relationships found from modern river deltas to our understanding of how river deltas grow, by presenting an overview of the numerical modelling and morphometric measurements that was subsequently acquired. The last section 'Ancient river deltas observation' of this chapter discusses the methods I used to collect the dataset from the ancient river deltas to answer the third research question, linked to Chapter 5 and 6.

I cover 114 river deltas located across arid, cold, polar, temperate, and tropical climate regions to cover the global distribution of river deltas (Fig. 2.1). Criteria for selecting the modern river deltas include any channel mouth that intersects with the open seawater depositing sediment that protrudes beyond the lateral shoreline, with or without the characteristic morphology of river-dominated deltas (e.g. subaerial mouth-bar deposit, elongate distributary channels) (Olariu and Bhattacharya, 2006). A sub-set of ten deltas, defined as wave-dominated by Nienhuis et al. (2020) and 7 tide-dominated deltas, are also investigated.

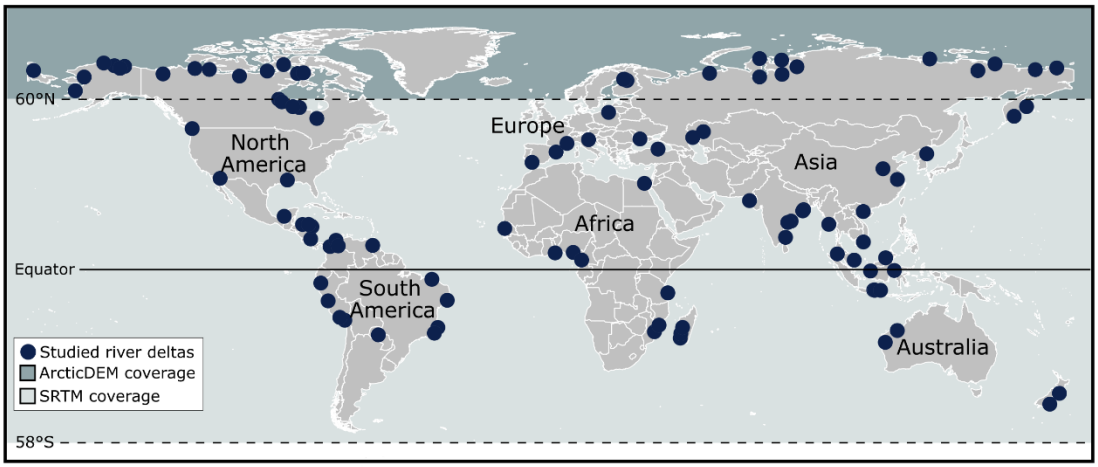

Figure 2.1 Global distribution of the 114 studied deltas. Different colour shades represent the coverage of satellite imageries used in this study.

2.1. Modern river deltas observation

2.1.1. Satellite data overview

Landsat 5 and digital elevation models (DEMs) from the Shuttle Radar Topographic Mission (SRTM) and ArcticDEM were used to acquire morphometric measurements from modern river deltas. I used Landsat 5 Thematic Mapper (TM) with calibrated top-of-atmosphere (TOA) reflectance to accommodate the oldest satellite image available (i.e. 1984) to minimise the anthropogenic effects such as channel diversion, dams, levee protection and bridges that may directly influence the river delta geometry. Eventhough I acknowledge that the boom in large dam construction was mainly around 1950s globally (Wang et al., 2022). The TM sensor offered better spatial, spectral, radiometric and geometric performance than the earlier Multispectral Scanner (MSS) sensor as in Landsat 1, 2 or 3 (Chander et al., 2009). The spatial resolution of Landsat 5 is 30 m (Table 2.1) for the six reflective bands and 120 m of the thermal band (Markham et al., 2018). The short-wave infrared (1.55 - 1.75 µm), near infrared (0.76 - 0.90 µm) and blue band (0.45 - 0.52 µm) from the Landsat 5 were extracted from those satellite imageries to better distinguish the water from the land and to increase the confidence in morphometric measurement. By choosing the near- and short-wave-infrared, water will look darker due to all light at these wavelengths being absorbed by water.

A DEM is a generic name for topographic information that describes the Earth surface. DEM can be a Digital Surface Model (DSM) that describes topographic information that includes surface features such as vegetation and built structures (Mudd, 2020) or a Digital Terrain

Model (DTM) that describes the representation of the Earth's surface with the built and natural surface features removed; also referred to bare-earth. The DEMs used in this study consist of the Shuttle Radar Topography Mission (SRTM) and ArcticDEM. SRTM was launched in February 2000 and covered the land surface between latitudes of 60 degrees North and 58 degrees South with approximately 90 m resolution near the equator (Farr et al., 2007) (Fig. 2.1; Table 2.1). The SRTM dataset was verified with over 2 million ground check points producing 90% absolute linear errors between 5-9 m with the greater 10% errors likely be concentrated in mountainous regions (Rodríguez et al., 2006). To cover area beyond 60 degrees North, ArcticDEM covers the North of 60 degrees latitude Earth's surface with the spatial resolution of 2 meters (Fig. 2.1; Table 2.1) (Morin et al., 2016; Mudd, 2020). The average accuracy of ArcticDEM is 0.1 ± 0.07 meter when being compared to ICESat data (Mudd, 2020).

Dataset	Spatial resolution	Visit interval	Temporal coverage	Spatial coverage
Landsat 5 TM	30 m	16 days	1984-2012	Global
SRTM	30-90 m	Single	2000	60°N-54°S
ArcticDEM	2 m	Single	2016-2018	North of 60°N

Table 2.1 Dataset used in this study (modified from Gorelick et al., 2017)

The Landsat and DEMs dataset were extracted using Google Earth Engine (GEE), a cloud-based platform with a multi-petabyte geospatial dataset provided by Google (Fig. 2.2) (Gorelick et al., 2017). The code was written in this platform to extract the desired data (Appendix 1). Firstly, a polygon was manually drawn around each delta (N=114 river deltas). The polygon covered the delta region up to the first exit valley of the fluvial region. The oldest available images were then chosen to avoid anthropogenic impacts such as sand mining that reduces sediment delivery to the ocean, dike building, riverbank construction. I do not use globally available delta dataset due to their exclusion of single channel delta (Caldwell et al., 2019) and equivocal delta definition that includes all rivers mouths without any delta deposit (N=10.848 deltas) (Nienhuis et al., 2020). The stacked imageries were then sorted based on the cloud cover. The least cloud cover was mosaicked and extracted to the Google drive platform to be analysed locally in ArcMap software. Since the oldest composite images (1984) rarely satisfy the cloud cover defined in the code, relatively wide variance of images taken dates must be compromised in this study.

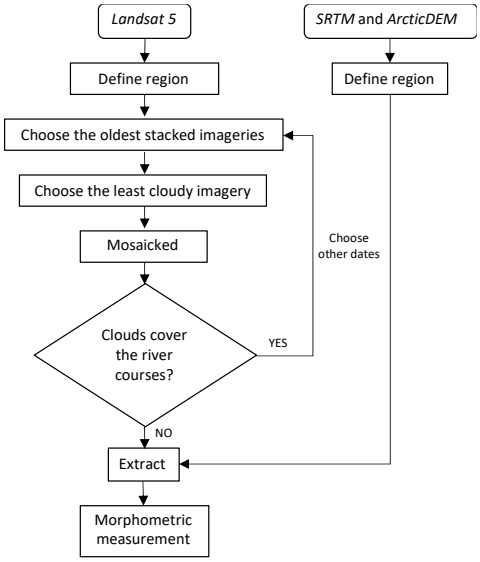

Figure 2.2 Flow diagram showing the process of extracting Landsat and Digital Elevation Model (SRTM and ArcticDEM) rasters from the Google Earth Engine (GEE) platform. This method was run using JavaScript within GEE.

2.1.2. Morphometric measurements from the modern river deltas

Several morphometric parameters are measured in this study to answer the research questions about the consistency of avulsion-backwater lengths scaling relationships and about the applicability of the scaling relationship found from the modern river deltas to deltaic deposits. Morphometric measurements were manually digitised using ArcMap software. All the Landsat and DEMs data were projected using WGS84 reference system and processed in the ArcMap software (10.6.1). Using the Landsat data, avulsion length was measured as the river distance from the longest distributary channel to the first avulsion node. When there is only a single distributary channel with no bifurcation, avulsion length is measured up to the farthest upstream valley exit identified from its DEM, following the method from Hartley et al., 2017. Like the avulsion length, valley-exit-to-shoreline length was measured as the river distance from the shoreline to the valley exit point identified from the DEMs (Hartley et al., 2017). Please refer to Fig. 3.6 to see examples of the measured avulsion length, valley-exit-to-shoreline length and calculated backwater length produced from this study.

Backwater length (L_b) was calculated (Chatanantavet et al., 2012) as:

$$L_b = \frac{h_c}{S} \tag{2.1}$$

$$h_c = \left(\frac{C_f {Q_c}^2}{g {W_{av}}^2 S}\right)^{\frac{1}{3}} \quad (2.2)$$

where h_c is the characteristic flow depth (m) and S is water surface slope (m/m) (Eq. 2.1). Characteristic flow depth (Eq. 2.2) was calculated using the bed friction coefficient C_f = 0.002 for large lowland rivers (Parker et al., 2007). Q_c is the characteristic water discharge (m^3/s), g is gravitational acceleration (m/s^2) and W_{av} is the channel width (m) at the avulsion node at the time of the image (Parker et al., 2007). Characteristic water discharge (Q_c) is taken as the 2-year recurrence interval flood (Q_2) as close to the upstream limit of the delta as data availability allows, to provide an indicator of the dominant channel-forming flow (Wolman and Miller, 1960; Ganti et al., 2016a). Q_2 was calculated from daily river discharge data available from the Global Runoff Data Centre (GRDC; https://www.bafg.de/GRDC/EN/Home/homepage_node.html). Channel width (W_{av}) was measured on the Landsat imagery at the avulsion node to avoid influence by wave or tidal processes. Slope (S) was calculated from the water elevation profile along the centreline of each river.

Measuring the slope break lengths involved pre-processing the DEMs. ArcMap's 3D analyst toolbox was used to build the elevation profile along one active and longest distributary channel course from the shoreline up to the valley exit point identified earlier (Hartley et al., 2017). Since SRTM and ArcticDEM data consist of scattered error values caused by various factors like speckle noise, vegetation, man-made objects, water surface, filtering and smoothing techniques were needed to build a 'clean' elevation profile. Locally weighted polynomial regression (lowess) was found to be an ideal technique to effectively removing outlier values, while maintaining the shape of the longitudinal river long profile, including major breaks in slope and knickpoints (Aiken & Brierley, 2013).

Lowess is a method for smoothing the scatterplot data (i.e. elevation) using the fitted value that comes from a polynomial fit to the raw data using weighted least squares (Cleveland, 1979). The weight is a function of a distance between data points, with the decrease in weight representing the increase in distance. Lowess was undertaken in R software, where the user needs to input the weight value Sm in which $0<Sm\leq1$. By choosing the bigger value, the variability in the smoothed points will be minimised without distorting the pattern in the data (Cleveland, 1979).

Filtering the raw data involved finding the most conformable lowess curve and removing the values bigger than 1- or 2-times standard deviation in every 100 data points from this fitted curve (Fig. 2.3a). The fittest curve was then iterated again using the same lowess method from the filtered data to find the best smoothed curve (Fig. 2.3b). The best smoothed curves using the same *Sm*-value could either come from the raw or the filtered data and the lowess smoothed curve from the filtered data mostly faced difficulty in preserving the overall data especially in the start and end points because of the nature of the method. To mitigate this, the lowess smoothed curves from the raw data which showed a better fit most of the time, used in this study as the final elevation profile (Fig. 2.3c). The final filtered and smoothed data were then used to identify the location of the slope breaks.

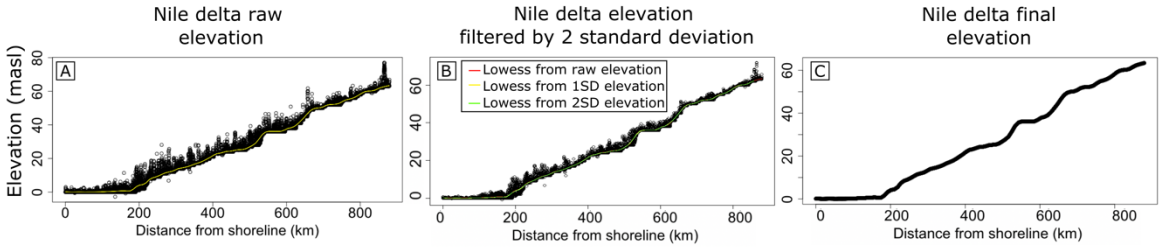

Figure 2.3 Filtering and smoothing elevation profile from the Nile Delta (a) raw elevation profile extracted from the SRTM data with lowess curve using *Sm* = 0.035 fits the raw data (b) filtering the elevation profile by removing elevation values beyond 2-times standard deviation from the smoothed curve and choosing the best fitted lowess curve with *Sm* = 0.035 (c) result of the filtering and smoothing process.

The slope break locations were identified using semi-automated slope break extraction method coupled with Hack Stream-Length (SL-index) to justify the location of the slope break (Hayakawa & Oguchi, 2006; Hack, 1973). Hayakawa and Oguchi (2006) used long profile geometry to isolate slope breaks based on their gradient (*Gd*) values. I defined *l* as the horizontal length used in calculating *Gd* (Eq. 2.3). The *l* value should be at least two times the distance between two adjacent measurement points to accommodate local gradient changes. As an example, the averages of two adjacent measurement points in Nile delta are ~90 m, and ~30 m for the Comal delta, thus using *l* = 180 m for the Nile and *l* = 60 m for the Comal would be appropriate. The *l* value was then multiplied by 2, 3, 4, and so on to test the sensitivity of the gradient measurement towards the *l* value (Fig. 2.4).

The gradient (*Gd*) is then:

$$Gd = \frac{E_1 - E_2}{l} \tag{2.3}$$

where E_1 and E_2 are the elevations of upstream and downstream points $l/2$ away from the measured elevation obtained from the DEMs (Fig 2. on Hayakawa and Oguchi, 2006). I then calculated the relative steepness (*Rd*) as:

$$Rd = \frac{Gd}{l} \tag{2.4}$$

and plotted this against distance from shoreline from different *l* values (Fig. 2.4). The slope break location is defined by *Rd* > *SD(Rd)*, with the standard deviation of *Rd* being *SD(Rd)*. I then measured the distance from the delta shoreline to the first slope break across our global dataset. To justify the location of the first slope break, I calculated the Hack *SL*-index from above and below the slope breaks (e.g. represented as values in parentheses in Fig. 2.4) (Hack, 1973; Zaprowski, et al., 2001). Higher *SL*-index values indicate steeper longitudinal profiles.

The above method gave consistent results across different delta sizes and gradients. Since this method is very sensitive to elevation change, it is suited to extracting slope breaks in lowland deltaic rivers which have very low slopes (up to 3 orders of magnitude lower than in typical fluvial systems) and over long distances (3 orders of magnitude longer than the rivers investigated by Bishop et al. (2005) and Hayakawa and Oguchi, (2006). Fig. 2.4a-c and Fig. 2.4d-e show the reliability of this method in detecting the first slope breaks from both cases with visibly sharp (e.g. Nile delta) and very gentle changes in channel gradient in small delta (e.g. Comal delta). Nonetheless, manual visual inspection is still needed to supervise the location of the first slope break in sub-vertical resolution changes of channel gradient (~5-8 meter absolute vertical accuracy for the SRTM globally) (Rodríguez et al., 2006).

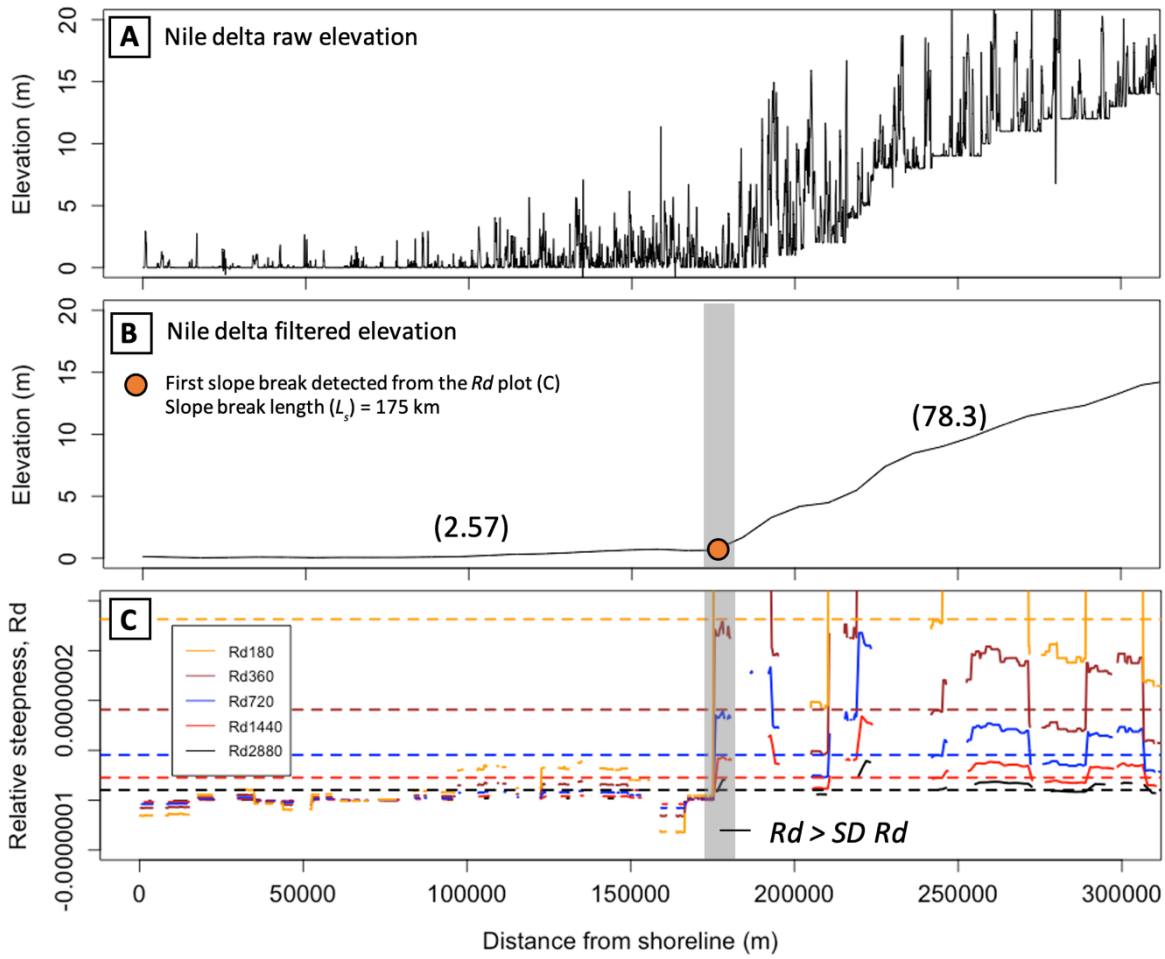
A
Nile delta raw elevation
Elevation (m)
0
5
10
15
20
B
Nile delta filtered elevation
First slope break detected from the Rd plot (C)
Slope break length (L_s) = 175 km
(2.57)
(78.3)
C
Rd180
Rd360
Rd720
Rd1440
Rd2880
Rd > SD Rd
Relative steepness, Rd
-0.0000001
0.0000002
0
50000
100000
150000
200000
250000
300000
Distance from shoreline (m)

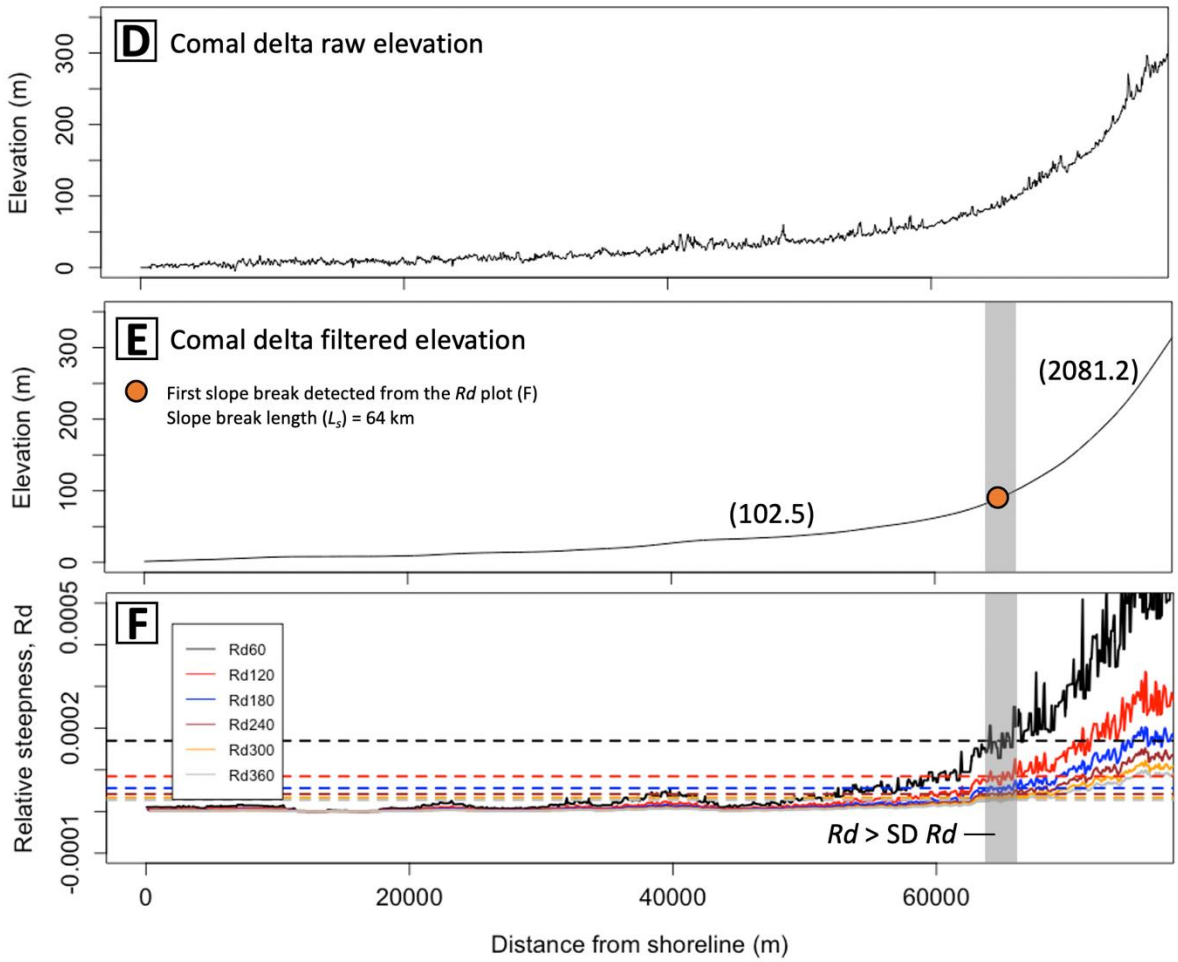

Figure 2.4 Elevation profile filtering and slope break detection process from the Nile (a-c) and Comal (d-f) deltas. (a,d) Raw elevation profile with spikes of error (~5-15 meter) from the Nile and Comal deltas; slope breaks were difficult to define from the raw data. (b,e) Filtered elevation profile using lowess method with Hack *SL*-index value in parentheses. (c,f) Relative steepness (*Rd*) against distance from shoreline plots from Nile and Comal delta respectively. Colour represents different *Rd* plot using different *l* values with the horizontal dashed lines represented each standard deviation for each *l* value. The point where *Rd* values that are larger than the standard deviation (SD) *Rd* are considered as slope breaks. We focus only on the detection of the first slope break. Thus, slope breaks detected upstream of the first slope break will be neglected, as in Nile delta. The slope break length (L_s) was then measured as the distance from the shoreline to the first slope break as seen from the filtered elevation profile (B,E).

Using Landsat imagery, I measured channel width across 114 global river deltas from the shoreline to the delta apex assuming that the first delta avulsion is a delta apex (Jerolmack & Swenson, 2007). I adopted channel width measurements from Sassi et al. (2012), in which a semicircular grid *s/L* is used to define a dimensionless distance from the delta apex point to the shoreline, where *s* represents along river distance from the delta apex to the shoreline and *L* is the channelized distance along the longest distributary channel (Fig. 2.5). This grid allows the measurement of the widths of multiple distributary channels located at the same dimensionless distance from the apex point, allowing comparison across different sizes of deltas. The semicircular grid has a resolution of ~10 times the width of the river channel at the first avulsion point to maintain consistent dimensionless distance and data frequency across deltas of varying size. Only channel widths along distributary channels were included,

excluding tidal creeks and any other non-riverine channels. Please refer to the Chapter 5 and 6 for details of the channel measurement method.

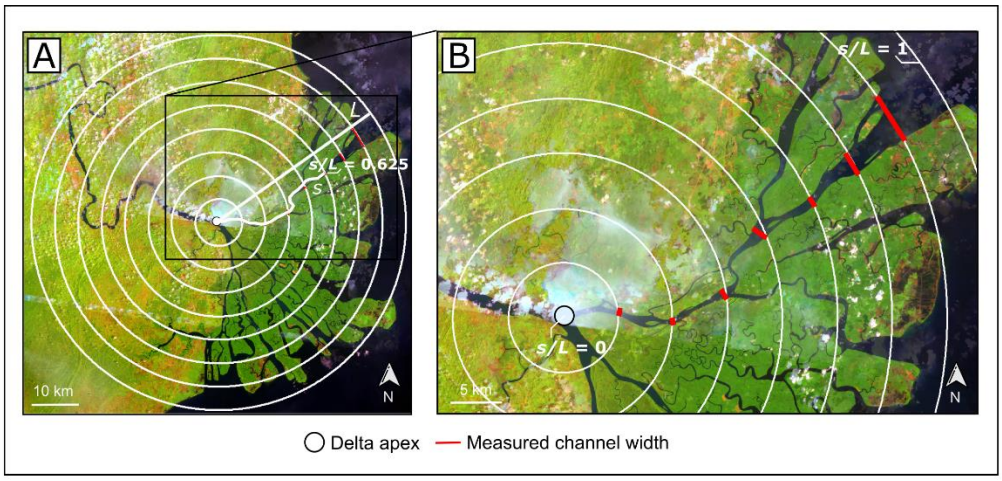

Figure 2.5 a) Semicircular grid *s/L* method to measure the channel widths from Mahakam delta, Indonesia (0°34'58.9"S, 117°16'39.7"E). b) Inset image shows the more detailed semicircular grid used for measuring one of the northeast distributary channels. Measured channel widths are red lines shown across wetted distributary channels. The spacing of the circular grid is ~10 times the channel width at the upstream limit of the delta. Stitched Landsat 5 images were taken from January 1994 via Google Earth Engine (GEE).

2.1.3. Global dataset used from the modern river deltas

To build the scaling relationships from modern river deltas, I compiled the morphometric measurements explained before with other global datasets. The first global dataset I used was the global river discharge available from the Global Runoff Data Centre (GRDC) with the gauge located as close to the upstream limit of the delta as data availability allows, to provide an indicator of the dominant channel-forming flow (Ganti et al., 2016; Wolman & Miller, 1960). Q_2 was calculated from daily river discharge data available from the Global Runoff Data Center (GRDC) using 'fasstr' package in R. Compiled table is available in the Table S1 of Prasojo et al. (2022).

Daily discharge across multiple years available from the GRDC is plotted along with their percentiles in Fig. 2.6a. From this data, 'fasstr' will then extract the dominant flow for specific recurrence interval as the input (Fig. 2.6b). This R package works by finding the correlation between the recurrence intervals (or probability of the return period) with their consecutive discharges. The correlations were then approached by producing several empirical functions that are based on the event intervals (e.g. 1-day, 3-day up to 30-day). I used the 1-day interval empirical function to define the discharge value that has 50% probability or 2-year recurrence interval as the dominant channel-forming flow (Wolman and Miller, 1960; Ganti et al., 2016a).

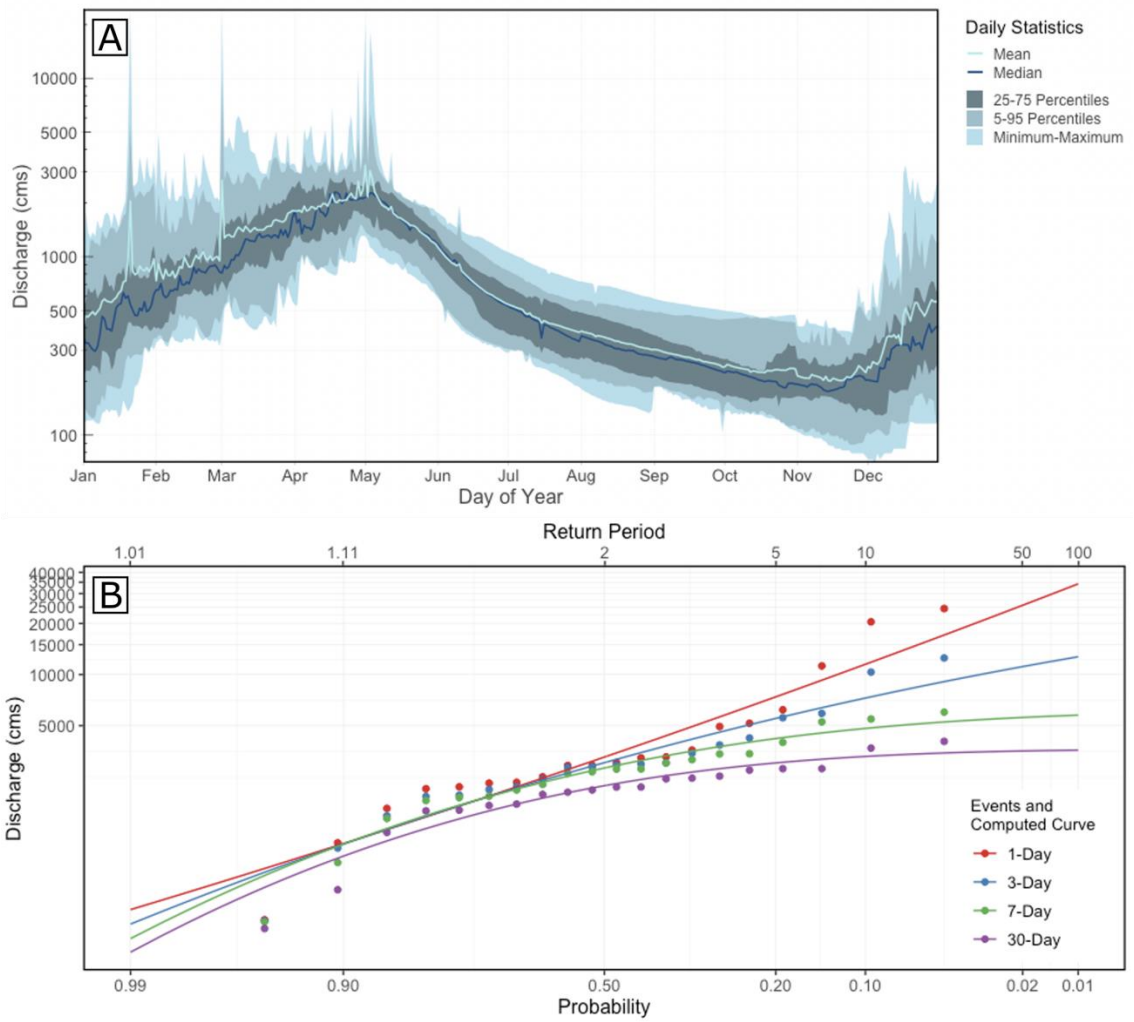

Figure 2.6 a) Hydrographs representing the whole dataset of daily discharge values from Rufiji River delta using the 'fasstr' package in R. b) Return period-discharge empirical functions built using the daily discharge dataset from the same river delta. The computed empirical functions were built automatically using several event intervals (e.g. 1-day, 3-day, 7-day and 30-day).

From 75 sites, 56 of these sites have daily mean discharge. However, at the other 19 sites, only monthly means were provided. To ensure comparability between the sites with daily and monthly flow data I then calculated transfer functions. As flow duration characteristics are climate-dependent, I adopted the Köppen-Geiger climate classification for this transformation (Fig. 2.7; Beck et al., 2018).

For both the daily and monthly discharge data sets, I calculated the 2-year recurrence interval flows (Q_{2daily} & $Q_{2monthly}$) using The Flow Analysis Summary Statistics Tool for R ('fasstr' package) as explained before. Q_{2daily} and $Q_{2monthly}$ were used to generate transfer functions using ordinary least square (OLS) regression for each climate zone (Fig. 2.7; Burgers et al., 2014). For the 19 sites where only the monthly discharge data are available, I obtained the 2-year recurrence interval or bankfull water discharge from these transfer functions.

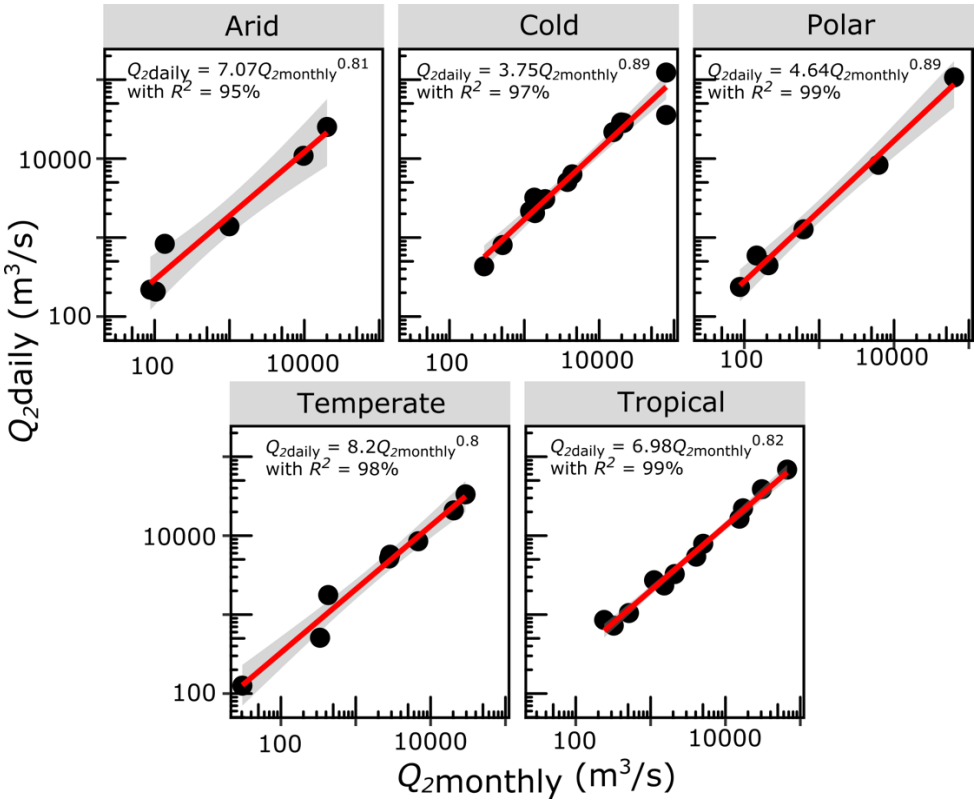

Figure 2.7 Transform function between monthly and daily discharge per climate. When only the monthly discharge data are available, 2-year recurrence interval (Q_2) or bankfull water discharge is obtained from the transform function applied separately to sites from each climate zone.

I also gathered another global dataset available from the HydroSHEDS that is freely available in https://www.hydrosheds.org/page/hydrobasins. I extracted the catchment area of 114 modern river deltas using the Pfafstetter Level 6 that allows sub-catchment delineation that contribute to the flow of river deltas. I then used these catchment area datasets to be used in ArcGIS by integrating it with other morphometric measurements (e.g. avulsion lengths, channel widths, slope-break lengths, etc). Please refer to the HydroSHEDS website for further details about Pfafstetter sub-basin delineation.

The last global dataset I used was the global river width that also covers the global distributary channel width studied here (Pavelsky et al., 2018). The Landsat-derived river width dataset is freely available from https://zenodo.org/record/1297434#.YfAwAfXP2dY. I used both the distribution of fluvial and delta channel widths measured in Pavelsky *et al*'s (2018) study to be compared with channel width measured manually in this study. The detail comparison of these datasets is explained in the Chapter 5.

2.2. Synthetic river deltas observation

2.2.1. Delft3D overview

I modeled several scenarios of deltaic processes using Delft3D software provided freely from the Deltares. Delft3D is a physics-based model that simulates the hydrodynamics and also morphodynamics of diverse environments such as rivers, estuaries, tidal and also river deltas (Edmonds and Slingerland, 2010; Caldwell and Edmonds, 2014; Nienhuis et al., 2018b, 2018a). The software has been validated for a wide range of hydrodynamic-morphodynamic environments, including self-formed rivers deltas (Edmonds and Slingerland, 2007, 2008; Geleynse et al., 2011; Nijhuis et al., 2015; Rossi et al., 2016; Williams et al., 2016; Nienhuis et al., 2018b; Morgan et al., 2020). The flow simulation is calculated through the depth-averaged, nonlinear, shallow-water equation from three-dimensional Reynolds-averaged Navier-Stokes equations (Edmonds and Slingerland, 2010). The velocity distribution in the model is then used to compute suspended and bed load transport (only suspended load is applied in the my model) and to update the bed elevation (or bathymetry) according to divergences in sediment transport (Caldwell and Edmonds, 2014). Please refer to Deltares (2021) for more detail of hydro-morphodynamic calculations.

2.2.2. Model design

The design of synthetic river deltas is based on the findings from the modern river deltas explained in Chapter 3. In the modern system, I have found that the avulsion nodes from 105 river deltas are more strongly correlated to the slope breaks locations in comparison to the previously known avulsion-backwater length and avulsion-valley exit length scaling relationships (Chatanantavet et al., 2012; Ganti et al., 2016a; Hartley et al., 2017). Since the location of the first avulsion or the first site of the delta first built is correlated with the slope break location, the model was designed to observe how the morphometric properties of river deltas also strongly correlate to the slope break location. This effort is to prove if the growth of river deltas is strongly correlated with the slope break as suggested from the modern river deltas observations (Prasojo et al., 2022; Chapter 3).

I extracted the slope values of upstream and downstream of the slope breaks identified in Chapter 3. I then calculated the ratio of upstream-downstream slopes from the 105 river deltas and extracted the representative percentiles values of the upstream-downstream slope

ratios (Fig. 2.8) to cover the overall distribution of upstream-downstream slopes from natural river deltas. The representative percentiles from the upstream-downstream slope distribution were then used to represent a range of upstream slope values in the model (Fig. 2.9).

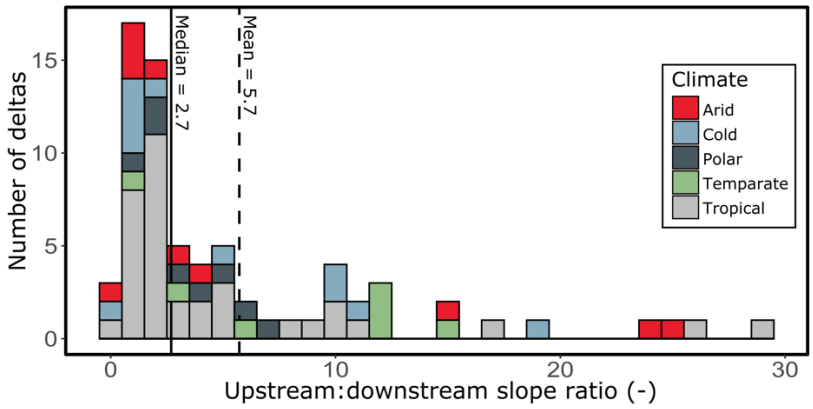

Figure 2.8 Distribution of the upstream (US) – downstream (DS) slope ratio from 114 modern river deltas distributed across five climate regions. The vertical line represents the median value with the dashed vertical line shows the mean value, respectively.

I adopted the geometry and parameters from a synthetic model ('scenario o') from Edmonds and Slingerland (2010) and Caldwell and Edmonds (2014). However, I modified the extent of the model to represent 7.5 km x 7.5 km area to accommodate the upstream slope break and slope-avulsion length scaling relationship that I found from the modern deltas (Fig. 2.10). Hence, I created 6 scenarios that represent models with 6 different upstream slopes that are comparable with the modern fluvial slopes (Cohen et al., 2018). I maintained other physical and numerical parameters constant across these 6 scenarios.

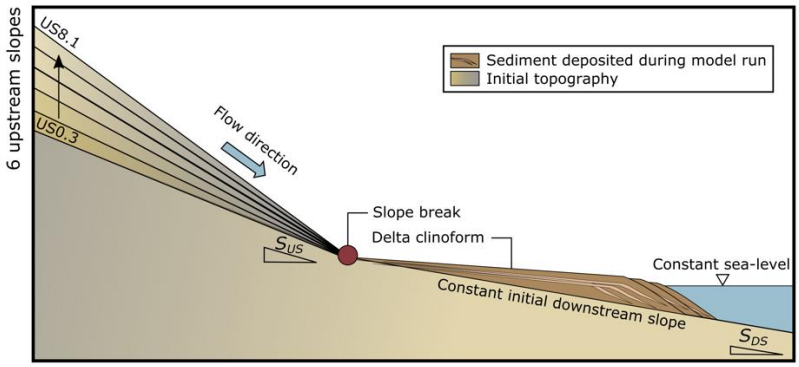

Figure 2.9 Schematic diagram of the model's design. The upstream slopes of the river delta models are from the representative percentiles from the upstream-downstream slope ratios from the modern river deltas shown in Fig. 2.8. The downstream is kept constant at 0.000375 adopted from the downstream slope of the modern Mississippi delta.

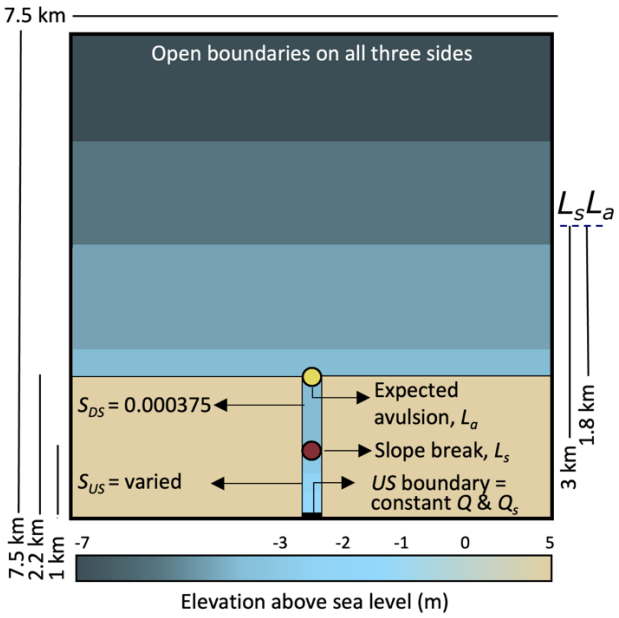

Figure 2.10 The map view of the model's design with L_a and L_s are avulsion length and slope break length, respectively. The avulsion-slope break length ratio is adopted from the modern system scaling relationship explained in the Chapter 3 (L_a:L_s = 6:10). *DS* and *US* are abbreviation for downstream and upstream. The non-erodible bed at 5 meter above sea level is assumed to represent non-erodible bed rock of natural delta.

2.2.3. Morphometric measurements from synthetic river deltas

Avulsion timescale has been analysed in river delta deposits using various approaches. Previously, the simplified avulsion frequency was calculated by harnessing the ratio between the aggradation rate over a single channel aggradation thickness necessary for avulsion (Jerolmack & Mohrig, 2007; Mohrig et al., 2000). However, this approach will only be useful in depicting avulsion timescale of a single channel that is not heavily influenced by the backwater such as in the fluvial system and does not take into account the role of multiple lobes and sediment partitioning between lobe aggradation and progradation. Hence, this approach will not fit to calculate the avulsion timescale in the region that is influenced by the backwater phenomenon with changing deposited lobes such as in river deltas.

Other approaches that consider the 2-dimensional expansion of river deltas are radially averaged model and channel-averaged model. The radially averaged model assumes the delta apex as a fixed point with sea-level rise causes delta radius to shrink until the sediment load is sufficient to keep delta top aggradation at pace with sea level. Consequently, aggradation rate in this model is enhanced during marine transgression because with a fixed delta apex, the delta land is reduced (Muto & Steel, 1997; Muto, 2001). Radially averaged model fits to calculate the avulsion timescale in a steep experimental fan delta with fixed

apex, but lowland deltas' apexes are not geographically fixed (backwater-scaled) (Chatanantavet et al., 2012; Ganti et al., 2016, 2014; Jerolmack & Swenson, 2007).

Similar to the simplified avulsion frequency harnessing the aggradation rate over a single channel, channel-averaged model constrains aggradation rate using sediment mass balance of a channel. It is based on the finding of Reitz et al. (2010) where they found the avulsions occurred in a fan-delta experiment to be at the rate sediment supply could fill the channel. Again, the discretisation of a single channel in this model could not take into account the backwater hydrodynamics, multiple lobes or sediment partitioning in delta plain.

The most realistic and recent analytical approach to calculate the avulsion timescale used in this study is from Chadwick et al. (2020) who developed a generic framework to predict the response of avulsion frequency to different rates of sea-level rise and fall. However, since no sea-level change is introduced in this study, I kept the parameter for sea-level change as zero. Nevertheless, several assumptions are introduced in Chadwick et al's model such as only one lobe is active at a given time, there is a distributive channel pattern instead of single channel as in previous models, sediment partitioning occurs between lobe topset and foreset, lobes are abandoned and reoccupied during avulsion cycle, and there is no other allogenic forcing (e.g. wave, ocean current, tide).

Chadwick et al. (2020) derived the avulsion frequency as:

$$f_a = \frac{1}{(1-\lambda_p)} \frac{Q_s}{(L_a - D)B_a H + DB_a \left(H_b + z + \frac{DS_{topset}}{2}\right)} \; if \; D \geq 0 \tag{2.5}$$

$$f_a = \frac{1}{(1-\lambda_p)} \frac{Q_s}{L_a B_a H} \; if \; D < 0 \tag{2.6}$$

$$D = (H - z)/S_{topset} \tag{2.7}$$

$$H = H^* h_c \tag{2.8}$$

with the bankfull depth is approached using Parker et al., 2007 method:

$$h_c = \left(\frac{C_f {Q_c}^2}{g {B_c}^2 S_{topset}}\right)^{\frac{1}{3}} \tag{2.9}$$

with f_A = avulsion frequency, Q_s = sediment load, B = lobe width of each avulsion, L_a = avulsion length, λ_p = sediment porosity, H = aggradation thickness necessary for avulsion, H^* = avulsion threshold = 0.2-1.4 in lowland deltas (Ganti et al., 2019), h_c = bankfull depth, C_f = bed friction coefficient, Q_c = bankfull discharge, B_c = channel width at avulsion node, S = topset slope, D = lobe-progradation distance, z = sea level rise.

In using this analytical approach, I assume the avulsion threshold (H^*) to be 0.5 that is realistic for lowland deltas (Ganti et al., 2019) and $D > 0$ since there is no allogenic forcing applied in my model that makes a delta to regress. Sediment porosity (λ_p) is assumed to be 0.4 (Jerolmack, 2009), bed friction = 0.002 for lowland rivers (Parker et al., 2007), bankfull discharge = 1050 m^3/s as the representative value of global river delta discharge (Edmonds & Slingerland, 2010; Caldwell & Slingerland, 2014) and sea level rise (z) to be 0 since I did not introduce sea-level change in my numerical models. Sediment load (Q_s) is kept constant by measuring it from the inlet of the river delta once the model has reached a dynamic equilibrium phase.

Parameters mentioned in the equations 2.5-2.9 such as Q_s and Q_c were extracted directly from DELFT3D-QUICKPLOT, a Delft3D visualisation and animation of numerical data in-house software. Geomorphic parameters (B, L_a, B_c, and S) were measured manually in ArcGIS by extracting bathymetry of each simulation timestep during the delta building process from DELFT3D-QUICKPLOT. I also measured the foreset and bottomset slope of each simulation timestep even though they were not used for analyses.

Bifurcation timescale is adopted from the fractality concept in mouth bar repeated deposition process. To build a river delta, a river containing water and sediment facing relatively standing body of water (e.g. lake or sea) will start to deposit the sediments as a mouth bar due to the decreasing sediment transport rate because of deceleration of the flow due to its rapid expansion in cross-sectional area (Edmonds & Slingerland, 2007; Olariu & Bhattacharya, 2006). This sediment-laden channelised flow will then be split to flow around the mouth bar deposit instead of on top the mouth bar deposit once the thickness of the mouth bar deposit reaches 0.4 of the total water depths (Edmonds & Slingerland, 2007). The mouth bar deposition process repeats until they form a branching-like delta plain that follows the fractality concept that opens the opportunity to predict the growth law of river delta plains.

Previously, Wright & Coleman (1971) discovered that a distributary channel length (L_D) in between bifurcated points located in a delta plain scale with the channel width upstream of the bifurcation (B_b) ($L_D \approx 10B_b$). For a river delta without any wave or tide influence, a delta progradation rate (v_p) can be written as:

$$v_p = \frac{Q_s}{B_b H_b} \tag{2.10}$$

Consequently, bifurcation timescale can be written as

$$T_b = \frac{L_D}{v_p} = \frac{\alpha B_b}{Q_s} . B_b H_b = \frac{\alpha {B_b}^2 H_b}{Q_s} \tag{2.11}$$

with α = dimensionless parameter ≈ 10 (Wright & Coleman, 1971), Q_s = sediment load, H_b = near shore water depth (Swenson, 2005; Jerolmack & Swenson, 2007), B = channel width upstream of the bifurcation. As explained before, sediment load is measured at the model inlet during dynamic equilibrium phase. The near shore water depth (D) is kept constant at 7.5 meter since the basin depth is constant across the scenarios (Edmonds & Slingerland, 2010). Channel width upstream of the bifurcation (B) is manually measured in ArcGIS from the georeferenced images produced by the Delft3D at every timestep.

Island size is measured automatically in Google Colab that uses Python language. In short, the island size is measured by exporting image from the Delft3D, cropping and binarisation process in Google Colab using Otsu's thresholding, contour retrieval and exporting the island sizes out from the Google Colab to Microsoft Excel. The island size produced by this method is in pixel and since 1 pixel = 25 m x 25 m, I then multiplied the island size values produced by this method by 625 m^2 to get the island size in square meter.

I exported the bathymetry produced for each timestep from the Delft3D using a value classes colour code. The value classes colour code is defined as 'white' or 'grey' if the elevation is above the sea level (0 meter) and is defined as 'black' if the elevation is below the sea level. By having these value classes, binarisation process in Python can be done more accurately than by having continuous colour codes (e.g. blue-to-green colour code to represent land and water).

I begin the image binarisation by cropping the images produced by Delft3D in Google Colab. I then binarise the images using the Otsu's thresholding (Jarriel et al., 2021). The binarised image will comprise of what I constitute as land or delta as 'white' or having 0 value and the water in the model as 'black' or having 1 value. The binarised image is then analysed using the contour retrieval and contour approximation algorithms. These algorithms calculate the number of pixels that constitute the 'white' colour from any binarised image. Since the land or delta plain is binarised as 'white' in the previous step, these algorithms will then directly calculate the number of pixels that constitute the delta plain in every timestep of the models (Fig. 2.11). By having the number of pixels, converting it to the island size in square meter will need the multiplication of 25 m x 25 m (as the pixel size) as explained earlier. The tabulated array of island size produced using this method will then be further analysed in R software. Refer to the Appendix 2 for the full written code.

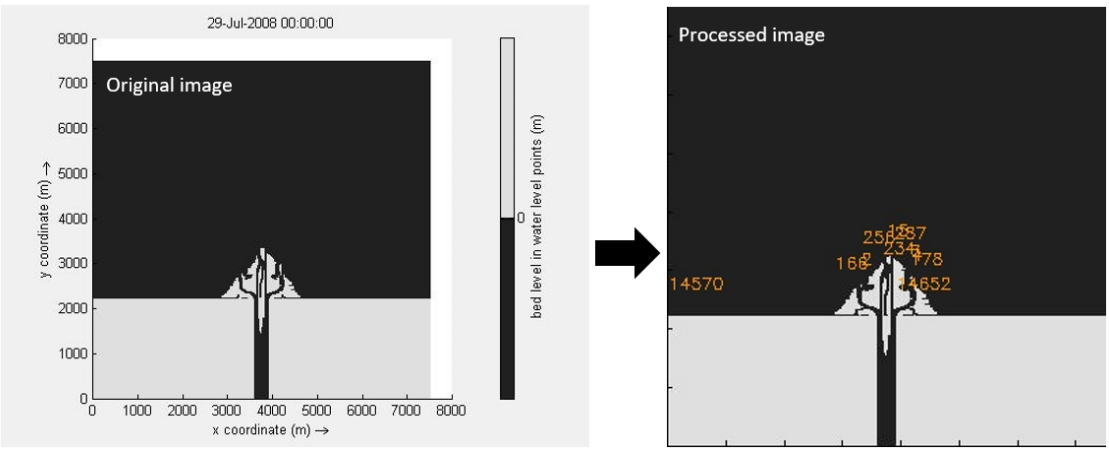

Figure 2.11 Binarisation and automated island size pixel calculation in Google Colab using the Python language. Orange numbers represented on the image on the right are the pixel size of each island that is then converted in square meter by multiplying the shown numbers with 625 m^2.

2.3. Ancient river deltas observation

2.3.1. Scaling relationships in ancient river deltas

In rock records, scaling relationship are found between sediment flux, water discharge, dimension of river systems, and the contributing drainage area (Milliken et al., 2018). In general, there will be a number of relationships that exist between various dimensional parameters across different sizes of the catchment (Strahler, 1952; Allen and Hovius, 1998; Dade, 2001; Castelltort and Simpson, 2006; Sømme et al., 2009a; Sassi et al., 2012; Frasson et al., 2019). Scaling relationships in the ancient river system generally follow power laws of catchment area to the corresponding sediment and water fluxes (Milliken et al., 2018). In

rock records, one of the most prominent scaling relationships comes from the empirical approach on estimating palaeodischarge and deep time sediment flux based on the modern system scaling relationships such as BQART model, regional hydraulic geometry curves, and the Fulcrum model (Syvitski and Milliman, 2007; Holbrook and Wanas, 2014; Eide et al., 2018a; Brewer et al., 2020; Nyberg et al., 2021).

In the application for the ancient system, the BQART model integrates the information about the palaeorelief and palaeocatchment area of a sedimentary system (Bhattacharya et al., 2016). Estimating palaeodischarge using the BQART model needs dune-scale cross-sets or fully preserved fining-upward facies successions of the largest trunk associated with incised valleys above the regional sequence boundary. Bankfull channel dimension and sediment characteristics were then used to estimate the palaeoslope and palaeodischarge values later on using the Manning's or Brownlie's (1983) equations. Consequently, the reliance of estimated palaeodischarge value to the estimated palaeoslope value makes the estimated palaeodischarge sensitive to estimated palaeoslope value. Even though BQART model has been proven as the first-order estimates that could produce values within the same or two order of magnitudes (Sømme et al., 2009b), BQART model has limited applicability in cold-warm temperate climate (Nyberg et al., 2021), innate uncertainty when various bedforms present in one channel trunk (Bhattacharya et al., 2016) and involves assumptions and non-straightforward parameters that are challenging to be extracted from the rock records. Similar to the BQART model, regional hydraulic geometry curves (Davidson and North, 2009) and Fulcrum model (Holbrook and Wanas, 2014) rely on the bankfull channel dimension and palaeoslope estimation to estimate the palaeodischarge value from the rock records. Consequently, robust palaeogeography interpretation from extensive fluvial outcrop or subsurface data is needed (Bhattacharya et al., 2016).

This study takes a route to estimate palaeodischarge value specifically for river deltas by using the simplest scaling relationships (power laws) of channel width-bankfull discharge (*w*-*Q*) and catchment area-bankfull discharge (*A*-*Q*) that are gathered from the modern system. I collected 4459 distributary channel width measurements from 114 global modern deltas that are spread across 5 climate regions and 3 end members of river delta type (e.g. wave-, tide- and river-dominated) to build rock-record-focused *Q*-*w* and *Q*-*A* scaling relationships. These simplest scaling relationships will benefit the sedimentologists working with limited exposure of outcrops or subsurface dataset, which is the case most of the time. Instead of using the equation 1.1 and 1.2, I inverse the relationships assuming that causality

relationships exist between bankfull discharge, channel width and catchment area. The applicability of these scaling relationships was then tested towards palaeodischarge estimation using Fulcrum model from the Ferron, Dunvegan, McMurray and lower Mesa Rica Formation. Moreover, detailed along-axis exposure of lower Mesa Rica distributary channels motivates this study to run bootstrapping simulation to investigate the sensitivity of the scaling relationships towards limited number of samples being used to estimate the palaeodischarge values.

2.3.2. Lower Mesa Rica Formation overview

I test the reliability of the scaling relationship I found from the modern system to the ancient deltaic formation such as Ferron, Dunvegan and McMurray Formation explained in Chapter 5. However, in Chapter 6, I focus on lower Mesa Rica Formation that has 13 downdip measurements of distributary channel widths. By having systematic downdip measurement, I can simulate the reliability of my scaling relationship found from the modern system if I have limited exposure of distributary channel widths from the rock record. The 13 measurements could be reduced up to certain number using bootstrap method to mimic limited number of measurements that is common for geologists working with the rock records.

Cenomanian lower Mesa Rica Formation was deposited in the Tucumcari foreland basin located in the northern tip of Western Interior Seaway (van Yperen et al., 2019). The early sedimentation of this formation was triggered by the subduction of the Farallon plate beneath the west coast of North America that triggered the Cordilleran orogeny (DeCelles, 2004). The lower Mesa Rica Fm., a part of the Dakota Group, lies unconformably on top of the Tucumcari marine shale along with middle-upper Mesa Rica, Pajarito and Romeroville sandstone formations (Scott et al., 2018). Regional sequence boundary SB3.1 underlies the base of the lower Mesa Rica Fm. is related to late Albian-early Cenomanian regression that triggered widespread erosion surface across southeast Colorado to northeast New Mexico (Holbrook and Dunbar, 1992; Holbrook, 1996; van Yperen et al., 2019).

The lower Mesa Rica Fm. is estimated to be deposited as deltaic system on a low-gradient (10^{-6}-10^{-4} m/km) depositional setting (Oboh-Ikuenobe et al., 2008). It is believed to be deposited as a prograding delta based on the evidence of a rapid transition both vertically and laterally from marine to fluvial or distributary channel deposits along ~400 km

depositional-dip profile (Gage and Asquith, 1977; van Yperen et al., 2020). Deposition took place on a location ~35°N latitude with a warm and humid climate condition during the Cretaceous time (Chumakov et al., 1995). The deltaic lower Mesa Rica represents low accommodation river-dominated delta with multiple distributary channels (van Yperen et al., 2019). Due to the long exposure of depositional-dip profile, the lower Mesa Rica formation serves as a perfect example to test the applicability of my palaeodischarge estimation and bootstrap simulation explained in the previous sub-chapter.

2.3.3. Morphometric measurements from the ancient river deltas

The COVID-19 pandemic halted my data collection in the USA that was initially planned at the beginning of my PhD. To tackle this issue, the methodology was redesigned by collaborating with Dr Anna van Yperen and Dr Ivar Midtkandal from the University of Oslo. This collaboration produced a data-sharing agreement that is very useful in testing the paleodischarge estimation I produced in this study. Dr van Yperen measured the distributary channel widths from the lower Mesa Rica Fm. from the proximal to distal direction of exposed outcrops along various locations around North-East of New Mexico, United States (Gage and Asquith, 1977). The measured channel widths were corrected based on the outcrop face orientation and palaeocurrent direction (Fabuel-Perez et al., 2009) to achieve the real distributary channel width values. Thirteen measurements of lower Mesa Rica distributary channels were then used for estimating the palaeodischarge values and bootstrap simulation discussed in Chapter 6.

Chapter 3 - Slope break and avulsion locations scale consistently in global deltas

The following chapter is adapted from Prasojo, O. A., Hoey, T. B., Owen, A., & Williams, R. D. (2022). Slope break and avulsion locations scale consistently in global deltas. Geophysical Research Letters, 49, e2021GL093656. https://doi.org/10.1029/2021GL093656

Abstract

Understanding how deltas respond to changing sea level is crucial as deltas provide important ecosystems, are inhabited by ~500 million people, and are nexuses of food, energy and economic activity. The response of delta distributary channels to sea-level rise depends on the geomorphic controls on delta morphology and their scaling relationships. Our data from 105 deltas globally show strong scaling between the upstream distances to slope breaks and to avulsion nodes, and confirm the previously-known scaling between backwater and avulsion lengths. The break in slope is proposed to be the principal control on delta development, along with other proposed secondary controls. We identify and discuss the implications of this slope break-avulsion length scaling, leading to a conceptual model of delta morphology and sedimentology. This model suggests how deltas may respond to future sea level rise and guides interpretation of deltaic deposits in the rock record.

3.1. Introduction

Deltas, alluvial protrusions beyond lacustrine or marine shorelines, are one of Earth's essential landscape types and provide a wide range of ecosystem services (Besset et al., 2017); ~500 million people currently live on deltas which have been important locations in the development of human societies and are significant centers for biodiversity (Ericson et al., 2006; Syvitski and Saito, 2007; Nienhuis et al., 2020). However, deltas are particularly vulnerable to a combination of changing sea-levels, reduced sediment influx and subsidence, causing increasing flood risk and degradation of ecosystems (Yang, 2005; Syvitski et al., 2009; Tessler et al., 2015; Hoitink et al., 2017; Mueller et al., 2017; Wang et al., 2017; Besset et al., 2019; Warrick et al., 2019; Wu et al., 2020).

When a sediment-conveying river enters a water body, delta lobes start to develop from mouth bar deposition, forming a delta planform with distributary channel networks. Excepting many lake deltas, most open water deltas are exposed to marine energy in the form of tides, waves, and storm surges and are also affected by relative sea-level rise (Hoitink et al., 2017). The complexity of distributary channel networks depends on interactions between factors including sediment supply, slope, climate, channel bifurcation and avulsion, with delta morphology reflecting the balance of these factors (Jerolmack and Mohrig, 2007; Edmonds and Slingerland, 2008; Syvitski et al., 2009). To understand how

distributary channels will respond to rising sea level, the controls on the morphology of these channels need to be firstly understood.

The presence of a body of water generates a distal backwater in delta channels, the length of which has been proposed as a fundamental hydrodynamic boundary in delta systems (Paola and Mohrig, 1996; Jerolmack and Swenson, 2007). This backwater zone is characterized by downstream decreases in grain size, channel migration rates and channel belt widths, and increased channel depth (Fernandes et al., 2016). A study of nine modern deltas showed that the backwater length (L_b) scales with the avulsion length (L_a), which is the distance from the shoreline to the first (i.e. farthest upstream) bifurcation along the river centerline (L_a:L_b ~1:1 to 1:2) (Jerolmack and Swenson, 2007; Chatanantavet et al., 2012; Ganti et al., 2016a). This scaling relationship is considered crucial for defining the location of the preferential avulsion node and for understanding avulsion migration in the delta lobe building process (Chatanantavet et al., 2012; Nijhuis et al., 2015; Ganti et al., 2019a; Chadwick et al., 2019a; Brooke et al., 2020). However, Hartley et al. (2017), found a less consistent avulsion and backwater length scaling relationship from 13 modern deltas. Hartley et al. (2017) argued that an avulsion node, that they referred to as the delta apex, is primarily controlled by processes at the valley mouth where unconfined deposition commences. The position of the valley mouth coincides with the location of a longitudinal slope break that triggers the onset of delta construction in an unconfined setting, due to sediment transport capacity being reduced downstream from this location to the shoreline. Thus, there should be spatial correlation between valley mouth locations and avulsion node positions. However, valley mouth location is not necessarily the upstream limit of the coastal backwater. Hence, for deltas in equilibrium with external controls, Hartley et al.'s (2017) results suggest 1:1 scaling relationships between both the avulsion (L_a) and slope break (L_s) lengths measured from the shoreline and the valley-exit-to-shoreline distance (L_v).

The discrepancies between previous results, from small numbers of deltas, highlight the need to investigate generic scaling relationships on deltas using a larger data set. This study investigates morphometric boundaries (backwater, avulsion and slope break lengths, and valley-exit-to-shoreline distance) from a global data set of 105 modern deltas, considering the effects of landscape-scale (catchment size, river discharge, valley type) and local (water surface slope) factors. We also identify and discuss the processes contributing to these generic scaling relationships. Scaling relationships are fundamental to our understanding of

delta development, allowing insights into how delta distributary channels will respond to changing allogenic and autogenic forcing.

3.2. Materials and Methods

A global dataset of 105 mostly river-dominated deltas that debouch into open seawater was analyzed (Fig. 3.1a; https://doi.org/10.6084/m9.figshare.16429998.v1). We used Google Earth Engine (GEE) to compile 30 m resolution Landsat 5 tile images from 1984-2009, and digital elevation models (DEM) from the Shuttle Radar Topography Mission (SRTM) for 60°S to 60°N and ArcticDEM for north of 60°N (Tucker et al., 2004; Farr et al., 2007; Morin et al., 2016). We chose the least cloudy and oldest Landsat 5 images available from GEE to avoid engineered riverbanks that have become increasingly more prevalent. SRTM and ArcticDEM resolutions are ~30 m and ~0.5 m, respectively. We used the DEMs to generate elevation profiles along the centerline of the main distributary channel in QGIS using the Terrain Profile™ tool. Only four deltas, all within ArcticDEM, show gross error that prevent extraction of a reliable elevation profile (Błaszczyk et al., 2019). We defined valley types through analysis of the topography using the method from Hartley et al. (2017). Catchment areas were obtained from the HydroBASINS level 6 global watershed dataset (Lehner and Grill, 2013). Since climate is a fundamental factor influencing delta morphology (e.g. river discharge, sea-level, wave action, storm energy, sediment yield), we classified deltas according to their dominant climate zone (Ta et al., 2002; Correggiari et al., 2005; Syvitski and Saito, 2007). Climate-based classification enables us to classify the data set more consistently across different delta morphologies (Table S3.1).

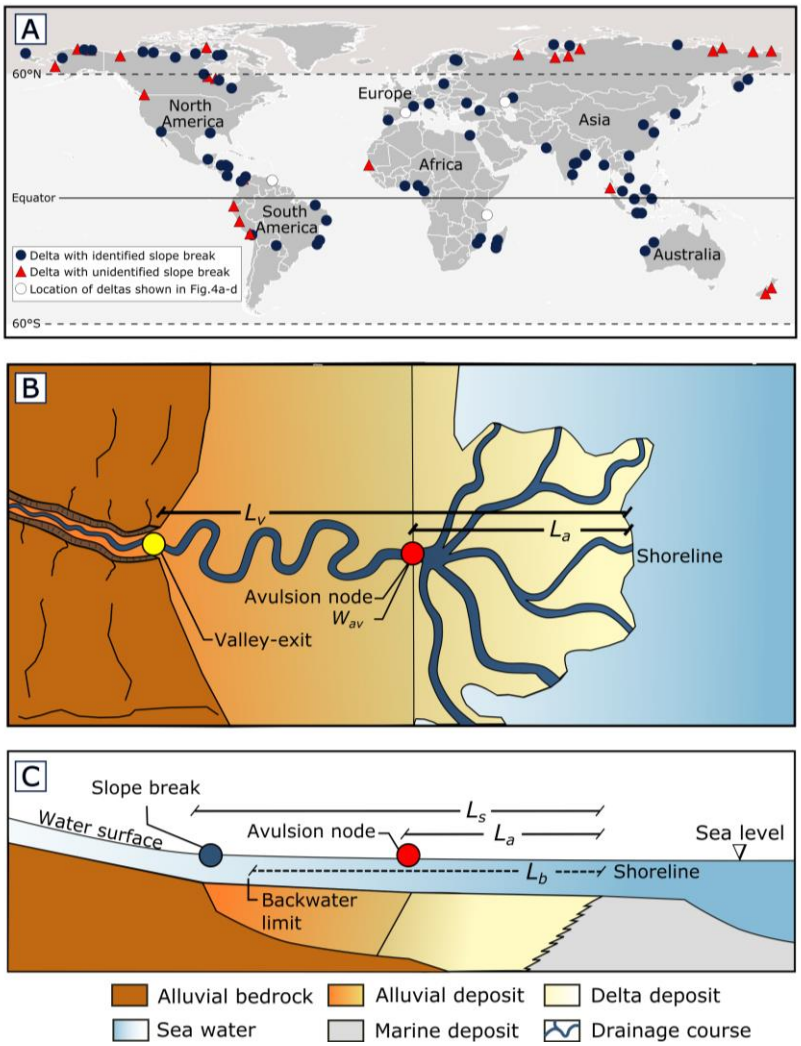

Figure 3.1 Distribution of deltas investigated, and schematic diagram used in this study. (a) Distribution of 105 river deltas used in this study. Different shadings on the map show the spatial extent of the use of the SRTM (60°N-60°S) and the ArcticDEM (north of 60°N). (b) Schematic diagram showing the valley-exit-to-shoreline distance (Lv) and the avulsion length (La) measurements obtained from satellite imagery. (c) Schematic section showing the backwater length (Lb) in addition to slope break length measurement (Ls) and the representation of La in the schematic section.Unidentified slope breaks are mainly due to changes in longitudinal gradient being too gentle to detect using either a manual or semi-automated local gradient method and/or due to vertical uncertainty in ArcticDEM (Hayakawa & Oguchi, 2006).

The satellite imagery analyzed here provides static snapshots of modern delta conditions. Dynamic environmental variables, including daily to annual tides and wave conditions, and decadal sea-level change and local subsidence are thus excluded. We manually identified each delta that has a subaerial deposit that protrudes beyond the lateral shoreline (Caldwell et al., 2019). Criteria for selection include any channel mouth that intersects with the open seawater depositing sediment that protrudes beyond the lateral shoreline, with or without the characteristic morphology of river-dominated deltas (e.g. subaerial mouth-bar deposit, elongate distributary channels) (Olariu and Bhattacharya, 2006). A sub-set of ten deltas, defined as wave-dominated by Nienhuis et al. (2020), are also investigated.

Landsat imagery and the DEMs (i.e. The Shuttle Radar Topography Mission and ArcticDEM) were extracted using Google Earth Engine (GEE), a cloud-based platform with a multi-petabyte geospatial dataset and intrinsic high-performance parallel computation service provided by Google (Gorelick et al., 2017). A JavaScript was written on the platform to sort, mosaic and extract the desired Landsat and DEMs for each delta. Firstly, a polygon was manually drawn around the extent of each delta (n = 105). Each polygon covered the delta region upstream to the first valley exit in the fluvial region. The Near-Infrared Band 5 and 4 (1.55 - 1.75 µm and 0.76 - 0.90 µm) and Visible Band 1 (0.45 - 0.52 µm) were mosaicked from the available Landsat imagery to distinguish water from land. This process makes morphometric measurement more straightforward. The oldest available images were chosen (e.g. from 1984 to 2009) to minimize the anthropogenic impacts on delta channels (e.g. engineered river banks, dikes infrastructures). With this wide time frame, we have more options to select the least cloudy images. The stacked images were then sorted based on the cloud coverage. The image with the least cloud coverage was mosaicked and extracted to the local server to be analyzed in ArcGIS (Fig. 3.2).

Avulsion length (L_a) was measured in ArcGIS along the river centerline from the shoreline at the time of the Landsat image to the first (farthest upstream) deltaic avulsion, hence assuming that this first avulsion is the delta apex node (Jerolmack and Swenson, 2007); Fig. 3.1.b). Where there is a single active channel and no bifurcation, L_a was measured up to the farthest upstream valley exit point identified in the DEM, following (Hartley et al., 2017). The slope break length (L_s) was defined from the elevation profile as the river distance between the shoreline and the first break in slope (Fig. 3.1b,c and Fig. 3.2). Slope breaks were identified using a semi-automated local gradient method and Hack's Stream-Length (SL) index (Hayakawa and Oguchi, 2006; see Chapter 2.1.2). Valley-exit-to-shoreline distance (L_v) was measured along the river centerline from the shoreline to the valley exit point identified from the DEMs (Hartley et al., 2017).

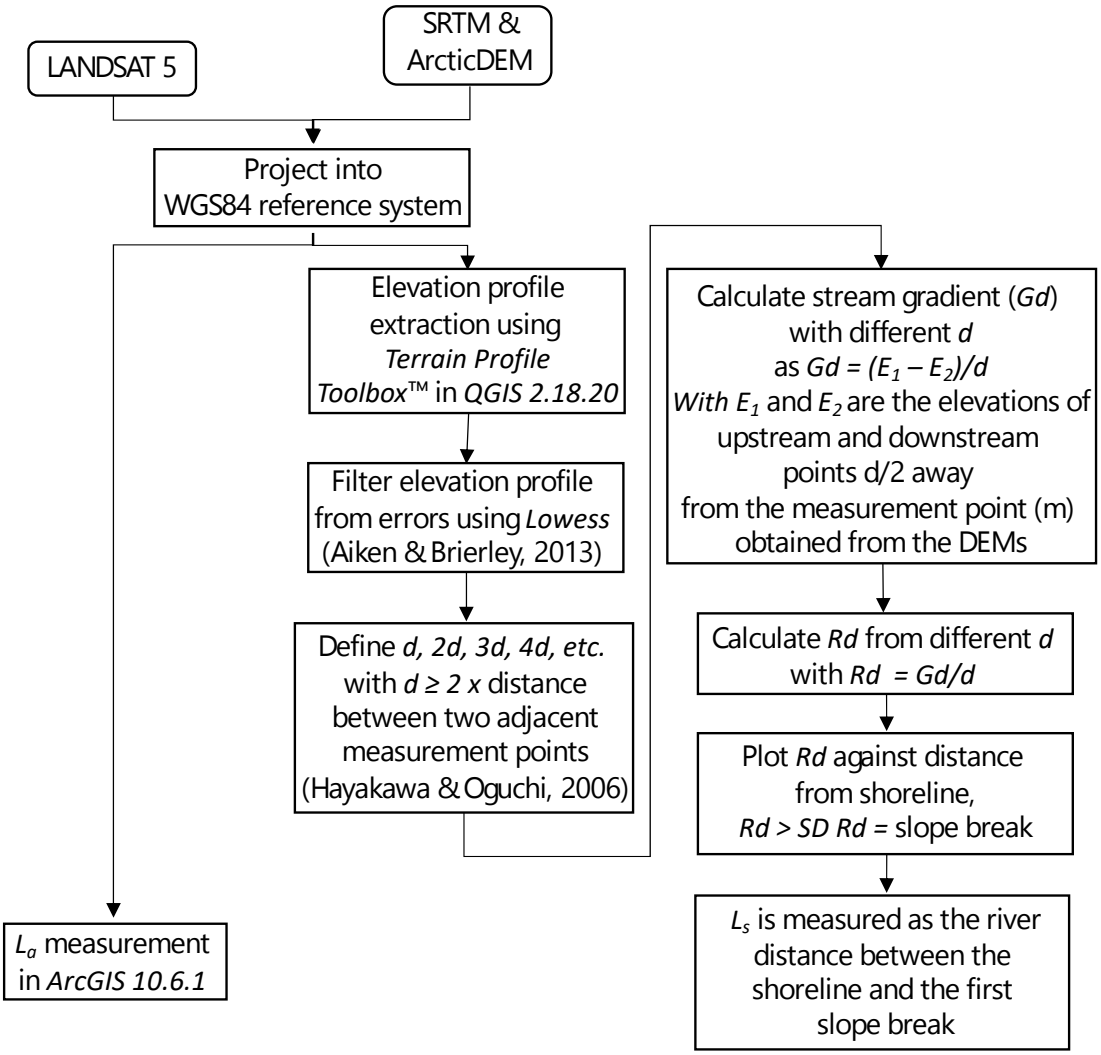

Figure 3.2 Flow diagram of morphometric measurements involved in this study. Avulsion lengths (L_a) were measured on Landsat 5 images, while the SRTM and ArcticDEM were used to extract the slope break lengths (L_s) across the global dataset. The flow diagram for extracting L_s follows (Hayakawa and Oguchi, 2006; Aiken and Brierley, 2013). Detail explanation of the workflow is presented in the text.

Backwater length (L_b) was calculated (Chatanantavet et al., 2012) as:

$$L_b = \frac{h_c}{S} \tag{3.1}$$

and

$$h_c = \left(\frac{C_f {Q_c}^2}{g {W_{av}}^2 S}\right)^{\frac{1}{3}} \tag{3.2}$$

where h_c is the characteristic flow depth (m) and S is water surface slope (m/m) (Eq. 3.1). Characteristic flow depth (Eq. 3.2) was calculated using the bed friction coefficient C_f =

0.002 for large lowland rivers (Parker et al., 2007). Q_c is the characteristic water discharge (m^3/s), g is gravitational acceleration (m/s^2) and W_{av} is the channel width (m) at the avulsion node at the time of the image (Parker et al., 2007).

Characteristic water discharge (Q_c) is taken as the 2-year recurrence interval flood (Q_2) as close to the upstream limit of the delta as data availability allows, to provide an indicator of the dominant channel-forming flow (Wolman and Miller, 1960; Ganti et al., 2016a). Q_2 was calculated from daily river discharge data available from the Global Runoff Data Centre (GRDC). For some deltas, only monthly river discharge data were available and Q_2 from these monthly data were converted to equivalent daily Q_2 values using empirical transformations for different climates (see Chapter 2.1.3; Beck et al., 2018). Channel width (W_{av}) was measured on the Landsat imagery at the avulsion node to avoid influence by wave or tidal processes (Fig. 3.1b). Slope (S) was calculated from the water elevation profile along the centerline of each river.

3.3. Results

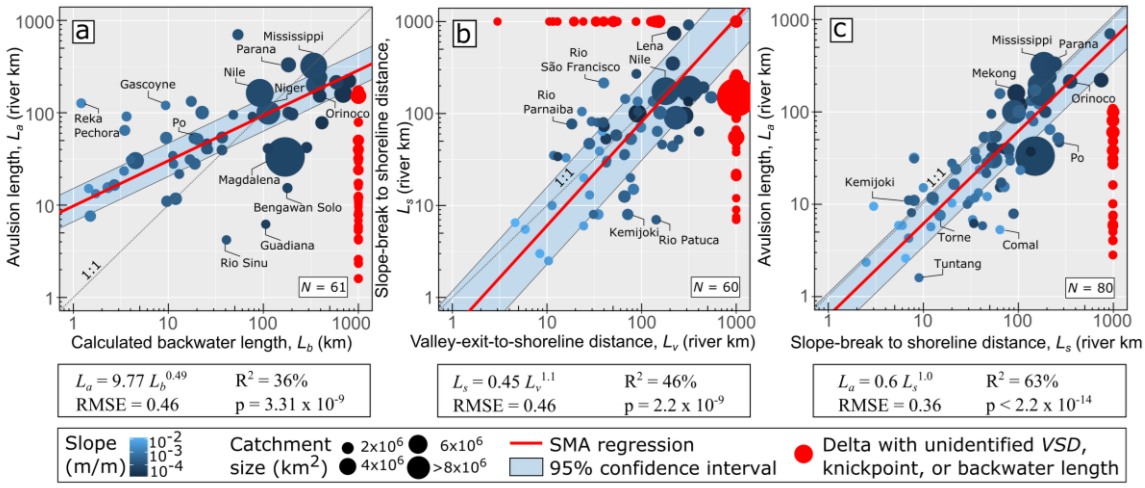

Figure 3.3 Morphometric correlations produced from this study. (a) Measured avulsion length (L_a) against calculated backwater length (L_b). (b) Slope break distance from the shoreline (L_s) against the valley-exit-to-shoreline distance (L_v). (c) Measured avulsion length (L_a) against the slope break distance from the shoreline (L_s). We used standard major axis (SMA) regression (red lines) to determine functional relationships. Point size is scaled with the catchment area; point color shade represents the slope of each delta. Root mean square error (RMSE) is in log units. Red points representing unidentified L_v, L_s and L_b are positioned on the border of the plots.

Measured (valley-exit-to-shoreline distance, avulsion and slope break lengths) and calculated backwater lengths are plotted in Figure 3.3. The L_a-L_b plot (Fig. 3.3a) shows a power-law relationship $L_a = 9.77L_b^{0.49}$ (R^2 = 36%; RMSE = 0.46). The equivalent L_s-L_v relationship is $L_s = 0.45L_v^{1.10}$ (R^2 = 46%; RMSE = 0.46) (Fig. 3.3b). Statistically, the most

significant scaling is for the avulsion length against the slope break distance from the shoreline, with $L_a = 0.6L_s^{1.00}$ (R^2 = 63%; RMSE = 0.36) (Fig. 3.3c). Note that we show fewer than 105 deltas on Fig. 3.3 due to river discharge data being unavailable for some rivers, unidentified valley-exit points, and indeterminate slope breaks.

Decreases in water surface slope (blue points in Fig. 3.3 are shaded from dark to light as slope increases) are neither correlated with longer backwater, avulsion nor slope break lengths (Fig. 3.3a-c). Compared to the plot against the backwater length (Fig. 3.3a), larger catchment areas show a more significant correlation with slope breaks and avulsion lengths, consistent with prior literature (Fig. 3.3c; Fig. 3.4; (Syvitski and Saito, 2007). The data contain some significant outliers, mainly from European sites, which are potentially affected by engineered riverbanks (e.g. Guadiana, Po). Smaller deltas (L_a < 50 km; e.g. Tuntang, Comal) also contribute to these outliers. Therefore, the L_a:L_s scaling relationship is stronger in relatively larger deltas (Fig. 3.3c). Additionally, wave-dominated deltas as defined by Nienhuis et al. (2020), also show a consistent L_a:L_s relationship. Note that some calculated backwater lengths in this study vary from, but lie within the same order of magnitude, as backwater lengths previously reported for the same sites (Chatanantavet et al., 2012; Ganti et al., 2016a). This calculation difference is due to using different representative channel widths to calculate the characteristic flow depth. We used the channel width at the avulsion node (W_{av}), while the choice of channel width is not always explicitly stated in previous studies.

All power law relationships in Figure 3.3 are statistically significant. However, the relationship between the avulsion and slope break length for the global dataset has the strongest correlation (Fig. 3.3c; R^2 = 63%, RMSE = 0.36). Of the studied deltas (n = 80), 65% lie within the 95% confidence interval of the regression line (Fig. 3.3c) in comparison to Fig. 3.3a and 3.3b (64% and 55%, respectively). L_a and L_s are related with exponent 1, showing a direct scaling relationship.

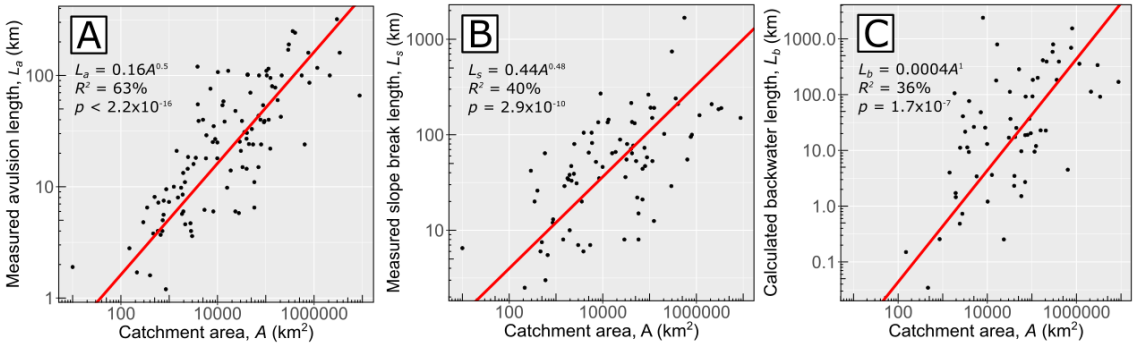

Figure 3.4 Relationships between catchment area and the measured and calculated variables. (a) Catchment area vs. avulsion length. (b) Catchment area vs. slope break length. (c) Catchment area vs. backwater length. We used standard major axis (SMA) regression (red lines) to extract the relationships between those variables.

We also classified the L_a:L_s relationship (Fig. 3.3c) by valley type to test whether this scaling remains consistent for all valley types (Fig. 3.5). Regression slopes from alluvial, bedrock and Pleistocene valley types are not significantly different from the full data set although valley-confined deltas do show a difference. The p-values shown next to regression lines (Fig. 3.5) are all >0.05, and the dashed lines in Fig. 3.5 lie within 95% confidence bands for the overall relationships (Fig. 3.5a-c). Valley-confined deltas are not significantly different (p-value = 0.06) from the proposed L_a:L_s from the full data set, but the regression line for this valley type deviates from our proposed L_a:L_s relationship (dashed line in Fig. 3.5d). The small (N=5) number of valley-confined deltas prevents interpretation of the significance of this result (Fig. 3.5d). Appreciable scatter is observed (1 order of magnitude of the avulsion length; range of residuals = ±0.2 in log units) in the alluvial valley deltas (Fig. 3.5a). Relatively small deltas also contribute to the scatter for bedrock valley types (Fig. 3.5b). However, the strong and relatively consistent L_a:L_s correlation across different valley types provokes consideration of the importance of this scaling relationship in the context of the previously known L_a-L_b relationship and valley-exit control on delta apex position (Ganti et al., 2016a; Hartley et al., 2017).

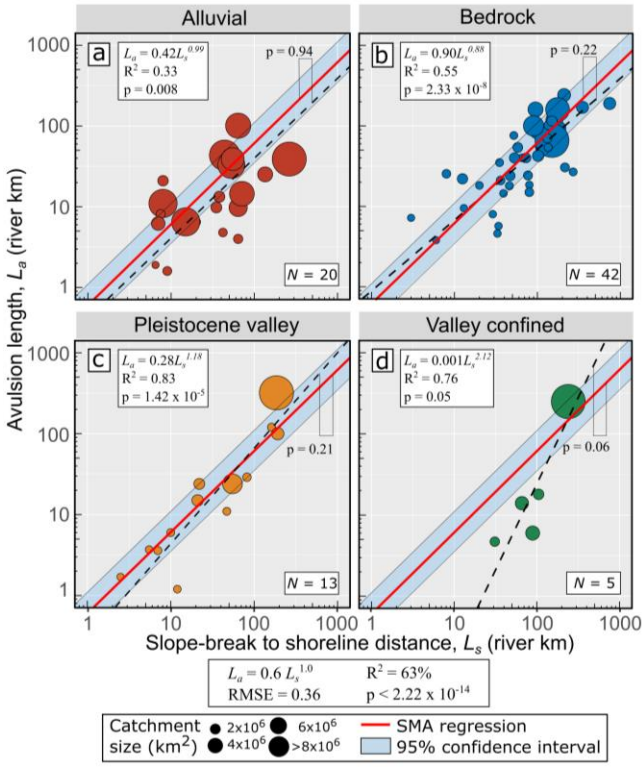

Figure 3.5 (a-d) Data from Fig. 3.3c (avulsion length (L_a) against slope break distance from the shoreline (L_s)) for each valley type. Red lines are the SMA regression lines from the full data set, dashed lines are separate SMA regression lines from each valley type with L_a-L_s relationships shown on panel. Point size is scaled with the catchment area and p-values near the regression lines are the significance of the difference between the gradient from L_a-L_s SMA regression for each valley type versus the L_a-L_s SMA regression from the full data set (i.e. slope test).

3.4. Discussion

3.4.1. Morphometric scaling and delta morphology

We demonstrate here how the calculated morphometric scaling relates to scaling on some modern deltas. Examples from the Rufiji, Ebro, Orinoco and Volga deltas show the locations of the morphometric boundaries and how the scaling between the avulsion and slope break lengths measured from the shoreline is consistent across a range of delta sizes (Fig. 3.6a-d). Visual observation from satellite images shows that the apices of each of these deltas coincide with measured avulsion lengths (yellow points in Fig. 3.6a-d). As for most other deltas in the dataset, these four examples have developed in approximately their current locations since the early Holocene due to the decreasing rate of sea-level rise. Detailed studies of their avulsion histories (Kroonenberg et al., 1997; Aslan et al., 2003; Nienhuis et al., 2017) suggest that the avulsion nodes have remained in a constant location as these deltas have developed. The avulsion-slope break length scaling ratios in these deltas are $L_a \sim 0.6L_s$ for the Rufiji delta and $L_a \sim 0.5L_s$ for the Ebro, Orinoco and Volga deltas. However, the calculated backwater lengths (L_b) from the Rufiji and Ebro deltas are located farther

downstream of the avulsion nodes (white points in Fig. 3.6a,b,d). Both the Rufiji and Ebro deltas have $L_a \sim 1.2L_b$ instead of $L_a \sim 0.5L_b$ (or $L_a{:}L_b \sim 1{:}2$) as previously suggested (Jerolmack and Swenson, 2007; Chatanantavet et al., 2012; Ganti et al., 2016a) due to the effects of using different representative channel widths to calculate backwater lengths. The Orinoco delta, however, has a calculated backwater length of 585 km that lies upstream of the delta in the river, outside of the mapped area (i.e. $L_a \sim 0.3L_b$). The Volga delta backwater length of 184 km, hence $L_a \sim 0.5L_b$, coincides with the location of the slope break ($L_s{:}L_b \sim 1{:}1$). These examples from natural deltas are consistent with our overall finding that $L_a \sim 0.6L_s$.

3.4.2. Processes involved in the proposed scaling relationship

Mouth-bar deposition should dominate the most distal part of a delta due to input sediment being deposited in a relatively static water body (Olariu and Bhattacharya, 2006). Upstream parts of deltas will be dominated by partial avulsion or crevasse bifurcation (Kleinhans et al., 2013), or by avulsion by incision (Slingerland and Smith, 2004) induced by in-channel aggradation due to the slope break and/or the backwater effect (Slingerland and Smith, 2004; Kleinhans et al., 2013). As shown in this study, the stronger global L_a-L_s scaling relationship suggests that the slope break is the predominant driver of channel response in the upstream part of a delta, rather than the backwater effect (L_a-L_b relationship). In-channel aggradation could then trigger avulsion in the upstream region of a delta, maintaining the scaling relationship between L_a and L_s. Hence the avulsion nodes, the most upstream bifurcation nodes of deltas, are proposed to be related to the process of in-channel aggradation due to the change in slope and may not be directly related to bifurcation or backwater processes downstream. A study from the Huanghe (Yellow) River delta showed avulsion related to a slope break (bedslope-mediated) ~700 km upstream from the shoreline, that also coincides with the valley exit from the Loess plateau, while backwater-influenced avulsions are clustered downstream near the shoreline (Ganti et al., 2014). Thus, we divide the delta development domain into upstream and downstream zones with different processes dominating in each of these two areas (Fig. 3.6e). Note that the upstream and downstream process domains are not necessarily sequential and may operate over different timescales. Controls over the timing and thresholds of avulsion-bifurcation cycles remain to be explored further.

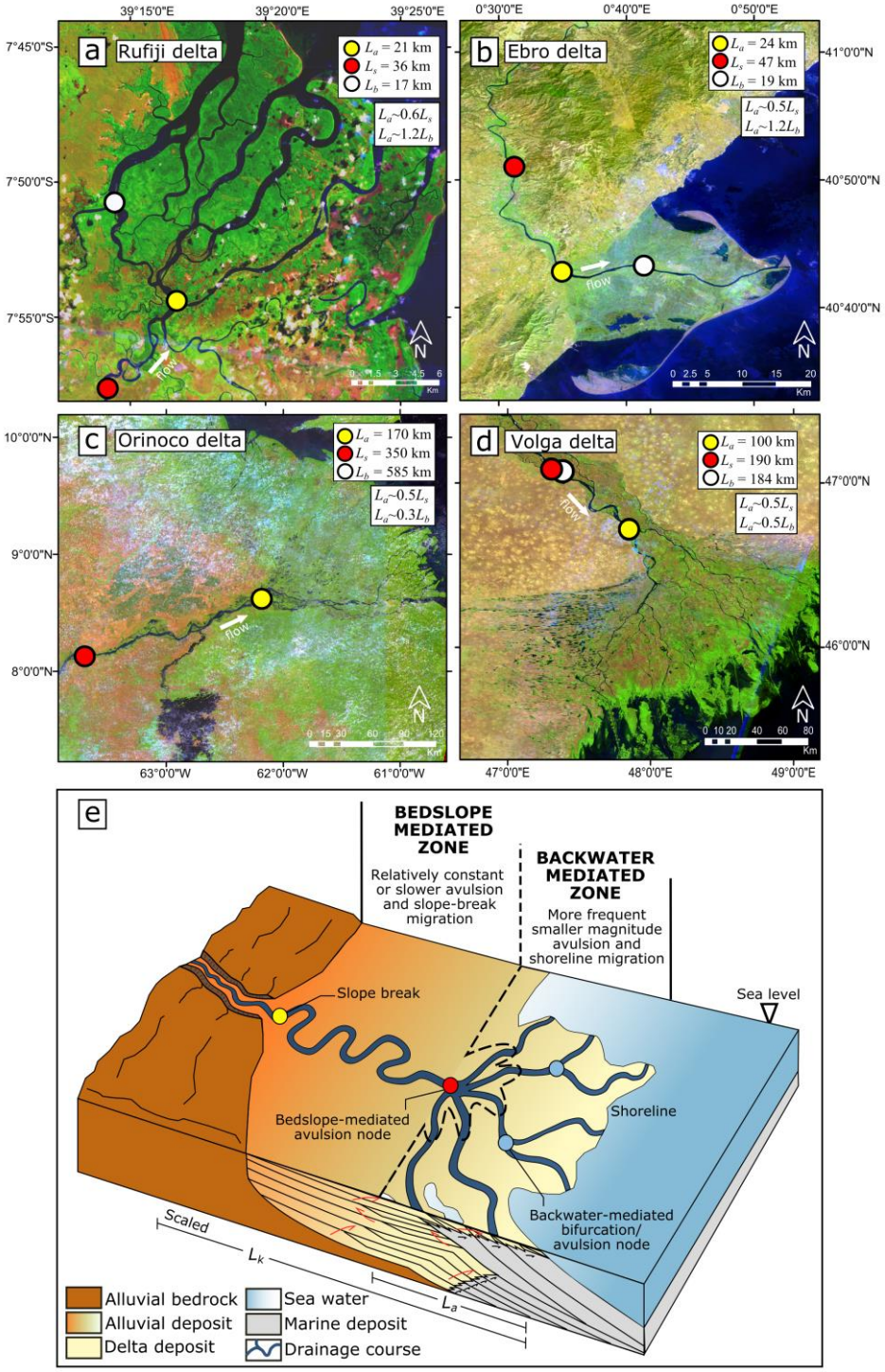

Figure 3.6 Stitched composite Landsat 5 images from year 2000 from Rufiji (a), Ebro (b) and Volga (d) deltas. The Orinoco (c) used tiled composite Landsat 7 images due to unavailability of complete near cloud-free coverage of the delta plain from Landsat 5. (e) Depositional model for deltas with bedslope- and backwater-mediated zonation. The Near-Infrared Band 5 and 4 (1.55 - 1.75 µm and 0.76 - 0.90 µm) and Visible Band 1 (0.45 - 0.52 µm) are shown to better distinguish water and land. Values of measured avulsion (La) and slope break (Ls) lengths are plotted as yellow and red points, respectively. The calculated backwater lengths (Lb) are plotted as white points; the backwater location for Fig. 3.6c lies outside the area shown. For Fig. 3.6e, the red thick arrows are the sequence packages and smaller black arrows show the smaller parasequence packages.

The controls on slope breaks in delta channels also remain an area for further investigation. Valley-exit and alluvial-bedrock transitions, as seen from the DEMs used in this study, may

control the slope break location with 1:1 L_s-L_v scaling (Fig. 3.3b). However, the location of the slope break is also controlled by a range of interacting factors including grain size transitions and associated changes in Shields' stress, geological controls (e.g. subsidence and lithology), and the nature of the overbank material (e.g. cohesive vs non-cohesive).

3.4.3. Correlation with the valley types

Fig. 3.5a-d show the overall scaling relationship across different valley types, but Fig. 3.5d shows how deltas located in valley-confined settings may depart from our calculated $L_a \sim 0.6L_s$ scaling relationship. Valley-confined deltas have limited lateral space. When in-channel aggradation triggers an avulsion, there is a higher possibility that a newly avulsed channel will rejoin the parent channel due to this limited lateral space, limiting the chance of the growth of distributary channels by delta plain progradation (Slingerland and Smith, 2004). Thus, our L_a-L_s scaling relationship does not fit in this valley type (Fig. 3.5d). As an example, the Paraná delta (Argentina) is valley confined from the hinterland all the way to the shoreline which confines the lateral growth of the delta as seen in its DEM (Fig. 3.7). Additionally, alluvial valleys that are under the influence of erosion instead of prograding or aggrading may contribute to the scattered data in Fig. 3.5a. These observations enhance our understanding that the valley exit does not necessarily coincide with the slope break, but that valley exit is coincident with the avulsion node only in certain valley types (Hartley et al., 2017).

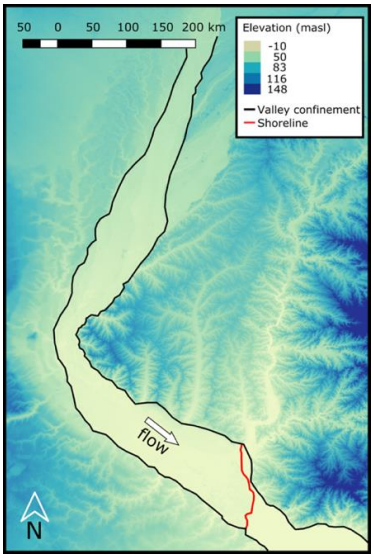

Figure 3.7 SRTM image from Paraná delta in Argentina showing valley confinement from the hinterland up to the shoreline that restricts the lateral growth of the delta.

3.4.4. Implication of the proposed scaling relationship

From the close relationship between the slope break length and the avulsion length, we propose an updated conceptual model of delta lobe building (Fig. 3.6e). We divide deltas into bedslope-mediated and backwater-mediated zones, as proposed by (Ganti et al., 2014) from their Huanghe (Yellow) delta case study. The bedslope-mediated zone includes the upstream catchment area and fluvial environments as far downstream as the first avulsion point, initiating the onset of delta construction and generation of avulsion-driven stratigraphy. The backwater-mediated zone consists of delta distributary channels down to the shoreline. In the bedslope-mediated zone, the slope break and avulsion lengths (shown in distal stratigraphy, and red and yellow circle symbols on the delta plain in Fig. 3.6e) will migrate over long (~10-100 ka) avulsion timescales, depending on the size of the delta involved. In the backwater-mediated zone, bifurcation nodes and shorelines will be more sensitive to allogenic forcing (sea-level fluctuation, subsidence) and thus they may migrate more frequently (i.e. $\sim 10^1$-10^3 years) at smaller magnitudes (shown in the proximal stratigraphy and light blue circle symbols on the delta plain in Fig. 3.6e). Different response times are due to different compensation scale and different channel depths and aggradation rates between the upstream and downstream parts of a delta (Jerolmack and Paola, 2010; Li et al., 2016, 2018; Straub et al., 2020). Transgressive and regressive parasequences may be recorded in the stratigraphy of the backwater-mediated zone in a more serrated manner (stratigraphy shown in Fig. 3.6e), whereas in the upstream part, the smaller allogenic forcing may be shredded due to longer timescales involved in the bedslope-mediated zone (Li et al., 2018). These differences imply that the distal zone will have more frequent shoreline and bifurcation node migration compared to the proximal area. Thus, changes in sea-level or subsidence may cause migration of the backwater-mediated avulsion nodes, but the bedslope-mediated avulsion node will remain constant due to its connection with aggradation at the slope break.

This conceptual model is corroborated by recent numerical modelling (Ratliff et al., 2021) which demonstrated the interconnection between avulsion and the slope break length. They proposed that the location of the avulsion node always occurs at the slope break due to the linear diffusion of aggradation and erosion of the river profile. Under sea-level rise, the slope break and avulsion lengths (in the form of backwater length) will remain constant under varying magnitudes of sea-level rise rate (*SLRR*), consistent with our conceptual model (Fig. 3.6e; their Fig. 2a and 2b). Our data set also includes 10 wave-dominated deltas that follow

the same L_a-L_s scaling relationship as the river-dominated deltas in our study. The Ratliff et al.'s (2021) study shows the consistency of this L_a-L_s geometric constraint across different wave energies (their Fig. 2b). Nonetheless, upstream retreat of the avulsion node and slope break may happen under sea-level rise (their Fig. 1d). Even so, the L_a-L_s (avulsion and slope break length) scaling remains constant even under sea-level rise, supporting our conceptual model (Fig. 3.6e).

3.4.5. Scatter in the dataset

Most modern global deltas have developed since the early Holocene, associated with a decreasing eustatic sea-level rise rate, during which there have been natural and anthropogenic changes of boundary conditions (e.g. sediment supply, water discharge, sea-level rise) (Stanley and Warne, 1994; Ericson et al., 2006; Bird et al., 2010). The data that we derived from satellite imagery represent snapshots of delta response to these cumulative interacting boundary conditions. Although some measured individual delta morphologies may be transient responses to changing boundary conditions, we assume that the overall data set represents deltas in dynamic equilibrium with the environmental controls (Mackin, 1948). However, some of the scatter in Figure 3.3 may be attributed to transient responses to, for example, reductions in river flow and sediment input (Li et al., 2017) or sea-level rise (Nienhuis and van de Wal, 2021).

The relative age of a delta should also impact its L_a:L_s scaling. Adopting the theoretical approach to delta distributary networks from (Jerolmack and Swenson, 2007), delta building by bifurcation-dominated processes will occur early in delta development. As bifurcation continues, a landward-shift in aggradation or channel backfilling will trigger avulsion by deposition in upstream reaches, previously known as backwater length-controlled (Slingerland and Smith, 2004; Edmonds et al., 2009). Thus, it is proposed that older (or larger) deltas will be avulsion-dominated or bedslope-mediated instead of bifurcation-dominated, where the change in surface water slope induces a decrease in sediment transport capacity, triggering bedslope-mediated avulsion (Ganti et al., 2016a). Similarly, it is proposed that small, or relatively younger, deltas tend to be characterized by bifurcation-dominated processes, and therefore may depart from the overall L_a:L_s scaling relationship (Fig. 3.3c).

The Po, Mississippi and Mekong deltas demonstrate how engineering work may disrupt the dynamic equilibrium assumption that underpins the proposed scaling relationships. The Po delta has experienced extensive hydraulic works over several centuries, including the 'Porto Viro' bypass in 1604, dredging, beach reclamation, channel bank protection, and subsidence due to groundwater extraction (Ninfo et al., 2018). Channel bypassing directly influenced the delta avulsion length that makes the $L_a \sim 0.6L_s$ scaling relationship overestimate the present day avulsion length by a factor of 4 (i.e. $L_a \sim 0.15L_s$) (Fig. 3.3c). Anthropogenic modification is also evident on the Mississippi delta. Artificial cutoff in 1831 minimized the flow coming into the human-made Atchafalaya delta complex, but then dredging in 1880 in the Old River area maintained the flow to both Atchafalaya and Balize delta complexes. The $L_a \sim 0.6L_s$ scaling relationship that we calculate underestimates the modern avulsion node in the Mississippi delta that is consistently located at Old River (~320 km from the recent shoreline; $L_a \sim 1.7L_s$) (Fig. 3.3c) (Aslan et al., 2005). Detailed study of Mekong delta morphodynamics has also shown how sediment starvation and dam construction is significantly decreasing the delta progradation rate (Li et al., 2017). This human-made modification causes our scaling relationship to underestimate the present-day avulsion length (i.e. $L_a \sim 1.7L_s$) (Fig. 3.3c). Hence, century-scale engineering can affect the proposed scaling relationship even in large deltas.

Data quality also contributes to the uncertainty of the $L_a \sim 0.6L_s$ scaling relationship. For smaller deltas that have relatively short avulsion lengths (e.g. the Comal delta; $L_a = 4$ km) shows uncertainty in extracting the slope break location from the elevation profile, in contrast to the larger ($L_a = 160$ km) Nile delta. Common gross error shown in the ArcticDEM dataset also contributes to the difficulty in defining the exact location of a slope break from the elevation profile (Błaszczyk et al., 2019).

3.5. Conclusions

A sample of 105 global deltas provides a comprehensive assessment of delta morphometric scaling relationships. We show that the avulsion-backwater length scaling relationship is less consistent in this global dataset than previously proposed. The results also show that the valley exit does not necessarily coincide with a break in slope but rather with the avulsion node in certain valley types. Further to these scaling relationships, we show that the avulsion length scales most consistently and most strongly with the slope break length, followed by the valley-exit-to-shoreline distance. These findings open the opportunity to explore

alternative hypotheses for the controls over delta development. Along with the possible processes that produce these scaling relationships, we propose a framework for understanding delta lobe building by dividing a delta into bedslope- and backwater-mediated zones. The proposed framework allows potential insights into how delta systems will respond to changing boundary conditions. This framework also contributes to our understanding of the location and frequency of avulsion nodes in a delta system that is fundamental for the large populations that live on the world's delta plains.

Chapter 4 – The role of the topset slope in autogenically controlling avulsion and bifurcation timescales in river deltas

The following chapter is a reformatted version of a manuscript submitted to the Journal of Geophysical Research: Earth Surface by Prasojo, O. A., Hoey, T. B., Owen, A., & Williams, R. D. available at 10.1002/essoar.10512273.1.

Abstract

River deltas are under external stress from sea-level rise, subsidence, and decreases in sediment and water discharges caused by anthropogenic activity. Naturally, delta channels respond to these stressors by avulsing and bifurcating. Avulsion involves an abrupt change of channel course that changes the locus of sediment deposition. Bifurcation occurs in the most seaward parts of river deltas where channels divide due to mouth bar deposition. However, how avulsion (top-down) and bifurcation (bottom-up) processes interact in river deltas is poorly understood. We conducted a suite of morphodynamic numerical model experiments using six scenarios with different slopes, selected within the range observed in natural deltas, upstream from the delta apex. The experiments allow us to understand the internal (autogenic) interaction of avulsion and bifurcation in the absence of external (allogenic) forcing. We find that topset slope (S_{topset}) primarily controls the avulsion timescale (T_a) with $T_a = 0.3S_{topset}^{-1.18}$ ($R^2 = 69\%$; $p < 0.05$). Avulsion and bifurcation are shown to occur simultaneously based on the non-unimodal distribution of dimensionless island sizes created in our model, even though these are mechanistically different processes. Comparing our findings to natural deltas, we find consistent avulsion timescale-topset slope (T_a -S_{topset}) relationships. Our findings show how the delta topset slope serves as the first order control of the avulsion timescale, and how avulsion and bifurcation interact throughout delta building processes. This interaction is significant due to their direct impact on coastal and inland hazards that arise from rapid geomorphic change and flooding on densely populated deltas.

4.1. Introduction

River deltas are home for ~339 million people worldwide, are hotspots for biodiversity, and crucial carbon sinks (Ericson et al., 2006; Syvitski and Saito, 2007; Shields et al., 2017; Loucks, 2019; Hackney et al., 2020). However, the geomorphic dynamism of river deltas in the modern era has been altered by growing stressors such as change in hydrologic regimes, sea-level rise, and accelerated subsidence (Syvitski et al., 2009; Giosan et al., 2014; Wallace et al., 2014; Tessler et al., 2015), putting human and other systems that rely on river deltas at considerable risk. To anticipate how river deltas may respond to these growing pressures, we need to understand how deltas internally (i.e. autogenically) build and evolve through time.

River delta growth depends on upstream catchment properties as inputs of water and sediment, and also as the (external) cause of the gradient of the input river to the delta plain. The growth of a river delta is initiated through repeated mouth bar deposition due to sudden expansion and deceleration of a sediment-laden jet of water entering relatively still water, usually the sea or a lake (Bates, 1953; Wright, 1977; Edmonds et al., 2011; Kleinhans et al., 2013). Mouth bars grow in both upstream and downstream directions from the point of initiation, reach a height of around 0.4-0.6 of the initial flow depth, and stop growing once the sediment flux is advected around the mouth bar rather than accelerated over the bar (Edmonds and Slingerland, 2007; Kleinhans et al., 2013; Fagherazzi et al., 2015). Simultaneously, avulsion takes place in more upstream parts of a delta plain when mouth-bar deposition and stagnation induce parent channel backfilling, triggering an avulsion to create a smaller channel by breaching the channel levee in the upstream part of a mouth bar (Ganti et al., 2016a). Another type of avulsion involves blocking of a channel by sediment advected from upstream, promoted by in channel aggradation that is independent from the distal process (Kleinhans et al., 2013). Overall, the combination of bifurcation and avulsion creates a distributary channel network that merges upstream at the delta apex (Edmonds and Slingerland, 2007).

Many studies have shown that different processes are involved in the mechanics of avulsion and bifurcation in river deltas (Edmonds and Slingerland, 2007; Jerolmack and Swenson, 2007; Edmonds et al., 2009; Chatanantavet et al., 2012; Kleinhans and Hardy, 2013; Ganti et al., 2016a). Based on different processes that dominate within each, a river delta may be divided into bedslope-mediated and backwater-mediated zones (Ganti et al., 2014; Prasojo et al., 2022). The bedslope-mediated zone consists of the river environment downstream as far as the first avulsion point, initiating the onset of delta building and avulsion-driven stratigraphy. In contrast, the backwater-mediated zone consists of delta distributary channels down to the delta shoreline, with backwater-triggered avulsion or bifurcation dominating the stratigraphy.

The bedslope-mediated zone is controlled by in-channel aggradation (Prasojo et al., 2022), demonstrated by the strong correlation between the upstream slope and the location of avulsion nodes based on the study of 105 natural deltas. In-channel aggradation can then trigger avulsion by incision (Slingerland and Smith, 2004), partial avulsion (Kleinhans et al., 2013) or full avulsion (Prasojo et al., 2022). In contrast, bifurcation in the backwater-mediated zone of a delta is caused by channel splitting around the mouth bar due to flow

deceleration when entering a relatively still body of water (Olariu and Bhattacharya, 2006; Edmonds and Slingerland, 2007; Ganti et al., 2016a). This phenomenon can then induce channel backfilling that can also act as an avulsion trigger in the backwater-mediated zone. Hence, we may have bifurcation-triggered avulsion located within the backwater-mediated zone, as also found in Huanghe (Yellow) delta by Ganti et al. (2014).

However, our knowledge about the internal interdependency between avulsion and bifurcation is limited, despite their direct influence on coastal and inland flood risk on river deltas. Hypothetically, catchment properties have varying slope gradients located upstream of a deltas first avulsion point. These catchment properties control transport capacity and the sediment flux feeding into a delta. Consequently, these top-down properties also play an important role in controlling the avulsion length of a delta. With homogeneous sediment size and constant input of water and sediment discharge, steeper upstream slopes will lead to larger deltas and more frequent avulsion and bifurcation. Conversely, lower upstream slopes lead to smaller river deltas and slower avulsion and bifurcation processes. If this hypothesis is true, upstream slope may exert an important role in defining the frequencies of both avulsion and bifurcation in river deltas. Since our understanding of the internal controls triggering avulsion-bifurcation response is currently underdeveloped (Kleinhans et al., 2010; Ganti et al., 2014), this investigation aims to: (1) identify the first order controls of avulsion and bifurcation timescales from a suite of numerical model experiments that have various upstream slopes; (2) understand the avulsion-bifurcation causalities through investigation of each step of the delta building process; and, (3) assess the implications from this numerical model for understanding the dynamics of contemporary and ancient deltas. Further, a robust understanding of these processes has practical implications due to their direct impact on coastal and inland flood risk on highly populated river deltas. We created a suite of numerical simulations with six different scenarios representing different upstream slopes, based on natural river deltas, to understand autogenically-controlled avulsion and bifurcation.

4.2. Methods

We designed a set of numerical experiments to model a natural scale river delta (7.5 x 7.5 km) where we control the slope upstream of the delta avulsion node (S_{US}) while keeping other physical parameters constant. We adopted the Delft3D river delta models from Edmonds and Slingerland (2010) and Caldwell and Edmonds (2014), with bathymetry modified as necessary to accommodate our various upstream slopes. The physical

parameters set in the model were based on real deltas and we measured the avulsion timescale (T_a) based on the analytical approach by Chadwick et al. (2020) and the bifurcation timescale (T_b) using the scaling approach of Coleman and Wright (1971).

4.2.1. Scenario

The model uses various slopes upstream of the slope break location (Fig. 4.1a), with slopes chosen to be representative of natural river deltas. The slopes upstream (S_{US}) and downstream (S_{DS}) of slope breaks identified from 105 globally distributed river deltas from Prasojo et al. (2022) were used to calculate the ratio of upstream:downstream slopes, from which we determine representative percentiles of this ratio (Fig. 4.1b; Table 4.1). These representative percentiles were then used to calculate upstream slope values in the model assuming constant initial downstream slope (S_{DS}=0.000375) from the Mississippi delta (Edmonds and Slingerland, 2010).

4.2.2. Model setup

We use Delft3D (4.04.02) software (Deltares, https://oss.deltares.nl/web/delft3d) to model six different scenarios. Delft3D is a physics-based model that simulates the hydrodynamics and morphodynamics of environments including rivers, estuaries and river deltas (Edmonds and Slingerland, 2010; Caldwell and Edmonds, 2014; Nienhuis et al., 2018a, 2018b). The software has been validated for a wide range of environments, including self-formed river deltas (Edmonds and Slingerland, 2007, 2008; Geleynse et al., 2011; Burpee et al., 2015; Rossi et al., 2016; Williams et al., 2016; Nienhuis et al., 2018a; Morgan et al., 2020). Flow is computed using the depth-averaged, nonlinear, shallow-water equations, obtained from three-dimensional Reynolds-averaged Navier-Stokes equations (Edmonds and Slingerland, 2010). The velocity distribution in the model is then used to compute sediment transport (only suspended load is applied in our model) and to update the bed elevation (or bathymetry) according to divergence in sediment transport (Caldwell and Edmonds, 2014).

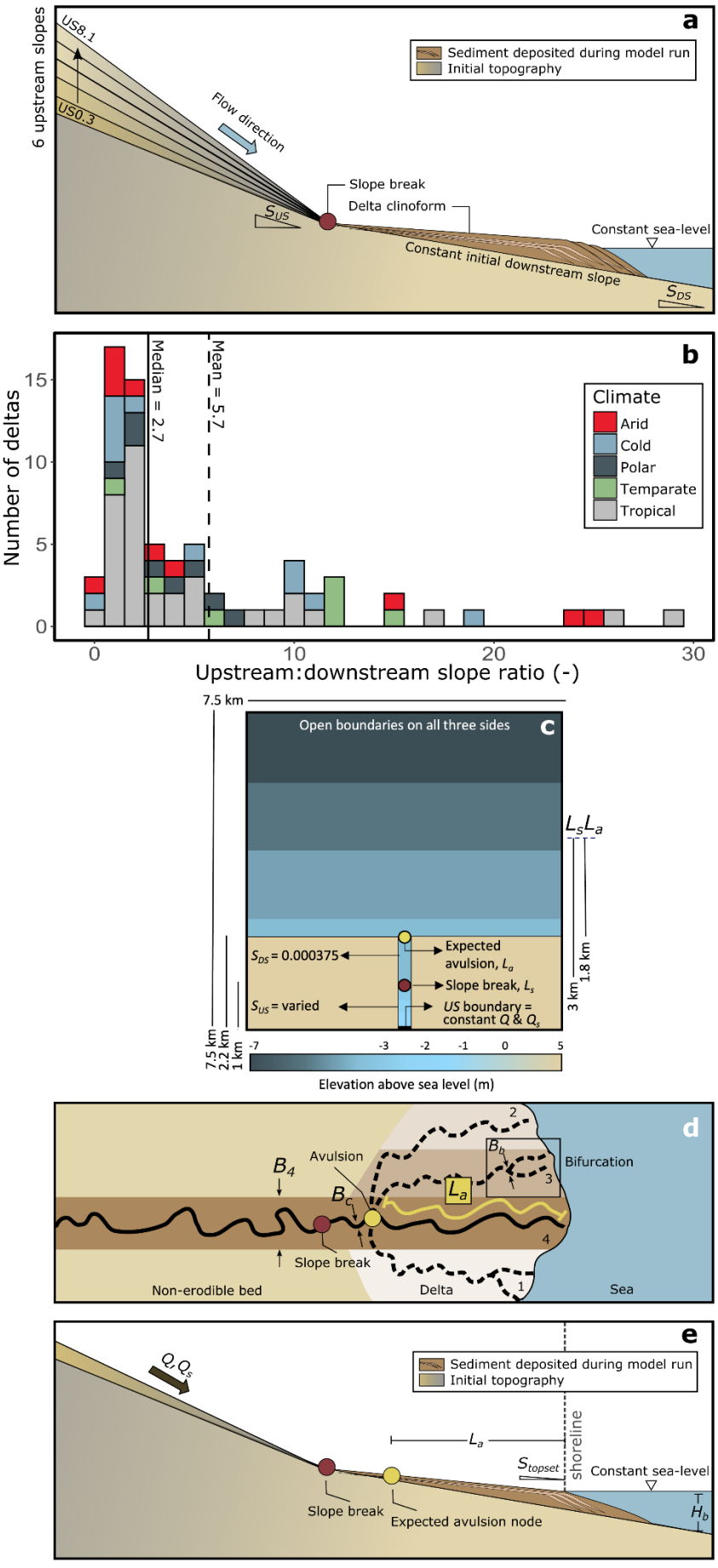
a
6 upstream slopes
US8.1
US0.3
Flow direction
Sediment deposited during model run
Initial topography
Slope break
Delta clinoform
S_{US}
Constant sea-level
Constant initial downstream slope
S_{DS}
b
Number of deltas
Median = 2.7
Mean = 5.7
Climate
Arid
Cold
Polar
Temparate
Tropical
Upstream:downstream slope ratio (-)
c
7.5 km
Open boundaries on all three sides
L_s L_a
S_{DS} = 0.000375
Expected avulsion, L_a
Slope break, L_s
S_{US} = varied
US boundary = constant Q & Q_s
3 km
1.8 km
7.5 km
2.2 km
1 km
Elevation above sea level (m)
d
B_4
Avulsion
B_c
B_b
Bifurcation
L_a
Slope break
Non-erodible bed
Delta
Sea
e
Q, Q_s
Sediment deposited during model run
Initial topography
L_a
shoreline
S_{topset}
Constant sea-level
Slope break
Expected avulsion node
H_b

Figure 4.1 Schematic diagram of model design.(a) The upstream slopes are from 6 representative percentiles from the upstream-downstream slope ratios of modern river deltas shown in Fig. 4.1b. Initial downstream slope, S_{DS} is kept constant at 0.000375, the downstream slope of the modern Mississippi delta (Edmonds & Slingerland, 2010). (b) Distribution of the upstream (*US*) – downstream (*DS*) slope ratio from 105 modern river deltas distributed across five climate regions. Median (solid vertical) and mean (dashed vertical) values are indicated. (c) Plan view of the model design. L_a and L_s are avulsion length and slope break length, respectively. The non-erodible bed at 5m above sea level represents non-erodible bedrock. (d) Schematic diagram of a river delta showing avulsion and bifurcation locations, inlet sediment load (Q_s), lobe width of each avulsion (B), avulsion length (L_a), and channel widths measured at avulsion (B_c) and bifurcation (B_b) nodes. Modified from Chadwick et al. (2020). Numbers near the shoreline represent the number of delta lobes that were used to measure B; e.g. B_4 on (d) represents the width of the fourth lobe built. Schematic cross-section showing basin depth (H_b) and topset slope (S_{topset}). Parameters in Fig. 4.1d-e are measured in each timestep during the delta building process.

Table 4.1 Numerical modelling scenarios. IDs refer to ratio of the upstream slope (*US*) to the downstream (*DS*) slope (i.e. US2.7 means upstream slope is 2.7 times the downstream slope).

Run ID	Percentile from US/DS ratio	Upstream slope	Downstream slope
US0.3	2.5	1.13×10^{-4}	3.75×10^{-4}
US0.68	10	2.55×10^{-4}	3.75×10^{-4}
US1.4	25	5.25×10^{-4}	3.75×10^{-4}
US2.7	50	1.01×10^{-3}	3.75×10^{-4}
US6	71	2.25×10^{-3}	3.75×10^{-4}
US8.1	75	3.04×10^{-3}	3.75×10^{-4}

We adopted the geometry and physical parameters from a synthetic self-formed river delta model ('scenario o') from Edmonds and Slingerland (2010) and Caldwell and Edmonds (2014) (Fig. 4.1c). The model is rectangular with four boundaries, the incoming river discharge being located at the 'South' boundary of the model and the other three boundaries set to 0 m elevation above sea level. The incoming river discharge, uniformly spreads across the 250 m wide inlet channel, is constant at 1050 m^3/s, a representative value for global river discharge (Edmonds and Slingerland, 2010; Caldwell and Edmonds, 2014), and sediment discharge was in equilibrium with transport capacity at this inlet. The model was enlarged to 7.5 km x 7.5 km to avoid the delta plain extending across the model boundaries. We modified the upstream part of the model domain by introducing a slope break and slope-avulsion length scaling (L_a:L_s = 6:10) that we determined from modern systems (Fig. 4.1c-d, Table 4.1) to accommodate different upstream slope scenarios. Modification of the upstream part of the model domain involves changing the bathymetry to introduce this slope break - avulsion length scaling. We maintained other physical (e.g. grain sizes, critical bed shear stress for erosion and deposition) and numerical parameters constant across all scenarios (Table 4.2). Moreover, we ran additional sensitivity analyses using 25 subsurface layers instead of one to see its impact on the stratigraphy produced in each scenario.

Table 4.2 User-defined model parameters (adopted from Edmonds & Slingerland (2010); Caldwell & Edmonds (2014)).

Parameter	Value	Units
Grid size	300 x 300	cells
Cell size	25 x 25	m
Run duration	17	days
Downstream basin bed slope	0.000375	(-)
Initial channel dimension (width x depth)	250 x 2.5	m
Upstream non-erodible bed elevation	5	m
Initial upstream length	1000	m
Initial avulsion length from the expected shoreline	1800	m
Initial slope break length from the expected shoreline	3000	m
Inlet open boundary: water discharge	1050	m^3/s
Downstream open boundary: constant water surface elevation	0	m
Initial sediment layer thickness at bed	5	m
Number of subsurface stratigraphy bed layers	1	(-)
Time step	0.2	min
Morphological scale factor	175	(-)
Spin-up interval	720	min

4.2.3. Surface metrics

We define avulsion and bifurcation timescales as the times needed for the delta distributary channel to create one avulsion or bifurcation, respectively. The analytical model for calculating avulsion timescales assumes switching of flow and sediment partitioning between multiple lobes in a delta plain, and considers the influence of backwater hydrodynamics in calculating the avulsion timescale (Chadwick et al., 2020).

Chadwick et al. (2020) derived the avulsion frequency as:

$$f_a = \frac{1}{(1-\lambda_p)} \frac{Q_s}{(L_a - D)B_a H + DB_a\left(H_b + z + \frac{DS_{topset}}{2}\right)} \; if\; D \geq 0 \tag{4.1}$$

$$f_a = \frac{1}{(1-\lambda_p)} \frac{Q_s}{L_a B_a H} \; if\; D < 0 \tag{4.2}$$

$$D = (H - z)/S_{topset} \tag{4.3}$$

$$H = H^* h_c \tag{4.4}$$

with the bankfull depth calculated using Parker et al.'s (2007) method:

$$h_c = \left(\frac{C_f {Q_c}^2}{g {B_c}^2 S_{topset}}\right)^{\frac{1}{3}} \tag{4.5}$$

with f_a = avulsion frequency [year], Q_s = sediment load [km^3/year], B_a = lobe width of each avulsion [km], L_a = avulsion length [km], λ_p = sediment porosity [-], H = aggradation thickness necessary for avulsion [m], H_b = basin depth [m], H^* = avulsion threshold [-] = 0.2-1.4 in lowland deltas (Ganti et al., 2019a), h_c = bankfull depth [m], C_f = bed friction coefficient [-], Q_c = bankfull discharge [m^3/s], B_c = channel width at avulsion node [m], S_{topset} = topset slope [-], D = lobe-progradation distance [km] and z = magnitude of sea level rise [m].

We assume the avulsion threshold (H^*) to be 0.5, which is realistic for lowland (Ganti et al., 2019a), and $D > 0$ since there is no allogenic forcing that would make the delta regress. Since sea-level is constant in this investigation, sea level rise $z = 0$. Sediment porosity (λ_p) is assumed to be 0.4 (Jerolmack, 2009), bed friction coefficient (C_f) = 0.002 for lowland rivers (Parker et al., 2007), and bankfull discharge (Q_c) = 1050 m^3/s. The upstream sediment boundary condition is for the inlet to be in equilibrium so that sediment load changes every timestep to match the sediment transport capacity at the inlet. We use equation (4.1) to calculate avulsion timescale (T_a = 1/avulsion frequency) throughout the model run.

To calculate the bifurcation timescale, we adopted the approach of Coleman and Wright (1971) (also used by Swenson (2005) and Jerolmack and Swenson (2007)). Coleman and Wright (1971) discovered that the length of distributary channels (L_D) in between adjacent bifurcation nodes in a delta plain scales with the channel width upstream of the bifurcation (B_b) ($L_D \approx 10\ B_b$). For a river delta without any wave or tide influence, delta progradation rate (v_p) can be written as:

$$v_p = \frac{Q_s}{B_b H_b} \tag{4.6}$$

Consequently, bifurcation timescale is

$$T_b = \frac{L_D}{v_p} = \frac{\alpha B_b}{Q_s} . B_b H_b = \frac{\alpha {B_b}^2 H_b}{Q_s} \tag{4.7}$$

with α = dimensionless parameter ≈ 10 (Coleman and Wright, 1971), Q_s = sediment load (km^3/year), and H_b = basin depth (m) (Swenson, 2005; Jerolmack and Swenson, 2007). The basin depth (H_b) is kept constant at 7.5 m since we do not introduce sea-level rise in any scenario (Edmonds and Slingerland, 2010).

All the surface metrics are measured once the model has reached a dynamic equilibrium state in which the sediment load (Q_s) that a channel must transport is balanced by the water discharge (Q) supplied to the channel and the channel slope (S) (Lane, 1954). The lobe width of each avulsion (B), channel width at avulsion nodes (B_c), channel width upstream of a bifurcation (B_b) and avulsion length (L_a) were measured in QGIS from the georeferenced images produced by Delft3D at every timestep. Topset slope ($\underline{S_{topset}}$) for every timestep was measured from a longitudinal cross-section located through the centre of the model by conducting linear regression through topset elevation points. Lobe progradation distance (D) and bankfull depth (h_c) were calculated using Eq. 4.3 and 4.5 consecutively to obtain the avulsion timescale at each timestep during delta building. The model produces 52 computational timesteps in total, which equals ~400 years.

The calculated avulsion and bifurcation timescales are related to the measured topset slopes (S_{topset}) to assess the role of topset slope in affecting avulsion and bifurcation mechanisms. We recorded the stratigraphy produced during each run using representative transverse (E-W) and longitudinal (S-N) cross sections at every timestep. Transverse profiles are located at: proximal (2.38 km downstream of the model South boundary); medial (4.5 km); and distal (5.25 km) locations on the delta plain. The model results are then compared to avulsion and bifurcation timescales obtained from 19 modern river deltas, two fan deltas and one physical model that cover similar topset slope magnitudes to our model. Avulsion timescales from the natural and physical deltas are calculated using Eq. 4.1, with the dataset available from Chadwick et al. (2020). Bifurcation timescale is calculated using Eq. 4.7, using Qs from Chadwick et al. (2020) and assuming the channel width at avulsion nodes (B_c) ≈ the channel width upstream of a bifurcation (B_b). Finally, we discuss our model's implications for natural systems by drawing on Jerolmack and Mohrig (2007) and Chadwick et al. (2020) results.

4.3. Results

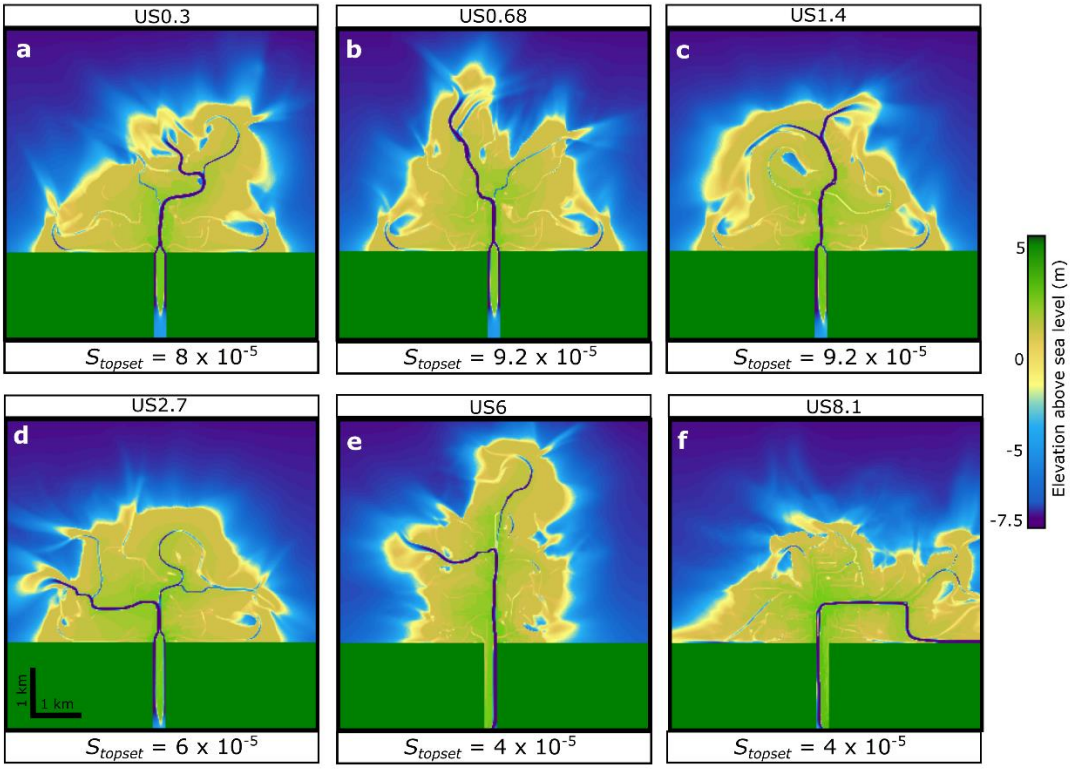

Figure 4.2 (a-f) Terrain models at their final time steps of each scenario. US0.3 represents upstream slope of 0.3 times the downstream slope, US0.68 represents upstream slope of 0.68 times the downstream slope and so on. S_{topset} represents topset slope measured at the final timestep of the simulation. US8.1 scenario reached the model's boundary. Consequently, the simulation was repeated with a larger domain size shown in Fig. 4.3.

4.3.1. Delta plain morphology

Fig. 4.2 shows the morphology of the deltas in each scenario at the final timestep. Overall, the different upstream slopes produce variable topset slopes, and the resulting delta plains show different shoreline configurations, different numbers of active distributary channels and slightly different delta plain sizes. One delta plain reached the model boundary (US8.1) and this scenario was repeated with a larger domain size (Fig. 4.3) and the avulsion and bifurcation timescales were calculated from this larger domain.

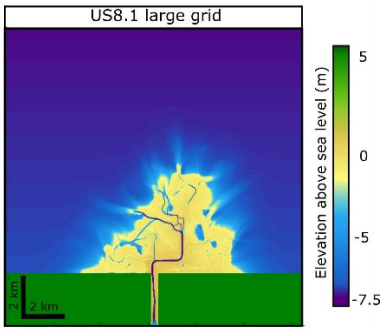

Figure 4.3 Results of the numerical model at its final timestep from scenario US8.1 using a larger grid size (12.5 km x 12.5 km).

Steeper upstream slopes are associated with longer avulsion lengths (L_a) (Fig. 4.4a) and larger lobe widths created by each avulsion (B_a) (Fig. 4.4b). However, steeper upstream slopes produce slightly narrower channel widths upstream of a bifurcation (B_b) (Fig. 4.4c) with no impact on the channel width at the avulsion node (B_c) (Fig. 4.4d). Statistical significance tests (one-way ANOVA and Kruskal-Wallis tests applied to normally- and non-normally distributed data, respectively) show that upstream slopes significantly control the geometry variables of the river deltas measured in this study ($p < 0.05$).

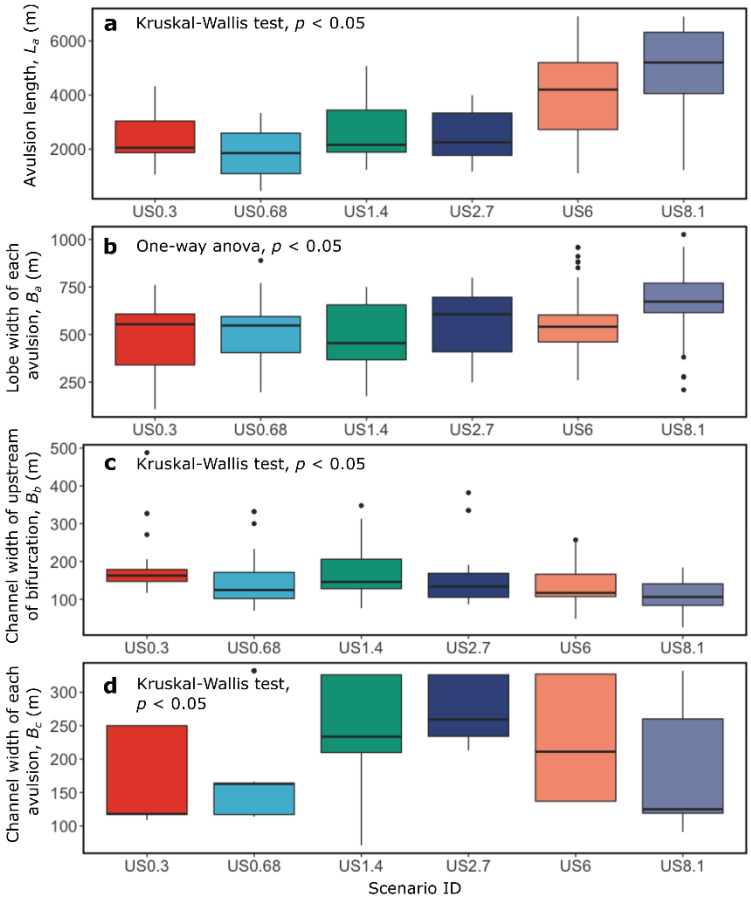

Figure 4.4 Distribution of independent variables measured in this investigation across scenarios (a) avulsion length distribution, L_a (b) lobe width of each avulsion distribution, B_a (c) channel width of upstream of bifurcation distribution, B_b (d) channel width of each avulsion distribution, B_c.

Figure 4.5 shows the distribution of avulsion and bifurcation timescales, noting that these can be examined at different times during each run. The range of avulsion and bifurcation timescales span different orders of magnitude from both between-scenario and within-scenario variability. Avulsion period ranges from 1.2 x 10^3 - 1.9 x 10^5 year (median = 1.2 x 10^4 year; N = 229) (Fig. 4.5a). Bifurcation timescales are in the range of 2 x 10^{-2} - 5.7 years (median = 4 x 10^{-1} year; N = 201) (Fig. 4.5b; Fig. 4.6). The different magnitudes in response times for avulsion and bifurcation processes may be caused by the different compensation scale, the tendency for sediment to preferentially fill lower topography, and also by different channel depths and aggradation rates between the upstream (i.e. bedslope-mediated) and downstream (i.e. backwater-mediated) parts of deltas (Jerolmack and Paola, 2010; Li et al., 2016, 2018; Straub et al., 2020).

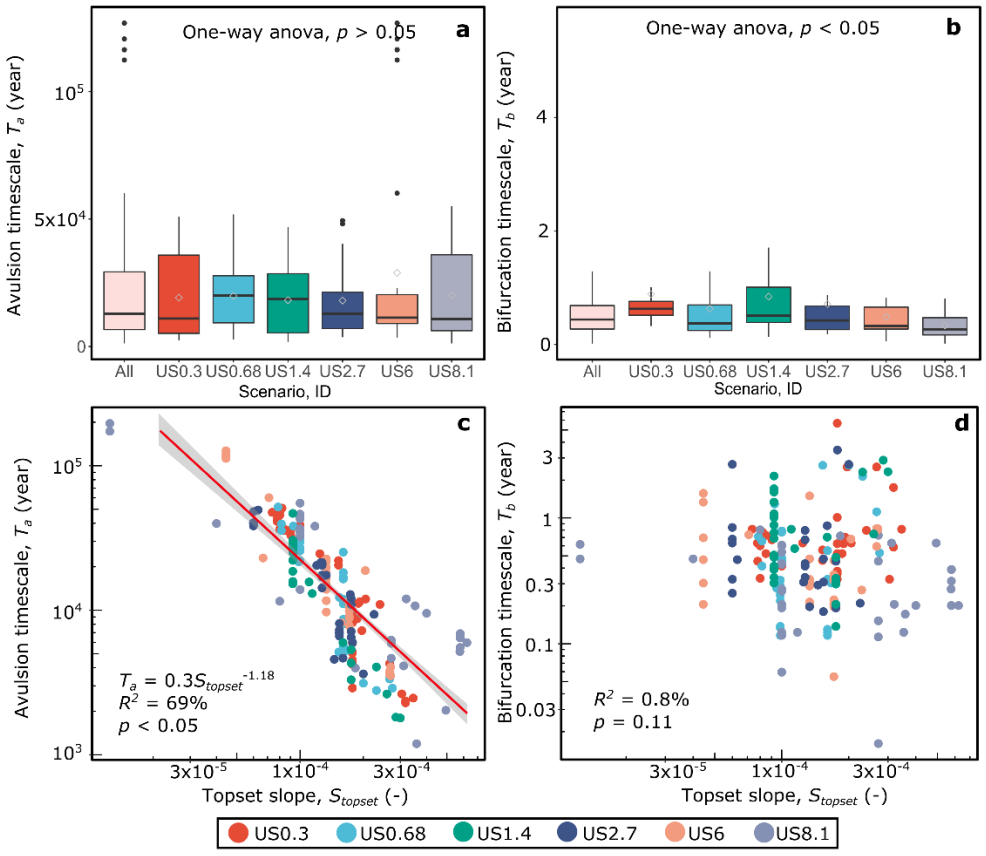

Figure 4.5 (a-b) Distributions of avulsion and bifurcation timescales for all model and individual scenarios. (c-d) Correlations between avulsion and bifurcation timescale and topset slopes. Shaded zone is the 95% confidence interval about the ordinary least square (OLS) regression line.

Across all the scenarios, the distributions of the avulsion and bifurcation timescales remain constant (Fig. 4.5a,b). One-way ANOVA shows that the scenario (upstream slope) does not

significantly influence (p > 0.05) the avulsion timescale. However, there is a significant influence of the upstream slope on the bifurcation timescale (ANOVA; p < 0.05). Correlations between the other independent variables (B_a, B_c, and L_a) and the avulsion and bifurcation timescales (Fig. 4.7) are generally not significant, although some do have significant (e.g. T_a-B, T_a-L_a), although weaker than the avulsion timescale-topset slope (Fig. 3c), correlations.

To understand the first order control of these avulsion and bifurcation timescales, we examine the independent variables used in their calculation. The topset slopes (S_{topset}) play a significant role in defining the avulsion timescale (Fig. 4.5c) but not in the bifurcation timescale (Fig. 4.5d). The avulsion timescale (T_a) has a statistically significant negative power law relationship with the topset slope ($T_a = 0.3S_{topset}^{-1.18}$; R^2 = 69%, p < 0.05) (Fig. 4.5c).

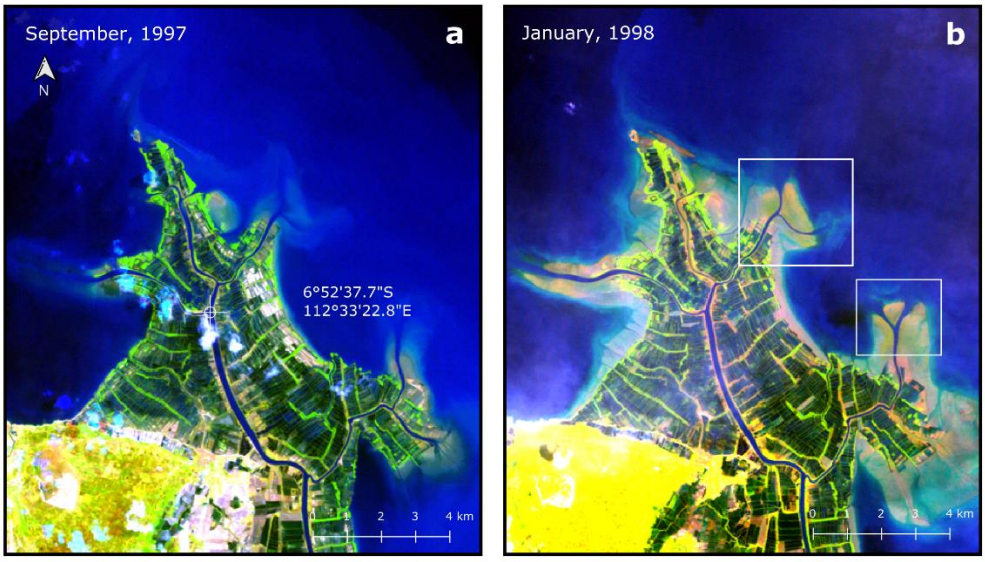

Figure 4.6 Example from Bengawan Solo delta showing the process of (a) before bifurcation in September 1997 and (b) after bifurcation in January 1998. See the white boxes for the details of bifurcation on (b). We used Landsat 5 composite satellite images and show only band 5, 4 and 1 to highlight the water surrounding the bifurcations.

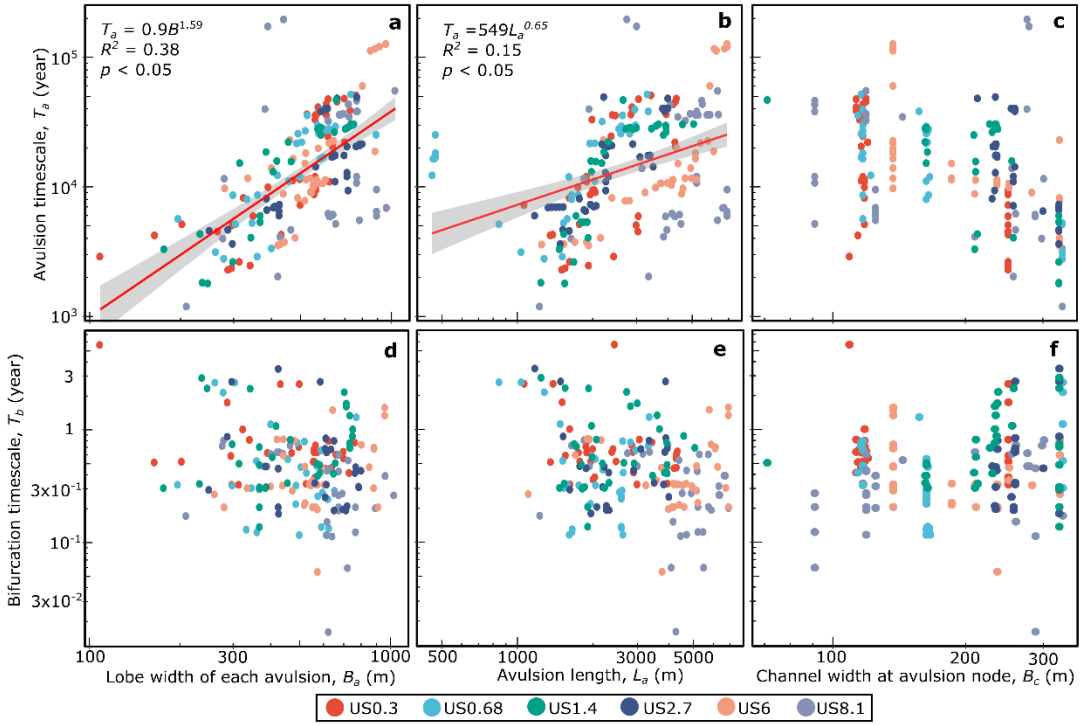

Figure 4.7 Correlations between the avulsion-bifurcation timescales with the independent variables measured in this investigation (a) avulsion timescale-lobe width of each avulsion correlation, (b) avulsion timescale-avulsion length correlation, (c) avulsion timescale-channel width at avulsion node correlation, (d) bifurcation timescale-lobe width of each avulsion correlation, (e) bifurcation timescale-avulsion length correlation and (f) bifurcation timescale-channel width at avulsion node correlation.

4.3.2. Stratigraphy during delta growth

Fig. 4.8a shows the evolution of the delta including both foreset progradation and topset aggradation. These elevation data enable examination of changes to bathymetry during each timestep. Sedimentation occurs simultaneously offshore and within the input channel within the valley at the head of the delta. The transverse proximal cross section shows that distributary channels reach similar depths across all timesteps (Fig. 4.8b). Note that the deep channel erosion located at 2.2 - 3.6 km on Fig. 4.8a is caused by a full depth erosion mixing of a five-metre-thick subsurface layer. Sensitivity analyses using 25 subsurface layers produced similar topography (Fig. 4.9).

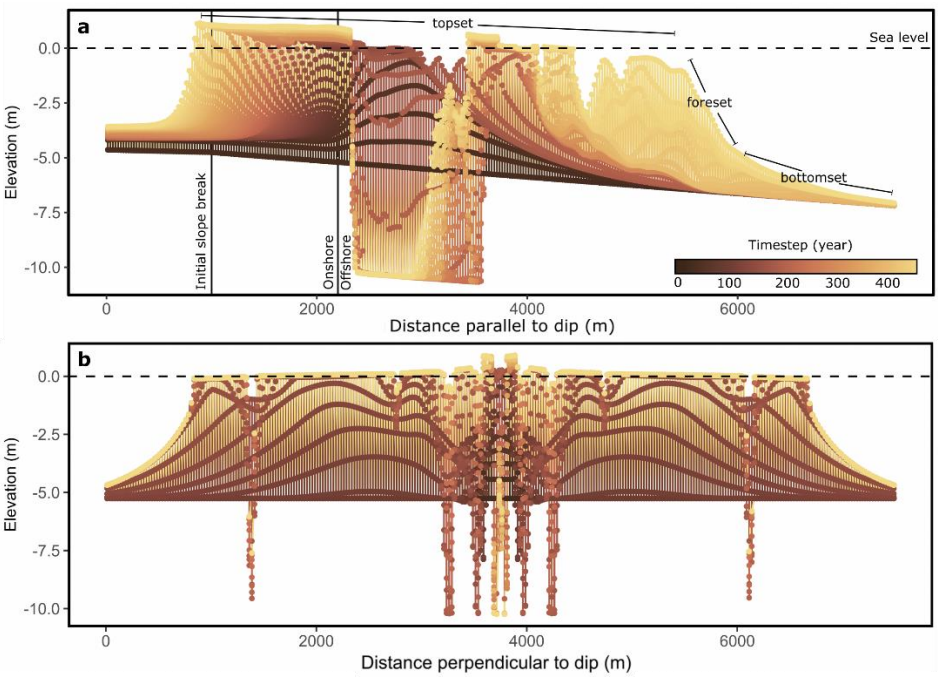

Figure 4.8 Longitudinal cross section (S-N on Fig. 4.1) showing the stratigraphy produced for each timestep from the US0.3 scenario. Vertical lines represent the locations of the initial slope break and the limit between the depositional offshore and the onshore non-erodible bed (Fig. 4.1) from where the river delta starts to develop. Lines on top of the stratigraphy represent the location of topset, foreset and bottomset. (b) Transverse cross section located within the proximal part (2.38 km downstream from the model upstream boundary) of a river delta showing consistent depth of distributary channels across all timesteps in the US0.3 scenario.

The elevations from transverse cross-sections of the delta plain at representative proximal, medial and distal sections are summarised as boxplots (Fig. 4.10). The elevations are consistent in all cases, although US6 has slightly higher topography due to a longer and straight distributary channel developing (Fig. 4.2e). Overall, the down-dip longitudinal section and the transverse cross sections all produced elevations that are statistically similar across all scenarios and all timesteps (Table 4.3).

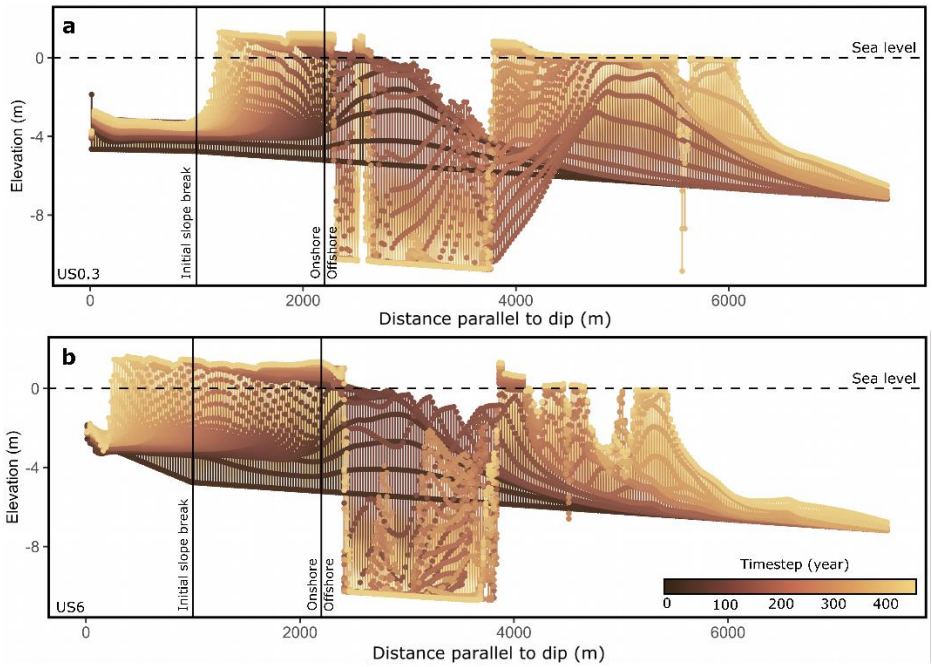

Figure 4.9 Longitudinal profile from (a) scenario US0.3 and (b) US6 with 25 subsurface layers showing similar subsurface patterns with scenarios using one subsurface layer as shown in Fig. 4.8a.

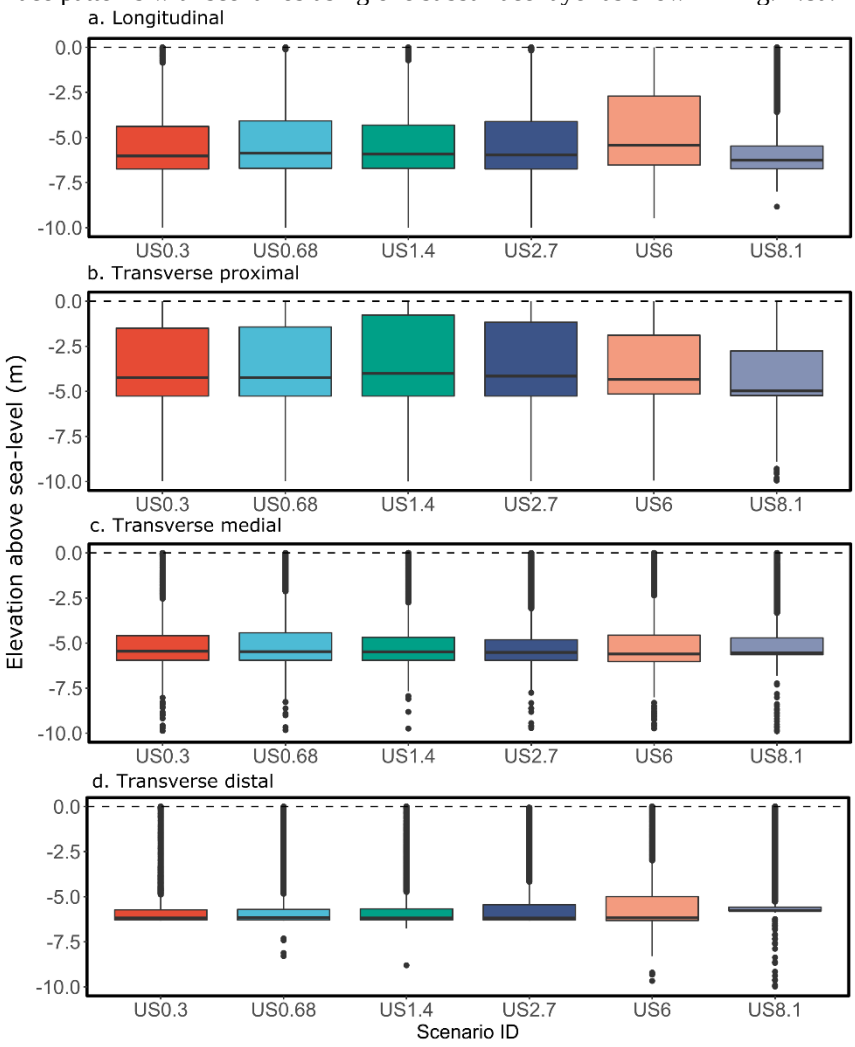

Figure 4.10 Boxplots of topographic elevation for each scenario from: (a) longitudinal cross section; (b) proximal transverse cross section; (c) medial transverse cross section; and (d) distal transverse cross section from all 52 timesteps. Each timestep represents 8.72 years, or ~400 years in total.

Table 4.3 Summary elevations from topographic profiles at all timesteps in all model scenarios. Data from longitudinal (S-N on Fig. 4.1) and transverse (proximal, medial and distal) cross sections are shown. SL = sea-level.

	Longitudinal		Transverse[1]					
			Proximal		Medial		Distal	
	Above SL	Below SL	Above SL	Below SL	Above SL	Below SL	Above SL	Below SL
Max	1.30	11.45	1.35	10.25	0.81	11.05	0.62	11.31
Mean	0.35	5.65	0.17	3.64	0.13	4.93	0.11	5.47
Median	0.33	6.18	0.09	4.57	0.10	5.53	0.05	5.99
Min	0.00	0.00	0.00	0.00	0.00	0.00	0.00	0.00
N	10346	98802	42097	108703	5463	145337	879	149921

[1]Transverse profiles located at: proximal node 95 (2.38 km downstream of the model boundary); medial node 180 (4.5 km); distal node 210 (5.25 km).

4.4. Discussion

The six scenarios used in this study provide details of avulsion and bifurcation processes from the inception of delta building. Since avulsion is infrequent, by calculating the avulsion and bifurcation timescales of each timestep we can estimate the range of possible magnitudes of these processes (assuming that the equations we used are accurate). Correlation with the independent parameters that we control during the modelling suggests that topset slope provides the first order control of avulsion timescales. The avulsion-bifurcation causalities and their implications for the contemporary and ancient deltas are also discussed in the following sections.

4.4.1. First-order control of avulsion and bifurcation timescale

The avulsion timescale is strongly correlated with the topset slope at each timestep (Fig. 4.5c). The topset slope is partly a function of the scenario (which determines upstream slope). However, when being compared across scenarios, none of the scenarios show a strong correlation with the avulsion timescale (Fig. 4.5a) and the topset slope produced. Correlations between avulsion and bifurcation timescales and other independent variables (Fig. 4.7) also show weak to no correlations. Moreover, correlating the bifurcation timescale to the width upstream of a bifurcation (B_b), the only varied independent variable in this experiment, shows exponential relationship as expected from the Eq. 4.7.

The independent variables that we correlate with the avulsion and bifurcation timescales are all geometrical (avulsion length, lobe size, channel widths). Importantly, none of these variables are well-correlated with the avulsion or bifurcation timescales. These results imply

that avulsion and bifurcation timescales may not be dependent on the geometry of the delta or the size of the delta. Rather, topset slope may be the variable that controls the avulsion timescale (Fig. 4.5c). The topset slope controls the avulsion timescale due to stream power increasing with steeper topsets and hence avulsion occurs more frequent in a steeper delta plain. The topset slope itself is mainly controlled by the top-down forcing of in-channel vertical aggradation. While the bifurcation timescale is controlled by the width upstream of a bifurcation (B_b) as shown in the Eq. 4.7 and directly related to the sediment load (Q_s), which we do not vary in this study. Significant correlation between scenario and bifurcation timescale shown in Fig. 4.5b may be caused by statistical artefacts. Further statistical analysis shows that bifurcation timescale does not correlate with the upstream slopes used to define the scenarios, with $R^2 = 7.6\%$.

In river deltas, fine-grain and cohesive sediment frequently dominate the system since sediment loads fine downstream. With finer and more cohesive sediments and possibly more vegetation, channel bars are stifled, promoting overbank floodplain deposition with fewer number of distributary channels (Kleinhans et al., 2018; Ielpi and Lapôtre, 2019). With sinuous delta distributary channels and more stable riverbanks due to cohesive sediments, vertical aggradation is a more important geomorphic mechanism than the lateral migration of distributary channels. Because of this, avulsion in river deltas is more likely to be progradational, in which the avulsion disturbs the surrounding delta plain rather than reoccupying pre-existing channels, in contrast to braided rivers. This avulsion style is similar to the avulsion style of a meandering river investigated by Valenza et al. (2020); slope also serves as the important control of the avulsion in this channel type. In this avulsion style, top-down forcing of in-channel vertical aggradation, in which topset slope is its direct product, controls the likelihood for superelevated channel to discharge or avulse most of its water and sediment on to the surrounding water in the form of mouth bar deposition.

Although the topset slope controls avulsion timescale in this model, other potentially significant variables are held constant in our model (e.g. dz/dt, H_b, λ_p, Q_s). Hence, further sensitivity studies on the effects of varying these other independent variables could be undertaken. As an example, since we set Q_s as a constant, we are excluding the influence of changes in Q_s on avulsion and bifurcation timescales that directly impacts in-channel aggradation rates and the avulsion or bifurcation thresholds (H or H^*). Chadwick et al. (2020) considered the influence of sea-level rise on the avulsion timescale. By integrating theory, numerical model and field datasets, they found that avulsion timescale is controlled

by the balance between relative sea-level rise (z) and sediment supply (Q_s), where sea-level rise promotes a more frequent avulsion.

Stratigraphically, as shown in the consistency between delta size and shape and the proximal, medial, distal and parallel cross sections, changing the upstream slope in our scenario did not greatly influence the deposit thickness (Fig. 4.10a-d). This result is similar to the homogeneous thicknesses of stratigraphy from the Mississippi delta (Chamberlain et al., 2018). Comparing scenarios with a steeper slope (US6) with a gentler slope (US0.3) does not show deeper erosion (i.e. deeper autogenic reworking depth) or a thicker autogenic signal (i.e. thicker sediment deposited on foresets and topsets) (Fig. 4.9). The statistics in Table 4.3 corroborate that all the upstream slope scenarios maintain the autogenic signal and autogenic reworking depth in the model. Further statistical significance tests also show that topset slope significantly controls the avulsion length (L_a) and channel width at the avulsion node (B_c) but not the lobe width of each avulsion (B_a) or the channel width at bifurcation (B_b). Consequently, we hypothesize that the upstream slope may not control the magnitude of autogenic signals and hence that the topset slope only partly controls this magnitude.

We show in this study that neither the autogenic thickness nor the autogenic reworking depth (Ganti et al., 2020) are controlled by the upstream slope in this model, shown by the similar topographic patterns in Fig. 4.10a-d and Table 4.3. The different upstream slopes may not influence the autogenic reworking depths due to the equilibrium sediment load and constant water discharge defined at the inlet boundary of the model. Autogenic reworking depths may be controlled either by sediment load and water discharge variability (Jerolmack and Paola, 2010; Simpson and Castelltort, 2012; Li et al., 2016) or by a non-equilibrium flow (Leary and Ganti, 2020). (Leary and Ganti, 2020) found that the preservation of cross strata (i.e. autogenic signal) is higher under unsteady or non-equilibrium flow than under the equilibrium flow conditions used in this study. Consequently, varying discharge and/or sediment loads in further modelling work will provide a framework to assess how autogenic parameters could control the magnitude and/or timescale of avulsion.

The independence of the timescale and the magnitude of autogenic signals in our study may be influenced by the dynamic equilibrium upstream boundary condition. In the equilibrium state, the model keeps adjusting its sediment load (Q_s) to match its transport capacity in the prior timestep. We show that upstream slopes across an order of magnitude (Table 4.1) do not significantly influence the sediment load carried by the channel once the model has

reached dynamic equilibrium. Consequently, similar volumes of sediment are being input to the delta across all scenarios, as shown by the relatively similar delta plain sizes (Fig. 4.2a-f). Although different upstream slopes may produce significantly different morphologies (avulsion length, delta lobe size, channel width at avulsion node and bifurcation node (Fig. 4.4)), the geomorphology of the delta plains does not significantly affect the bifurcation timescale, except that the avulsion timescale is determined by the topset slope (Fig. 4.5c; Fig. 4.7).

4.4.2. Avulsion and bifurcation causalities

In this section, we investigate the causalities between the avulsion and bifurcation processes in river deltas to assess whether bifurcation leads to avulsion through backward sedimentation processes (Hoyal and Sheets, 2009; Kleinhans et al., 2010; Reitz and Jerolmack, 2012; Ganti et al., 2016a), or vice versa. Visual observation of the model runs showed that avulsion and bifurcation may occur within the same timestep. Jerolmack and Swenson (2007) hypothesized that bifurcation processes will dominate early in a delta's development. As bifurcation continues, a landward-shift in aggradation or channel backward sedimentation will trigger avulsion by in-channel deposition in more upstream reaches (Slingerland and Smith, 2004; Edmonds et al., 2009). Consequently, more established (or larger) deltas will be more avulsion-dominated or bedslope-mediated rather than bifurcation-dominated. Through time, the change in surface water slope induces a decrease in sediment transport capacity, triggering bedslope-mediated avulsion, particularly in proximal reaches, in more established or larger deltas (Ganti et al., 2016a).

Edmonds et al. (2011) modelled a theoretical delta by parameterising their model to enable bifurcation processes but prevent avulsion. When the island areas normalised by the total delta plain areas were measured, this theoretical delta has a unimodal distribution of normalised island area, as also found in the recent delta numerical models (Hariharan et al., 2021). Through time, a relatively older delta will deviate from this unimodality due to avulsion triggered by in-channel aggradation (Mohrig et al., 2000; Slingerland and Smith, 2004; Jerolmack and Swenson, 2007) or due to the exposure of bedrock on the delta plain, as found in The Mossy delta (Edmonds et al., 2011).

By measuring the island size in all model runs, we produced distributions of normalised island area at each timestep (Fig. 4.11). There is no unimodality of the normalised island

areas at any timestep in any of the model runs, which corroborates the interpretation of our data that bifurcation and avulsion occur simultaneously throughout the delta building process, as also suggested by model stratigraphy for all scenarios. Bifurcation never dominates the early delta building process, nor does avulsion dominate the later stage of the delta building process with both avulsion and bifurcation occurring throughout each simulation.

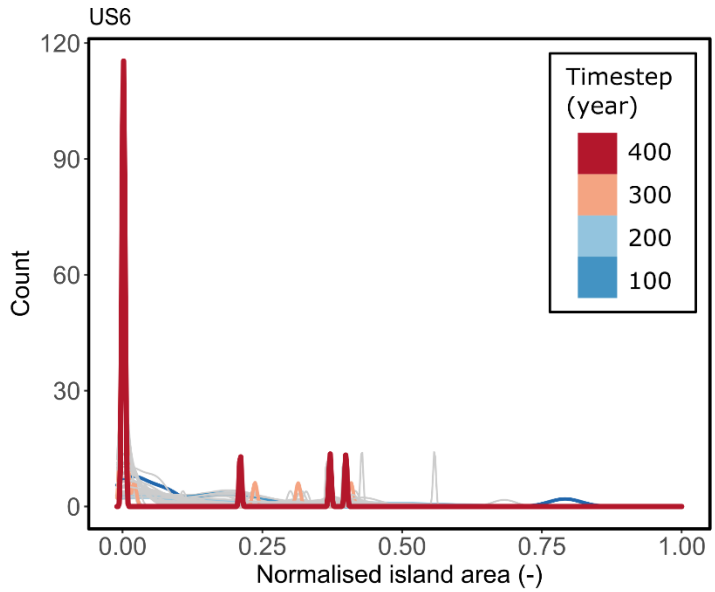

Figure 4.11 Distribution of normalised island area measured from US6 scenario showing multi-modality across different timesteps. Each line represents island area measured at each timestep in the model. We measured island size using pixel counting method from Otsu's binarized image in Google Colab (Cao et al., 2021).

4.4.3. Implications for natural deltas

Data from natural deltas show a similar avulsion timescale-topset slope relationship to our model results, even though the natural and laboratory delta avulsion timescales are 1.5 orders of magnitude lower than in our models (Fig. 4.12a). Similarly, the relationships between bifurcation timescale to topset slope in natural deltas shows no correlation, consistent with our model results (Fig. 4.12b).

The lower order of magnitude of avulsion timescales in natural and laboratory deltas may be caused by allogenic forcings that we did not incorporate in our model. Sea-level rise rate, subsidence, variable sediment load, channel engineering and human-made avulsion can directly influence the avulsion timescales found in modern deltas (Heyvaert and Walstra, 2016; Pierik et al., 2018). Even though we show that there is no correlation between T_a-S_{topset} and the sea-level rise rate (dz/dt) as shown on Fig. 4.12, sea-level rise rate does play an important role in affecting the avulsion timescale in other studies (Li et al., 2022b; Chadwick

et al., 2022). Consequently, our models could imply that anthropogenic and allogenic forcing may reduce avulsion timescales, increasing the risk of avulsion for populations living on delta plains.

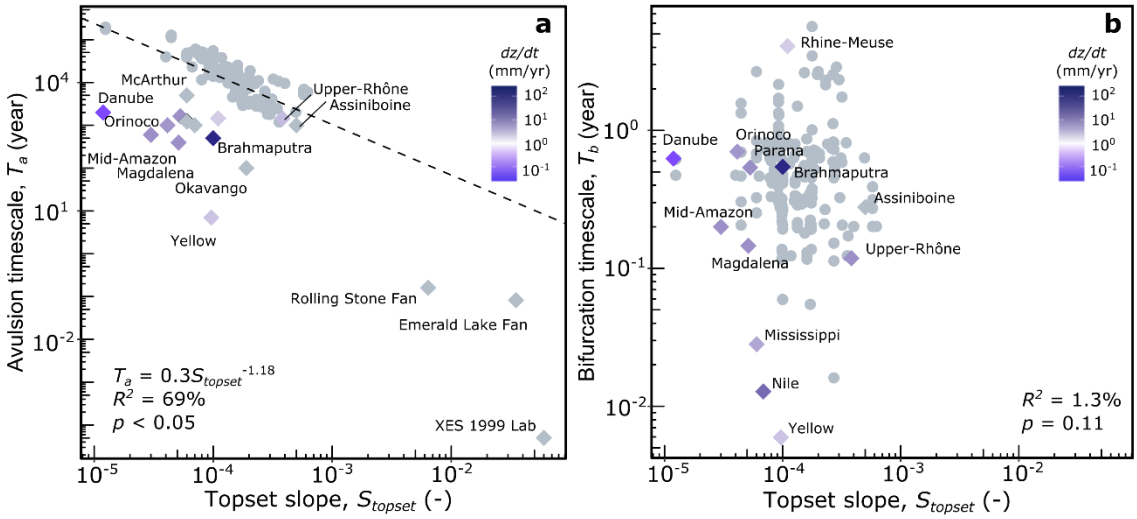

Figure 4.12 Relationships between: (a) avulsion timescale and topset slope; and (b) bifurcation timescale and topset slope, from our study (grey points) along with natural deltas gathered from the literature (colored diamonds) (Chadwick et al., 2020; Jerolmack & Mohrig, 2007; Prasojo et al., 2022). Color code represents relative sea-level rise (*dz/dt*). The equation on Fig. 4.12a refers to avulsion timescale-topset slope relationship from our model results. Delta avulsion and bifurcation timescale are calculated using Eq. 4.1 and Eq. 4.7, respectively, by assuming the channel width at avulsion nodes (B_c) ≈ the channel width upstream of a bifurcation (B_b). Data from natural deltas and the laboratory experiment are available in Table 4.4.

The avulsion timescales in our model span 10^1-10^5 years, whereas previous studies reported timescales of 10^1-10^3 years (Ganti et al., 2020). These avulsion timescales are sufficiently long that they overlap with the timescales of, and responses to, allogenic forcings that contribute to avulsion (e.g. base-level change) (Fig. 4.13). Hence, separating autogenic signals based on their timescales may not be effective due to the major overlap between these timescales. Consequently, a more careful examination of the preservation of allogenic base-level signal to the preserved stratigraphy is needed due to this long overlap. As an example, early investigation of spatial and temporal thresholds as the balance of input allogenic signal versus the system's autogenic signal suggest that a relatively smaller delta, in which the compensation time scale is smaller, will be more likely to preserve base-level change signal (Jerolmack and Paola, 2010; Li et al., 2016). Conversely, a relatively larger delta will be more likely to smear the base-level change signal. However, in this study, we show that the autogenic timescale does not depend on delta geometry or sizes (Fig. 4.7). We imply that defining one dimensional temporal or spatial threshold is more complex than previously suggested (Toby et al., 2019, 2022). We suggest that disentangling autogenic and allogenic forcing in the rock record may need a more comprehensive perspective, adding

data on sedimentary structures, fossil assemblages and other sedimentary features to morphological information.

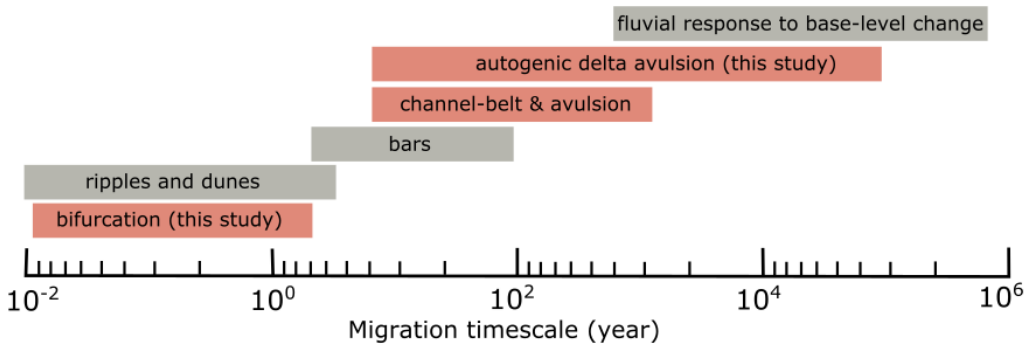

Figure 4.13 Autogenic and allogenic timescales from terrestrial environments adopted from Ganti et al. (2020).

Avulsions also affect preserved stratigraphy. Steeper delta topset slopes lead to more frequent avulsion and so may produce more avulsions in a given time interval (Fig. 4.5c). With more avulsions, increased abundance of paleosols, abandoned channel plugs, and floodplain sedimentary assemblages could be expected in the rock records. However, the preservation of evidence of autogenic signals is a function of both the timescale of this signal and the preservation potential of its stratigraphic products (Li et al., 2016; Straub et al., 2020). Evidence of autogenic signals will be preserved if either the autogenic signal timescale exceeds that of the allogenic signal (Straub et al., 2020) or the autogenically generated stratigraphic products are smaller than the autogenic reworking depth (Li et al., 2016).

In our model, the autogenic signal produced by avulsion may be autogenically reworked in the following timesteps, as shown by consistent and deep channel incisions in the upstream part of the delta (Fig. 4.8a). Here, the channel incised from 0-400 years during the simulation as shown in the down-dip cross section (Fig. 4.8a). The timescale of this autogenic reworking (0-400 years) is less than that of autogenic avulsion timescale (10^3 - 10^5 years) and hence the incision and reworking may have shredded the signal of autogenic avulsion in the preserved stratigraphy.

Table 4.4 River delta avulsion and bifurcation timescales from natural and laboratory experiment collected from the literature.

ID	h_c [m]	B_c [m]	Q_s [km^3/y]	H_b [km]	L_a [km]	σ^1 [mm/y]	B [km]	N	v_a [m/yr]	H [m]	S_{topset} [-]	T_a [year]	T_b [year]	Source
Parana	11.8	1270	0.03	40	210	3	50.8	4	0.005		0.000053	1633	0.54	Chadwick et al., 2020; Prasojo et al., 2022
Danube	6.3	1250	0.03	50	95	0.2	50	4	0.0025		0.0000119	1991	0.63	Chadwick et al., 2020; Prasojo et al., 2022
Nile	16.2	240	0.05	120	210	4.5	9.6	4			0.0000686		0.01	Chadwick et al., 2020; Prasojo et al., 2022
Mississippi	21	650	0.15	80	490	2.3	26	4	0.01		0.0000602	1250	0.03	Chadwick et al., 2020; Prasojo et al., 2022
Assiniboine	4.2	100	0.00	7	12		4	4	0.0014	4.2	0.0005	1000	0.28	Chadwick et al., 2020; Jerolmack & Mohrig, 2007; Prasojo et al., 2022
Rhine-Meuse	5	700	0.00	18	51	1.6	28	4	0.0016		0.00011	1450	4.08	Chadwick et al., 2020; Prasojo et al., 2022
Magdalena	6	1100	0.08	200	67	2.9	44	4	0.0038	6	0.0000512	394.7	0.15	Chadwick et al., 2020; Jerolmack & Mohrig, 2007; Prasojo et al., 2022
Orinoco	8	2000	0.06	110	78	2.7	80	4	0.0021		0.0000413	1000	0.7	Chadwick et al., 2020; Prasojo et al., 2022
Mid-Amazon	12	3000	0.45	50	404	2.9	120	4	0.005	12	0.00003	600	0.2	Chadwick et al., 2020; Jerolmack & Mohrig, 2007; Prasojo et al., 2022
Upper-Rhone	5.4	377	0.01	70		2.9	15.08	4	0.002	5.9	0.000382	1450	0.12	Chadwick et al., 2020; Prasojo et al., 2022
Yellow	3.5	500	0.42	30	31	1.7	20	4	0.1		0.0000965	7	0.01	Chadwick et al., 2020; Prasojo et al., 2022
Brahmaputra	7	3300	0.20	80		11.4	132	4	0.02	7	0.0001	500	0.55	Chadwick et al., 2020; Prasojo et al., 2022
Goose	2	100	0.00	10		-3	4	4	0.00198			333	0.77	Chadwick et al., 2020; Prasojo et al., 2022

Mitchell	7	100	0.00	15	-0.25	4	4				63	0.09	Chadwick et al., 2020; Prasojo et al., 2022
Trinity	5	200	0.00	8	4.2	8	4	0.0011				0.17	Chadwick et al., 2020; Prasojo et al., 2022
Okavango										0.00019	100		Jerolmack & Mohrig, 2007; Prasojo et al., 2022
Gilbert							7	0.0007	6	0.00006	1224.4898		Jerolmack & Mohrig, 2007; Prasojo et al., 2022
Suwanee							3	0.001	3	0.00007	1000		Jerolmack & Mohrig, 2007; Prasojo et al., 2022
McArthur							2	0.0005	5	0.00006	5000		Jerolmack & Mohrig, 2007; Prasojo et al., 2022
Emerald Lake Fan							1	3.65	0.3	0.035	0.08		Jerolmack & Mohrig, 2007; Prasojo et al., 2022
Rolling Stone Fan							1	0.63	0.1	0.0064	0.16		Jerolmack & Mohrig, 2007; Prasojo et al., 2022
XES 1999 Lab Fan Run 1, Stage 3							9	17.52	0	0.06	0.00005		Jerolmack & Mohrig, 2007; Prasojo et al., 2022

[1]relative sea-level rise rate as the sum of the coastal subsidence rate and eustatic sea-level rise rate

4.4.4. Future work

Our model results advance understanding about how delta topset slope controls autogenic timescale. We vary a single factor (upstream slope), although this drives and is closely correlated with upstream sediment input. The mutual adjustment of water and sediment discharge produces complex morphological and sedimentary responses. If these responses scale similarly to our results for topset slope and avulsion timescale, applying the approach used here to other autogenic forcings will reveal how deltas internally respond to these controls. Hence, our ability to disentangle autogenic and allogenic drivers will be enhanced in both modern systems and the rock record. An important extension of this work is to vary input discharge and sediment load as variability in these may affect the geomorphic processes controlling avulsion and bifurcation timescales. Multi-temporal observation of well-studied natural river deltas, such as the Yellow (Moodie et al., 2019), Mississippi (Chamberlain et al., 2018) or Rhine-Meuse (Stouthamer et al., 2015; Pierik et al., 2018), could then be used to quantify the interactions between avulsion and bifurcation that we found in our investigation.

The results from this study suggest the following areas of future study: (a) How does the autogenic forcing studied here (i.e. upstream, and the consequent topset slopes) interact with a combination of allogenic forcings (e.g. sea-level, different wave, tides, and anthropogenic effects)? (b) How do the other autogenic controls (e.g. *Qs*, *Q*, riverbank material, vegetation) in river deltas influence avulsion timescale? How are these signals preserved or shredded in the rock record? And lastly, (c) How do seasonal or longer-term changes in input flow autogenically impact avulsion and bifurcation timescales and their interaction?

4.5. Conclusion

We conducted a suite of numerical modelling experiments with upstream slopes ranging from 10^{-4} to 10^{-3} to understand autogenically-controlled avulsion and bifurcation in river deltas. There is a statistically significant correlation between the topset slope produced in the model and the avulsion timescale with $T_a = 0.3S_{topset}^{-1.18}$; $R^2 = 69\%$, $p < 0.05$. Topset slope appears to be the dominant control of the timescale of autogenic signals, but it does not control the stratigraphy produced in the models which is remarkably consistent. Avulsion timescales span from 1.2×10^3 - 1.9×10^5 years with a median value of 1.2×10^4 years (N = 229). Bifurcation timescales are in the range of 2×10^{-2} - 5.7×10^1 years with a median value

of 4 x 10^{-1} years (N = 201). Our findings advance understanding of how the delta topset slope serves as the first order control on autogenic timescales and how avulsion and bifurcation are not well correlated throughout the delta building process. Avulsion and bifurcation can occur at the same time during delta building, as shown by the non-unimodal distribution of dimensionless island sizes created in our model. Avulsion and bifurcation timescale from 22 river deltas from the literature are consistent with the avulsion timescale-topset slope and bifurcation timescale-topset slope relationships proposed from our model. These findings contribute to progressing our understanding of autogenically controlled avulsion and bifurcation processes, before taking into account the influence of allogenic variables. A robust understanding of these processes has important implications due to their direct impact on coastal and inland hazards that arise from geomorphic change and flooding on highly populated river deltas.

Chapter 5 - Down-delta hydraulic geometry and its application to the rock record

The following chapter is adapted from Prasojo, O. A., Hoey, T. B., Owen, A., & Williams, R. D. (2023). Down-delta hydraulic geometry and its application to the rock record. Sedimentology, 70, 2, p.289-605, https://doi.org/10.1111/sed.13062

Abstract

Paleodischarge estimation is largely undertaken within fluvial settings, and there are limited paleodischarge estimates specifically from delta deposits, despite their significance globally. Making water paleodischarge estimates for deltas using catchment-based approaches developed using data from fluvial settings requires estimation of parameters from the rock record (e.g. paleotemperature, paleoslope, paleorelief) that may be difficult to determine, and may lead to under- or over-estimation of paleodischarge values due to differences in process-form relationships between alluvial rivers and deltas. When a sediment-conveying fluvial channel starts to debouch into a standing body of water, delta lobes develop through repeating mouth bar deposition due to flow deceleration, forming a deltaic morphology with distributary channel networks that differ morphologically from those developed in unidirectional flowing alluvial rivers. This study provides empirical relationships determined across five climate regions, using 3823 measurements of distributary channel width from 66 river deltas alongside their bankfull discharge, by applying the concept of hydraulic geometry. Empirical relationships are developed from the global delta dataset between bankfull discharge and catchment area (Q_b-A) and also bankfull discharge and distributary channel width (Q_b-w). These empirical relationships produce very strong statistical correlations, especially between Q_b and w, across different climate regions ($Q_b = 0.34w^{1.48}$, $R^2 = 0.77$). However, both Q_b-A and Q_b-w relationships have outliers that may be explained by particular hydrological or geomorphic conditions. These new empirical relationships derived from modern systems are applied to Cretaceous outcrops (Ferron Sandstone, Dunvegan and McMurray formations). The comparatively simple scaling relationships derived here produced paleodischarge estimates within the same order of magnitude as the paleodischarge values derived from existing, more complex approaches. Our study contributes to source-to-sink investigations by enabling paleodischarge estimates that intrinsically account for climate impacts on channel geometry at the time of deposition, using measurements of channel width or catchment area of a deltaic outcrop.

5.1. Introduction

Paleodischarge can be estimated through several approaches including geometric scaling relationships (e.g. between channel width and discharge), hydraulic calculations (e.g. derived from grain size, and sedimentary structures, such as the Fulcrum model (Holbrook & Wanas, 2014), and multivariate statistical equations relating, for example, the catchment

erodibility (*B*), water discharge (*Q*), area (*A*), relief (*R*) and annual temperature (*T*) (the BQART model - (Syvitski & Milliman, 2007). Some of these approaches require measurements or estimates of parameters that are commonly challenging to obtain from rock record datasets (e.g. paleotemperature, relief, paleoslope, catchment area, bankfull depth) (Syvitski and Saito, 2007; Davidson and North, 2009; Holbrook and Wanas, 2014; Brewer et al., 2020). All available methods make assumptions, for example when using geometric scaling the channel geometry is assumed to be in equilibrium with the bankfull water discharge.

One of the most commonly used models, the Fulcrum model, assumes dynamic equilibrium where all sediment mass transported through a trunk channel is balanced by sediment mass eroded upstream and deposited downstream (Holbrook and Wanas, 2014). This model also assumes a fixed position and dimension of a rectangular paleochannel geometry. Values of dimensionless bankfull Shields' stress and the Chezy friction coefficient are assumed, from which paleoslope, velocity and bankfull depth hence paleodischarge are calculated (Brewer et al., 2020; Lyster et al., 2021). The Shield's stress (Ganti et al., 2019b) and median formative flow depth (Trampush et al., 2014) are challenging to estimate from ancient deposits, although they can be constrained using information on, for example, grain-size distribution.

The second widely applied model for estimating paleodischarge is the BQART model, which utilizes catchment-scale parameters. Although the original goal of this model was to estimate the total suspended solid load (TSS) brought by the fluvial system to the ocean, it can be used to estimate discharge or paleodischarge and is applicable to ancient sedimentary systems (Blum & Hattier-Womack, 2009; Sømme et al., 2011; Allen et al., 2013; Watkins et al., 2019). The BQART model parameters can often be only partially constrained. For example, estimating paleotemperature relies on proxy information (e.g. biomes of flora and fauna, paleosols, mineralogy) combined with plate tectonic reconstructions, which increase the uncertainty in BQART sediment load estimates, especially in cooler climates (Nyberg et al., 2021).

Scaling between discharge and channel width and depth is an inevitable consequence of channel size adjusting to the volume of water being conveyed. Hydraulic geometry provides a theoretical basis for such scaling. Hydraulic geometry refers to empirical relationships relating channel width (*w*), depth (*d*) and velocity (*v*) to discharge (*Q*) (Leopold and

Maddock, 1953). As discharge fluctuates at a single site, strong power relationships of the following form are found:

$$w = aQ^b \text{ (}w\text{-}Q\text{ relationship)} \quad (5.1)$$

$$d = cQ^f \text{ (}d\text{-}Q\text{ relationship)} \quad (5.2)$$

$$v = kQ^m \text{ (}v\text{-}Q\text{ relationship)} \quad (5.3)$$

with the coefficients (*a, c, k*) and exponents (*b, f, m*) derived empirically from repeat measurements (Leopold and Maddock, 1953). From the continuity equation $Q = w.d.v$, it follows that $a.c.k = (b+f+m) = 1$. The values of *b*, *f* and *m* are constrained by the hydraulics of water flow (Ferguson, 1986). For a discharge of specified recurrence interval, such as bankfull discharge, consistent downstream hydraulic geometry relationships exist, taking the same form as Eq. 5.1-5.3. In distributary deltas, the downstream relationships reflect abrupt reductions in discharge at bifurcations and also the increasing influence of bidirectional flow towards the downstream margin of the delta. Hence, 'down-delta' hydraulic geometry is complex but at any location along a distributary channel Eq. 5.1-5.3 apply consistently due to the continuity of discharge.

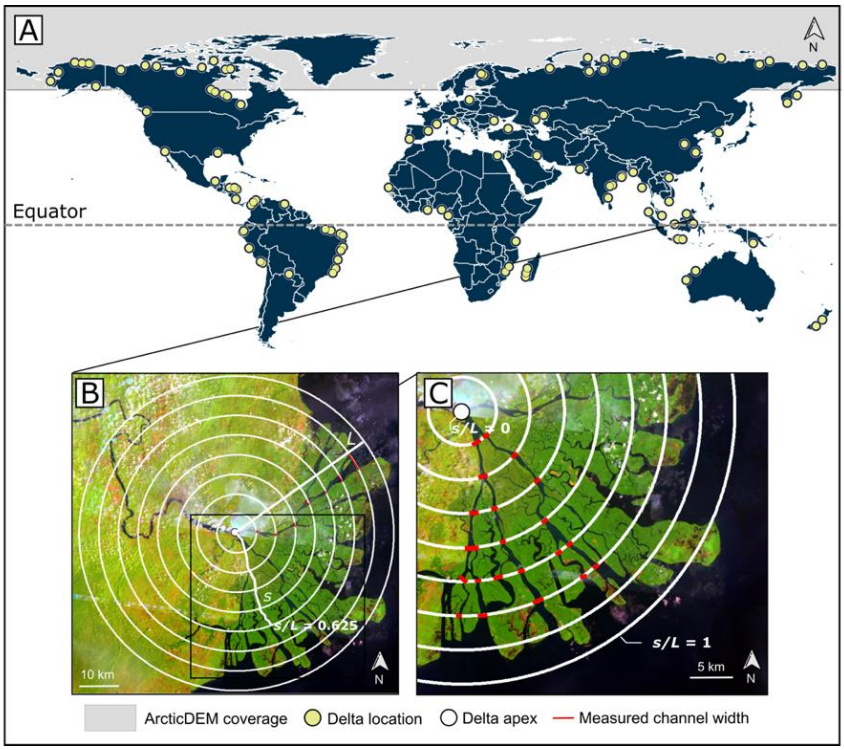

Figure 5.1 (A) Distribution of the observed river deltas; (B,C) circular grid used to measure the channel widths from Mahakam delta, Indonesia (0°34'58.9"S, 117°16'39.7"E). Measured channel widths are red lines shown across wetted distributary channels. The spacing of the circular grid is ~10 times the channel width at the upstream limit of the delta. Stitched Landsat 5 images were taken from January 1994 via Google Earth Engine (GEE).

Here, we investigate empirical relationships from 66 catchments feeding river deltas across different climate regions, that include 3823 distributary channel width measurements available at https://doi.org/10.6084/m9.figshare.19574938.v2 (Fig. 5.1A). We relate catchment areas and their associated bankfull discharges to the median channel width measured across each delta. The median is chosen for three reasons: firstly, it provides a more conservative estimate of central tendency than the mean in cases where there may be very wide channels close to the downstream limit of the delta; secondly, the preservation potential of delta channel deposits is greater away from the downstream limit and the median thus better represents channels that are likely to be preserved (Olariu and Bhattacharya, 2006); and, in ancient deposits the number of preserved channels will often be small and the influence of outliers is reduced by using the median. Assuming that the measured distributary channel widths are approximately bankfull widths, scaling relationships are determined between the measured median distributary channel widths and Q_2 (2-year recurrence flood as an estimate of bankfull discharge, Q_b) in the river, and between catchment area and Q_2 (Leopold and Maddock, 1953; Gleason, 2015b). A re-arrangement of Eq. 5.1, $Q_b = \alpha w^{\beta}$ (Q_b-w relationship) is used as this provides a basis for sedimentologists to estimate bankfull discharge from channel widths, measurement of which is often achievable in ancient deposits.

5.3. Methods

Empirical statistical relationships were found between the median widths of delta distributary channels gathered from satellite imagery and their site-specific discharges. Although backwater effects in the form of wave and tidal influences may be present, other studies have demonstrated the effectiveness of this relationship in deltaic environments (Mikhailov, 1970; Andrén, 1994; Edmonds and Slingerland, 2007; Sassi et al., 2012; Gleason, 2015b). Bankfull discharge has widely been considered as the flow that controls channel geometry in alluvial rivers (de Rose et al., 2008; Haucke and Clancy, 2011; Gleason, 2015b), and is estimated here as Q_2, where 2 is the recurrence interval (years) of the discharge, as also used by others (Eaton, 2013; Jacobsen & Burr, 2016; Morgan & Craddock, 2019)

Distributary channel widths on the 66 river deltas were measured in ArcGIS software using annual composite Landsat 5 satellite images. Delta apex (i.e. valley exit) locations were obtained from digital elevation models (DEM) from the Shuttle Radar Topography Mission

(SRTM) and ArcticDEM (Tucker et al., 2004; Farr et al., 2007; Morin et al., 2016) (Fig. 5.1A). Satellite imagery from 1984 were used where available, with some imagery dated to more recent years. Using the older (1984) images reduces the impact of infrastructure and bank protection on channel widths. The satellite images and DEMs were projected using World Geodetic System (WGS 1984) in ArcGIS to measure the channel widths and to extract valley exit locations (Hartley et al., 2017).

River deltas were identified based on their protrusion beyond the original lateral shoreline (Caldwell et al., 2019). Criteria for selecting river deltas includes any channel mouth that intersects with the open seawater, depositing sediment that protrudes beyond their lateral shoreline. Nonetheless, we do not classify our river deltas based on their dominant forces (e.g. wave-, tide-, or river-dominated deltas) due to delta morphodynamics varying in time and space (e.g. a tide-dominated delta could transform into a river-dominated delta or a wave-dominated delta into a river-dominated delta) and very few delta end-members exist in nature (Syvitski & Saito, 2007). We also note that some influence of tide and wave processes may exist in the dataset (Ta et al., 2002; Correggiari et al., 2005; Syvitski & Saito, 2007). However, as this paper focuses on the estimation of river discharge from distributary channel morphology, we avoid river deltas with clear wave and tidal morphologies (e.g. abundant tidal creeks, deflected delta distributaries, elongated/parallel shoreline).

Channel widths were measured using a method, adapted from Sassi et al. (2012), in which a semicircular grid s/L is used to define a dimensionless distance from the delta apex to the shoreline, where s represents channelized distance from the delta apex and L is the channelized distance along the longest distributary channel (Fig. 5.1B). This grid allows measurement of the widths of multiple distributary channels located at the same dimensionless distance from the apex, hence allowing comparison across differently sized deltas. The apexes were defined as the valley exit points as recognized on DEMs (Hartley et al., 2017) or as the most landward avulsion node within the delta (Ganti et al., 2016a). The semicircular grid has a resolution of ~10 times the width of the river channel at the first avulsion point to maintain consistent dimensionless distance and data frequency across deltas of varying size. As an example, the Mahakam delta, Indonesia, has a 500 m wide channel at the avulsion point which is ~40000 m following the longest channel from the shoreline (L). Channel widths are measured every 5000 m from the delta apex (i.e. $s/L = 0$) to the delta shoreline where $s/L = 1$ (Fig. 5.1C). Widths of distributary channels were included, and tidal creeks were omitted.

Catchment areas were delineated in ArcGIS using the watershed polygons available from the HydroBASINS dataset (Lehner and Grill, 2013). River discharge data for the closest measuring location to the delta apex were extracted from the Global Runoff Data Centre (GRDC) dataset (https://www.bafg.de/GRDC/EN/Home/homepage_node.html). The 2-year recurrence interval flood (Q_2) was used to estimate the bankfull discharge, or the dominant channel-forming flow, and is referred to as discharge (Q) subsequently for simplification (Wolman and Miller, 1960; Phillips and Jerolmack, 2016, 2019; Edwards et al., 2019; Rhoads, 2020; Dunne and Jerolmack, 2020). Q_2 was calculated from daily discharge data using the Flow Analysis Summary Statistics Tool (*'fasstr'*) package in R (https://github.com/bcgov/fasstr). For some locations, only monthly discharge data are available. Thus, conversion of Q_2 from monthly to daily was applied for each climate region (Beck et al., 2018; Prasojo et al., 2022). The climate region for each delta is defined based on a Köppen-Geiger climate classification map (Beck et al., 2018).

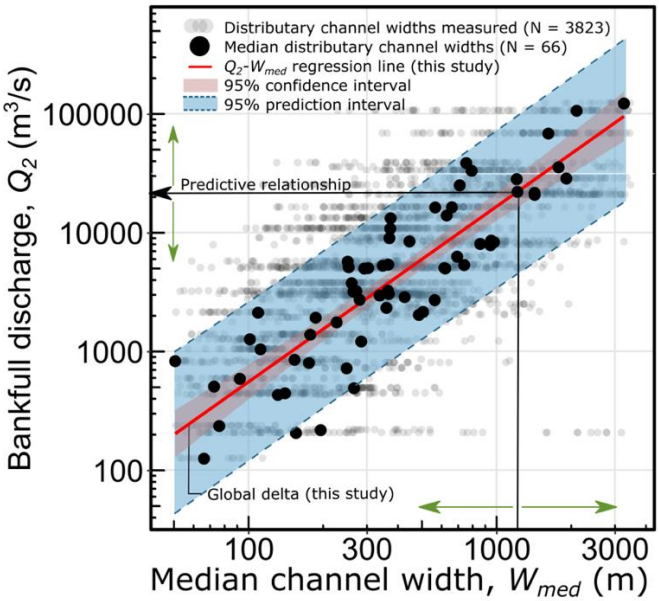

Figure 5.2 Illustration of the use of median distributary channel widths to obtain the predictive relationships between median distributary channel widths and bankfull discharge from 66 river deltas measured in this study. The green arrow on the y-axis shows the uncertainty on the discharge estimation, while the green arrow on the x-axis shows the uncertainty on the width measurement.

The predictive Q-W_{med} relationships use the median channel width measured for each delta as statistically representative values of right-skewed channel width distributions (Fig. 5.2, 5.3). The 66 median width values were obtained from 3823 individual measurements (mean number of width measurements per delta = 58; range from 15 to 177 m) (Fig. 5.2). Note that these data do not allow prediction of the discharge/paleodischarge value of a single distributary channel but enable calculation of the total riverine discharge that contributes

sediment to builds the delta plain. Ordinary least square (OLS) regressions were then used to calculate power-law scaling relationships between both channel widths and catchment areas with bankfull discharge (Leopold and Maddock, 1953). We used OLS regression, which assumes error only in the dependent variable, as the aim is to produce predictive equations. The 95% confidence interval around the overall relationship for the 66 deltas is narrow, reflecting the statistical strength of the median channel width-bankfull discharge relationship across over three orders of magnitude of discharge. Using the regression equation to predict the discharge for an individual delta based on the estimate of the median channel width obtained from N width measurements yields a greater uncertainty (wider confidence interval) on account of the scatter in widths on individual deltas (blue shaded region in Fig. 5.2). The uncertainty in the median channel width estimate reduces as the number of width measurements increases since the uncertainty in the median decreases as a function of $N^{-1/2}$. OLS regressions were determined for each climate region to generate *Q*-*A* and *Q*-*w* morphometric scaling relationships.

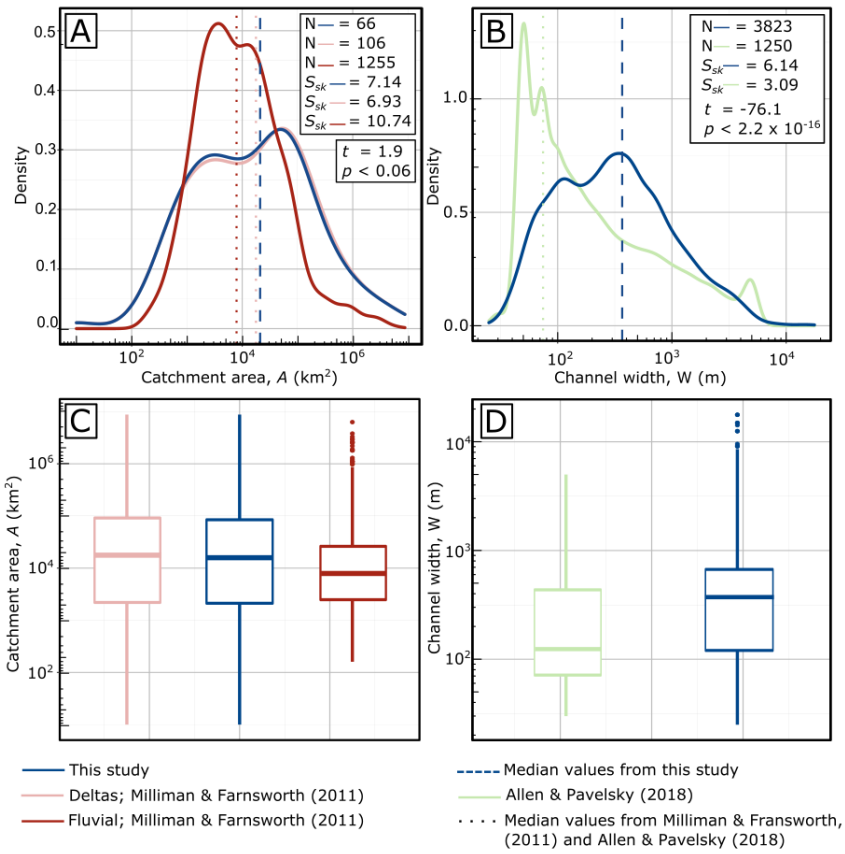

Figure 5.3 Catchment area and channel width distributions from this study, compared with data from Milliman and Farnsworth (2011) and Allen and Pavelsky (2018). (A) Distributions of catchment areas; (B) channel widths measured in this study; (C) boxplots of catchment areas measured in this study and by Milliman & Farnsworth (2011); (D) boxplots of channel widths measured in this study and by Allen & Pavelsky (2018). In (A) and (B), N is the sample number, S_{sk} is skewness, and *t* and *p* are the t-statistic and the associated probability from t-test comparison between the delta and fluvial datasets. The skewness values on (A) and (B) were calculated from the raw data, hence do not look skewed on log scales.

The applicability of the power-law relationships determined from modern deltas was tested by applying the relationships to the channel widths and catchment areas derived from published outcrop data from three Cretaceous formations in continental North America (Brownlie, 1983; Sageman and Arthur, 1994; Bhattacharya and MacEachern, 2009; Musial et al., 2012; Bhattacharya et al., 2016). Paleodischarges were estimated in these studies using the Fulcrum method applied to outcrop and subsurface data. These data were selected due to their relatively complete and observable exposures in the Ferron, Dunvegan and McMurray formations.

5.4. Results

5.4.1. Data distribution

The 66 catchment areas are log-normally distributed (Fig. 5.3A), similar to the global fluvial system dataset (pink and blue lines on Fig. 5.3A) (Milliman and Farnsworth, 2011). The fluvial catchment areas (Milliman & Farnsworth, 2011) are not significantly different from the delta catchment areas used in this study ($t = 1.9$; $p < 0.06$).

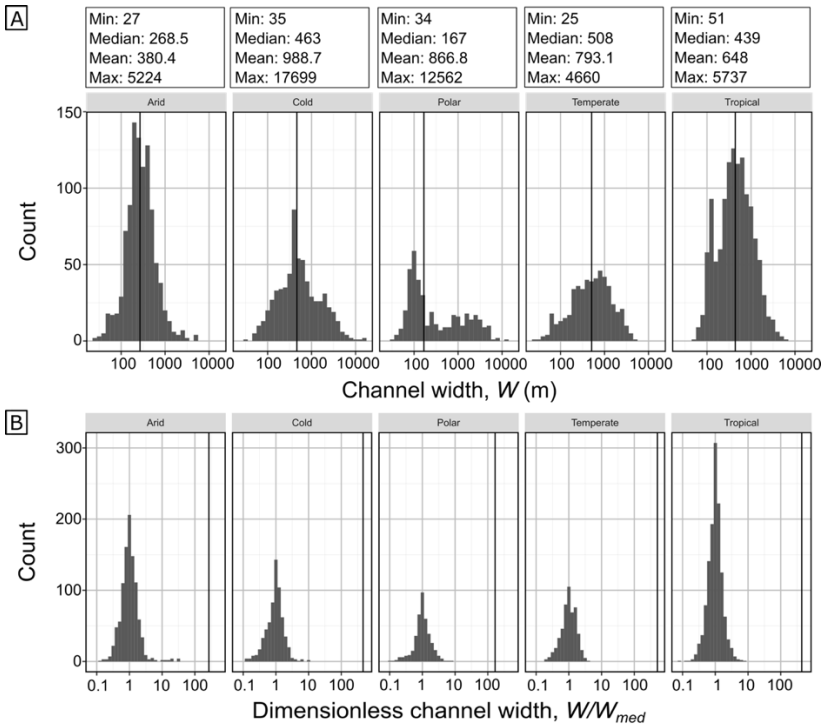

Figure 5.4 (A) Histograms showing the distribution of measured distributary channel widths and (B) dimensionless channel width (w/W_{med}) from arid, cold, polar, temperate, and tropical climate region, consecutively. Vertical lines on the plots (A) refers to median channel width values for each climate region.

The median width of delta channels is almost one order of magnitude larger than the median in the global river channel width database (Allen & Pavelsky, 2018; Fig. 5.3B, 5.4), although the range of widths are similar in both data sets. The channel widths in our delta data set are statistically significantly larger than in the fluvial data (t = -76.1; p < 2.2x10^{-16}). This difference suggests that scaling relationships from fluvial systems may not be able to be readily used for delta channels.

5.4.2. Water discharge and catchment scaling relationship (Q-A relationship)

Globally, Fig. 5.5 shows a statistically significant (p = 3.3 x 10^{-8}; R^2 = 0.39; N = 66) power law relationship between catchment area and bankfull discharge, $Q_2 = 50.1A^{0.42}$ with 22 of the 66 deltas lying within the 95% confidence interval. Some of the more distant outliers are interpreted to be present due to extensive river engineering (e.g. embankments along riverbanks in Colorado, Nile and Ebro deltas) or due to wave and tide effects (e.g. Orinoco, Mackenzie, Godavari, Ob and Irrawaddy deltas). In comparison to the global river Q-A relationship ($Q = 0.075A^{0.8}$), the scaling relationship for global deltas has a non-significantly lower regression slope (p = 0.1) using the significance of the difference, or slope test (Syvitski and Milliman, 2007).

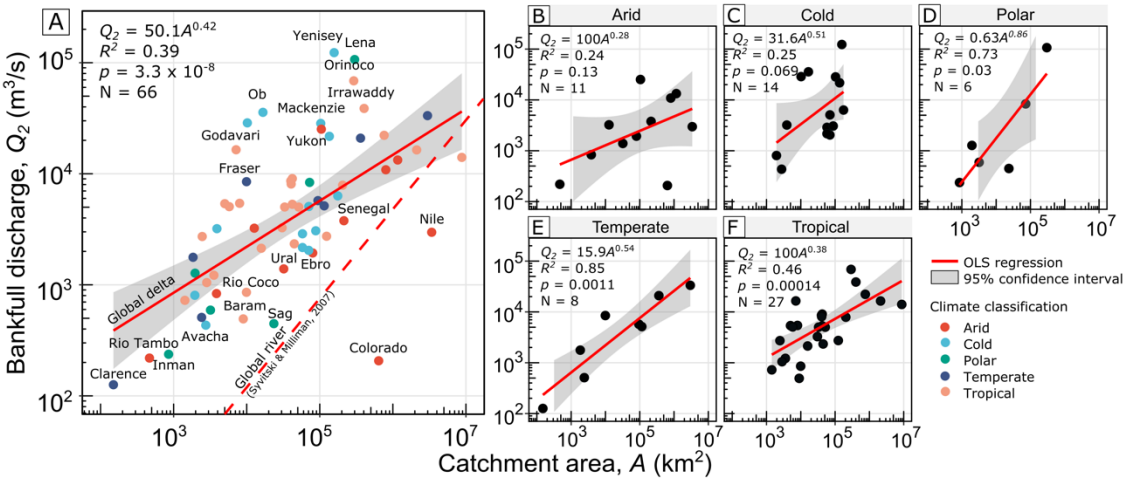

Figure 5.5 (A) Climate-classified bankfull discharge – catchment area (Q-A) relationship from all deltas; (B-F) Q-A relationships from the arid, cold, polar, temperate and tropical climate regions, respectively. Red continuous lines are Ordinary Least Squares (OLS) regressions for the data on each plot. The red dashed line on (A) is the global river Q-A relationship from Syvitski & Milliman (2007). The significance of the difference (slope) test between the gradient from delta Q-A OLS regression versus the global river from Syvitski & Milliman (2007) produces p = 0.1.

The relatively low R^2 value for the global data set can be explained in part by differences between climate regions. Separating the data into different climate regions produces significant relationships between A and Q_2 except in arid and cold regions where the

relationships are not significant (R^2 = 0.24 and 0.25; p = 0.13 and 0.069; N = 11 and 14, respectively).

5.4.3. Water discharge and channel width scaling relationship (*Q-w* relationship)

In total 66 paired measurements of discharge and median channel width were used to build the *Q-w* relationship. Overall, there is a statistically significant relationship with $Q_2 = 0.34W_{med}^{1.48}$ (R^2 = 0.77; $p = 2.2 \times 10^{-16}$; N = 66) (Fig. 5.6). The *Q-w* relationship produces a better fit globally than the *Q-A* relationship above (Fig. 5.5A). In comparison to the global river *Q-w* relationship ($w = 17Q^{0.45}$) (Moody and Troutman, 2002), the *Q-w* delta channel relationship has a statistically significant lower regression slope ($p = 2.6 \times 10^{-5}$). As an example, predicting the discharge from a delta with median channel width of 300 m will result in Q_2 = 1576 m^3/s, while the equivalent for a fluvial setting would be Q_2 = 589 m^3/s. Deltas have multiple channels, hence using W_{med} = 300 m will have maximum width of larger than 300 m near the apex (i.e. trunk channel), hence producing larger estimated bankfull discharge than the fluvial settings. These results suggest that predicting discharges from widths will produce different results if the channels are deltaic or fluvial.

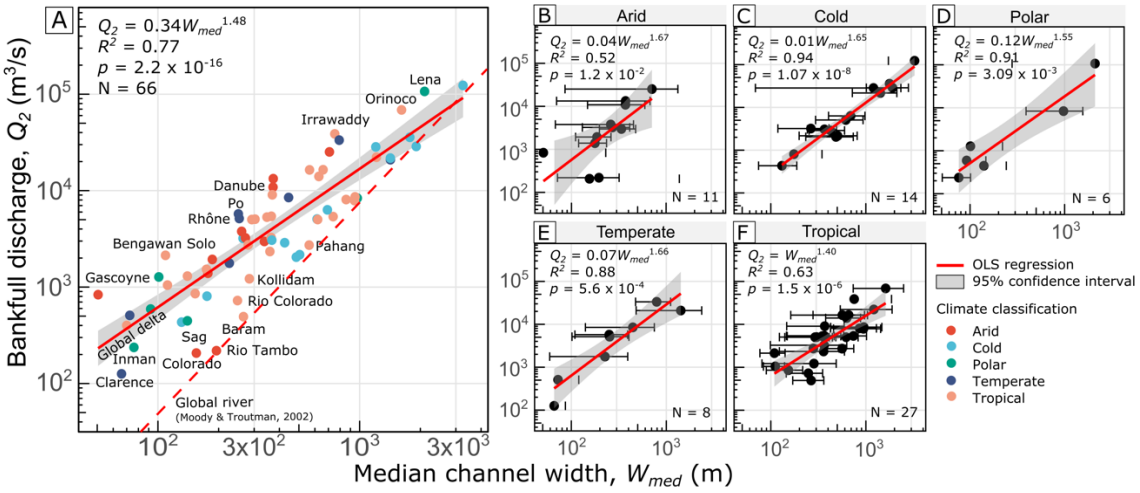

Figure 5.6 (A) Climate-classified *Q-w* relationship from the global deltas; (B-F) *Q-w* relationships from the arid, cold, polar, temperate and tropical climate regions, respectively. Red continuous lines are the OLS regression obtained from the data shown on each plot. The red dashed line is the regression line obtained from the global river *Q-w* relationship from Moody & Troutman (2002). Error bars represent median channel width ± 1 standard deviation. The significance of the difference test between the gradient from delta *Q-w* OLS regression versus the global river equation from Moody & Troutman (2002) produces p = 2.6 x 10-5.

When classified by climate region, *Q-w* relationships consistently show significant relationships ($p < 0.05$) with the strongest relationship for cold climate (N = 14) (Fig. 5.6C).

Polar, temperate, and tropical regions also show strong relationships with R^2 values equal to 0.91, 0.88, 0.63, respectively (Fig. 5.6D-F). Similar to the *Q-A* relationship, the *Q-w* relationship from arid regions (N =11) shows the lowest R^2 although it is statistically significant ($p = 1.2 \times 10^{-2}$) (Fig. 5.6B).

In summary, compared with the *Q-A* relationships on Fig. 5.5A-F, the *Q-w* relationships proposed in this study consistently show more statistically significant ($p < 0.05$) relationships that also have higher R^2 values (Fig. 5.6A-F). The *Q-A* relationship from the temperate region is the strongest (Fig. 5.5E) and the strongest *Q-w* relationship is for the cold climate region (Fig. 5.6C). The weakest relationships consistently come from the arid settings from both *Q-A* and *Q-w* (Fig. 5.5B & 5.6B).

5.4.4. Application to the rock record

The scaling relationships obtained above from global modern river deltas are here applied to estimate paleodischarges from several deltaic deposits. Data were compiled from paleodischarge studies from well-exposed Cretaceous outcrops and subsurface dataset deposited in temperate-tropical climates. The data compiled from the literature used the Fulcrum approach to estimate paleodischarge values (Table 5.1).

The Ferron Sandstone, exposed near Ivie Creek, SW Utah, USA, is composed of Turonian (93.9-89.8 Ma) deltaic deposits from the western margin of the Western Interior Seaway (Bhattacharya and MacEachern, 2009; Braathen et al., 2018) (Fig. 5.7). The delta prograded NE with an estimated drainage area of around 50000 km^2 (Bhattacharya and Tye, 2004). Previous paleodischarge studies on the Ferron Sandstone were based on trunk river characterization and estimation of paleoflow velocity from its grain size, bedform size and inferred flow depth. The interpretation of a tropical paleoclimate was obtained through facies analysis and catchment area is estimated from paleogeographic reconstructions.

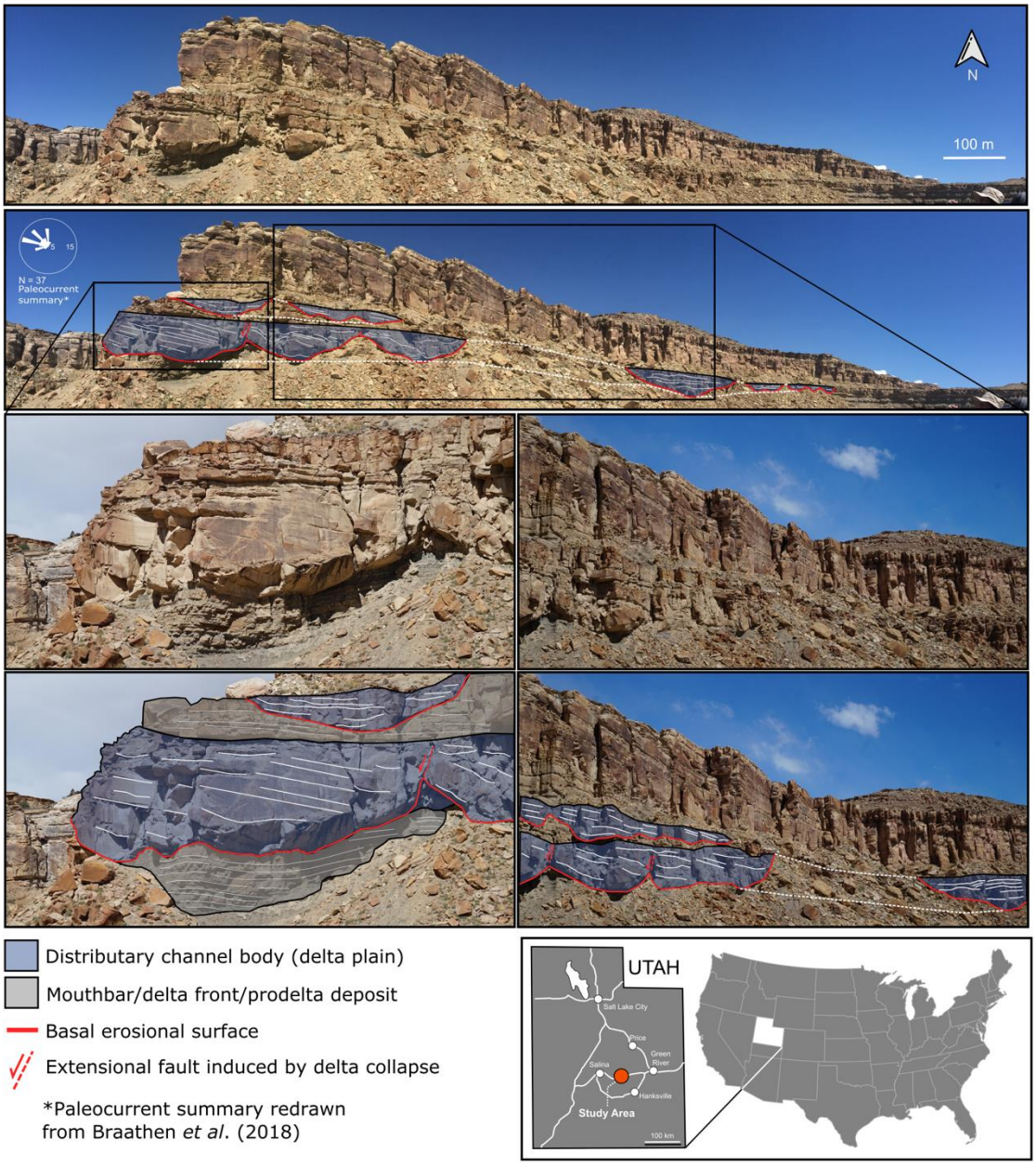

Figure 5.7 Ferron Sandstone outcrop photographs from Ivie Creek, Utah showing the distribution of distributary channels and associated lobes of Cretaceous delta deposited along the western margin of Western Interior Seaway. Interpreted distributary channel bodies and paleocurrent directions are redrawn from Braathen et al. (2018).

The Cenomanian (100.5-93.9 Ma) Dunvegan Formation was deposited in a temperate climate, and contains deposits from a large delta complex that are predominantly massive and cross-bedded non-marine and marine sandstones (Plint, 2002). The delta complex prograded 400 km NW to SE into the actively subsiding foreland basin of Alberta. It is estimated that the delta had a catchment area of around 100000 km^2 (Bhattacharya & Walker, 1991; Sageman & Arthur, 1994; Bhattacharya & MacEachern, 2009; Plint, 2000; Hay & Plint, 2020).

The McMurray Formation (Barremian-Aptian; 130-112 Ma), NE Alberta, Canada, contains delta deposits in a N-NE direction in conjunction with the Rocky Mountains orogenesis (Musial et al., 2012; Shinn et al., 2014). The McMurray formation consists of wave rippled sands, highly burrowed sands, heterolithic sands and highly burrowed silts and muds deposited in a bay/deltaic setting (Musial et al., 2012). Previous studies estimate the McMurray Formation had a paleodischarge of about 15000 m^3s^{-1} as the maximum bankfull discharge located at 56-58° North in temperate humid to mid-latitude warm humid climatic belt (Musial et al., 2012; Martinius et al., 2015).

Measured channel widths and estimated catchment areas were obtained from the literature that compiled subsurface dataset with outcrop observations (Sageman and Arthur, 1994; Plint and Wadsworth, 2003; Bhattacharya and MacEachern, 2009; Bhattacharya et al., 2016) and were used to calculate paleodischarge using the equations calculated above from the modern systems. Four equations from our analysis of modern delta systems are used: (1) the global discharge-area relationship $Q_2 = 50.1A^{0.42}$ (Fig. 5.5A) (2) the climate-classified *Q*-*A* relationships, $Q_2 = 100A^{0.38}$ for the tropical region and $Q_2 = 15.9A^{0.54}$ for the temperate region (Fig. 5.5E,F); (3) the global discharge – width relationship (Fig. 5.6A) $Q_2 = 0.34W_{med}^{1.48}$; and (4) the climate-classified *Q*-*w* relationships, $Q_2 = W_{med}^{1.4}$ for the tropical region and $Q_2 = 0.07W_{med}^{1.66}$ for the temperate region (Fig. 5.6E,F). Paleodischarges were calculated using these equations and channel widths measured from the rock record obtained from previously published work. The paleodischarge values estimated using our equations were compared with previous paleodischarge estimates (Fig. 5.8) (Sageman and Arthur, 1994; Bhattacharya and MacEachern, 2009; Bhattacharya et al., 2016).

Our new estimates of bankfull discharges lie within one order of magnitude of the paleodischarge values reported from the Fulcrum approach (Fig. 5.8) (Sageman and Arthur, 1994; Bhattacharya and MacEachern, 2009; Bhattacharya et al., 2016). Note that the climate-classified *Q*-*w* relationship provides a better fit to the previous estimates than the global *Q*-*w* relationship. Conversely, the global *Q*-*A* relationship estimates correspond better to previous estimates than do estimates from scaling relationships for individual climate zones (Fig. 5.5E, F). Overall, the statistical models proposed in this study perform similarly to the established Fulcrum method by producing values within the same order of magnitude as the paleodischarge values derived from the literature.

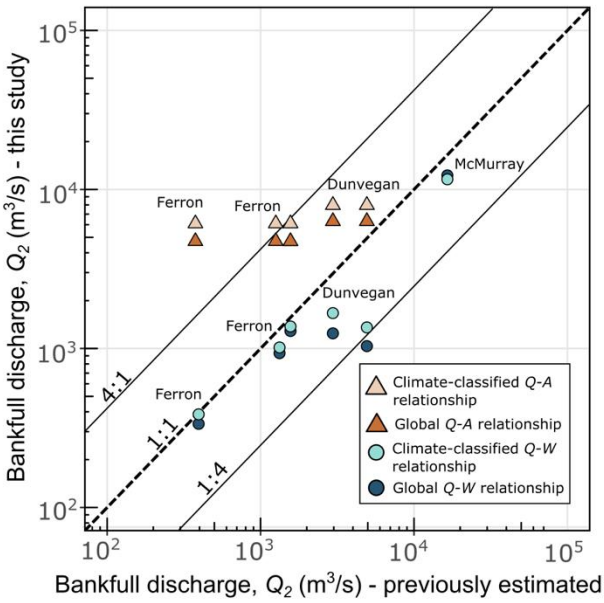

Figure 5.8 Comparison of bankfull discharges estimated from previous studies with the estimated bankfull discharges calculated using the Q-$_W$ and Q-A relationships, both global and climate-specific, proposed in this study (Sageman & Arthur, 1994; Bhattacharya & MacEachern, 2009; Bhattacharya et al., 2016).

Table 5.1 Secondary delta channel width data from the literature and predicted *Q* values from both *Q-A* and *Q-w* relationships.

Formation Name	Channel Width (m)	Estimated Paleodischarge (m^3/s)	Paleodrainage area (km^2)	Geological age	Predicted *Q* from global *Q-A* relationship (m^3/s)	Predicted *Q* from climate-classified *Q-A* relationship (m^3/s)	Predicted *Q* from global *Q-w* relationship (m^3/s)	Predicted *Q* from climate-classified *Q-w* relationship (m^3/s)	Source
Ferron[1]	174	1525	50000	Turonian	6104 ± 87900	4714 ± 87900	1284 ± 527	1370 ± 527	(Sageman and Arthur, 1994; Bhattacharya and MacEachern, 2009)
Ferron[2]	140	1300	50000	Turonian	6104 ± 87900	4714 ± 87900	930 ± 527	1011 ± 527	(Bhattacharya et al., 2016)
Ferron[3]	70	400	50000	Turonian	6104 ± 87900	4714 ± 87900	334 ± 527	383 ± 527	(Bhattacharya et al., 2016)
Dunvegan	170	2829	100000	Cenomanian	7969 ± 87900	6307 ± 87900	1240 ± 527	1664 ± 527	(Sageman and Arthur, 1994; Bhattacharya and MacEachern, 2009)
Dunvegan[2]	150	4641	100000	Cenomanian	7969 ± 87900	6307 ± 87900	1030 ± 527	1352 ± 527	(Sageman and Arthur, 1994; Bhattacharya and MacEachern, 2009)

McMurray	800	15000	NA	Barremian-Aptian	NA	NA	12273 ± 527	11597 ± 527	(Bhattacharya et al., 2016)

[1,2,3]end members channel width measurement extracted from the literature

± represents 95% prediction intervals from the global dataset. Wide prediction intervals are due to scatter in the data and the small number of deltas measured in this study, leading to high standard error of the residuals.

5.5. Discussion

5.5.1. Comparison to other paleodischarge estimations

Analysis of river discharges, catchment areas and median channel widths from 66 river deltas has generated new global equations $Q_2 = 50.1A^{0.42}$ and $Q_2 = 0.34W_{med}^{1.48}$. These relationships have also been classified by five climate regions (Table 5.2). Applying these comparatively simple equations to the rock record produced paleodischarge estimates within the same order of magnitude as the paleodischarge values derived from existing, more complex approaches.

Table 5.2 Summary of the scaling relationships proposed in this study

Water discharge and catchment area scaling relationships			
Classification	N	Equation	Statistical significance
Global	66	$Q_2 = 50.1A^{0.42}$	$R^2 = 0.39$; $p = 3.3 \times 10^{-8}$
Arid	11	$Q_2 = 100A^{0.28}$	$R^2 = 0.24$; $p = 1.3 \times 10^{-1}$
Cold	14	$Q_2 = 31.6A^{0.51}$	$R^2 = 0.25$; $p = 6.9 \times 10^{-2}$
Polar	6	$Q_2 = 0.63A^{0.86}$	$R^2 = 0.73$; $p = 3 \times 10^{-2}$
Temperate	8	$Q_2 = 15.9A^{0.54}$	$R^2 = 0.85$; $p = 1.1 \times 10^{-3}$
Tropical	27	$Q_2 = 100A^{0.38}$	$R^2 = 0.46$; $p = 1.4 \times 10^{-4}$
Water discharge and median channel width scaling relationships			
Classification	N	Equation	Statistical significance
Global	66	$Q_2 = 0.34W_{med}^{1.48}$	$R^2 = 0.77$; $p = 2.2 \times 10^{-16}$
Arid	11	$Q_2 = 0.04W_{med}^{1.67}$	$R^2 = 0.52$; $p = 1.2 \times 10^{-2}$
Cold	14	$Q_2 = 0.01W_{med}^{1.65}$	$R^2 = 0.94$; $p = 1.07 \times 10^{-8}$
Polar	6	$Q_2 = 0.12W_{med}^{1.55}$	$R^2 = 0.91$; $p = 3.09 \times 10^{-3}$
Temperate	8	$Q_2 = 0.07W_{med}^{1.66}$	$R^2 = 0.88$; $p = 5.6 \times 10^{-4}$
Tropical	27	$Q_2 = W_{med}^{1.4}$	$R^2 = 0.63$; $p = 1.5 \times 10^{-6}$

The new relationships proposed in this study allow quantification of paleodischarge from the rock record based on measurements of channel width, estimates of paleoclimate and morphometric scaling relationships derived from modern systems. Our approach uses fewer input parameters to estimate paleodischarge than existing methods, the BQART model or the Fulcrum model. Channel width is often measured from the rock record where channels are preserved, and cross-channel exposures are available. The proposed morphometric scaling relationships simplify paleohydrological calculations and enable more robust assessment of the uncertainties in the input parameter (channel width) to be accounted for when calculating paleodischarges.

In comparison to the Fulcrum and BQART models that intrinsically include climate parameters, our work provides separate predictive equations for various climate regions. Our proposed models show statistically significant correlations, especially between channel width and bankfull discharge across different climate regions, that have not previously been explicitly accounted for (Table 5.2). These climate-classified models will benefit source-to-sink studies by providing calculations tailored to individual paleoclimates.

Nyberg et al. (2021) provide a comprehensive overview of the uncertainties, sensitivities and practicalities of the BQART model in estimating sediment load on geological timescales. They discussed in detail every parameter needed to estimate the paleodischarge and paleo-sediment load. For estimating the paleodischarge, the BQART model uses a global *Q-A* power law scaling relationship similar to this study but without explicitly allowing for climate. Eide et al., (2018a) added runoff (*Ro*) parameters to take into account the impact of climate by applying a different multiplier value to discharges calculated for each climate region (e.g. *Ro* = 0.0005 for arid and *Ro* = 0.0161 for humid regions). However, adding *Ro* constants shift the models, but does not change the models' gradients. In contrast, we produce different equations for each climate region, allowing the models' gradients to change, reflecting the role of soils or vegetation in controlling runoff. Also, the climate-classified models proposed in this study make paleodischarge estimation more straightforward if the paleoclimate can be deduced from the rock record.

Although the equations are statistically robust, defining paleoclimate from the rock record is not straightforward due to the often-sparse exposure of preserved channels, complexities in stratigraphic correlation and the need for paleoclimate evidence. Reconstructing the relationship between evidence requires significant effort and may not always yield conclusive results (Shuman, 2014). Hence, it is reasonable to assess whether our climate—specific equations significantly improve paleodischarge estimates. ANOVA tests were used to compare the global *Q-w* and *Q-A* regression equations to the climate-classified *Q-w, Q-A* relationships. Comparing the global and the climate-classified *Q-w* regression lines produced p= 0.62. While the comparison of the global *Q-A* and climate-classified *Q-A* regression lines produced p= 0.07. Both tests showed that both global and climate-classified *Q-w* and *Q-A* relationships are not significantly different, hence could be used interchangeably. The tests imply that when the paleoclimate is challenging to be deduced from the rock record, the global *Q-w* or *Q-A* scaling relationship could be used instead.

5.5.2. Limitation of the proposed scaling relationships

For the *Q-A* and *Q-w* relationships, the standard error of residuals are 1.23 and 0.76 in log units, respectively. Despite overall significance of the regressions, additional factors may affect both relationships such as anthropogenic effects on channel width and/or river flows that may disrupt the dynamic equilibrium assumption that underpins the proposed scaling relationships (Aslan et al., 2005; Li et al., 2017; Ninfo et al., 2018), vegetation type and density (Huang and Nanson, 1997), sediment load (Hey and Thorne, 1986), grain size (Eaton, 2013), anabranches of multi-thread channel systems (Tabata and Hickin, 2003), material forming the channel boundary (Ellis and Church, 2005) and flood variability for each climate region (Rodier and Roche, 1978). Although the accuracy of predictive models can be improved by adding more variables (Mosley, 1981) this addition leads to models becoming increasingly less applicable to the rock record. For example, using our calculations, paleodischarge can be determined from any data set in which a catchment area or channel width can be determined (e.g. outcrop or seismic). However, if other variables such as grain size or paleoslope are needed these additional data may not always be readily available. Thus, keeping the variables as simple as possible (e.g. catchment areas and channel widths) is beneficial in creating models that are applicable to the rock-record. Also, adding more variables does not necessarily result in an increase in model accuracy. Mosley (1981) showed that channel cross-sectional area (e.g. width, depth) is 90% controlled by the bankfull discharge, bed sediment size and bank sediment character, with only 30% of the variability being explained by morphologic variables (e.g. braiding and sinuosity index). For reconstruction purposes, there is merit in simplicity and careful examination of the contributing factors of channel cross section and bankfull discharge should be undertaken before adding in more variables into the morphometric scaling relationships proposed in this study.

The prediction intervals for palaeodischarge (Table 5.1; Fig.5.2) are wide because of scatter in the observations and the small number of width measurements available for the prediction. These wide prediction intervals need to be acknowledged when using the proposed scaling relationships. Consequently, when applying the scaling relationships to the rock record they should be further constrained as far as possible using all contextual information gathered from the rock record (e.g. grain size, bedforms interpreted from sedimentary structures, stratigraphic position) to justify the paleodischarge estimation produced by this approach. Our source data set of modern measurements are spatially distributed across the delta in one

time horizon, from which we determine a median width to use for prediction. However, deltas are depositional systems and due to transgression/regression measurements made in outcrop or from subsurface imaging may produce biased samples across the delta, hence yielding a biased estimate of median channel width, or may aggregate measurements across time horizons with different external controls, such as changing Q_2 due to climatic fluctuations. Hence, as noted above in the context of climate interpretation, applying the new statistical models to the rock record requires interpreting the stratigraphic context of the measured distributary channels. As more data become available, larger data sets, modern and ancient, will be able to be used to constrain what are 'reasonable' paleodischarge estimates. This constraint will be quantitative as more data sets such as those in Table 5.2, are obtained.

Our approach uses width measurements from satellite imagery as width is the most readily obtained measure of channel scale on such images. In outcrop or subsurface datasets, it is commonly easier to measure distributary channel depths (d) than widths. Channel widths and depths are very highly correlated empirically and theoretically (Ferguson, 1986), and depth and width measurements from distributary channels reported in the literature are summarized in Table 5.3. Although the depth and width exponents in Eq. 5.1-5.3 are consistent, variations in the multipliers mean that the $w:d$ ratio cannot be taken as a global constant due to the influence of additional factors on channel geometry (e.g. vegetation, bank sediment cohesion). Some studies have found that $w:d$ varies with discharge (Wang and Li, 2011) or with the measurement location (Kästner et al., 2017).

Table 5.3 In-situ measurement of width and depth of several river deltas collected from the literature.

Location	Year	Width (w) (m)	Depth (d) (m)	$w:d$ ratio (-)	Note	Source
Lijin, Yellow delta	1977	621	6.26	99.14	Depth is defined as the averaged bed level in the deepest part of the channel width from a cross-sectional area of 500 m^2	https://doi.org/10.1016/S1001-6279(08)60002-5
Lijin, Yellow delta	1987	615	6.60	93.19	Depth is defined as the averaged bed level in the deepest part of the channel width from a	https://doi.org/10.1016/S1001-

					cross-sectional area of 500 m^2	6279(08)60002-5
Lijin, Yellow delta	1997	622	5.14	121.01	Depth is defined as the averaged bed level in the deepest part of the channel width from a cross-sectional area of 500 m^2	https://doi.org/10.1016/S1001-6279(08)60002-5
Lijin, Yellow delta	1950 - 1999			200	*w:d = f(Qw)*, using the same data as above	https://doi.org/10.1016/j.quaint.2010.09.002
35 km above Head of Passes, Mississippi delta	1974 - 1975	800	22	36	*Qw* > 35.000 m^3/s, depth is calculated by differencing the water-surface elevation from the 40th-percentile depth from the distribution of all wetted elevations for a transect, beginning from the channel bed.	https://doi.org/10.1130/B30497.1
100 km above Head of Passes, Mississippi delta	1974 - 1975	770	23	33.48	*Qw* > 35.000 m^3/s, depth is calculated by differencing the water-surface elevation from the 40th-percentile depth from the distribution of all wetted elevations for a transect, beginning from the channel bed.	https://doi.org/10.1130/B30497.1
200 km above Head of Passes, Mississippi delta	1974 - 1975	750	20	37.5	*Qw* > 35.000 m^3/s, depth is calculated by differencing the water-surface elevation from the 40^{th}-percentile depth from the distribution of all wetted elevations for a transect, beginning from the channel bed.	https://doi.org/10.1130/B30497.1
Fly				15-30	Meandering, slope is always very gentle	http://dx.doi.org/10.1016/j.geomorph.2008.05.035

Amazon				20 - >100	Anabranching, suspended load dominant	http://dx.doi.org/10.1016/j.geomorph.2008.05.035
Brahmaputra				>100	Complex anabranching	http://dx.doi.org/10.1016/j.geomorph.2008.05.035
Atchafalaya Delta	1983			Few hundreds	Depth is measured from the terminal distributary channel	https://doi.org/10.2110/jsr.2006.026
Wax Lake Delta	2002			Few hundreds	Depth is measured from the terminal distributary channel	https://doi.org/10.2110/jsr.2006.026
Volga Delta	2000	10-20	1-3	±10	Depth is measured from the terminal distributary channel	https://doi.org/10.2110/jsr.2006.026
Lena Delta	2000	100-400	1	100-400	Width is taken from the highest frequency from their Fig. 8E	https://doi.org/10.2110/jsr.2006.026
Eocene Battfjellet Deltas		50-200	5	10-40	-	https://doi.org/10.2110/jsr.2006.026
Kapuas Delta	2013 - 2015			16-128	-	https://doi.org/10.1002/2016JF004075

To accommodate the complexity of the relationship between channel width and depth in river deltas, we assume that the flow was steady during the *w* and *d* measurements in Table 5.3, and in an equilibrium depth and slope. The range of measured *w:d* ratios is from 10-200 with typical values of *w:d* = 30:1 (e.g. Mississippi delta; (Nittrouer et al., 2012) and Fly delta (Latrubesse, 2008)), to 100:1 (e.g. Yellow River delta (Wang et al., 2008; Wang and Li, 2011), Amazon and Brahmaputra deltas (Latrubesse, 2008)) and the extreme value of *w:d* = 200:1 from Wax Lake and Lena deltas (Olariu and Bhattacharya, 2006) (Table 5.3). By assuming that delta channel *w:d* relationships globally lie within the range suggested by the

available measurements, we rescale our *Q-w* relationship to yield a novel discharge-depth (*Q-d*) scaling for *w:d* = 30, 100 and 200 (Table 5.4). We then classify the *Q-d* scaling based on climate regions. All of the *Q-d* relationships are statistically significant, with different *w:d* ratios affecting scaling constants only.

Table 5.4 Global and climate-classified discharge:depth (*Q-d*) scaling relationships proposed based on three width:depth (*w:d*) ratios found from a number of modern river deltas.

Classification	*w:d* = 30:1	*w:d* = 100:1	*w:d* = 200:1
Global	$Q = 54.95d^{1.69}$ $R^2 = 0.76$ $p < 2.2 \times 10^{-17}$	$Q = 421.7d^{1.69}$ $R^2 = 0.77$ $p < 2.2 \times 10^{-17}$	$Q = 1349d^{1.69}$ $R^2 = 0.77$ $p < 2.2 \times 10^{-17}$
Arid	$Q = 19.95d^{2.32}$ $R^2 = 0.52$ $p = 1.2 \times 10^{-2}$	$Q = 331.13d^{2.32}$ $R^2 = 0.52$ $p = 1.2 \times 10^{-2}$	$Q = 1659.59d^{2.32}$ $R^2 = 0.52$ $p = 1.2 \times 10^{-2}$
Cold	$Q = 33.11d^{1.70}$ $R^2 = 0.94$ $p = 1.1 \times 10^{-8}$	$Q = 263.02d^{1.70}$ $R^2 = 0.94$ $p = 1.1 \times 10^{-8}$	$Q = 794.33d^{1.70}$ $R^2 = 0.94$ $p = 1.1 \times 10^{-8}$
Polar	$Q = 67.6d^{1.63}$ $R^2 = 0.91$ $p = 3.1 \times 10^{-3}$	$Q = 481.95d^{1.63}$ $R^2 = 0.91$ $p = 3.1 \times 10^{-3}$	$Q = 1479.11d^{1.63}$ $R^2 = 0.91$ $p = 3.1 \times 10^{-3}$
Temperate	$Q = 68.11d^{1.77}$ $R^2 = 0.88$ $p = 5.6 \times 10^{-4}$	$Q = 571.08d^{1.77}$ $R^2 = 0.88$ $p = 5.6 \times 10^{-4}$	$Q = 1940.89d^{1.77}$ $R^2 = 0.88$ $p = 5.6 \times 10^{-4}$
Tropical	$Q = 43.65d^{1.77}$ $R^2 = 0.63$ $p = 1.5 \times 10^{-6}$	$Q = 371.54d^{1.77}$ $R^2 = 0.63$ $p = 1.5 \times 10^{-6}$	$Q = 1255.59d^{1.77}$ $R^2 = 0.63$ $p = 1.5 \times 10^{-6}$

5.5.3. Climate impacts on the proposed scaling relationships

Climate-classified *Q-w* relationships may produce more reliable paleodischarge results than either the *Q-A* relationships or the global *Q-w* relationship due to the direct impacts of climatic factors on channel geometry. Most of the climate-classified *Q-w* relationships have higher R^2 values (0.52-0.94) than the global *Q-w* relationship (R^2 = 0.77). The *Q-A* relationships have R^2 values of 0.39 for the global data, and 0.24-0.85 for the climate-classified relationships. This does not necessarily mean that *Q-A* relationships should not be used, but depending on the data availability from the rock record, both *Q-A* and *Q-w* relationships remain useful for inferring paleodischarge.

Climate-classified *Q-A* relationships should give more reliable predicted paleodischarges than a single global *Q-A* relationship due to discharge being directly controlled by rainfall and runoff in each climate region (McCabe and Wolock, 2016; Eide et al., 2018a). However,

for paleodischarge studies catchment areas calculated from paleogeographic reconstructions may contain significant uncertainties due to the assumptions and interpretations involved in building paleogeographic maps. Hence, the ability to estimate paleodischarge through regional hydraulic geometry scaling relationships (Davidson and North, 2009) supported by provenance analysis (Blum et al., 2017), remains constrained by scatter in the modern data and the need to supplement the calculations with further estimated variables. Errors of at least one order of magnitude are not uncommon (Bhattacharya et al., 2016), but may provide valuable information that cannot be obtained by other means, or that supplements independent reconstructions of paleoenvironments.

Particular caution is required when estimating paleodischarge in arid and cold climates. Arid climates have annual rainfall between 150-200 mm (Thornthwaite, 1948) and a highly episodic runoff regime with flood flows lasting for only a few hours or days in a year (Rodier and Roche, 1978). This regime makes the definition of bankfull discharge challenging in this climate (Shamir et al., 2012). As an example, it is common to have rapid intermittent high flood with low and steady flow period throughout the year in an arid region (e.g. due to snowmelt in Colorado river catchment and intermittently anabranching river during low flow) (Segura and Pitlick, 2010). Catchment area and bankfull duration are poorly correlated in arid regions (Dodov and Foufoula-Georgiou, 2005), and interannual runoff irregularity and downstream loss of water are very significant in arid regions (Rodier and Roche, 1978).

In cold climate regions, flow may be non-continuous or substantially reduced in winter so reducing how representative Q_2 is as the bankfull discharge, also resulting in a weak correlation between catchment area and Q_2 (Beltaos and Prowse, 2009; Stonevičius et al., 2014). Flood hydrology in this region depends on interactions between snow and ice cover, precipitation and air temperature, that may induce shifts in runoff over decadal timescales (Stewart et al., 2005; Shiklomanov et al., 2007). Consequently, bankfull discharge estimation from both modern and ancient systems in these two climate regions should consider hydrological conditions in the relevant climate zone.

5.5.4. Further developments

Although the relationships calculated herein produce realistic discharge estimates in Cretaceous deltas constrained by outcrop and subsurface data, there is a need to test these relationships across different aged systems across different climate belts to understand the

extent to which they can be applied. Also, despite scaling relationships being available from modern estuaries (Diefenderfer et al., 2008; Gisen and Savenije, 2015) and tide-influenced river deltas (Sassi et al., 2012), development of similar rock-record focused scaling relationships for other systems (e.g. tidal creeks or other delta types) remains an area for further study.

Finally, our proposed method adopts metrics that are more easily extracted from the rock record and which is based on specific climate zones has potentially important implications with regards to assessment of hydrocarbon, hydrogen, geothermal and carbon capture and storage (CCS) sizes (Bhattacharya and Tye, 2004; Shinn et al., 2014). In addition, it will help in deducing climate and tectonic forcing on systems and paleohydraulics across various types of depositional systems in source-to-sink studies (Montgomery and Gran, 2001; Merritt and Wohl, 2003; Brardinoni and Hassan, 2006; Wohl and David, 2008; Davidson and Hartley, 2010; Eaton, 2013).

5.6. Conclusion

We have obtained *Q-A* and *Q-*W_{med} scaling relationships for 66 modern river deltas across different climate regions by extracting catchment areas for each delta, making 3823 distributary channel width measurements and calculating their associated bankfull discharges. These relationships are intended to provide quantitative information on source catchment properties from data typically available in the rock record. Applying the simple scaling relationships derived here from modern systems to the rock record, coupled with paleoclimate information, produced paleodischarge estimates within the same order of magnitude as paleodischarge values derived from existing, more complex, approaches that require a larger number of parameters. These new relationships promise enhanced deduction of climate and paleodischarges across various types of depositional systems in source-to-sink studies, assessment of hydrocarbon, hydrogen, geothermal and carbon capture and storage (CCS) sizes, and more accurate paleogeography interpretations. The relationships have been validated against data from some Cretaceous deltas, applying these scaling relationships to other paleoclimate regions, systems of different ages and to different types of deltaic environment, remain areas of further study.

Acknowledgements

The authors thank Prof. Gary Hampson and other anonymous reviewers for constructive comments on earlier versions. The global river discharge dataset is available from The Global Runoff Data Centre (GRDC), 56068 Koblenz, Germany or and via the web (http://www.bafg.de/grdc.htm).

Data Availability Statement

Data from this paper are publicly-available at https://doi.org/10.6084/m9.figshare.19574938.v2.

Chapter 6 – Practical sampling criteria for using delta channel width to estimate paleodischarge in the rock record

The following chapter is a reformatted version of a manuscript in review for the Journal of Sedimentary Research, by Prasojo, O. A., van Yperen, A.E., Hoey, T. B., Owen, A., & Williams, R. D. available at https://doi.org/10.31223/X5G061.

Abstract

Quantifying paleodischarge from geological field observations have been for decades, and remains, a key research challenge. Several paleodischarge scaling relationships have been developed for fluvial environments, such as BQART, Fulcrum and regional hydraulic geometry or for river deltas by precluding the role of wave and tide. In deltas where marine (wave, tide) energy causes bidirectional flow, the available paleodischarge scaling relationships are not applicable. Here, the spatial variability of distributary channel widths from a database of 114 global modern river deltas is assessed to understand the limit of marine influence on distributary channel widths. Compiling 4459 distributary channel width measurements enables improvements to distributary channel width-discharge scaling relationships specifically for river-, tide- and wave-dominated deltas. By bootstrapping the channel widths measured from modern deltas, the minimum number of width measurements needed to apply width-discharge scaling relationships to ancient deltaic deposits is estimated as 3 and 30 for upstream and downstream river-dominated deltas, consecutively, 6 for upstream part of tide-dominated deltas and 4 for wave-dominated deltas. This estimate will guide sedimentologists who often have limited numbers of distributary channel widths exposed in the rock record. Statistically significant width-discharge scaling relationships are derived for river- and wave-dominated deltas, with no significant relationships identified for tide-dominated deltas. To test the reliability of these improved width-discharge scaling relationships in the rock record, paleodischarges were estimated for the well-studied Cretaceous lower Mesa Rica Formation, USA. Comparison of these results with the more complex Fulcrum method suggests that these new scaling relationships are accurate. Hence these scaling relationships obtained from modern deltas can be applied to the rock record, and this approach requires less, and easier to measure, data inputs than previously published methods.

6.1. Introduction

Sedimentary deposits provide an important archive of interactions between tectonic and climate activity in deep geological time (Sharman et al., 2019). However, reconstructing paleodrainage settings from sedimentary deposits remains a challenge (Nyberg et al., 2021). Specifically, estimating rates of key earth surface processes such as sediment flux and paleodischarge has been a key research challenge for decades (Whittaker, 2012; Lyster et al., 2021). Estimating paleodischarge plays an important role in quantifying sediment

transport capacities and volumes (Allen et al., 2013; Holbrook and Wanas, 2014; Lin and Bhattacharya, 2017; Sharma et al., 2017), understanding the scale of ancient catchments (Bhattacharya and Tye, 2004; Bhattacharya et al., 2016; Eide et al., 2018b; Lyster et al., 2020), and investigating paleoclimate impact on paleochannel hydrology (Duller et al., 2010; Whittaker et al., 2011; Castelltort et al., 2012; Hampson et al., 2013).

Most of the models proposed to estimate paleodischarge, such as BQART (Syvitski and Milliman, 2007), the Fulcrum model (Holbrook and Wanas, 2014; Bhattacharya et al., 2016), or regional hydraulic geometry (Syvitski & Milliman, 2007; Davidson & North, 2009; Holbrook & Wanas, 2014; Bhattacharya et al., 2016) are suitable to purely unidirectional fluvial environments since they do not consider the influence of marine energies that may alter the unidirectionality of river current (Syvitski and Milliman, 2007; Davidson and North, 2009; Holbrook and Wanas, 2014; Bhattacharya et al., 2016). The BQART model incorporates a scaling relationship between the water discharge (Q) and catchment area (A) from the 63% of the world's river discharge ($Q = 0.075A^{0.8}$) to estimate sediment flux, assuming that these two variables are partly independent (Syvitski and Milliman, 2007). Consequently, applying BQART to ancient sedimentary systems needs robust paleogeographic reconstructions to estimate the paleocatchment area, itself challenging to reconstruct from the rock record (Nyberg et al., 2021). Similar to the BQART model, the Fulcrum model needs several parameters that are challenging to extract from rock records such as bankfull depth and width, estimated paleoslope, estimated bankfull Shield's stress and the dimensionless Chezy friction coefficient (Holbrook and Wanas, 2014; Bhattacharya et al., 2016; Brewer et al., 2020).

On the other hand, a new rock-record focused channel width-discharge scaling relationship for river deltas (Chapter 5; Prasojo et al., 2023) precludes the role of wave and tide, assuming distributary channels contain only unidirectional river currents. Another model, WBMSed, was recently applied for estimating the global river deltas discharges (Cohen et al., 2013; Nienhuis et al., 2020). Although WBMSed produced fairly reasonable prediction of several rivers in the USA and predictions were comparable with the BQART model, WBMSed model does not take into account the influence of marine energy that can significantly alter the geometry of delta distributary channels of river deltas (Nittrouer, 2013; Chatanantavet et al., 2012; Lamb et al., 2012; Fernandes et al., 2016; Ganti et al., 2016; Martin et al., 2018; Chadwick et al., 2019, 2020; Gugliotta & Saito, 2019).

It is expected that channel width scaling relationships in deltas weaken with more significant marine energy influence (wave, tide, longshore currents) due to bidirectional flow and channel deflection in more distal parts of delta plains (Besset et al., 2017). The presence of large tidal, wave energy or backwater-controlled flow regimes also significantly alters the geometry of delta distributary channels, hence directly weakening scaling between channel width and discharge (Fig. 6.1). The effect on channel geometry, including narrowing and deepening, due to marine influences has also been demonstrated (Chatanantavet et al., 2012; Lamb et al., 2012; Nittrouer, 2013; Fernandes et al., 2016; Ganti et al., 2016a; Martin et al., 2018; Gugliotta and Saito, 2019; Chadwick et al., 2019b, 2020). To consider the marine influence on width-discharge scaling relationship, the break in distributary channel morphology (i.e. channel width; Sassi et al., 2012) that classifies delta plains into upstream, assuming no marine influence, and downstream, marine-influenced parts needs to be identified for river-, tide- and wave-dominated deltas. This provides an opportunity to create a more accurate discharge/paleodischarge estimation from river deltas.

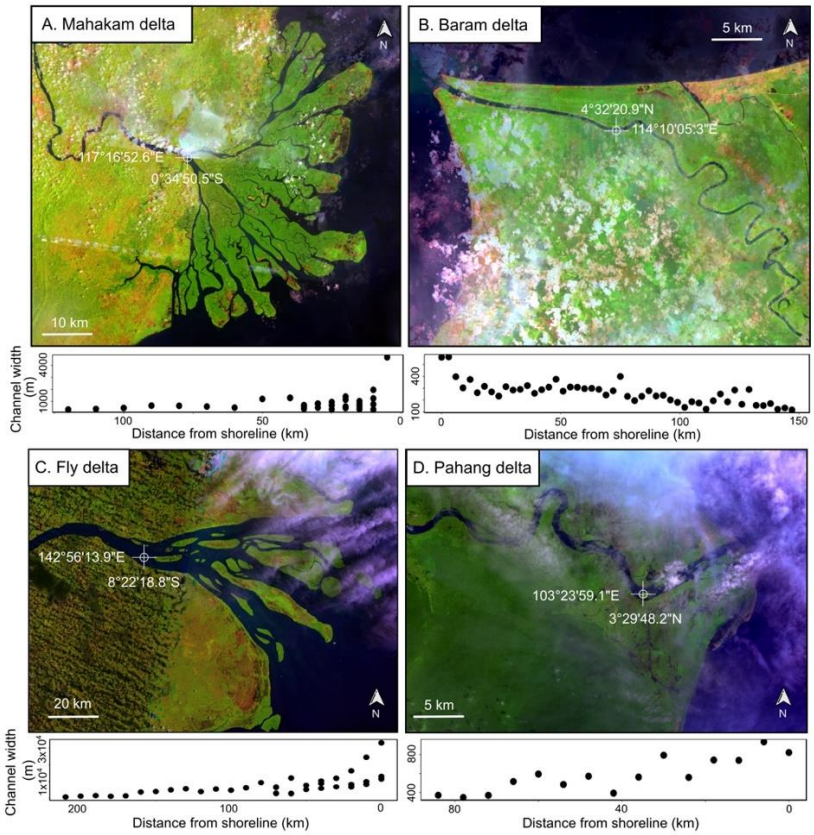

Figure 6.1 Landsat 5 images (all around year 2000) from several delta types. A. tide-influenced, river-dominated Mahakam delta, Indonesia; B. wave-influenced Baram delta, Malaysia; tide-dominated C. tide-dominated Fly delta, Papua New Guinea and D. river-dominated Pahang delta, Malaysia. Changes in channel width away from the distal limits, which are plotted in the lower panels. Differences in morphological patterns depend on the interaction between dynamic catchment (water and sediment inputs) and marine (wave energy, tidal energy) variables that interact to produce delta morphology.

This study aims to assess the spatial variability of distributary channel widths from a database of 114 global river deltas to improve channel width-discharge scaling relationships, in which a clear break in distributary channel widths is identified that separates upstream and downstream parts of the delta. The downstream parts are characterised by channels which widen towards the sea, whereas in upstream parts channel widths remain broadly constant between successive bifurcations to the delta apex. A total of 4459 distributary channel widths from the 114 river deltas were measured from the delta apex, or first avulsion point, to the shoreline.

In contrast with modern river deltas on which distributary channel widths can be measured directly from satellite images or in the field, ancient delta deposits typically have very limited distributary channel exposure or preservation hence the width cannot be determined directly. In this study we apply a bootstrap method to the large global modern delta dataset (N = 4459) to simulate the optimum number of measurements needed to estimate paleodischarge from a deltaic deposit. By applying bootstrapping, we provide a guideline for the minimum number of width measurements that are needed from the rock record to reliably use the newly established channel width-discharge scaling relationships.

Overall, the aims of this study are: (1) to identify any morphological break or down-dip spatial variation of delta distributary channel widths; (2) to improve channel width-discharge scaling relationships for delta channels based on analysing data with regard to down-delta breaks in channel width; (3) to apply a bootstrap method to the modern delta data to simulate the limited number of data points usually available from the rock record; and, (4) to compare the results from the improved channel width-discharge scaling relationships with those obtained using the Fulcrum method.

6.2. Methods

6.2.1. Dimensionless distributary channel widths of river deltas

The active channel width of distributary channels from 114 deltas (including 97 river-dominated deltas, 7 tide-dominated deltas, and 10 wave-dominated deltas) across different climate regions were measured from Landsat 5 satellite images in Google Earth Engine (GEE). The earliest (~2009) and the least cloudy images were chosen for image clarity purposes, as well as to minimize the influence of ongoing anthropogenic activities such as

embankment construction. Distributary channel widths were measured manually along all the identifiable distributary channels seen on Landsat 5 (minimum channel width of 100 m) from the delta apex to the shoreline. The delta apex is assumed to be the present-day most landward bifurcation point observed on satellite images (Ganti et al., 2016a). Where deltas have a single channel, the delta apex is associated with the valley exit point from its Digital Elevation Model (DEM) (Hartley et al., 2017). To enable comparison of channel widths measured from different sized deltas, we use the semicircular grid *s/L* method (Sassi et al., 2012) to ensure even spacing of measurements, where *s* represents the along-channel distance from the delta apex, and *L* is the along-channel distance of the longest distributary channel to the delta apex (Fig. 6.2). The semicircular grid allows measurement of multiple distributary channels located at the same dimensionless distance from the apex point. The grid resolution is ~10 times the river channel width at the delta apex to maintain consistent dimensionless distance and data collection frequency across deltas of varying size. As an example, if a delta has a 100 m wide channel at its apex, the semicircular grid will have diameters of 1, 2, 3... km until the grid covers the entire delta plain (Fig. 6.2). Thus, channel width is measured at *s/L* = 1, 0.9, 0.8... , 0.1, 0. Only channel widths along definite distributary channels (N = 4459) were included to exclude the influence of non-riverine influences in delta systems, such as tidal creeks. Where distributary channels contain mid-channel bars, the width of the wider channel was measured (inset Fig. 6.2).

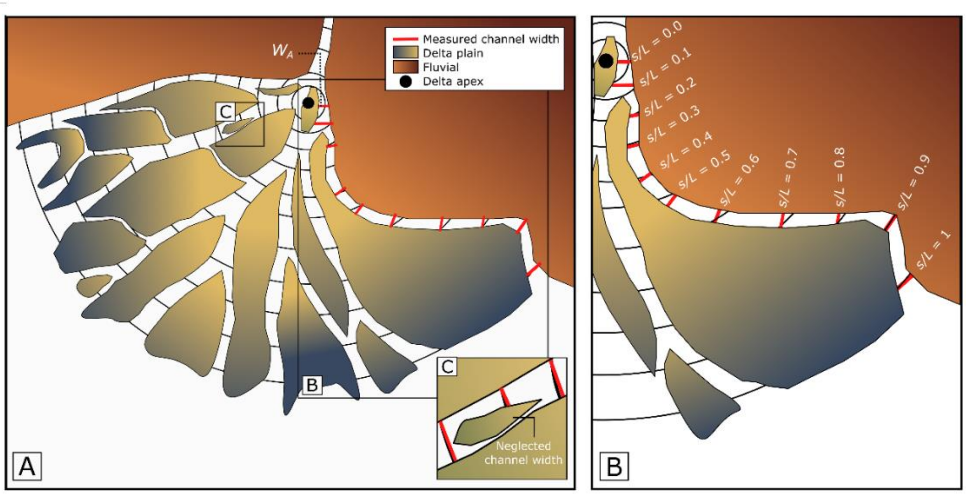

Figure 6.2 A: The semicircular grid used to measure the channel widths of distributary channels. B: Enlarged version of the measured channel width from Fig. 6.2A. Channel widths were made at the red lines which are perpendicular to the banks of the wetted distributary channels. Inset shows measurement method when mid-channel bars are present. The spacing of the semicircular grid is defined as ~10 times the channel width at the apex of the delta (W_A).

Deltas were identified based on protrusion of their visible deposits beyond their lateral shorelines (Caldwell et al., 2019). They were then classified as river-, wave- or tide-

dominated, based on Nienhuis et al. (2020) dataset. Morphologically, river-dominated deltas are characterized by multiple/single elongated distributary channels that protrude beyond the shoreline and subaerial mouth bar deposits (Olariu and Bhattacharya, 2006). Wave-dominated deltas have linear shorefaces and mouth bars modified by wave action. In most cases, the number of distributary channels in wave-dominated delta is limited (Bhattacharya and Giosan, 2003; Bhattacharya and Tye, 2004; Li et al., 2011). Tide-dominated deltas are characterized by a funnel-shaped distributary channels with abundant tidal creeks on adjacent delta plains. We simplify the classification into the three end-members of Galloway (1975) same as Nienhuis et al. (2020) but acknowledge other delta classifications (Li et al., 2011; Vakarelov and Ainsworth, 2013; Lin and Bhattacharya, 2021).

Dimensionless distance was plotted against dimensionless channel width (w^*) for each delta type. Dimensionless distance is defined as s/L consistent with the semicircular grid (Fig. 6.2) that originates at the delta apex. Dimensionless width (w^*) is defined as w/W_a where w is channel width and W_a is the channel width at the delta apex. Subsequently, down-dip changes in dimensionless channel widths form the basis of classifying the delta plain into 'upstream' and 'downstream' parts. To aid recognizing any contrasts between 'upstream' and 'downstream' distributary channel width patterns, the non-parametric Kruskal-Wallis one-way analysis of variance test was conducted. Data binning of 10% of original data was later used as the basis of 'upstream-downstream' classification due to its proper representativity of the overall data without producing significant bias (see Supporting Information and Fig. S6.1 for details). The classifications between 'upstream' and 'downstream' parts were then the basis of running a bootstrap method on to the dataset.

6.2.2. Bootstrapping the distributary channel width distribution from modern river deltas

Bootstrapping was undertaken to assess the impact of a limited sample size that may be retrieved from the rock record. This is a common resampling method that has been widely used in field studies with limited sample size (Cheng and Yeager, 2007; Cui et al., 2017; Debchoudhury et al., 2019). Bootstrapping involves repeat resampling of the original dataset with replacement (Efron, 1982, 2007). Resampling is repeated B times (B is typically a power of 10, e.g. 10, 100, 1000…) to transform a small number of measurements into a much larger sample size to improve the validity of statistical results obtained from analysing the data (Cui et al., 2017).

In this study, rather than increasing the sample size from a large number of measured channel widths from modern river deltas, bootstrapping was used to reduce this sample size to simulate the typically small number of distributary channel widths that can be measured from outcrops. Bootstrapping used from 100% to 3% of the original number of distributary channel widths measured from modern deltas. Standard errors of these re-sampled data sets were calculated and plotted against the number of samples to show the distribution of standard errors for different sample sizes. Standard error (S) is defined in Equation 6.1 as:

$$S = \frac{\sigma}{\sqrt{N}} \tag{6.1}$$

With σ representing the standard deviation of channel widths (m) and N the number of measurements in the sample. The plots simulate errors that may be encountered by measuring small numbers of distributary channel widths in the rock record. The relationships between sample size and standard error can be used to inform sample size determination for field studies as well as to quantify the uncertainties in measurements. Percentile standard errors were calculated to understand how the distribution of measured distributary channel widths influences the shape of the distribution of synthetic samples of different size. This analysis was designed to overcome the small sample sizes from ancient field measurements through analysis of a large contemporary data set; the influence of sample size on estimates of width is known for a normal distribution through equation (6.1), but using a large real data set provides understanding of the influence of the shape of the underlying distribution on the results.

6.2.3. Improving delta width-discharge scaling

To improve the previously available scaling relationships between channel width and total river discharge for river deltas (Prasojo et al., 2023), we apply the same method to the scaling relationship between distributary channel width and total discharge by correlating the median channel widths of distributary channels for each delta to its consecutive bankfull discharge using an ordinary least square (OLS) regression. We expand width-discharge scaling from river-dominated deltas to also include wave- and tide-dominated deltas based on (Nienhuis et al., 2020) dataset and reclassify each delta type based on down-dip (down-delta) changes in dimensionless distributary channel width, as explained above. This

approach provides refined width-discharge scaling relationships that take into account the marine influence on distal distributary channel widths.

All scaling relationships assume a power law relationship (i.e. linear on a log-log plot) between input river discharge and channel width (Leopold and Maddock, 1953). Hence, OLS regressions were then used to calculate relationships between these two variables. Median values of measured channel width (W_{med}) from each delta were plotted against the respective bankfull discharge values (Q_2). Median channel widths were preferred to means due to the width distributions being non-Gaussian, such that the median is more representative of the whole channel width population. Using the median also reduces the influence of extreme values, so reducing the need to identify and exclude channels where tidal influence controls their width. Further, as it is challenging to detect how many distributary channels were active at the same time in the rock record, using one median value of channel width per delta helps in minimizing the effect of this difficulty but explicitly assesses the statistical uncertainty associated with the number of measurements that could be made.

Bankfull discharge is widely considered as the flow that controls channel geometry in alluvial rivers (de Rose et al., 2008; Haucke and Clancy, 2011; Gleason, 2015b), although other factors also affect this geometry. Bankfull discharge is estimated from daily discharge data using Q_2, where 2 is the recurrence interval (years) of the discharge (see also Eaton, 2013; Jacobsen and Burr, 2016; Morgan and Craddock, 2019). Calculations used the Flow Analysis Summary Statistics Tool (‘*fasstr*’) package for R (https://github.com/bcgov/fasstr). For some sites only monthly discharge data were available, from which daily equivalent Q_2 values were obtained using a climate-classified transformation (see Chapter 2.1.3; Beck et al., 2018). The discharge dataset was extracted from the Global Runoff Data Centre (GRDC), using the river gauges located closest to the delta apex.

6.2.4. Applying width-discharge scaling relationships the rock record

To test the reliability of the scaling relationships produced in this study for the rock record, we utilized ~400 km transects of the Cenomanian Mesa Rica (Dakota Group, USA) exposed along an overall NNW- to SSE-oriented depositional profile in southeast Colorado and northeast New Mexico (Holbrook, 1996; R.W. Scott et al., 2004; Oboh-Ikuenobe et al., 2008; van Yperen et al., 2019; van Yperen et al., 2020). In east-central New Mexico, the

Mesa Rica is subdivided into lower, middle and upper units (Scott R.W. et al., 2004; van Yperen et al., 2019). The up-dip reaches of the lower Mesa Rica depositional system consist of single-story trunk channel deposits that form sheet like geometries (Holbrook, 1996, 2001). A down-dip transition from fluvial to deltaic deposits occurs at the northwestern rim of the Tucumcari sub-basin (Western Interior Basin). Here, the lower Mesa Rica consists of coalesced mouth-bar deposits overlain by amalgamated sandy distributary-channel deposits indicative of a river-dominated delta (van Yperen et al., 2019, 2020). During the Cretaceous, the Mesa Rica was located at ~35°N latitude, with a warm and humid climate (Chumakov et al., 1995).

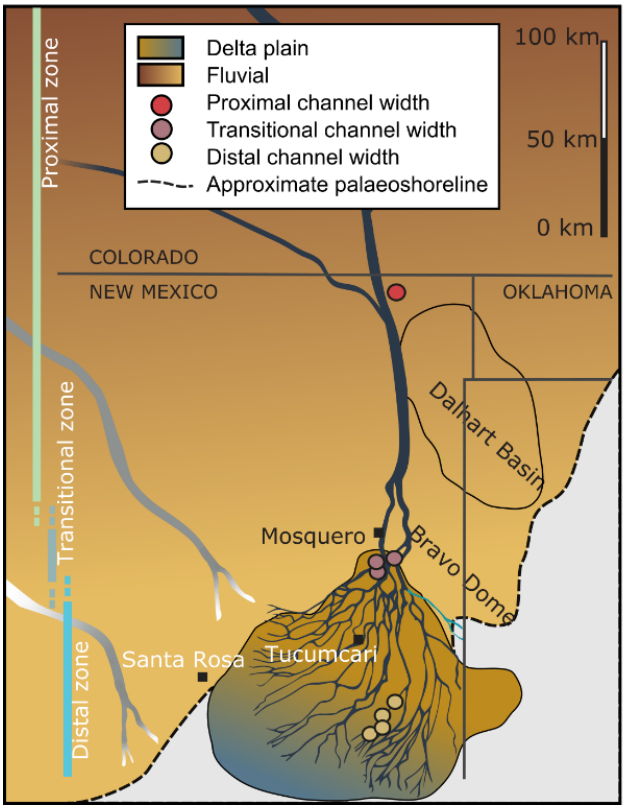

Figure 6.3 Paleogeographic reconstruction of the Cretaceous lower Mesa Rica fluvio-deltaic depositional system (modified from Van Yperen et al., 2019). Nevertheless, due to the scale of the figure, not all 13 data points could be drawn on the figure. See Table 6.1 for the exact location of all channel width measurements.

Distributary channel width measurements from the lower Mesa Rica consist of 13 data points distributed down-dip throughout the depositional system, from proximal (up-dip of the delta apex) to distal (Fig. 6.3; Table 6.1). The distributary channel widths were plotted as dimensionless width (w^*) and dimensionless distance down-dip (s/L), assuming that the proximal channel width is represented by the width at the delta apex. The bootstrap method was then applied to this rock record dataset with a range of repetition numbers (B = 1, 100, 1000, 10000). Subsequently, paleodischarges were estimated using the empirical

relationships generated in this study from modern deltas. To test the reliability of these calculated paleodischarge estimates, we also estimated paleodischarge using the Fulcrum method (Holbrook and Wanas, 2014). See Supporting Information for details of the paleodischarge calculation using the Fulcrum method (Table S6.1).

The Fulcrum method and the width-discharge scaling relationships developed in this study share the assumptions of the erosional geometry that defines the shape of the channel infill being in equilibrium with water discharge, and the paleochannel position being fixed. Preservation of a channel fill deposit requires aggradation, hence non-equilibrium.

Table 6.1 Distribution of the 13 measured channel widths from the lower Mesa Rica along with the zonation and latitude-longitude positions.

Measured width (m)	Zone	Latitude	Longitude
250	Proximal	36.93349	-103.62979
401	Transitional	35.49859	-103.81257
299	Transitional	35.53891	-103.84624
240	Transitional	35.53491	-103.86028
70	Transitional	35.54482	-103.84091
50	Transitional	35.53751	-103.84859
71	Distal	34.991298	-103.396205
92	Distal	34.991222	-103.41928
109	Distal	34.91677	-103.49411
33	Distal	34.86206	-103.54559
224	Distal	34.937565	-103.469176
74	Distal	34.93272	-103.48047
250	Distal	34.99736	-103.38935

6.3. Results

6.3.1. Down-dip changes in distributary channel widths

Description: Dimensionless widths from the distributary channels of 97 river-dominated deltas (Fig. 6.4A; Table S6.2) show a gradual downstream decrease towards s/L = 0.1. A substantial increase in w^* with higher variance occurs at the shoreline, s/L = 0, in comparison to up-dip counterparts. The abrupt change in w^* distinguishes the upstream from the downstream part of the delta plain in these river-dominated deltas. The non-parametric Kruskal-Wallis one-way analysis of variance test corroborates classification between the

upstream ($1 \leq s/L \leq 0.1$) and the downstream ($s/L = 0$) parts of distributary channel widths with $p < 0.05$.

Tide-dominated deltas (N = 7; Table S6.2) in this study show a gradual increase of w^* towards the shoreline (Fig. 6.4B). In the upstream part ($1 \leq s/L \leq 0.5$), spatial variation is apparent in w^*. However, this variation lies within the interquartile ranges of the data and may not be significant. In contrast, a substantial increase of w^* occurs at $s/L<0.5$ (Fig. 6.4B); this abrupt change in dimensionless channel is defined to mark the transition between upstream and downstream parts (Fig. 6.4E). Statistical significance test (Kruskal-Wallis test) corroborates the significance of upstream-downstream parts classification of w^* with $p < 0.05$.

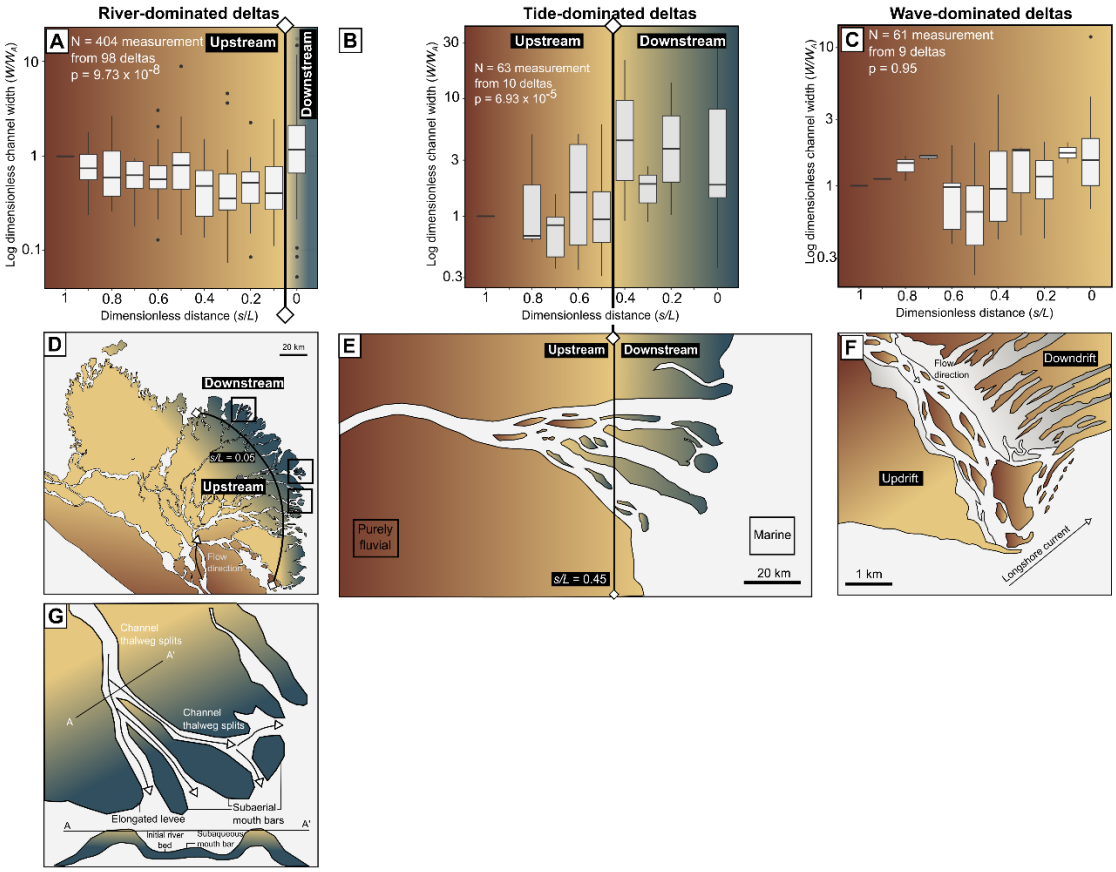

Figure 6.4 A-C: Distribution of dimensionless measured channel widths from (A) river-, (B) tide- and, (C) wave-dominated deltas. *P*-values are from the non-parametric Kruskal-Wallis one-way analysis of variance test comparing the distributions of channel width at different locations along the delta. D-E: examples of (D) river- and € tide-dominated deltas, with the upstream-downstream boundary positions inferred from the changes of channel width on (A) and (B). F: Map view the Paraibo do Sul delta in Brazil showing differences in 'updrift' and 'downdrift' characteristics of a wave-dominated delta (modified from Li et al., 2011). G: Map view and cross-section view of a mouth bar. Boxes on D depict the location of the mouth bars shown in G.

The wave-dominated deltas (N = 10; Table S6.2) show consistent dimensionless distributary channel width across the delta plain (Fig. 6.4C), with an abrupt decrease at $s/L \sim 0.6$ (Fig. 6.4C). Nonetheless, there is no significant change in w^* between $1< s/L <0.7$ and $0.6< s/L <0$ (Kruskal-Wallis test; $p > 0.5$), corroborating that distributary channel widths in wave-dominated deltas remain relatively constant downstream.

Interpretation: The abrupt and substantial increase in w^* at $s/L = 0$ in river-dominated deltas can be related to mouth-bar processes (Olariu and Bhattacharya, 2006). Mouth-bar deposition is mainly caused by a decrease in sediment carrying capacity due to the decreasing velocity of the river flow when it enters the standing body of seawater (Edmonds and Slingerland, 2007). Sediment carried by the distributary channels tends to be deposited along channel levees and also in a subaqueous mouth-bar that induces bifurcation as it grows (Fig. 6.4D, G; 'phase 2' of (Olariu and Bhattacharya, 2006). As channels become shallower due to mouth bar growth, bank erosion accelerates so increasing the channel width at the river mouth, $s/L = 0$, as shown in this study. The data in this study shows similar channel widening at distributary mouths of river-dominated deltas due to this phenomenon.

In tide-dominated deltas, the downstream increase of w^* downstream of $s/L<0.5$ is progressive rather than abrupt and results from the impact of tidal energy. The interaction between the unidirectional river flow and tidal currents within the standing body of seawater produces an interplay of physical (river, tides, waves), chemical (salinity), and biological (bioturbation) processes, seen in both modern and ancient systems (Dalrymple and Choi, 2007). To separate the upstream and downstream parts of tide-dominated deltas, we utilized the subzone classification of the fluvial-to-marine transition zone (FMTZ) (Gugliotta et al., 2016). The onset of the substantial increase of channel width downstream coincides with the boundary between the 'fluvially-dominated, tidally-influenced' and 'tidally-dominated, fluvially-influenced' zones. This boundary represents the sedimentological landward limit of tidal dominance. In the 'tidally-dominated, fluvially-influenced' zone, the role of river energy is predominantly as the sediment supplier. Additionally, the boundary position will shift landward and seaward due to the changes in the fluvial discharge (Dashtgard et al., 2012; Dalrymple et al., 2015; Jablonski and Dalrymple, 2016; Gugliotta et al., 2016) and cyclic fluctuations of tidal modulation (Allen et al., 1980; van den Berg et al., 2007; Dalrymple and Choi, 2007; Kravtsova et al., 2009). Even though each delta distributary channel could have a different FMTZ location, the boundary between the 'fluvially-dominated, tidally-influenced' and 'tidally-dominated, fluvially-influenced' zones

consistently show statistically significant change in channel width at s/L = 0.45 globally (Fig. 6.4B).

Wave-dominated deltas occur in coastal settings with strong longshore currents that redistribute sediment away from the river mouth, producing different updrift and downdrift characteristics (Fig. 6.4F) (Bhattacharya and Giosan, 2003). Longshore wave energy tends to produce a single dominant distributary channel in these deltas (Korus and Fielding, 2015). Increasing the long-term wave energy relative to fluvial input will increase longshore sediment dispersal, thereby reducing the rate of channel-belt aggradation and associated seaward extension and increasing the avulsion timescale by a factor of approximately 50 (Swenson, 2005). The increase in avulsion timescale, hence reduction in avulsion frequency, limits a distributary network growth like in river- or tide-dominated deltas. Also, strong longshore wave energy tends to sweep the mouth bar early deposit, hampering channel splitting due to mouth bar deposition. This absence of distal channel splitting explains the observed constant w^* from wave-dominated deltas from our global dataset (Fig. 6.4C). There is consequently no differentiation between upstream and downstream parts of wave-dominated deltas.

6.3.2. Bootstrapping estimation of sample standard error

Description: The standard error distributions produced by the bootstrapping dimensionless distributary channel widths in all delta types show a monotonic decrease with increasing number of measurements (Fig. 6.5A-E). The standard errors of dimensionless width (S_{w^*}) estimates are significantly lower in the upstream parts of river-dominated deltas than in any of the other data sets (y-axis values in Fig. 6.5A-E). In contrast, the downstream parts of both river- and tide-dominated deltas consistently show the highest standard error values.

The implication of these low mean standard errors in the upstream parts of river-dominated deltas, where standard error is consistently < 0.1 when N exceeds 30 (using B=10; Fig. 6.5A), is that the standard error remains low (S_{w^*}~0.2) with as few as three measurements (inset Fig. 6.5A). In the downstream part of river-dominated deltas, high variance of 75 measured dimensionless channel widths leads to high standard errors (S_{w^*} up to ~1) from 1000 bootstrap replications (B) (Fig. 6.5B). The standard error reduces to 0.5 only when N is about 30 (inset Fig. 6.5B).

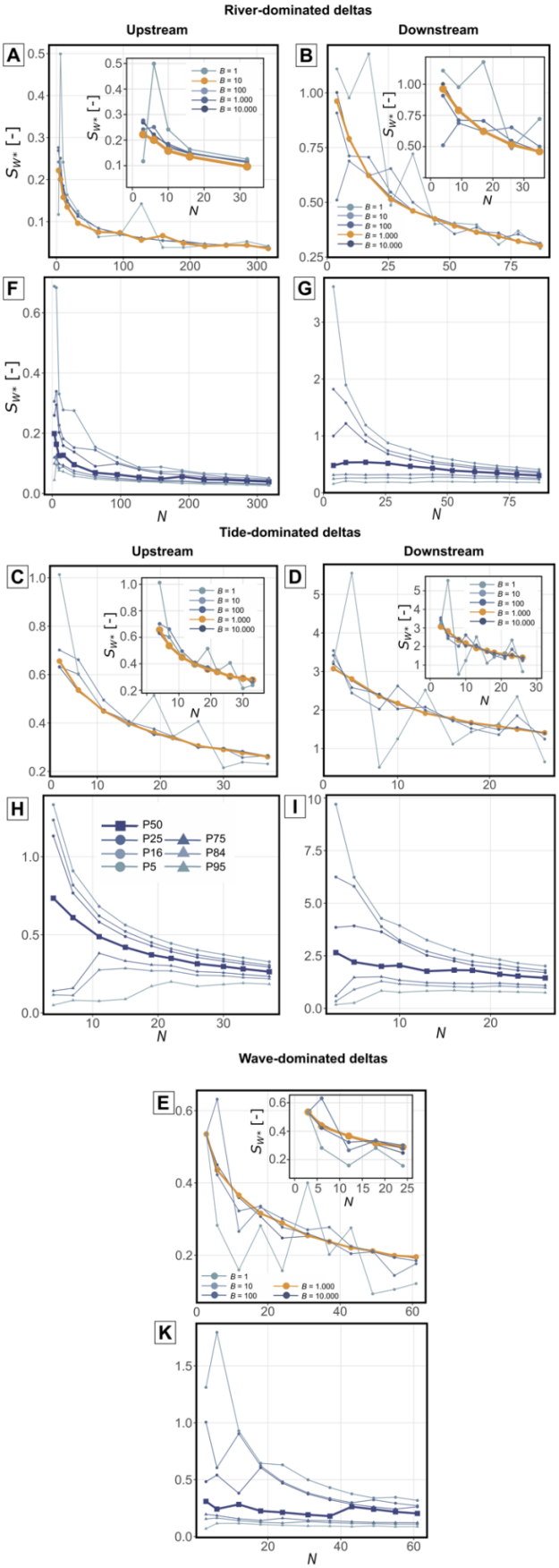

Figure 6.5 Mean standard error of dimensionless channel width (S_{W^*}) versus number of measurements (N) from the upstream and downstream parts of river- (A,B, respectively) and tide-dominated (C,D) deltas. E: Mean standard error versus N from wave-dominated deltas. F-K: Percentile standard errors of the dimensionless widths for the selected B values from plots (A-E). B indicates the number of repetitions in

the bootstrap calculations. Inset plots (A-E) show greater detail for low *N*. The dark orange lines show the number of repetitions (*B*) that produced the most stable, generally monotonic relationships between standard error of dimensionless width and number of measurements.

In tide-dominated deltas, upstream standard errors are lower (S_{w*}~0.4) than downstream (S_{w*}~2) from 1000 bootstrap replications (Fig. 6.5C, D). Only 6 data points are required to reduce the standard error (S_{w*}) to 0.5 (inset Fig. 6.5C). The standard errors in downstream parts of tide-dominated deltas remain high for all sample sizes (i.e. S_{w*} = 1.5-3) (inset Fig. 6.5D).

In wave-dominated deltas the standard error reduces monotonically from 1000 bootstrap replications (Fig. 6.5E). Using five data points, S_{w*}~0.4 (inset Fig. 6.5E), and increasing the number of samples to 60 only reduces the standard error (S_{w*}) to 0.2.

The distributions of mean standard errors for each percentile are plotted in Fig. 6.5F-K. All the delta types consistently show asymmetry in standard errors for equivalent percentiles (P5-P95; P16-P84; P25-P75) around their respective P50 standard error distributions. Tide-dominated deltas show the largest difference between the percentiles, reflecting the skewed distribution of dimensionless distributary channel widths, while the upstream parts of river-dominated deltas reflect a lower skew in this distribution of dimensionless distributary channel widths.

Interpretation: In the upstream section of river-dominated deltas where the unidirectional river current is dominant, changes in distributary channel patterns produced the least standard error compared to other delta types. While on the other extreme, the lack of a dominant unidirectional river current (e.g. in downstream part of tide-dominated deltas) shows the highest standard error distribution (Fig. 6.5D) due to the higher variance in the measured distributary channel widths. As shown in this study, when the river current becomes influenced by the large tidal or backwater-related processes that weaken the unidirectionality of river current, the standard error becomes higher (e.g. downstream part of tide-dominated deltas in Fig. 6.5D). On the other hand, the smaller the standard error, the less the influence of tidal or other backwater-related processes (e.g. upstream part of river-dominated deltas in Fig. 6.5A).

The positive skewness in dimensionless channel widths in all delta types and locations has also been reported from fluvial outcrops and seismic sections (Colombera et al., 2019). This

suggests that all consecutive statistical approaches on channel width measurement from river deltas should be treated with having non-normal distributions.

6.3.3. Improving delta hydraulic geometry models

Description: Log-log plots (Fig. 6.6A-E) show power law relationships between the bankfull discharge of the river upstream of the delta (Q_2) and median channel width (W_{med}) with Fig. 6.6F showing the power law relationship between the overall measured distributary channels (w) and the bankfull discharge (Q_2). River- and wave- dominated deltas show how hydraulic geometry theory (i.e. a significant, $p<0.05$, positive power law relationship between channel width and discharge) applies to these two delta types (Fig. 6.6A,B,E). However, in tide-dominated deltas negative power law relationships occur (Fig. 6.6C,D), although these are not significant due to small sample sizes. Correlations are high in the upstream parts of river-dominated, $Q_2 = 5.82w^{1.11}$ ($R^2 = 0.53$; s=0.13), and wave-dominated deltas, $Q_2 = 0.42w^{1.48}$ ($R^2 = 0.68$; s=0.36) (Fig. 6.6A, E). Standard error from regression (s) is higher in wave-dominated deltas due to smaller sample sizes than the river-dominated deltas and R^2 is lower (0.17; s=0.2) on the downstream part of river-dominated deltas.

Slope tests were conducted to identify the difference between upstream-downstream regression lines of bankfull discharge (Q_2) and median channel width (W_{med}) from river- and tide-dominated deltas. We also compared the regression lines from each delta type to the global w-Q_2 equation shown in Fig. 6.6F. The slope tests show $p < 0.05$ for all regressions when being compared to both the global and between upstream-downstream parts.

Interpretation: The scatter in median width-discharge data (Fig. 6.6) increases (and, although affected by sample size, so does the regression standard error s) where marine energy (tides, longshore currents, waves) is greater, and that this energy directly impacts distributary channel width. Tidal energy obstructs the down-delta flow and causes distal widening, reflected in the distribution of distributary channel widths (Fig. 6.4B) and the standard errors of width estimates derived from samples (Fig. 6.5C,D).

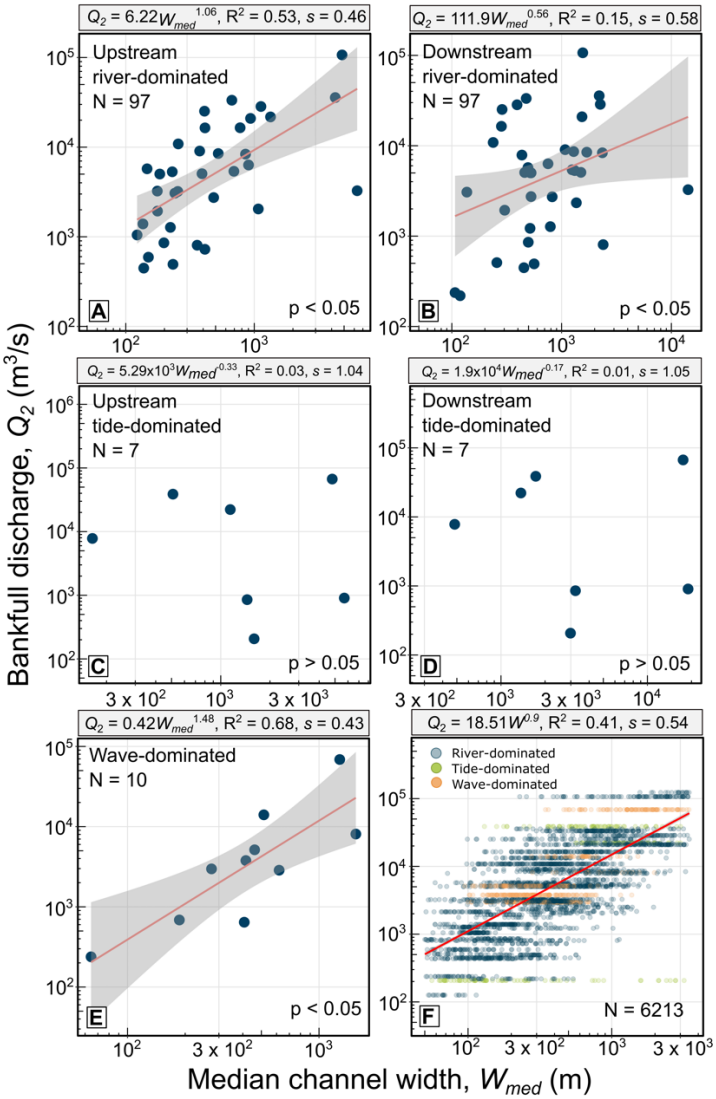

Figure 6.6 A-E: Scaling relationships between bankfull discharge (Q_2) and median channel widths (W_{med}) for river-, tide-, wave-dominated deltas. (F) Scaling relationship between bankfull discharge (Q_2) and channel widths (w) for overall dataset. (A) and (C) are for upstream parts of river- and/ tide-dominated deltas, and (B) and (D) are for their downstream parts, respectively Ordinary least squares regression lines and 95% confidence intervals (shaded areas) shown; R^2 = coefficient of determination of the scaling relationship, p = statistical significance, and s = standard error of residuals.

Mouth-bar deposition also affects channel width in the downstream part of river-dominated deltas (Fig. 6.4A, 6.5B, 6.6B), as noted by (Olariu and Bhattacharya, 2006). Subaqueous mouth-bar deposition triggers a drop in transport capacity due to jet expansion and flow deceleration, hence producing relatively wider distributary channels than the upstream part. Upstream of any influence of marine energy, channel width is directly related to the scale of the supplying river system (Fig. 6.4A,C, 6.5A,E, 6.6A,E). Longshore wave energy and sediment redistribution does not significantly affect the distributary channel width in wave-dominated deltas (Fig. 6.4C), thus river discharge retains a significant influence, and a statistically significant width-discharge scaling relationship is found (Fig. 6.6E). Power law relationships between W_{med} and Q_2 produced here do not allow prediction of the

discharge/paleodischarge value of a single distributary channel but enable calculation of the total riverine discharge that contributes sediment to builds the delta plain. These results imply that the principles of hydraulic geometry are applicable to river- and wave-dominated deltas but not to tide-dominated deltas. Since the slope tests show significant difference between upstream-downstream and between each delta type to the global w-Q_2 scaling, upstream-downstream and global scaling produced in this study could not be used interchangeably.

6.3.4. Testing width-discharge scaling relationships on a rock record case study

Description: In total, 13 measured distributary channels were measured at locations across the delta identified in the lower Mesa Rica Formation (Fig. 6.7A; Table 6.1). No significant changes occur in channel widths downstream (i.e. Wilcoxon test $p > 0.05$, variance test $p > 0.05$). The whole sample shows a bimodal distribution (Fig. 6.7B). As the proximal zone contains only one measurement, which is from a trunk channel, we can neglect this zone because it is part of the fluvial system and not a part of the delta plain. Consequently, we use the distributary channel widths measured from the transitional (N=5) and the distal zones (N=7) which show skewed distributions (Fig. 6.7B). Applying the bootstrap method on dimensionless distributary channel widths measured on the transitional and distal parts produced low standard error (S_{w*} ~0.13-0.18) from 1000 bootstrap replicates (B) (Fig. 6.7C). The standard error remains low (~0.18) when using only the seven measurements from the lower Mesa Rica (Fig. 6.7C).

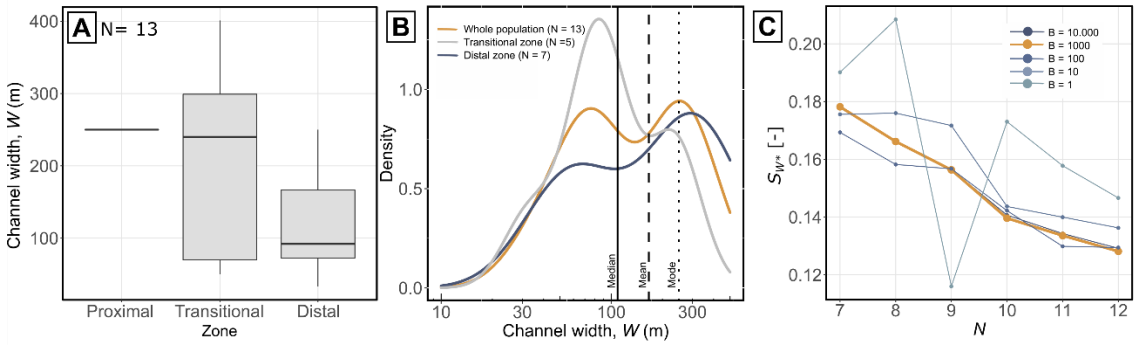

Figure 6.7 Width measurement from the lower Mesa Rica and the bootstrapping results. A: Distribution of 13 measured channel widths from the lower Mesa Rica, grouped by geographical zone across the delta plain. B: Density plot of the 13 measured channel widths: whole population (dark yellow); transitional zone (grey); and, distal zone (dark blue). Median, mean, and mode values (continuous, dashed and dotted vertical lines, respectively) are calculated from the combined transitional and distal data (N=12), excluding the single width measurement from the proximal zone. C: Standard error of dimensionless width (S_{W*}) versus number of samples (N) of the 12 measured channel widths from the lower Mesa Rica.

Interpretation: The delta front sandstone bodies of the lower Mesa Rica are interpreted to be deposits from a river-dominated setting (van Yperen et al., 2019). The down-dip decreasing values of measured distributary channel widths are similar to downstream trends in channel width from upstream parts of modern river-dominated deltas (Fig. 6.4A). To calculate paleodischarge from the distributary channels of the lower Mesa Rica, the median channel width of 12 measured distributary channel widths, 109 m, was input to the hydraulic geometry equation obtained above for the upstream part of river-dominated deltas, $Q_2 = 5.8w^{1.11}$ (Fig. 6.6A) giving $Q_2 = 1010 \pm 100$ m^3/s (i.e. ± showing error propagation from upstream part of river-dominated delta regression line and measured channel widths from Lower Mesa Rica Formation). The Fulcrum method, based on trunk channel deposits, produces a range of $Q_2 = 1085\text{-}1392$ m^3/s (see Supporting Information for details). These values overlap, although the central estimate that we obtained is 10% lower than from the Fulcrum method.

6.4. Discussion

6.4.1. Down-dip changes in distributary channel width in modern and ancient deltas

Modern deltas perspective.---From 4459 measured channel widths across different delta types in various climate regions, it is shown that marine processes (waves, tides, longshore currents) influence the distributary channel widths differently according to the type of delta. In river-dominated deltas, the data consistently show that channel width decreases down-dip before a sharp increase at the shoreline due to mouth-bar deposition (Fig. 6.4A). Olariu and Bhattacharya (2006) provide a similar case study from the Trovimovskaya River, a distributary channel from the river-dominated Lena delta. In tide-dominated deltas, tides lead to increased channel widths up to around half of the distance from the shoreline to the delta apex, consistent with observations made for several geometrical properties (channel curvature, width/depth ratio, bed level, bifurcation order) in the Kapuas, Mahakam and Mekong modern deltas (Sassi et al., 2012; Kästner et al., 2017; Gugliotta et al., 2019). Longshore currents in wave-dominated deltas lead to lateral sediment redistribution parallel to the shoreline and formation of a cuspate geometry, rather than in the down-dip direction. However, these marine processes do not produce statistically significant down-dip change of channel widths in wave-dominated deltas. Understanding the boundaries between upstream and downstream sections across different delta types is imperative in applying the

hydraulic geometry models we proposed from the modern system. However, finding the upstream-downstream patterns from deep time delta deposits will remain challenging yet interesting to be tested, considering the fact that hydraulic geometry behaves significantly different ($p < 0.05$) in each delta type.

Ancient delta perspective.---The study has demonstrated both the overall controls over channel width and down-dip patterns of distributary channel widths from modern systems and how this information can be used in interpreting ancient systems. Limited exposure often prevents the collection of large numbers of channel width measurements. The 4459 measurements from modern distributary channels allow us to simulate the consequences of sampling limited numbers of distributary channel widths in the rock record. Using bootstrapping, we simulate standard error distributions that may be expected when limited numbers of channel widths are able to be measured from outcrops. If it is possible to identify the relative down-delta position of measurements, specific width-discharge relationships are available and the uncertainties in estimating discharge can be determined. As well as quantifying uncertainty, these results can be used in field work planning by enabling dynamic estimation of the number of samples required as data are gathered.

The example from the lower Mesa Rica provides an example of how the down-dip pattern of distributary channel widths could be recognized from the rock record and compared with modern systems. By having the down-dip pattern, the same bootstrapping method to reduce the number of samples could produce a range of standard error values that could be expected from the rock record (Fig. 6.7C). By recognizing the down-dip pattern along with the context of the depositional setting through the sedimentary structure and facies distribution, upstream part of river-dominated delta was then used to estimate the paleodischarge value from this formation due to their similar down-dip patterns. The other scaling relationships proposed in this study can be applied to deltaic outcrops that have evidence for different dominant energies (e.g. wave- or tide-dominated deltas).

Standard error distribution of deltas distributary channel widths.---Fig. 6.5 shows the relationships between number of measured distributary channel widths and the mean standard error using bootstrapping method. In river- and wave-dominated deltas, low standard errors of dimensionless width occur (Fig. 6.5A,B,E). These low errors imply that reliable estimates of median channel width (i.e. depends on the aims of the study) can be obtained from a small number of measurements. However, for tide-dominated deltas it is

challenging to produce reliable width estimates that can be related to input river discharge due to the significant influence of tidal energy on channel form. Even with 30 data points in the downstream part of tide-dominated deltas, the standard error of dimensionless width remains high (S_{w*}>1). Thus, caution should be taken when applying tide-dominated delta discharge-width scaling relationship from either the modern system or the rock records.

Channel width distributions across all delta types and climate regions are skewed, implying that mean distributary channel width may not be statistically representative (Fig. 6.5F-K) and that median values are better representative values of channel width. This has implications for the application of other scaling relationships where small sample sizes are available; many such relationships are used including those with catchment area, meander wavelength, channel sinuosity, total river-atmosphere carbon dioxide flux, mean and peak discharge, and sediment transport mode (Leopold and Maddock, 1953; Bridge and Mackey, 1993; Bhatt and Tiwari, 2008; Gleason et al., 2018; Allen and Pavelsky, 2018; Frasson et al., 2019; Dunne and Jerolmack, 2020; Lyster et al., 2021).

6.4.2. Comparing width-discharge relationships with the Fulcrum method

Bankfull discharges estimated from the width-discharge relationships in this study lie within 10% of those obtained using the Fulcrum method, and their uncertainty ranges overlap significantly, suggesting that these approaches are consistent. Our method uses only a single parameter, channel width, whereas the Fulcrum method uses estimates of bankfull channel depth and width, paleoslope, mean bedform height and wavelength (Bridge and Tye, 2000; Leclair and Bridge, 2001; Holbrook and Wanas, 2014; Trampush et al., 2014). As well as relying on a single input parameter, where stratigraphic and/or paleoclimate data are available, our method allows estimates to be tailored to delta type, the along-dip location of the measured widths, and climate zone.

Further data will allow systematic down-dip scaling relationships to be developed for other channel types, such as tidal creeks, and may enable further differentiation of delta types. Similar work has been undertaken in modern estuaries (Diefenderfer et al., 2008; Gisen and Savenije, 2015) and tide-influenced deltas (Sassi et al., 2012). Improved understanding of the system scale is important to further source-to-sink analyses and hence improve volumetric assessment of resource reservoirs, and carbon capture and storage facilities, as well as deducing climate and tectonic forcing and refining paleohydraulic reconstructions

(Montgomery and Gran, 2001; Merritt and Wohl, 2003; Bhattacharya and Tye, 2004; Brardinoni and Hassan, 2006; Wohl and David, 2008; Davidson and Hartley, 2010; Eaton, 2013).

6.4.3. Limitations of applying modern delta scaling relationships to the rock record

We show that distributary channel width (W_{med}) scales with input river bankfull discharge (Q_2) from our global dataset (Fig. 6.6F). However, this study provides empirical evidence of how deltaic width-discharge scaling relationships start to weaken with the increasing influence of marine processes that directly influence hydraulic and sediment processes (Fig. 6.6A-E). Scaling relationships derived from the upstream parts of river-dominated deltas, from which marine influence is largely absent, show strong statistical correlation between median channel width and input river discharge ($R^2 = 0.53$; $p < 0.05$) (Fig. 6.6A). The correlations are weaker ($R^2 = 0.17$; $p < 0.05$) for downstream parts of river dominated deltas and stronger ($R^2 = 0.68$; $p < 0.05$) for wave-dominated deltas and becomes statistically insignificant in the upstream part of tide-dominated deltas ($R^2 = 0.04$; $p > 0.05$), and downstream tide-dominated deltas ($R^2 = 0.01$; $p > 0.05$) (Fig. 6.6A-E). The trend for correlation to decrease with increased marine influence (e.g. tidal, wave or backwater-controlled flow regimes) is anticipated, and existing hydraulic geometry models assume unidirectional river flow (Gleason and Smith, 2014). However, in wave–dominated systems the wave energy appears to have minimal impact on channel widths, and thus significant width-discharge scaling relationships can be obtained (Fig. 6.6E).

Reconstructing water discharge of an ancient fluvial and/or delta system relies on accurate measurement of channel geometry from channel fills (Parker et al., 2007; Hayden et al., 2019). In outcrop or subsurface datasets, it is commonly easier to measure distributary channel depths than widths. However, satellite imageries that we used in this study limit our observation of distributary channel depths. If width-depth empirical relationships from modern river deltas exist, transformation from our width-discharge to depth-discharge could be scaled accordingly by assuming a steady flow and equilibrium depth and slope. Moreoever, several issues influence the accuracy of width measurements from outcrops. The measured channel fill may not be perpendicular to the paleoflow (Holbrook and Wanas, 2014; Bhattacharya et al., 2016) and infill deposits are often incompletely preserved (Bridge and Mackey, 1993; Bridge and Tye, 2000). When the channel fill deposit is incomplete,

width-depth scaling relationships can still be used, albeit they contain substantial uncertainty because channel fill dimensions can differ significantly from formative channel dimensions (Hayden et al., 2019; Greenberg et al., 2021). On the contrary, some the widths of some distributary channel deposits may not represent formative channel width as the channel may have migrated laterally. This is because a distributary channel deposit is the sum product of infilled channel plus lateral migration of the formative channel. Hence, measuring the width from ancient distributary channels needs a careful examination.

The proposed scaling relationships should not be used as a standalone model to interpret the paleodischarge from the rock record. Uncertainties exist in both the field data and the statistical relationships; hence, the results provide discharge ranges based on the propagation of these uncertainties. Additional information should be gathered from outcrops to further constrain the predicted paleodischarge; this may include stratigraphic context, sedimentary structures, grain size, fossil assemblages and vegetation amongst others. As an example, using the scaling relationship for the upstream part of river-dominated deltas (Fig. 6.6A), a median distributary channel width of 300 m gives a discharge range of Q_2 = 3077±12 m^3/s (i.e. ± is from the error propagation produced by regression and distributary channel width of the upstream part of river-dominated deltas). The uncertainty in paleodischarge values is considerably greater in marine-influenced deltas, namely the downstream part of river-dominated deltas or wave-dominated deltas. Thus, the interpretation of paleodischarge requires contextual information that may support or challenge the calculated values.

In order to assess paleodischarge estimated using our approach, we utilize the case study from the lower Mesa Rica. The plain of the lower Mesa Rica delta is approximately 100 km long, measured in river kilometres from the shoreline to the most landward avulsion node (Fig. 6.3). In terms of delta plain size, the lower Mesa Rica is comparable with the modern Brahmani (1800 km^2) and Mahanadi (1700 km^2) deltas, although in terms of average bankfull channel depth (Table S6.1), the smaller Danube (5800 km^2), Ebro (460 km^2) and Mahanadi are better comparisons. The discharge of the lower Mesa Rica is more comparable to total system discharge coming into Ebro, Cauvery, Wax Lake, Sanaga and Rio Sinú deltas (GRDC; Bhattacharya and Tye, 2004). These comparisons indicate that the lower Mesa Rica is comparable with many modern deltas but none of them provides a perfect fit in terms of geometry (delta area, bankfull channel depth) and in input discharge. The number and diversity of potential modern delta analogues for the Mesa Rica Formation illustrates how scaling relationships from modern systems should not be used in isolation.

The difference in widths in river-dominated deltas between their upstream and downstream parts leads to differences in the statistical significance and uncertainty associated with scaling relationships for the two parts. Consequently, the number of measurements required to estimate input discharge to a specified level of uncertainty varies with the location of measurements along the delta. In some well-studied systems this specification of location is possible, potentially alongside information on climate type, and thus the methods shown in this study are applicable. Where context is unknown the scaling relationships provided here should be used with caution.

6.5. Conclusion

Distinct down-dip patterns of dimensionless distributary channel widths are recognized from measurements from 114 modern global river deltas. River- and tide-dominated deltas show significant channel widening at s/L = 0.05 (i.e. near shoreline) and 0.45 (i.e. approximately halfway across the delta plain from the shoreline to the apex), respectively. Mouth bar depositional cycles in river-dominated deltas and tidal energy obstructing unidirectionality of channel currents in tide-dominated deltas are the main cause of these distinct patterns. In contrast, wave-dominated deltas show consistent dimensionless distributary channel width down-dip. Calculation of paleodischarge is based on empirical relationships between median channel width and input river discharge. By bootstrapping the dimensionless distributary channel widths from modern deltas, this study provides estimates of the minimum number of measurements required to estimate median width to a specified standard error. We calculate the minimum number of measurements required to reduce the standard error of dimensionless width to 0.5 as follows (in parentheses): upstream (3) and downstream (30) parts of river-dominated deltas; upstream part of tide-dominated deltas (6); and, wave-dominated deltas (4). The downstream part of tide-dominated deltas produces very high standard error (>1.5) with any number of samples and input discharge cannot be reliably estimated from channels in these locations. Applying the proposed distributary channel width-discharge scaling relationships from modern deltas to the well-studied lower Mesa Rica formation produced a comparable paleodischarge estimate to that from the Fulcrum method. The results from this study improve paleoclimate and tectonic reconstruction, volumetric assessment of hydrocarbon, hydrogen and geothermal reservoirs, in diverse depositional environments. Second, the results enable more detailed paleohydraulics reconstruction across various types of depositional systems in source-to-sink investigations.

Supporting Information

Data bias induced by different data frequency

The semicircular method proposed by Sassi et al. (2012) provides consistent measured channel width frequency along a delta axis. Nonetheless, when being compared to other deltas with different sizes, data frequency becomes less consistent across deltas. This was due to the method centralizes the avulsion length and channel width as the basis of creating the semicircular grid. By having different avulsion length and channel width, each delta will have its unique semicircular grid sizes.

For example, if a delta has channel width at delta apex as 100 meter wide and avulsion length as 100-kilometer-long, the *s/L* could have the range of values from 0-1 with each semicircular will have a radius distance from the apex for every *s/L* = 0.01 that will produce 100 width measurement points for this delta. But imagine a delta with 50 meter wide at the delta apex with 10-kilometer-long avulsion length. The semicircular grid will have a radius distance from the apex for every *s/L* = 0.05 that will produce 20 width measurement points for this delta. For these two deltas, the data frequency will be 100 and 20, consecutively.

To mitigate this, different data binning frequencies were deployed to see their impacts on inducing the bias in defining the upstream and downstream channel width pattern. The original data (upper row in Fig. S6.1) show too frequent boxplots with high variance. The along delta axis data that are too frequent makes them difficult to see the changing pattern of channel width from upstream to downstream. By having 10% data binning frequency from its original data, the upstream to downstream profile shows less variance in channel width distribution, making it easier to see the changes of channel width along the axis (middle row in Fig. S6.1). In contrast, reducing the data frequency too much (i.e. 20% from original data) may lead to the data scarcity, obscuring the pattern between the upstream and downstream channel widths (lowermost row in Fig. S6.1).

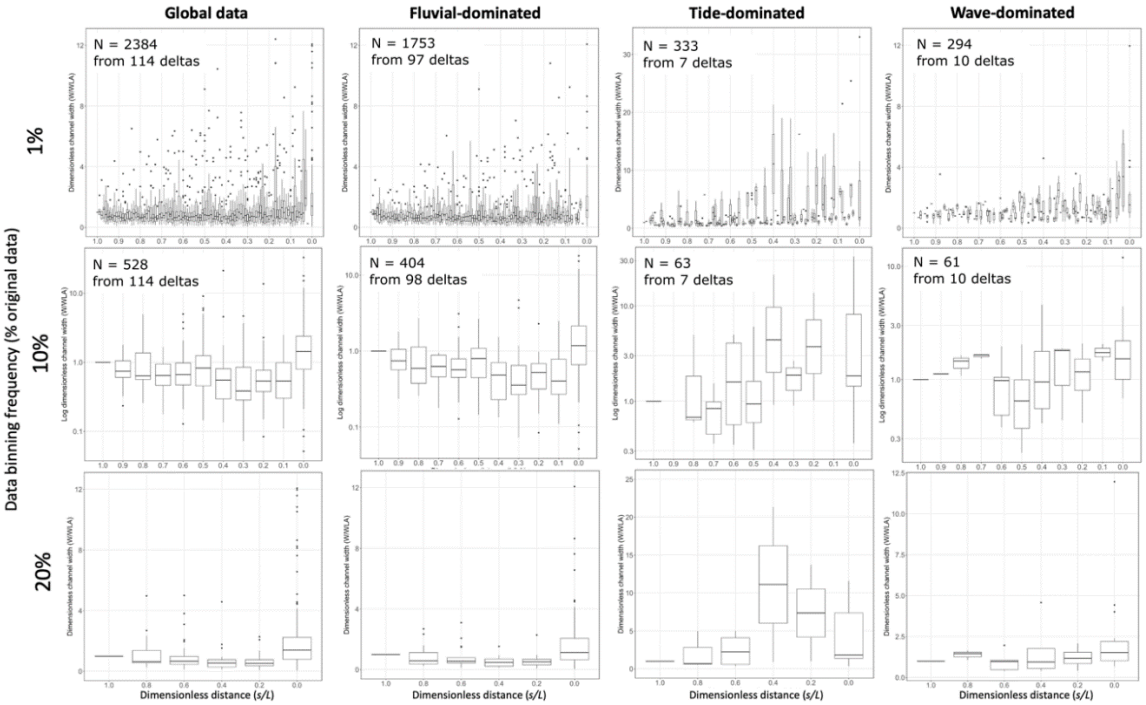

Figure S6.1 Different data binning frequency across global dataset (first column), fluvial-dominated (second column), tide-dominated (third column) and wave-dominated deltas (fourth column). The 10% data binning frequency were chosen as the basis of upstream-downstream channel width classification due to its less noise/variance along the delta axis in comparison to 1% and 20% data binning frequency.

Lower Mesa Rica paleodischarge estimation using the Fulcrum method

The Fulcrum method is originally proposed by Holbrook & Wanas (2014) to estimate basin-fill water and sediment volumes over geologic time. The main assumption used is that the water and sediment mass collected and transported by the rivers from a catchment should be in balance with the mass deposited in the basin. Also, the Fulcrum method does not require assumptions about the source catchment area and longitudinal trends (e.g. grain size and geometry change) within the fluvial system (Holbrook & Wanas, 2014) as in other methods (e.g. BQART; Syvitski & Milliman, 2007; trunk-based model; Bhattacharya et al., 2016; regional hydraulic geometry curves; Davidson & North, 2009). The Fulcrum method also limits the use of single paleochannel (i.e. trunk channel) that may be particularly difficult to be adapted to distributary system like in river deltas (Holbrook & Wanas, 2014). The compilation of previously published data is used in this study to calculate the bankfull paleodischarge (*Qbf* or Q_2 in this study) of the lower Mesa Rica trunk channel using the Fulcrum method:

$$Q_b = \sqrt{\frac{g {h_c}^3 S {W_b}^2}{C_f}} \quad \text{(S6.1)}$$

And

$$C_f^{-\frac{1}{2}} = 8.32\left(\frac{h_c^{\,2}}{k_s}\right) \quad \text{(S6.2)}$$

$$k_s = 3D_{90} + 1.1\Delta(1 - e^{-25\psi}) \quad \text{(S6.3)}$$

$$\Delta = \frac{h_c}{8} \quad \text{(S6.4)}$$

$$\psi = \frac{\Delta}{\lambda} \quad \text{(S6.5)}$$

$$\lambda = 7.3h_c \quad \text{(S6.6)}$$

With

g = gravitational acceleration (m^2/s) = 9.8 m^2/s

h_c = average bankfull channel depth (m)

S = slope or paleoslope (dimensionless)

W_b = bankfull channel width (m)

C_f = dimensionless Chezy friction coefficient

Δ = mean bedform height (m)

λ = bedform wavelength

Input values are listed in Table S6.1). The calculation for paleoslope is using an empirical equation S6.7 (Holbrook & Wanas, 2014; Trampush et al., 2014):

$$\tau^*_{b50} = \frac{h_c S}{R D_{50}} \quad \text{(S6.7)}$$

With

τ^*_{b50} = bankfull Shields number for dimensionless bed shear stress; is assumed to be 1.86 (Holbrook & Wanas, 2014)

h_c = average bankfull channel depth (m)

S = paleoslope

R = submerged density in water of standard density; assuming the sediment are quartz, the R becomes 1.65 g/cm^3

D_{50} = average grainsize for the lowermost portion of a channel; represents the coarsest material transported as bedload.

The bankfull paleodischarge values for the trunk channel (Q_b = 1085-1392 m^3/s) is in the same order of magnitude with the bankfull paleodischarge values estimated based on distributary channels (i.e. 1010 m^3/s) using the models proposed in this study.

Table S6.1 Estimates of paleohydrologic parameters and discharge from the lower Mesa Rica Sandstone. h_c, W_b and D_{50} from Van Yperen et al. (2021).

Channel story name	Average bankfull channel depth, h_c (m)	Bankfull channel width, W_b (m)	D_{90} (mm)	D_{50} (mm)	Δ (m)	λ	S	k_s	Dimensionless Chezzy friction coefficient (C_f)	Bankfull paleodischarge, Q_b (m^3/s)
Corazon Hill	5.5	200	0.48	0.28	0.6875	40.15	0.00015624	0.26	0.005	1392
Canadian River	5.5	200	0.25	0.17	0.6875	40.15	0.00009486	0.26	0.005	1085
CR C15A	5.5	200	0.44	0.23	0.6875	40.15	0.00012834	0.26	0.005	1262
Red Tongue Mesa	5.5	200	0.34	0.22	0.6875	40.15	0.00012276	0.26	0.005	1235

Chapter 7 - Synthesis and further works

In this chapter, results from Chapters 3, 4, 5 and 6 are synthesised by addressing the thesis' research questions (section 1.4). Discussion is structured around each research question, along with an evaluation and identification of prospects for future work.

7.1. Discussion

RQ1. Can a globally consistent avulsion-backwater length scaling relationship be derived for river deltas?

Motivated by the importance of the backwater length (L_b) in controlling the location of delta avulsion nodes (Paola and Mohrig, 1996; Chatanantavet et al., 2012; Ganti et al., 2016a; Chadwick et al., 2019), backwater – avulsion length scaling was re-assessed using a larger global dataset. Avulsion-backwater length (L_a-L_b) scaling is less consistent across this set of 114 deltas. This is consistent with the finding from Hartley et al. (2017), albeit their analysis used only 15 sites. Rather than avulsion length scaling with backwater length, it was found that avulsion-slope break length (L_a-L_s) (R^2 = 63%, RMSE = 0.36, p = 2.2 x 10^{-14}) scaling is statistically more significant across this new global dataset (Fig. 3.3c).

The stronger global L_a-L_s scaling relationship suggests that the slope break is the predominant driver of channel response in the upstream part of a delta, rather than the backwater effect (L_a-L_b relationship). In relation to the delta building process, mouth-bar deposition should dominate the most distal part of a delta due to input sediment being deposited in a relatively static water body (Olariu and Bhattacharya, 2006). Upstream parts of deltas will be dominated by partial avulsion or crevasse bifurcation (Kleinhans et al., 2013), or by avulsion by incision (Slingerland and Smith, 2004) induced by in-channel aggradation due to the slope break and/or the backwater effect (Slingerland and Smith, 2004; Kleinhans et al., 2013). In-channel aggradation could then trigger avulsion in the upstream region of a delta, maintaining the scaling relationship between L_a and L_s. Hence the avulsion nodes, the most upstream bifurcation nodes of deltas, are proposed to be related to the process of in-channel aggradation due to the change in slope and may not be directly related to bifurcation or backwater processes downstream.

The occurrence of slope breaks along the river longitudinal profiles could be controlled by a range of interacting factors including grain size transitions and associated changes in Shields' stress (Dong et al., 2019; Dingle et al., 2021), geological controls (e.g. lithology; Ganti et al., 2014; Hartley et al., 2017), and the nature of the overbank material (e.g. cohesive vs non-cohesive; Valenza et al., 2020) that are not covered in this study. However, the slope break controls the initiation of the delta building process by its consistent scaling with the length measured from the shoreline to its avulsion node. The slope break-avulsion length scaling found from the modern system motivated the building of a conceptual model of how a river delta grows in relation to the location of the slope break. In this model, bedslope- and backwater-mediated zones of river deltas are identified, as explained in Chapter 3. Using this classification, a delta channel may behave differently depending on where it is located on delta plain. This conceptual model is corroborated by a recent numerical model by Ratliff et al. (2021) who found consistent slope break-avulsion length scaling even under several scenarios of sea-level rise.

RQ2. What are the implications of the scaling relationships found from modern river deltas for our understanding of the growth and internal dynamics of river deltas?

The finding of a consistent scaling relationship from the global river delta dataset suggests a shift in our current understanding of how a river delta naturally builds and evolves. Using the importance of the slope break in controlling the growth of river deltas as a starting point, a suite of numerical experiments was used to test if different slope gradients located upstream of the slope break will control how a river delta grows (Chapter 4). Using six scenarios, each having a different upstream slope value, the experiments show that delta topset slope, which evolves in response to upstream sediment input, serves as the first-order control of autogenic avulsion in river deltas. Furthermore, by correlating the delta topset slope and avulsion timescale from the model with natural deltas, consistent agreement is found, justifying the reliability of the model built in this study.

The hypothesis based on modern systems that river deltas can be divided into distinct bedslope- and backwater-mediated zones is also coherent with the results from the numerical river deltas (Fig. 3.6e, Fig. 4.5a-b). This division separates the timescales of avulsion from those of bifurcation due to different processes influencing avulsion and bifurcation phenomena. Avulsion involves changing locus of sediment deposition by breaching or overtopping the riverbanks, while bifurcation is a channel splitting around the mouth bar due

to flow deceleration when entering a relatively still body of water. Avulsion occurs as a consequence of in-channel sediment aggradation (Kleinhans et al., 2013) and the rate of this aggradation is a function of the topset slope as this controls the rate at which sediment is transported onto the delta plain. The steeper the topset slope, the faster the sediment is transported due to a higher transport capacity. Conversely, the gentler the topset slope, the lower the transport capacity hence the slower sediment is transported or deposited as long as the sediment transport is at equilibrium. Equilibrium here implies that transport is at the full capacity of the flow and is not supply-limited. At equilibrium, similar volumes of sediment were transported in each model scenario due to the model adjusting its sediment load to fully match its channel transport capacity. The similar volumes of sediment in each scenario are shown by the similar deltas size produced under all scenarios (Fig. 4.2). Sediment load adjustment under an equilibrium state may result in a complex morphological adjustment such as slope or channel width adjustment (Lane, 1954). Since the width of the channel feeding the river delta in my model is maintained constant (Fig. 4.1c), slope adjustment can be expected as the consequence of an equilibrium flow.

In contrast to avulsion, bifurcation occurs as a consequence of mouth bar deposition, and hence water depth and sediment load (Edmonds & Slingerland, 2007). When the sediment deposited offshore has reached ~40% of the total water depth in the supplying channel, a distributary channel is formed by the flow bifurcating around the mouth bar. Hence, this bifurcation process is independent of the topset slope values as shown in the modelling (Fig. 4.5d). Although avulsion and bifurcation are independent, they are simultaneous processes due to avulsion and bifurcation depend on the delivery of sediment from upstream (and hence on the size of channels created by avulsion), which is shown by the overlap of their timescales. The numerical modelling thus contributes to our understanding of how avulsion and bifurcation interact during the delta building process.

Being motivated to investigate what factors control the consistent deltaic stratigraphy under avulsion-bifurcation interaction discussed in Chapter 4, additional numerical experiments were undertaken to assess the effect of pulses of river discharge, in and out of equilibrium with sediment input, on delta stratigraphy. Physically, the flow and sediment input are not at equilibrium when a sediment-laden channel feeding a river delta contains sediment volume that does not match its transport capacity, so that it erodes or aggrades (Kleinhans et al., 2008). In contrast, an equilibrium flow contains sediment load to fully match its channel transport capacity as in the model explained in Chapter 4. The non-equilibrium

model run had pulses of high flow and low flow alternately, each lasting for one day, and non-equilibrium sediment input. As in the earlier experiments, the high flow is 1050 m^3/s, the representative value of the global river delta discharge (Edmonds & Slingerland, 2010; Caldwell & Edmonds, 2014). The non-equilibrium input sediment load is four times that of the control run, similar to Toby et al's. (2019) simulations. The low flow is defined as 6 m^3/s, the P50 (median) value of the global river delta discharge dataset (Nienhuis et al., 2020). Sediment load is 25% that of the control run. The equilibrium runs have the same alternating high flow and low flow as the unstable runs, but the input sediment load is at equilibrium, where the sediment load matches the flow transport capacity. The equilibrium and non-equilibrium experiments were compared to the control experiment that has constant discharge and equilibrium state used in Chapter 4 (top panel of Fig. 7.1). The control, equilibrium and non-equilibrium upstream boundary conditions were used for three upstream slopes, as in scenarios US0.3, US6 and US8.1, defined here as 'gentle, medium, and steep' to cover the range of upstream slopes found in modern river deltas.

Non-equilibrium flow significantly affects both the delta size and stratigraphy by creating a larger delta plain and thicker deposit in comparison with both the equilibrium and control runs (Fig. 7.1a-i). However, different upstream slopes did not significantly affect the delta plain and stratigraphy produced in the experiments as shown by consistent stratigraphy and similar delta plain sizes. Qualitative observations of the distributary channels produced by the non-equilibrium runs also show that these runs produced more sparse distributary channels laterally (Fig. 7.1c, f, i) and more overbank deposition on the delta plain (i.e. sediment deposited above the sea level) from the stratigraphy shown in Fig. 7.1c, f, i in comparison to the control and stable experiments.

Differences between experiments were quantified by calculating the delta island growth rates, channel dispersion rates and hypsometric curves for each experiment (Fig. 7.2) (see the Chapter 2.2.3 or Appendix A.2. for details of the method). Under the same 17 days simulation time, non-equilibrium experiments have the fastest island growth rates, and hence produce larger delta plains (Fig. 7.2a) than either the stable or control experiments. However, the difference of delta island growth rate between the three upstream slopes for the non-equilibrium case is not statistically significant ($p > 0.05$; slope test) (Fig. 7.2a). Under the equilibrium and control runs, different upstream slopes produce different total island growth rates. In contrast, in the non-equilibrium runs, different upstream slopes produce similar total island growth rates. Although the precise mechanism causing this behaviour is unclear, these

results may imply that the delta island growth rates are affected by the upstream slopes only if the flow and sediment input are in equilibrium as is the case in both the equilibrium and control experiments.

Hypsometric (area-altitude) analysis (Strahler, 1952) is used to quantify the distinct stratigraphy produced by each run (Fig. 7.2c, d). The non-equilibrium experiments consistently produce steeper hypsometric curves in comparison to the equilibrium and control experiments (Fig. 7.2d). Consistent with the qualitative observation of the delta plains from Fig. 7.1, non-equilibrium runs consistently produce larger and thicker delta plains. A two-way ANOVA test on the elevations produced by the control, equilibrium, and non-equilibrium runs shows $p = 3.87 \times 10^{-8}$, indicating that the nature of the flow and/or overloading the input with sediment can significantly affect the size and stratigraphy of the delta plain. However, two-way ANOVA on elevation produced by different upstream slopes shows $p = 0.95$, suggesting that the gradient upstream of the delta plain does not affect delta plain size and stratigraphy.

These numerical results suggest that nature of the flow and the balance between input sediment load and transport capacity significantly controls the growth of river deltas. Non-equilibrium overloading of the input flow with sediment produces a larger and thicker delta plain. This is because in these conditions, more sediment is transferred into the delta plain through distributary channels than in the control and equilibrium runs. Sediment loads in the control and equilibrium experiments are smaller because the sediment load entering the model is adapted to the local flow conditions to match its transport capacity.

Since distributary channels carry more sediment load in the non-equilibrium runs, the distributary channel backfilling process could occur faster in these conditions while producing thicker and larger delta plain deposits at the same time (Fig. 7.1, 7.2a, c, d). Faster backfilling processes reduce the accommodation of distributary channels downstream since sediment distributed faster into the offshore. Faster backfilling of distributary channels will also trigger more frequent avulsion upstream since avulsion frequency inversely correlates with sediment load (Chadwick et al., 2020). Avulsions are then clustered at the location where there was an imposed abrupt increase in channel width, which occurs at the end of the confined inlet in our model (Ratliff et al., 2021) or at a decrease in floodplain slope (Hartley et al., 2017; Prasojo et al., 2022). The higher frequency of avulsion in river deltas will then

induce significantly larger channel dispersion in the non-equilibrium experiments than in the control and equilibrium experiments (Fig. 7.2b).

The simulations show how the state of the sediment-laden flow feeding a river delta serves as an important control on the growth of the numerical river deltas. These preliminary results have implications for interpreting palaeoclimate from delta plain stratigraphy. In contrast to sequence stratigraphy concept that relies on the influence of base-level cycle to its sedimentary products, I show here that without any base-level changes, different stratigraphy and shoreline positions (Fig. 7.1) can happen internally due to a non-equilibrium flow state. The results also raise questions regarding the impact of non-equilibrium sediment inputs on autogenic signal preservation, and how the current trend of increasing likelihood of extreme flood events (Slater et al., 2021) may influence delta growth through non-equilibrium flow feeding into delta plains. Finally, there are implications for how the non-equilibrium flow framework could be taken into account in interpreting recent numerical, physical and field-based studies of delta morphodynamics.

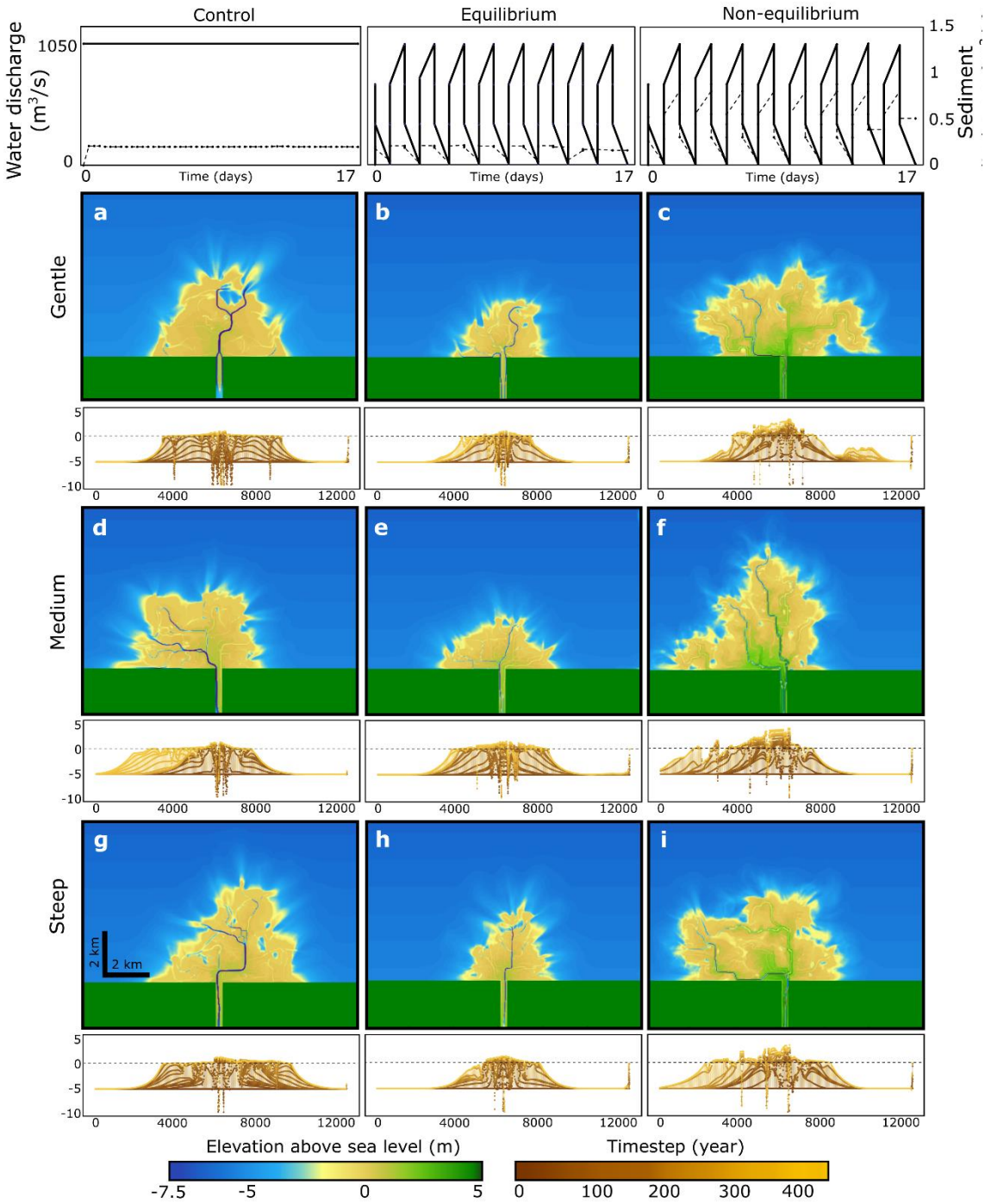

Figure 7.1 Plan view and consecutive stratigraphy of synthetic river deltas produced under control, equilibrium and non-equilibrium runs at the latest simulation timestep. Top row figures showing the discharge (continuous line) and sediment flux (dashed lines) for each experiment.

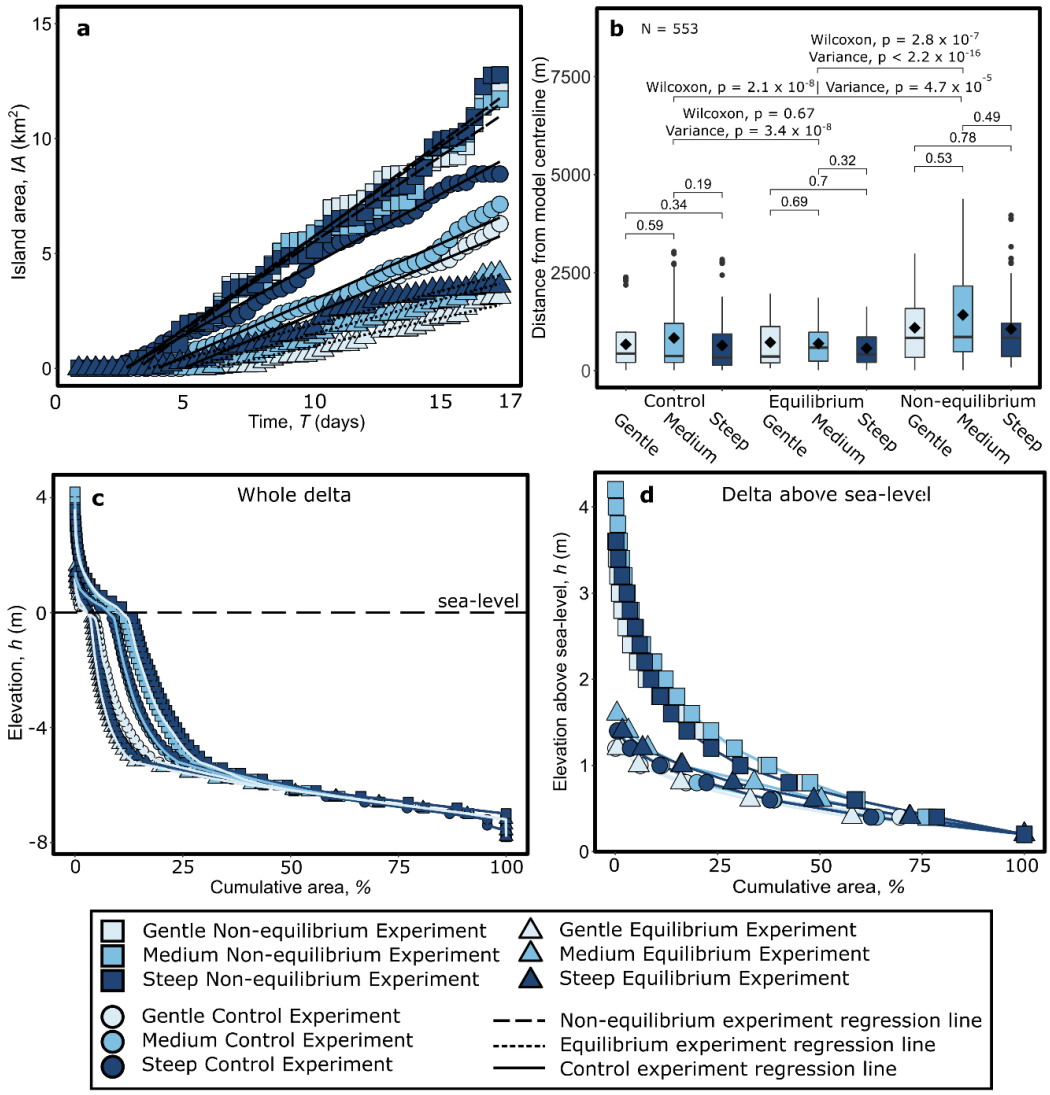

Figure 7.2 Results produced by control, equilibrium, and non-equlibrium experiments: a) delta island areas; b) the distribution of channel dispersion distance from the delta axis represented as boxplots along with the tests conducted to compare between the control, equilibrium and non-equlibrium experiments; c) hypsometric plots of delta area from all experiments; and d) hypsometric plots of the delta areas above sea-level from all experiments. Slope tests between the regression lines on Fig. 7.2a shows $p > 0.05$ while two-way ANOVA between experiments shown on Fig. 7.2b produces $p < 0.05$.

RQ3. To what extent is the scaling relationship found from the modern river deltas applicable to the deltaic deposit?

By measuring 4459 distributary channel widths from 114 river deltas (https://doi.org/10.6084/m9.figshare.19964549.v4) in parallel with their catchment areas and discharges, consistent scaling relationships were found between distributary channel width, catchment area and discharge across five climate regions. These scaling relationships from modern deltas were then applied to deltaic deposits to estimate palaeodischarges for a selection of ancient deltas. Using palaeodischarge values calculated independently from the literature using the BQART and Fulcrum methods, the palaeodischarge estimates calculated

using the new scaling relationships from modern deltas yield comparable results to the previous estimates. These results show how scaling based on hydraulic geometry is able to predict upstream water discharges into deltas not only in modern systems but also in deep geological time rock deposits.

The river deltas in the data set developed in this thesis contains data from channels that do not have a purely unidirectional down-delta river current. From the global dataset of distributary channel widths, 'upstream' and 'downstream' parts of deltas were separated based on the presence of a significant change of channel width that occurs in some systems due to backwater effects, waves or tidal influences. The separation relied on identifying a statistically significant change of distributary channel widths between the 'upstream' and 'downstream' parts of a delta. This approach, which takes into account the influence of non-unidirectionality of river flows in the distal (downstream) parts of river deltas due the wave and tidal effects, shows that width-discharge scaling is reliable for both river- and wave-dominated deltas. However, tide-dominated deltas show a weak channel width-discharge scaling relationship. The occurrence of any forcing that causes significant bi-directional flow limits application of hydraulic geometry scaling to river deltas especially in tide-dominated deltas (Gleason, 2015a). In wave-dominated delta, waves have less effect on flow, but rather eroding and transporting sediment in longshore direction.

The 4459 measurements of distributary channel widths from 114 modern river deltas obtained in this study also enable estimation of the standard errors that are associated with limited numbers of available measurements when applying the hydraulic geometry scaling models to the rock record. Using a bootstrap method, the minimum number of samples needed to apply the hydraulic geometry scaling models were estimated (Section 6.3.2; Fig. 6.5). Curves of the standard error versus the number of available samples were presented for river-, wave- and tide-dominated deltas. These relationships enable simulation of how the limited number of samples available in many studies may affect the errors in palaeodischarge estimates. These statistical analyses will be useful for sedimentologists working with deltaic deposits in the rock record.

Data uncertainty in geologic record is often substantial. Hence, I believe that an acknowledgement of standard error values from any data, especially from the rock record, is crucial. The bootstrapping method I presented in Chapter 6 could potentially be useful in estimating standard error values associated with palaeoflow, palaeoclimate or

palaeogeographic reconstruction from the rock record. The same approach in building scaling relationships by collecting global morphometric dataset such as from Global River Width from Landsat (GRWL) (Allen and Pavelsky, 2018) or from the river discharge from Landsat dataset (RODEO) recently produced by Riggs et al. (2022) could potentially enrich palaeodischarge estimates in more diverse systems such as tidal creek, estuary, braided river, etc.

7.2. Contributions of this research

In this thesis, a range of morphometric scaling relationships were developed from 114 modern river deltas. The contribution of these new scaling relationships from modern deltas, synthetic numerical river deltas, and from calculations using a sample of ancient systems, are as follows:

1. Morphometric properties of 114 modern river deltas across five climate regions were investigated for the first time (N = 4459) in this thesis. Channel width, avulsion, backwater, valley-exit-to-shoreline and slope break lengths were investigated from the modern river deltas along with identification of their valley types. Along with previously known scaling relationships, a statistically stronger and novel scaling relationship is proposed between the slope break and avulsion length. This new slope break-avulsion length relationship is consistent across all climate regions and all valley types. The location of the slope break along the river longitudinal transect also defines the location of the first avulsion of river delta. This finding implies that during river delta growth, there are two types of avulsions that come into play in a river delta. The first avulsion point relates to the location of the slope break point, but the avulsion points located downstream of the first avulsion point may be correlated to a backwater parameter (Ganti et al., 2014). This discovery triggers us to rethink what we know about the mechanism of how a river delta grows naturally and to reassess the inland and coastal flood risk associated with the mobility of an avulsion node.

2. Numerically modelled synthetic river deltas from six different scenarios were analysed. Analyses of avulsion timescale, bifurcation timescale and island size distribution of every timestep produced ~430 data points. Analysing these morphometric parameters for each timestep allows a novel, more detailed,

observation of avulsion-bifurcation interaction and how delta islands grow across ~400 years of simulated time. It is observed in this study that avulsion and bifurcation are independent but simultaneous processes occurring in river deltas. Different sedimentary processes are involved during avulsion and bifurcation, hence producing significantly different timescales for these two morphological adjustments. However, by observing changes during each timestep during the delta growth process, avulsion and bifurcation are found to sometimes occur at the same time in different parts of the delta. Observation island growth shows linear expansion across all scenarios. Also, by investigating delta growth in the absence of allogenic forcing (e.g. waves, tides, sea-level rise), autogenic morphological adjustment of river deltas was observed in the model. This observation fills the gap in our understanding of autogenic behaviour of river deltas, from which a better understanding of autogenic-allogenic interactions may be achieved in the future studies.

3. Novel rock-record focused scaling relationships were produced in this study by using the results from modern river deltas. These hydraulic geometry based scaling relationships developed in this study provide a novel, simple method for estimating palaeodischarge of the supplying river system from deltaic deposits by using only the channel width found from sedimentary deposits. These novel scaling relationships produce results of the same order of magnitude as the parameter-heavy palaeodischarge estimation methods (e.g. Fulcrum, BQART) that are commonly in use. The particular merit of these new scaling relationships is the ease of measuring the input parameters, most importantly channel width, in the rock record. Different equations are proposed for global climate regions, allowing the equations' gradients to change, reflecting the role of soils or vegetation in controlling runoff which will vary with catchment scale. Hence, the climate-classified models proposed in this study make reliable palaeodischarge estimation more straightforward if the palaeoclimate is able to be deduced from the rock record. Bootstrapping the dataset produce the minimum number of data points (width measurements) needed to obtain estimates with different statistical uncertainties, that will enable sedimentologists to quantify uncertainties in predictions when dealing with limited deposit exposures. Similar 'reverse bootstrapping' methods can potentially be useful in other geological contexts to assess the impact of a limited number of samples on results (Rice and Church, 1996).

7.3. Evaluation and future work

7.3.1. Evaluation

When making interpretations from the results and discussions presented above, several issues require consideration:

1. In this study, the development of hydraulic geometry-based scaling models was based on the manual measurement of distributary channel widths across 114 river deltas from Landsat imageries at specific times that are then correlated with the bankfull flow in the river. Use of the Global River Width from Landsat (GRWL) database, with 64 million data points could have produced more accurate hydraulic geometry models because of the higher data frequency (Allen & Pavelsky, 2018). Further, the morphometric measurements could be related directly to discharge at the time of the Landsat image acquisition.

2. The scaling relationships presented in this study use the river discharge from gauges located as close as possible to the deltas' apexes. The discharge values from these gauges are assumed to be the sole source of discharge flowing into the delta plain. However, river gauges located exactly at the delta apexes could improve the scaling relationships produced here. This issue may be resolved by improved discharge estimation from river width, such as the river discharge from Landsat dataset (RODEO) recently produced by Riggs et al. (2022).

3. The application of hydraulic geometry-based scaling models produced in this study is currently limited to Cretaceous outcrops due to the paucity of palaeodischarge estimation in other geological periods from the literature. However, if such data for other geological times is available, the reliability of the models proposed in this study could be tested in older/younger rocks, triggering further discussion of the reliability of using hydro-geomorphic conditions from modern deltas to represent palaeohydrological conditions under particular conditions in the past.

7.3.2. Future work

To improve our understanding of morphometric scaling relationships of channels in global river deltas, a list of future work is suggested:

1. In this chapter, the role of equilibrium and non-equilibrium sediment loads on river delta morphology has been introduced. Non-equilibrium boundary conditions significantly alter the delta plain growth rate, distributary channel dispersion distance and also the elevation of the delta plain, all of which will potentially affect the delta's morphometric scaling relationships. Moreover, different upstream slopes do not significantly affect the river delta morphology if the flow is not at equilibrium with the sediment input rate. The upstream slopes only affect the river deltas growth rates if the flow and sediment input are in equilibrium. Despite these quantitative observations from numerical simulations, more mechanistic explanations are required, and a wider range of non-equilibrium flow scenarios should be conducted to understand their impacts on delta morphology. As an example, sediment starvation, that can also cause a non-equilibrium flow, is consistent with a more rapid delta shoreline erosion (Anthony et al., 2015). Future work should also cover the impact of the non-equilibrium sediment input on delta avulsion and bifurcation frequencies and locations, due to the importance of these processes for flood risk, as explained in Chapter 4. Finally, further field observations from modern and ancient river deltas should be made to test and evaluate the role of non-equilibrium sediment input on delta morphology.

2. Chapter 4 covers the role of autogenic forcing on interactions between avulsion and bifurcation interaction. However, as presented by many other studies, allogenic forcing (e.g. sea-level rise, tides, waves) also plays an important role in affecting the timescale of avulsion and bifurcation in river deltas. Consequently, the effect of allogenic and autogenic (e.g. upstream slopes) drivers on avulsion and bifurcation timescales, stratigraphy and delta size should be conducted in future studies due to the importance of these parameters for the sustainability of river deltas. To represent the behaviour of natural river delta morphodynamics realistically, future modelling work should use realistic magnitudes of allogenic forcing and cover all delta types (Nienhuis et al., 2020). This work will contribute to a theoretical basis for morphodynamic responses of river deltas facing various combinations of allogenic and autogenic forcing. This effort is imperative since avulsion and bifurcation present hazard to communities living close to river delta or delta coast.

Chapter 8 - Conclusion

In this thesis, I explored the possibility of adopting scaling relationships originally developed for quantitative watershed analysis, initially proposed by Strahler (1957), to river delta systems. Under the assumption that similarity across systems of various sizes exists in nature, I adopted this concept to solve disparity in understanding scaling relationship in modern river deltas, to investigate avulsion and bifurcation interaction from synthetic river deltas, and to produce simple model to estimate palaeodischarge of a deltaic deposit. My thesis shows that:

1. In global modern river deltas discussed in Chapter 3, avulsion length scales more consistently with the slope break length instead of with the backwater length as has been previously reported (Chatanantavet et al., 2012; Ganti et al., 2016a). Furthermore, my global dataset also shows that avulsion-slope break length scales consistently across valley types (e.g. alluvial, bedrock, Pleistocene and confined valley). These findings open the opportunity to explore alternative hypotheses of parameters that control river delta development and evolution. My novel scaling elucidates variables that control avulsion and helping predict where the next avulsion may happen in the future that is vital for people live on river deltas because of the strong tie between avulsion and the risk from inland flooding.

2. Based on the finding of the consistent avulsion-slope break length scaling, I built 6 synthetic river delta scenarios, having various slopes upstream of the delta slope break, to explore the role of this novel scaling to the growth, and the interaction of avulsion and bifurcation in river deltas. I found that delta topset slope serves as the first order control of avulsion timescales in river deltas. Avulsion and bifurcation interact simultaneously during the delta building process but are independent processes, mechanistically. Using synthetic river deltas, I produced a novel understanding on how avulsion and bifurcation interact with one another. This is imperative in advancing our understanding to mitigate flood risk both inland and coastal of river deltas.

3. Using the scaling relationship concept, in Chapter 5 and 6, I define novel scaling relationships between catchment area, distributary channel widths and discharge from modern river deltas. By applying theses simple scaling relationships to several

deltaic deposits, I calculated estimated palaeodischarge values that are in the same order of magnitude with existing, more complex approaches. Palaeodischarge can now be determined from any data set such as outcrop or seismic datasets in which a catchment area or channel width can be determined. These rock-record focused scaling relationships promise enhanced deduction of variables in climate and palaeodischarges estimation across various types of depositional systems in source-to-sink studies, assessment of hydrocarbon, hydrogen, geothermal and carbon capture and storage (CCS) sizes, and more accurate palaeogeography interpretations.

References

Aiken, S.J., and Brierley, G.J., 2013, Analysis of longitudinal profiles along the eastern margin of the Qinghai-Tibetan Plateau: Journal of Mountain Science, v. 10, p. 643–657, doi:10.1007/s11629-013-2814-2.

Allen, P.A., Armitage, J.J., Carter, A., Duller, R.A., Michael, N.A., Sinclair, H.D., Whitchurch, A.L., and Whittaker, A.C., 2013, The Qs problem: Sediment volumetric balance of proximal foreland basin systems: Sedimentology, v. 60, p. 102–130, doi:10.1111/sed.12015.

Allen, P.A., and Hovius, N., 1998, Sediment supply from landslide-dominated catchments: implications for basin-margin fans: Basin Research, v. 10, p. 19–35, doi:10.1046/J.1365-2117.1998.00060.X.

Allen, G.H., and Pavelsky, T.M., 2018, Global extent of rivers and streams: Science, v. 361, p. 585–588, doi:10.1126/science.aat0636.

Allen, G.P., Salomon, J.C., Bassoullet, P., du Penhoat, Y., and de Grandpré, C., 1980, Effects of tides on mixing and suspended sediment transport in macrotidal estuaries: Sedimentary Geology, v. 26, p. 69–90, doi:10.1016/0037-0738(80)90006-8.

Andrén, H., 1994, Development of the Laitaure Delta, Swedish Lappland: Uppsala Universitet, 188 p.

Anthony, E.J., Brunier, G., Besset, M., Goichot, M., Dussouillez, P., and Nguyen, V.L., 2015, Linking rapid erosion of the Mekong River delta to human activities: Scientific Reports 2015 5:1, v. 5, p. 1–12, doi:10.1038/srep14745.

Aslan, A., Autin, W.J., and Blum, M.D., 2005, Causes of river avulsion: Insights from the late Holocene avulsion history of the Mississippi River, U.S.A: Journal of Sedimentary Research, v. 75, p. 650–664, doi:10.2110/jsr.2005.053.

Aslan, A., White, W.A., Warne, A.G., and Guevara, E.H., 2003, Holocene evolution of the western Orinoco Delta, Venezuela: GSA Bulletin, v. 115, p. 479–498,

http://pubs.geoscienceworld.org/gsa/gsabulletin/article-pdf/115/4/479/3389566/i0016-7606-115-4-479.pdf (accessed June 2021).

Baker, V.R. et al., 2022, Fluvial palaeohydrology in the 21st century and beyond: Earth Surface Processes and Landforms, v. 47, p. 58–81, doi:10.1002/ESP.5275.

Bates, C.C., 1953, Rational Theory of Delta Formation: AAPG Bulletin, v. 37, p. 2119–2162, doi:10.1306/5ceadd76-16bb-11d7-8645000102c1865d.

Beck, H.E., Zimmermann, N.E., McVicar, T.R., Vergopolan, N., Berg, A., and Wood, E.F., 2018, Present and future köppen-geiger climate classification maps at 1-km resolution: Scientific Data, v. 5, p. 1–12, doi:10.1038/sdata.2018.214.

Beltaos, S., and Prowse, T., 2009, River-ice hydrology in a shrinking cryosphere: Hydrological Processes, v. 23, p. 122–144, doi:10.1002/hyp.7165.

van den Berg, J.H., Boersma, J.R., and van Gelder, A., 2007, Diagnostic sedimentary structures of the fluvial-tidal transition zone - Evidence from deposits of the Rhine and Meuse: Geologie en Mijnbouw/Netherlands Journal of Geosciences, v. 86, p. 287–306, doi:10.1017/s0016774600077866.

Besset, M., Anthony, E.J., and Bouchette, F., 2019, Multi-decadal variations in delta shorelines and their relationship to river sediment supply: An assessment and review: Earth-Science Reviews, v. 193, p. 199–219, doi:10.1016/j.earscirev.2019.04.018.

Besset, M., Anthony, E.J., and Sabatier, F., 2017, River delta shoreline reworking and erosion in the Mediterranean and Black Seas: the potential roles of fluvial sediment starvation and other factors: Elem Sci Anth, v. 5, p. 54, doi:10.1525/elementa.139.

Bhatt, V.K., and Tiwari, A.K., 2008, Estimation of peak streamflows through channel geometry / Estimation de pics de débit fluviatiles à l'aide de la géométrie des cours d'eau Estimation of peak streamflows through channel geometry: Hydrological Sciences-Journal-des Sciences Hydrologiques, v. 53, p. 401–408, doi:10.1623/hysj.53.2.401.

Bhattacharya, J.P., Copeland, P., Lawton, T.F., and Holbrook, J., 2016, Estimation of source area, river paleo-discharge, paleoslope, and sediment budgets of linked deep-time

depositional systems and implications for hydrocarbon potential: Earth-Science Reviews, v. 153, p. 77–110, doi:10.1016/j.earscirev.2015.10.013.

Bhattacharya, J.P., and Giosan, L., 2003, Wave-influenced deltas: Geomorphological implications for facies reconstruction: Sedimentology, v. 50, p. 187–210, doi:10.1046/j.1365-3091.2003.00545.x.

Bhattacharya, J.P., and MacEachern, J.A., 2009, Hyperpycnal Rivers and Prodeltaic Shelves in the Cretaceous Seaway of North America: Journal of Sedimentary Research, v. 79, p. 184–209, doi:10.2110/jsr.2009.026.

Bhattacharya, J.P., and Tye, R.S., 2004, Searching for modern Ferron analogs and application to subsurface interpretation, *in* Chidsey, T.C., Adams, R.D., and Morris, T.H. eds., Regional to Wellbore Analog for Fluvial–Deltaic Reservoir Modeling: the Ferron Sandstone of Utah: American Association of Petroleum Geologists, Studies in Geology 50, American Association of Petroleum Geologists, p. 39–57.

Bhattacharya, J., and Walker, R.G., 1991, Allostratigraphic subdivision of the Upper Cretaceous Dunvegan, Shaftesbury, and Kaskapau formations in the northwestern Alberta subsurface: BULLETIN OF CANADIAN PETROLEUM GEOLOGY, v. 39, p. 145–164.

Bird, M.I., Austin, W.E.N., Wurster, C.M., Fifield, L.K., Mojtahid, M., and Sargeant, C., 2010, Punctuated eustatic sea-level rise in the early mid-Holocene: Geology, v. 38, p. 803–806, doi:10.1130/G31066.1.

Błaszczyk, M. et al., 2019, Quality assessment and glaciological applications of digital elevation models derived from space-borne and aerial images over two tidewater glaciers of southern spitsbergen: Remote Sensing, v. 11, p. 1121, doi:10.3390/rs11091121.

Blum, M.D., and Hattier-Womack, J., 2009, Climate Change, Sea-Level Change, and Fluvial Sediment Supply to Deepwater Depositional Systems, *in* Kneller, B., Martinsen, O.J., and McCaffrey, B. eds., External Controls of Deep-Water Depositional Systems, SEPM (Society for Sedimentary Geology), p. 15–39, doi:10.2110/SEPMSP.092.015.

Blum, M.D., Milliken, K.T., Pecha, M.A., Snedden, J.W., Frederick, B.C., and Galloway, W.E., 2017, Detrital-zircon records of Cenomanian, Paleocene, and Oligocene Gulf of

Mexico drainage integration and sediment routing: Implications for scales of basin-floor fans: Geosphere, v. 13, p. 2169–2205, doi:10.1130/GES01410.1.

Blum, M.D., and Roberts, H.H., 2009, Drowning of the Mississippi Delta due to insufficient sediment supply and global sea-level rise: Nature Geoscience, v. 2, p. 488–491, doi:10.1038/ngeo553.

Braathen, A., Midtkandal, I., Mulrooney, M.J., Appleyard, T.R., Haile, B.G., and van Yperen, A.E., 2018, Growth-faults from delta collapse – structural and sedimentological investigation of the Last Chance delta, Ferron Sandstone, Utah: Basin Research, v. 30, p. 688–707, doi:10.1111/bre.12271.

Brardinoni, F., and Hassan, M.A., 2006, Glacial erosion, evolution of river long profiles, and the organization of process domains in mountain drainage basins of coastal British Columbia: Journal of Geophysical Research, v. 111, p. F01013, doi:10.1029/2005JF000358.

Brewer, C.J., Hampson, G.J., Whittaker, A.C., Roberts, G.G., and Watkins, S.E., 2020, Comparison of methods to estimate sediment flux in ancient sediment routing systems: Earth-Science Reviews, v. 207, p. 103217, doi:10.1016/j.earscirev.2020.103217.

Bridge, J.S., and Mackey, S.D., 1993, A theoretical study of fluvial sandstone body dimensions, *in* The Geological Modelling of Hydrocarbon Reservoirs and Outcrop Analogues, wiley, p. 213–236, doi:10.1002/9781444303957.ch14.

Bridge, J.S., and Tye, R.S., 2000, Interpreting the Dimensions of Ancient Fluvial Channel Bars, Channels, and Channel Belts from Wireline-Logs and Cores: AAPG Bulletin, v. 84, p. 1205–1228, http://archives.datapages.com/data/bulletns/2000/08aug/1205/1205.htm (accessed June 2021).

Brooke, S.A.S., Ganti, V., Chadwick, A.J., and Lamb, M.P., 2020, Flood Variability Determines the Location of Lobe-Scale Avulsions on Deltas: Madagascar: Geophysical Research Letters, v. 47, p. e2020GL088797, doi:10.1029/2020GL088797.

Brownlie, W.R., 1983, Flow Depth in Sand-Bed Channels: Journal of Hydraulic Engineering, v. 109, p. 959–990, doi:10.1061/(asce)0733-9429(1983)109:7(959).

Brunier, G., Anthony, E.J., Goichot, M., Provansal, M., and Dussouillez, P., 2014, Recent morphological changes in the Mekong and Bassac river channels, Mekong delta: The marked impact of river-bed mining and implications for delta destabilisation: Geomorphology, v. 224, p. 177–191, doi:10.1016/j.geomorph.2014.07.009.

Burpee, A.P., Slingerland, R.L., Edmonds, D.A., Parsons, D., Best, J., Cederberg, J., McGuffin, A., Caldwell, R., Nijhuis, A., and Royce, J., 2015, Grain-Size Controls On the Morphology and Internal Geometry of River-Dominated Deltas: Journal of Sedimentary Research, v. 85, p. 699–714, doi:10.2110/jsr.2015.39.

Caldwell, R.L., and Edmonds, D.A., 2014, The effects of sediment properties on deltaic processes and morphologies: A numerical modeling study: Journal of Geophysical Research: Earth Surface, v. 119, p. 961–982, doi:10.1002/2013JF002965.

Caldwell, R.L., Edmonds, D.A., Baumgardner, S., Paola, C., Roy, S., and Nienhuis, J.H., 2019, A global delta dataset and the environmental variables that predict delta formation on marine coastlines: Earth Surface Dynamics, v. 7, p. 773–787, doi:10.5194/esurf-7-773-2019.

van Cappelle, M., Stukins, S., Hampson, G.J., and Johnson, H.D., 2016, Fluvial to tidal transition in proximal, mixed tide-influenced and wave-influenced deltaic deposits: Cretaceous lower sego sandstone, Utah, USA: Sedimentology, v. 63, p. 1333–1361, doi:10.1111/sed.12267.

Castelltort, S., Goren, L., Willett, S.D., Champagnac, J.D., Herman, F., and Braun, J., 2012, River drainage patterns in the New Zealand Alps primarily controlled by plate tectonic strain: Nature Geoscience, v. 5, p. 744–748, doi:10.1038/ngeo1582.

Castelltort, S., and Simpson, G., 2006, River spacing and drainage network growth in widening mountain ranges: Basin Research, v. 18, p. 267–276, doi:10.1111/J.1365-2117.2006.00293.X.

Celoria, F., 2015, Delta as a Geographical Concept in Greek Literature: https://doi.org/10.1086/350146, v. 57, p. 385–388, doi:10.1086/350146.

Chadwick, A.J., Lamb, M.P., and Ganti, V., 2020, Accelerated river avulsion frequency on lowland deltas due to sea-level rise: Proceedings of the National Academy of Sciences of the United States of America, v. 117, p. 17584–17590, doi:10.1073/pnas.1912351117.

Chadwick, A.J., Lamb, M.P., Moodie, A.J., Parker, G., and Nittrouer, J.A., 2019a, Origin of a Preferential Avulsion Node on Lowland River Deltas: Geophysical Research Letters, v. 46, p. 4267–4277, doi:10.1029/2019GL082491.

Chadwick, A.J., Lamb, M.P., Moodie, A.J., Parker, G., and Nittrouer, J.A., 2019b, Origin of a Preferential Avulsion Node on Lowland River Deltas: Geophysical Research Letters, v. 46, p. 4267–4277, doi:10.1029/2019GL082491.

Chadwick, A.J., Steele, S., Silvestre, J., and Lamb, M.P., 2022, Effect of Sea-level Change on River Avulsions and Stratigraphy for an Experimental Lowland Delta: Journal of Geophysical Research: Earth Surface, p. e2021JF006422, doi:10.1029/2021JF006422.

Chamberlain, E.L., Törnqvist, T.E., Shen, Z., Mauz, B., and Wallinga, J., 2018, Anatomy of Mississippi Delta growth and its implications for coastal restoration: Science Advances, v. 4, doi:10.1126/SCIADV.AAR4740/SUPPL_FILE/AAR4740_SM.PDF.

Chander, G., Markham, B.L., and Helder, D.L., 2009, Summary of current radiometric calibration coefficients for Landsat MSS, TM, ETM+, and EO-1 ALI sensors: Remote Sensing of Environment, v. 113, p. 893–903, doi:10.1016/J.RSE.2009.01.007.

Chatanantavet, P., Lamb, M.P., and Nittrouer, J.A., 2012, Backwater controls of avulsion location on deltas: Geophysical Research Letters, v. 39, p. 2–7, doi:10.1029/2011GL050197.

Cheng, A., and Yeager, M., 2007, Bootstrap resampling for voxel-wise variance analysis of three-dimensional density maps derived by image analysis of two-dimensional crystals: Journal of Structural Biology, v. 158, p. 19–32, doi:10.1016/j.jsb.2006.10.003.

Chumakov, N., Zharkov, M.A., Herman, A.B., Doludenko, M.P., Kalandadze, N.N., Lebedev, E.L., Ponomarenko, A.G., and Rautian, A.S., 1995, Climatic Belts of the Mid-Cretaceous Time: Stratigraphy and Geological Correlation, v. 3, p. 42–63, http://eprints.uni-kiel.de/37939/ (accessed May 2021).

Cohen, S., Kettner, A.J., Syvitski, J.P.M., and Fekete, B.M., 2013, WBMsed, a distributed global-scale riverine sediment flux model: Model description and validation: Computers and Geosciences, v. 53, p. 80–93, doi:10.1016/j.cageo.2011.08.011.

Cohen, S., Wan, T., Islam, M.T., and Syvitski, J.P.M., 2018, Global river slope: A new geospatial dataset and global-scale analysis: Journal of Hydrology, v. 563, p. 1057–1067, doi:10.1016/j.jhydrol.2018.06.066.

Coleman, J.M., and Wright, L.D., 1971, Analysis of Major River Systems and Their Deltas: Procedures and Rationale, With Two Examples:, https://apps.dtic.mil/sti/citations/AD0723575 (accessed April 2022).

Colombera, L., Mountney, N.P., Medici, G., and West, L.J., 2019, The geometry of fluvial channel bodies: Empirical characterization and implications for object-based models of the subsurface: AAPG Bulletin, v. 103, p. 905–929, doi:10.1306/10031817417.

Correggiari, A., Cattaneo, A., and Trincardi, F., 2005, Depositional Patterns in The Late Holocene Po Delta System, *in* Giosan, L. and Bhattacharya, J.P. eds., SEPM Special Publication, SEPM (Society for Sedimentary Geology), p. 365–392, http://radiocarbon.pa.qub.ac.uk/marine/ (accessed January 2021).

Cui, M., Xu, L., Wang, H., Ju, S., Xu, S., and Jing, R., 2017, Combining Nordtest method and bootstrap resampling for measurement uncertainty estimation of hematology analytes in a medical laboratory: Clinical Biochemistry, v. 50, p. 1067–1072, doi:10.1016/j.clinbiochem.2017.09.008.

Dade, W.B., 2001, Multiple Scales in River Basin Morphology: American Journal of Science, v. 301, p. 60–73, doi:10.2475/AJS.301.1.60.

Dalrymple, R.W., and Choi, K., 2007, Morphologic and facies trends through the fluvial-marine transition in tide-dominated depositional systems: A schematic framework for environmental and sequence-stratigraphic interpretation: Earth-Science Reviews, v. 81, p. 135–174, doi:10.1016/j.earscirev.2006.10.002.

Dalrymple, R.W., Kurcinka, C.E., Jablonski, B.V.J., Ichaso, A.A., and Mackay, D.A., 2015, Deciphering the relative importance of fluvial and tidal processes in the fluvial-marine

transition, *in* Developments in Sedimentology, Elsevier, v. 68, p. 3–45, doi:10.1016/B978-0-444-63529-7.00002-X.

Dashtgard, S.E., Venditti, J.G., Hill, P.R., Sisulak, C.F., Johnson, S.M., and Croix, A.D. la, 2012, Sedimentation Across the Tidal-Fluvial Transition in the Lower Fraser River, Canada: The Sedimentary Record, doi:10.2110/sedred.2012.4.4.

Davidson, S.K., and Hartley, A.J., 2010, Towards a quantitative method for estimating paleohydrology from clast size and comparison with modern rivers: Journal of Sedimentary Research, v. 80, p. 688–702, doi:10.2110/jsr.2010.062.

Davidson, S.K., and North, C.P., 2009, Geomorphological regional curves for prediction of drainage area and screening modern analogues for rivers in the rock record: Journal of Sedimentary Research, v. 79, p. 773–792, doi:10.2110/jsr.2009.080.

Debchoudhury, S., Sengupta, S., Earle, G., and Coley, W., 2019, A Bootstrap-Based Approach for Improving Measurements by Retarding Potential Analyzers: Journal of Geophysical Research: Space Physics, v. 124, p. 4569–4584, doi:10.1029/2018JA026314.

DeCelles, P.G., 2004, Late Jurassic to Eocene Evolution of the Cordilleran Thrust Belt and Foreland Basin System, Western U.S.A.: American Journal of Science, v. 304, p. 105–168.

Deltares, 2021, Delft3D - User Manual: Deltares, 1–695 p.

Diefenderfer, H.L., Coleman, A.M., Borde, A.B., and Sinks, I.A., 2008, Hydraulic geometry and microtopography of tidal freshwater forested wetlands and implications for restoration, Columbia River, U.S.A.: Ecohydrology and Hydrobiology, v. 8, p. 339–361, doi:10.2478/V10104-009-0027-7.

Dingle, E.H., Kusack, K.M., and Venditti, J.G., 2021, The gravel-sand transition and grain size gap in river bed sediments: Earth-Science Reviews, v. 222, p. 103838, doi:10.1016/J.EARSCIREV.2021.103838.

Dodov, B., and Foufoula-Georgiou, E., 2005, Fluvial processes and streamflow variability: Interplay in the scale-frequency continuum and implications for scaling: Water Resources Research, v. 41, p. 1–18, doi:10.1029/2004WR003408.

Dong, T.Y., Nittrouer, J.A., Czapiga, M.J., Ma, H., McElroy, B., Il'icheva, E., Pavlov, M., Chalov, S., and Parker, G., 2019, Roles of Bank Material in Setting Bankfull Hydraulic Geometry as Informed by the Selenga River Delta, Russia: Water Resources Research, v. 55, p. 827–846, doi:10.1029/2017WR021985.

Duller, R.A., Whittaker, A.C., Fedele, J.J., Whitchurch, A.L., Springett, J., Smithells, R., Fordyce, S., and Allen, P.A., 2010, From grain size to tectonics: Journal of Geophysical Research: Earth Surface, v. 115, p. 3022, doi:10.1029/2009JF001495.

Dunne, K.B.J., and Jerolmack, D.J., 2020, What sets river width? Science Advances, v. 6, p. eabc1505, doi:10.1126/sciadv.abc1505.

Eaton, B.C., 2013, Hydraulic Geometry: Empirical Investigations and Theoretical Approaches, *in* Treatise on Geomorphology, Elsevier Inc., v. 9, p. 313–329, doi:10.1016/B978-0-12-374739-6.00243-8.

Edmonds, D.A., Caldwell, R.L., Brondizio, E.S., and Siani, S.M.O., 2020, Coastal flooding will disproportionately impact people on river deltas: Nature Communications 2020 11:1, v. 11, p. 1–8, doi:10.1038/s41467-020-18531-4.

Edmonds, D.A., Hoyal, D.C.J.D., Sheets, B.A., and Slingerland, R.L., 2009, Predicting delta avulsions: Implications for coastal wetland restoration: Geology, v. 37, p. 759–762, doi:10.1130/G25743A.1.

Edmonds, D.A., Paola, C., Hoyal, D.C.J.D., and Sheets, B.A., 2011, Quantitative metrics that describe river deltas and their channel networks: Journal of Geophysical Research: Earth Surface, v. 116, p. 1–15, doi:10.1029/2010JF001955.

Edmonds, D.A., and Slingerland, R.L., 2007, Mechanics of river mouth bar formation: Implications for the morphodynamics of delta distributary networks: Journal of Geophysical Research: Earth Surface, v. 112, doi:10.1029/2006JF000574.

Edmonds, D.A., and Slingerland, R.L., 2010, Significant effect of sediment cohesion on deltamorphology: Nature Geoscience, v. 3, p. 105–109, doi:10.1038/ngeo730.

Edmonds, D.A., and Slingerland, R.L., 2008, Stability of delta distributary networks and their bifurcations: Water Resources Research, v. 44, doi:10.1029/2008WR006992.

Edwards, P.J., Watson, E.A., and Wood, F., 2019, Toward a Better Understanding of Recurrence Intervals, Bankfull, and Their Importance: Journal of Contemporary Water Research & Education, v. 166, p. 35–45, doi:10.1111/j.1936-704x.2019.03300.x.

Efron, B., 2007, Bootstrap Methods: Another Look at the Jackknife: The Annals of Statistics, v. 7, p. 1–26, doi:10.1214/aos/1176344552.

Efron, B., 1982, The Jackknife, the Bootstrap and Other Resampling Plans: Society for Industrial and Applied Mathematics, doi:10.1137/1.9781611970319.

Eide, C.H., Howell, J.A., Buckley, S.J., Martinius, A.W., Oftedal, B.T., and Henstra, G.A., 2016, Facies model for a coarse-grained, tide-influenced delta: Gule Horn Formation (Early Jurassic), Jameson Land, Greenland: Sedimentology, v. 63, p. 1474–1506, doi:10.1111/sed.12270.

Eide, C.H., Müller, R., and Helland-Hansen, W., 2018a, Using climate to relate water discharge and area in modern and ancient catchments: Sedimentology, v. 65, p. 1378–1389, doi:10.1111/sed.12426.

Eide, C.H., Müller, R., and Helland-Hansen, W., 2018b, Using climate to relate water discharge and area in modern and ancient catchments (V. Manville, Ed.): Sedimentology, v. 65, p. 1378–1389, doi:10.1111/sed.12426.

Ellis, E.R., and Church, M., 2005, Hydraulic geometry of secondary channels of lower Fraser River, British Columbia, from acoustic Doppler profiling: Water Resources Research, v. 41, p. 1–15, doi:10.1029/2004WR003777.

Ericson, J.P., Vörösmarty, C.J., Dingman, S.L., Ward, L.G., and Meybeck, M., 2006, Effective sea-level rise and deltas: Causes of change and human dimension implications: Global and Planetary Change, v. 50, p. 63–82, doi:10.1016/j.gloplacha.2005.07.004.

Fabuel-Perez, I., Hodgetts, D., and Redfern, J., 2009, A new approach for outcrop characterization and geostatistical analysis of a low-sinuosity fluvial-dominated succession

using digital outcrop models: Upper triassic oukaimeden sandstone formation, central high Atlas, Morocco: American Association of Petroleum Geologists Bulletin, v. 93, p. 795–827, doi:10.1306/02230908102.

Fagherazzi, S., Edmonds, D.A., Nardin, W., Leonardi, N., Canestrelli, A., Falcini, F., Jerolmack, D.J., Mariotti, G., Rowland, J.C., and Slingerland, R.L., 2015, Dynamics of river mouth deposits: Reviews of Geophysics, v. 53, p. 642–672, doi:10.1002/2014RG000451.

Farr, T.G. et al., 2007, The shuttle radar topography mission: Reviews of Geophysics, v. 45, doi:10.1029/2005RG000183.

Ferguson, R.I., 1986, Hydraulics and hydraulic geometry: Progress in Physical Geography: Earth and Environment, v. 10, p. 1–31, doi:10.1177/030913338601000101.

Fernandes, A.M., Törnqvist, T.E., Straub, K.M., and Mohrig, D., 2016, Connecting the backwater hydraulics of coastal rivers to fluviodeltaic sedimentology and stratigraphy: Geology, v. 44, p. 979–982, doi:10.1130/G37965.1.

Frasson, R.P. de M., Pavelsky, T.M., Fonstad, M.A., Durand, M.T., Allen, G.H., Schumann, G., Lion, C., Beighley, R.E., and Yang, X., 2019, Global Relationships Between River Width, Slope, Catchment Area, Meander Wavelength, Sinuosity, and Discharge: Geophysical Research Letters, v. 46, p. 3252–3262, doi:10.1029/2019GL082027.

Gage, J.E., and Asquith, G.B., 1977, Sedimentology of Mesa Rica Sandstone in Tucumcari Basin, New Mexico New Mexico Bureau of Mines & Mineral Resources:

Galloway, W.D., 1975, Process Framework for describing the morphologic and stratigraphic evolution of deltaic depositional systems: Houston Geological Society. Deltas: Models for Exploration, p. 87–98, doi:10.1038/NMAT3976.

Ganti, V., Chadwick, A.J., Hassenruck-Gudipati, H.J., Fuller, B.M., and Lamb, M.P., 2016a, Experimental river delta size set by multiple floods and backwater hydrodynamics: Science Advances, v. 2, p. e1501768, doi:10.1126/sciadv.1501768.

Ganti, V., Chadwick, A.J., Hassenruck-Gudipati, H.J., and Lamb, M.P., 2016b, Avulsion cycles and their stratigraphic signature on an experimental backwater-controlled delta:

Journal of Geophysical Research: Earth Surface, v. 121, p. 1651–1675, doi:10.1002/2016JF003915.

Ganti, V., Chu, Z., Lamb, M.P., Nittrouer, J.A., and Parker, G., 2014, Testing morphodynamic controls on the location and frequency of river avulsions on fans versus deltas: Huanghe (Yellow River), China: Geophysical Research Letters, v. 41, p. 7882–7890, doi:10.1002/2014GL061918.

Ganti, V., Hajek, E.A., Leary, K., Straub, K.M., and Paola, C., 2020, Morphodynamic Hierarchy and the Fabric of the Sedimentary Record: Geophysical Research Letters, v. 47, p. e2020GL087921, doi:10.1029/2020GL087921.

Ganti, V., Lamb, M.P., and Chadwick, A.J., 2019a, Autogenic Erosional Surfaces in Fluvio-deltaic Stratigraphy from Floods, Avulsions, and Backwater Hydrodynamics: Journal of Sedimentary Research, v. 89, p. 815–832, doi:10.2110/jsr.2019.40.

Ganti, V., Whittaker, A.C., Lamb, M.P., and Fischer, W.W., 2019b, Low-gradient, single-threaded rivers prior to greening of the continents: Proceedings of the National Academy of Sciences, v. 116, p. 11652–11657, doi:10.1073/PNAS.1901642116.

Geleynse, N., Storms, J.E.A., Walstra, D.J.R., Jagers, H.R.A., Wang, Z.B., and Stive, M.J.F., 2011, Controls on river delta formation; insights from numerical modelling: Earth and Planetary Science Letters, v. 302, p. 217–226, doi:10.1016/j.epsl.2010.12.013.

Giosan, L., Syvitski, J., Constantinescu, S., and Day, J., 2014, Climate change: Protect the world's deltas: Nature, v. 516, p. 31–33, doi:10.1038/516031a.

Gisen, J.I.A., and Savenije, H.H.G., 2015, Estimating bankfull discharge and depth in ungauged estuaries: Water Resources Research, v. 51, p. 2298–2316, doi:10.1002/2014WR016227.

Gleason, C.J., 2015a, Hydraulic geometry of natural rivers: Progress in Physical Geography: Earth and Environment, v. 39, p. 337–360, doi:10.1177/0309133314567584.

Gleason, C.J., 2015b, Hydraulic geometry of natural rivers: A review and future directions: Progress in Physical Geography, v. 39, p. 337–360, doi:10.1177/0309133314567584.

Gleason, C.J., Wada, Y., and Wang, J., 2018, A Hybrid of Optical Remote Sensing and Hydrological Modeling Improves Water Balance Estimation: Journal of Advances in Modeling Earth Systems, v. 10, p. 2–17, doi:10.1002/2017MS000986.

Gorelick, N., Hancher, M., Dixon, M., Ilyushchenko, S., Thau, D., and Moore, R., 2017, Google Earth Engine: Planetary-scale geospatial analysis for everyone: Remote Sensing of Environment, v. 202, p. 18–27, doi:10.1016/j.rse.2017.06.031.

Greenberg, E., Ganti, V., and Hajek, E., 2021, Quantifying bankfull flow width using preserved bar clinoforms from fluvial strata: Geology, v. 1, doi:10.1130/G48729.1.

Gugliotta, M., Flint, S.S., Hodgson, D.M., and Veiga, G.D., 2016, Recognition criteria, characteristics and implications of the fluvial to marine transition zone in ancient deltaic deposits (Lajas Formation, Argentina): Sedimentology, v. 63, p. 1971–2001, doi:10.1111/sed.12291.

Gugliotta, M., and Saito, Y., 2019, Matching trends in channel width, sinuosity, and depth along the fluvial to marine transition zone of tide-dominated river deltas: The need for a revision of depositional and hydraulic models: Earth-Science Reviews, v. 191, p. 93–113, doi:10.1016/j.earscirev.2019.02.002.

Gugliotta, M., Saito, Y., Nguyen, V.L., Ta, T.K.O., and Tamura, T., 2019, Sediment distribution and depositional processes along the fluvial to marine transition zone of the Mekong River delta, Vietnam: Sedimentology, v. 66, p. 146–164, doi:10.1111/sed.12489.

Hackney, C.R., Darby, S.E., Parsons, D.R., Leyland, J., Best, J.L., Aalto, R., Nicholas, A.P., and Houseago, R.C., 2020, River bank instability from unsustainable sand mining in the lower Mekong River: Nature Sustainability 2020 3:3, v. 3, p. 217–225, doi:10.1038/s41893-019-0455-3.

Hampson, G.J., Jewell, T.O., Irfan, N., Gani, M.R., and Bracken, B., 2013, Modest change in fluvial style with varying accommodation in regressive alluvial-to-coastal-plain wedge: Upper Cretaceous Blackhawk Formation, Wasatch Plateau, central Utah, U.S.A: Journal of Sedimentary Research, v. 83, p. 145–169, doi:10.2110/jsr.2013.8.

Hariharan, J., Xu, Z., Michael, H.A., Paola, C., Steel, E., and Passalacqua, P., 2021, Linking the Surface and Subsurface in River Deltas—Part 1: Relating Surface and Subsurface Geometries: Water Resources Research, v. 57, doi:10.1029/2020WR029282.

Hartley, A.J., Weissmann, G.S., and Scuderi, L., 2017, Controls on the apex location of large deltas: Journal of the Geological Society, v. 174, p. 10–13, doi:10.1144/jgs2015-154.

Haucke, J., and Clancy, K.A., 2011, Stationarity of streamflow records and their influence on bankfull regional curves: Journal of the American Water Resources Association, v. 47, p. 1338–1347, doi:10.1111/j.1752-1688.2011.00590.x.

Hay, M.J., and Plint, A.G., 2020, High-frequency sequences within a retrogradational deltaic succession: Upper Cenomanian Dunvegan Formation, Western Canada Foreland Basin: The Depositional Record, v. 6, p. 524–551, doi:10.1002/DEP2.114.

Hayakawa, Y.S., and Oguchi, T., 2006, DEM-based identification of fluvial knickzones and its application to Japanese mountain rivers: Geomorphology, v. 78, p. 90–106, doi:10.1016/j.geomorph.2006.01.018.

Hayden, A.T., Lamb, M.P., Fischer, W.W., Ewing, R.C., McElroy, B.J., and Williams, R.M.E., 2019, Formation of sinuous ridges by inversion of river-channel belts in Utah, USA, with implications for Mars: Icarus, v. 332, p. 92–110, doi:10.1016/J.ICARUS.2019.04.019.

Hey, R.D., and Thorne, C.R., 1986, Stable Channels with Mobile Gravel Beds: Journal of Hydraulic Engineering, v. 112, p. 671–689, doi:10.1061/(asce)0733-9429(1986)112:8(671).

Heyvaert, V.M.A., and Walstra, J., 2016, The role of long-term human impact on avulsion and fan development: Earth Surface Processes and Landforms, v. 41, p. 2137–2152, doi:10.1002/esp.4011.

Hoitink, A.J.F., Wang, Z.B., Vermeulen, B., Huismans, Y., and Kästner, K., 2017, Tidal controls on river delta morphology: Nature Geoscience, v. 10, p. 637–645, doi:10.1038/ngeo3000.

Holbrook, J.M., 1996, Complex fluvial response to low gradients at maximum regression: A genetic link between smooth sequence-boundary morphology and architecture of overlying sheet sandstone: Journal of Sedimentary Research, v. 66, p. 713–722, doi:10.1306/d42683ec-2b26-11d7-8648000102c1865d.

Holbrook, J., 2001, Origin, genetic interrelationships, and stratigraphy over the continuum of fluvial channel-form bounding surfaces: An illustration from middle Cretaceous strata, Southeastern Colorado: Sedimentary Geology, v. 144, p. 179–222, doi:10.1016/S0037-0738(01)00118-X.

Holbrook, J.M., and Dunbar, R.W., 1992, Depositional history of Lower Cretaceous strata in northeastern New Mexico: Implications for regional tectonics and depositional sequences: Geological Society of America Bulletin, v. 104, p. 802–813, https://watermark.silverchair.com/i0016-7606-104-7-802.pdf?token=AQECAHi208BE49Ooan9kkhW_Ercy7Dm3ZL_9Cf3qfKAc485ysgAAAvQwggLwBgkqhkiG9w0BBwagggLhMIIC3QIBADCCAtYGCSqGSIb3DQEHATAeBglghkgBZQMEAS4wEQQMqsNHCq57MHBCniN_AgEQgIICp0laM70R4mInv9DYT_FNrZhCsgfDQm65ky (accessed February 2022).

Holbrook, J., and Wanas, H., 2014, A fulcrum approach to assessing source-to-sink mass balance using channel paleohydrologic paramaters derivable from common fluvial data sets with an example from the cretaceous of Egypt: Journal of Sedimentary Research, v. 84, p. 349–372, doi:10.2110/jsr.2014.29.

Hoyal, D.C.J.D., and Sheets, B.A., 2009, Morphodynamic evolution of experimental cohesive deltas: Journal of Geophysical Research: Earth Surface, v. 114, p. 1–18, doi:10.1029/2007JF000882.

Huang, H.Q., and Nanson, G.C., 1997, Vegetation and channel variation; a case study of four small streams in southeastern Australia: Geomorphology, v. 18, p. 237–249, doi:10.1016/s0169-555x(96)00028-1.

Ielpi, A., and Lapôtre, M.G.A., 2019, A tenfold slowdown in river meander migration driven by plant life: Nature Geoscience 2019 13:1, v. 13, p. 82–86, doi:10.1038/s41561-019-0491-7.

Jablonski, B.V.J., and Dalrymple, R.W., 2016, Recognition of strong seasonality and climatic cyclicity in an ancient, fluvially dominated, tidally influenced point bar: Middle McMurray Formation, Lower Steepbank River, north-eastern Alberta, Canada: Sedimentology, v. 63, p. 552–585, doi:10.1111/sed.12228.

Jacobsen, R.E., and Burr, D.M., 2016, Greater contrast in Martian hydrological history from more accurate estimates of paleodischarge: Geophysical Research Letters, v. 43, p. 8903–8911, doi:10.1002/2016GL070535.

Jerolmack, D.J., 2009, Conceptual framework for assessing the response of delta channel networks to Holocene sea level rise: Quaternary Science Reviews, v. 28, p. 1786–1800, doi:10.1016/j.quascirev.2009.02.015.

Jerolmack, D.J., and Mohrig, D., 2007, Conditions for branching in depositional rives: Geology, v. 35, p. 463–466, doi:10.1130/G23308A.1.

Jerolmack, D.J., and Paola, C., 2010, Shredding of environmental signals by sediment transport: Geophysical Research Letters, v. 37, doi:10.1029/2010GL044638.

Jerolmack, D.J., and Swenson, J.B., 2007, Scaling relationships and evolution of distributary networks on wave-influenced deltas: Geophysical Research Letters, v. 34, p. n/a-n/a, doi:10.1029/2007GL031823.

Kästner, K., Hoitink, A.J.F., Vermeulen, B., Geertsema, T.J., and Ningsih, N.S., 2017, Distributary channels in the fluvial to tidal transition zone: Journal of Geophysical Research: Earth Surface, v. 122, p. 696–710, doi:10.1002/2016JF004075.

Kidder, T.R., and Liu, H., 2017, Bridging theoretical gaps in geoarchaeology: archaeology, geoarchaeology, and history in the Yellow River valley, China: Archaeological and Anthropological Sciences, v. 9, p. 1585–1602, doi:10.1007/S12520-014-0184-5/FIGURES/9.

Kleinhans, M.G., Ferguson, R.I., Lane, S.N., and Hardy, R.J., 2013, Splitting rivers at their seams: bifurcations and avulsion: Earth Surface Processes and Landforms, v. 38, p. 47–61, doi:10.1002/esp.3268.

Kleinhans, M.G., and Hardy, R.J., 2013, River bifurcations and avulsion: Earth Surface Processes and Landforms, v. 38, p. 317–318, doi:10.1002/esp.3354.

Kleinhans, M.G., de Vries, B., Braat, L., and van Oorschot, M., 2018, Living landscapes: Muddy and vegetated floodplain effects on fluvial pattern in an incised river: Earth Surface Processes and Landforms, v. 43, p. 2948–2963, doi:10.1002/ESP.4437.

Kleinhans, M.G., Weerts, H.J.T., and Cohen, K.M., 2010, Avulsion in action: Reconstruction and modelling sedimentation pace and upstream flood water levels following a Medieval tidal-river diversion catastrophe (Biesbosch, The Netherlands, 1421–1750 AD): Geomorphology, v. 118, p. 65–79, doi:10.1016/J.GEOMORPH.2009.12.009.

Korus, J.T., and Fielding, C.R., 2015, Asymmetry in Holocene river deltas: Patterns, controls, and stratigraphic effects: Earth-Science Reviews, v. 150, p. 219–242, doi:10.1016/j.earscirev.2015.07.013.

Kravtsova, V.I., Mikhailov, V.N., and Kidyaeva, V.M., 2009, Hydrological regime, morphological features and natural territorial complexes of the Irrawaddy River Delta (Myanmar): Water Resources, v. 36, p. 243–260, doi:10.1134/S0097807809030014.

Kroonenberg, S.B., Rusakov, G. v., and Svitoch, A.A., 1997, The wandering of the Volga delta: A response to rapid Caspian sea-level change: Sedimentary Geology, v. 107, p. 189–209, doi:10.1016/S0037-0738(96)00028-0.

Lamb, M.P., Nittrouer, J.A., Mohrig, D., and Shaw, J., 2012, Backwater and river plume controls on scour upstream of river mouths: Implications for fluvio-deltaic morphodynamics: J. Geophys. Res, v. 117, p. 1002, doi:10.1029/2011JF002079.

Lane, E.W., 1954, The Importance of Fluvial Morphology in Hydraulic Engineering:, https://semspub.epa.gov/work/01/554355.pdf (accessed August 2022).

Latrubesse, E.M., 2008, Patterns of anabranching channels: The ultimate end-member adjustment of mega rivers: Geomorphology, v. 101, p. 130–145, doi:10.1016/J.GEOMORPH.2008.05.035.

Leary, K.C.P., and Ganti, V., 2020, Preserved Fluvial Cross Strata Record Bedform Disequilibrium Dynamics: Geophysical Research Letters, v. 47, p. e2019GL085910, doi:10.1029/2019GL085910.

Leclair, S.F., and Bridge, J.S., 2001, Quantitative interpretation of sedimentary structures formed by river dunes: Journal of Sedimentary Research, v. 71, p. 713–716, doi:10.1306/2DC40962-0E47-11D7-8643000102C1865D.

Lehner, B., and Grill, G., 2013, Global river hydrography and network routing: Baseline data and new approaches to study the world's large river systems: Hydrological Processes, v. 27, p. 2171–2186, doi:10.1002/hyp.9740.

Lentsch, N., Finotello, A., and Paola, C., 2018, Reduction of deltaic channel mobility by tidal action under rising relative sea level: Geology, v. 46, p. 599–602, doi:10.1130/G45087.1.

Leopold, L.B., and Maddock, T., 1953, The Hydraulic Geometry of Stream Channels and Some Physiographic Implications:, doi:10.3133/PP252.

Leopold, L.B., and Miller, J.P., 1954, A postglacial chronology for some alluvial valleys in Wyoming:, doi:10.3133/WSP1261.

Li, W., Bhattacharya, J.P., and Wang, Y., 2011, Delta asymmetry: Concepts, characteristics, and depositional models: Petroleum Science, v. 8, p. 278–289, doi:10.1007/s12182-011-0145-x.

Li, J., Ganti, V., Li, C., and Wei, H., 2022a, Upstream migration of avulsion sites on lowland deltas with river-mouth retreat: Earth and Planetary Science Letters, v. 577, p. 117270, doi:10.1016/J.EPSL.2021.117270.

Li, J., Ganti, V., Li, C., and Wei, H., 2022b, Upstream migration of avulsion sites on lowland deltas with river-mouth retreat: Earth and Planetary Science Letters, v. 577, p. 117270, doi:10.1016/J.EPSL.2021.117270.

Li, Q., Gasparini, N.M., and Straub, K.M., 2018, Some signals are not the same as they appear: How do erosional landscapes transform tectonic history into sediment flux records? Geology, v. 46, p. 407–410, doi:10.1130/G40026.1.

Li, X., Liu, J.P., Saito, Y., and Nguyen, V.L., 2017, Recent evolution of the Mekong Delta and the impacts of dams: Earth-Science Reviews, v. 175, p. 1–17, doi:10.1016/j.earscirev.2017.10.008.

Li, Q., Yu, L., and Straub, K.M., 2016, Storage thresholds for relative sea-level signals in the stratigraphic record: Geology, v. 44, p. 179–182, doi:10.1130/G37484.1.

Lin, W., and Bhattacharya, J.P., 2017, Estimation of source-to-sink mass balance by a fulcrum approach using channel paleohydrologic parameters of the cretaceous dunvegan formation, Canada: Journal of Sedimentary Research, v. 87, p. 97–116, doi:10.2110/jsr.2017.1.

Lin, W., and Bhattacharya, J.P., 2021, Storm-flood-dominated delta: A new type of delta in stormy oceans: Sedimentology, v. 68, p. 1109–1136, doi:10.1111/sed.12819.

Loucks, D.P., 2019, Developed river deltas: are they sustainable? Environmental Research Letters, v. 14, p. 113004, doi:10.1088/1748-9326/AB4165.

Lyster, S.J., Whittaker, A.C., Allison, P.A., Lunt, D.J., and Farnsworth, A., 2020, Predicting sediment discharges and erosion rates in deep time—examples from the late Cretaceous North American continent: Basin Research, v. 32, p. 1547–1573, doi:10.1111/bre.12442.

Lyster, S.J., Whittaker, A.C., Hampson, G.J., Hajek, E.A., Allison, P.A., and Lathrop, B.A., 2021, Reconstructing the morphologies and hydrodynamics of ancient rivers from source to sink: Cretaceous Western Interior Basin, Utah, USA: Sedimentology, doi:10.1111/sed.12877.

Mackin, J.H., 1948, Concept of the graded river: Bulletin of The Geological Society of America, v. 59, p. 463–512.

Markham, B.L., Arvidson, T., Barsi, J.A., Choate, M., Kaita, E., Levy, R., Lubke, M., and Masek, J.G., 2018, Landsat Program: Comprehensive Remote Sensing, v. 1–9, p. 27–90, doi:10.1016/B978-0-12-409548-9.10313-6.

Martin, J., Fernandes, A.M., Pickering, J., Howes, N., Mann, S., and McNeil, K., 2018, The Stratigraphically Preserved Signature of Persistent Backwater Dynamics in a Large Paleodelta System: The Mungaroo Formation, North West Shelf, Australia: Journal of Sedimentary Research, v. 88, p. 850–872, doi:10.2110/jsr.2018.38.

Martinius, A.W., Jablonski, B.V.J., Fustic, M., Strobl, R., and van den Berg, J.H., 2015, Fluvial to tidal transition zone facies in the McMurray Formation (Christina River, Alberta, Canada), with emphasis on the reflection of flow intensity in bottomset architecture: Developments in Sedimentology, v. 68, p. 445–480, doi:10.1016/B978-0-444-63529-7.00019-5.

McCabe, G.J., and Wolock, D.M., 2016, Variability and Trends in Runoff Efficiency in the Conterminous United States: JAWRA Journal of the American Water Resources Association, v. 52, p. 1046–1055, doi:10.1111/1752-1688.12431.

Merritt, D.M., and Wohl, E.E., 2003, Downstream hydraulic geometry and channel adjustment during a flood along an ephemeral, arid-region drainage: Geomorphology, v. 52, p. 165–180, doi:10.1016/S0169-555X(02)00241-6.

Mikhailov, V.N., 1970, Hydrologic-morphometric characteristics of delta branches: Stud. Rep. Hydrol., p. 146–158, http://iahs.info/redbooks/a090/iahs_090_0146.pdf.

Milliken, K.T., Blum, M.D., Snedden, J.W., and Galloway, W.E., 2018, Application of fluvial scaling relationships to reconstruct drainage-basin evolution and sediment routing for the Cretaceous and Paleocene of the Gulf of Mexico: Geosphere, v. 14, p. 749–767, doi:10.1130/GES01374.1.

Milliman, J.D., and Farnsworth, K.L., 2011, River discharge to the coastal ocean: A global synthesis: Cambridge University Press, 1–384 p., doi:10.1017/CBO9780511781247.

Mohrig, D., Heller, P.L., Paola, C., and Lyons, W.J., 2000, Interpreting avulsion process from ancient alluvial sequences: Guadalope-Matarranya system (Northern Spain) and

Wasatch formation (Western Colorado): Bulletin of the Geological Society of America, v. 112, p. 1787–1803, doi:10.1130/0016-7606(2000)112<1787:IAPFAA>2.0.CO;2.

Montgomery, D.R., and Gran, K.B., 2001, Downstream variations in the width of bedrock channels: Water Resources Research, v. 37, p. 1841–1846, doi:10.1029/2000WR900393.

Moodie, A.J., Nittrouer, J.A., Ma, H., Carlson, B.N., Chadwick, A.J., Lamb, M.P., and Parker, G., 2019, Modeling Deltaic Lobe-Building Cycles and Channel Avulsions for the Yellow River Delta, China: Journal of Geophysical Research: Earth Surface, v. 124, p. 2438–2462, doi:10.1029/2019JF005220.

Moody, J.A., and Troutman, B.M., 2002, Characterization of the spatial variability of channel morphology: Earth Surface Processes and Landforms, v. 27, p. 1251–1266, doi:10.1002/ESP.403.

Morgan, A.M., and Craddock, R.A., 2019, Assessing the Accuracy of Paleodischarge Estimates for Rivers on Mars: Geophysical Research Letters, v. 46, p. 11738–11746, doi:10.1029/2019GL084921.

Morgan, J.A., Kumar, N., Horner-Devine, A.R., Ahrendt, S., Istanbullouglu, E., and Bandaragoda, C., 2020, The use of a morphological acceleration factor in the simulation of large-scale fluvial morphodynamics: Geomorphology, v. 356, p. 107088, doi:10.1016/J.GEOMORPH.2020.107088.

Morin, P., Porter, C., Cloutier, M., Howat, I., Noh, M.-J., Willis, M., Bates, B., Willamson, C., and Peterman, K., 2016, ArcticDEM; A Publically Available, High Resolution Elevation Model of the Arctic, *in* Geophysical Research Abstracts, European Geosciences Union, v. 18, p. 2016–8396, https://ui.adsabs.harvard.edu/abs/2016EGUGA..18.8396M/abstract (accessed July 2020).

Mosley, M.P., 1981, Semi-determinate hydraulic geometry of river channels, South Island, New Zealand: Earth Surface Processes and Landforms, v. 6, p. 127–137, doi:10.1002/ESP.3290060206.

Mudd, S.M., 2020, Topographic data from satellites: Developments in Earth Surface Processes, v. 23, p. 91–128, doi:10.1016/B978-0-444-64177-9.00004-7.

Mueller, E.R., Schmidt, J.C., Topping, D.J., Shafroth, P.B., Rodríguez-Burgueño, J.E., Ramírez-Hernández, J., and Grams, P.E., 2017, Geomorphic change and sediment transport during a small artificial flood in a transformed post-dam delta: The Colorado River delta, United States and Mexico: Ecological Engineering, v. 106, p. 757–775, doi:10.1016/j.ecoleng.2016.08.009.

Musial, G., Reynaud, J.Y., Gingras, M.K., Féniès, H., Labourdette, R., and Parize, O., 2012, Subsurface and outcrop characterization of large tidally influenced point bars of the Cretaceous McMurray Formation (Alberta, Canada): Sedimentary Geology, v. 279, p. 156–172, doi:10.1016/j.sedgeo.2011.04.020.

Nienhuis, J.H., Ashton, A.D., Edmonds, D.A., Hoitink, A.J.F., Kettner, A.J., Rowland, J.C., and Törnqvist, T.E., 2020, Global-scale human impact on delta morphology has led to net land area gain: Nature, v. 577, p. 514–518, doi:10.1038/s41586-019-1905-9.

Nienhuis, J.H., Ashton, A.D., and Giosan, L., 2015, What makes a delta wave-dominated? Geology, v. 43, p. 511–514, doi:10.1130/G36518.1.

Nienhuis, J.H., Ashton, A.D., Kettner, A.J., and Giosan, L., 2017, Large-scale coastal and fluvial models constrain the late Holocene evolution of the Ebro Delta: Earth Surface Dynamics, v. 5, p. 585–603, doi:10.5194/esurf-5-585-2017.

Nienhuis, J.H., Hoitink, A.J.F., and Törnqvist, T.E., 2018a, Future Change to Tide-Influenced Deltas: Geophysical Research Letters, v. 45, p. 3499–3507, doi:doi.org/10.1029/2018GL077638.

Nienhuis, J.H., Törnqvist, T.E., and Esposito, C.R., 2018b, Crevasse Splays Versus Avulsions: A Recipe for Land Building With Levee Breaches: Geophysical Research Letters, v. 45, p. 4058–4067, doi:10.1029/2018GL077933.

Nienhuis, J.H., and van de Wal, R.S.W., 2021, Projections of Global Delta Land Loss From Sea-Level Rise in the 21st Century: Geophysical Research Letters, v. 48, p. e2021GL093368, doi:10.1029/2021GL093368.

Nijhuis, A.G., Edmonds, D.A., Caldwell, R.L., Cederberg, J.A., Slingerland, R.L., Best, J.L., Parsons, D.R., and Robinson, R.A.J., 2015, Fluvio-deltaic avulsions during relative sea-level fall: Geology, v. 43, p. 719–722, doi:10.1130/G36788.1.

Ninfo, A., Ciavola, P., and Billi, P., 2018, The Po Delta is restarting progradation: Geomorphological evolution based on a 47-years Earth Observation dataset: Scientific Reports, v. 8, doi:10.1038/s41598-018-21928-3.

Nittrouer, J.A., 2013, Backwater hydrodynamics and sediment transport in the lowermost Mississippi River delta: Implications for the development of fluvial-deltaic landforms in a large lowland river, *in* IAHS ed., Proceedings of HP1, IAHS-IAPSO-IASPEI Assembly, Gothenburg, Sweden, July 2013 (IAHS Publ. 358, 2013)., Gothenburg, IAHS Publication, v. 358, https://www.sedimentology.geo.ttu.edu/wp-content/uploads/2017/12/Nittrouer-2013.pdf (accessed June 2021).

Nittrouer, J.A., Shaw, J., Lamb, M.P., and Mohrig, D., 2012, Spatial and temporal trends for water-flow velocity and bed-material sediment transport in the lower Mississippi River: Bulletin of the Geological Society of America, v. 124, p. 400–414, doi:10.1130/B30497.1.

Nyberg, B., Helland-Hansen, W., Gawthorpe, R., Tillmans, F., and Sandbakken, P., 2021, Assessing First-Order BQART Estimates for Ancient Source-to-Sink Mass Budget Calculations: Basin Research, v. 00, p. 1–18, doi:10.1111/bre.12563.

Oboh-Ikuenobe, F., Holbrook, J., Scott, R., Akins, S., Evetts, M., Benson, D., and Pratt, L., 2008, Anatomy of Epicontinental Flooding: Late Albian-Early Cenomanian of the Southern U.S. Western Interior Basin: Special Paper - Geological Association of Canada, https://scholarsmine.mst.edu/geosci_geo_peteng_facwork/199 (accessed June 2021).

Olariu, C., and Bhattacharya, J.P., 2006, Terminal distributary channels and delta front architecture of river-dominated delta systems: Journal of Sedimentary Research, v. 76, p. 212–233, doi:10.2110/jsr.2006.026.

Paola, C., and Mohrig, D., 1996a, Palaeohydraulics revisited: Palaeoslope estimation in coarse-grained braided rivers:, doi:10.1046/j.1365-2117.1996.00253.x.

Paola, C., and Mohrig, D., 1996b, Palaeohydraulics revisited: palaeoslope estimation in coarse-grained braided rivers: Basin Research, v. 8, p. 243–254, doi:10.1046/j.1365-2117.1996.00253.x.

Parker, G., 2004, E-book: 1D Sediment Transport Morphodynamics with Applications to Rivers and Turbidity Currents:, http://hydrolab.illinois.edu/people/parkerg/morphodynamics_e-book.htm (accessed December 2021).

Parker, G., Wilcock, P.R., Paola, C., Dietrich, W.E., and Pitlick, J., 2007, Physical basis for quasi-universal relations describing bankfull hydraulic geometry of single-thread gravel bed rivers: Journal of Geophysical Research: Earth Surface, v. 112, doi:10.1029/2006JF000549.

Phillips, C.B., and Jerolmack, D.J., 2019, Bankfull Transport Capacity and the Threshold of Motion in Coarse-Grained Rivers: Water Resources Research, v. 55, p. 11316–11330, doi:10.1029/2019WR025455.

Phillips, C.B., and Jerolmack, D.J., 2016, Self-organization of river channels as a critical filter on climate signals: Science, v. 352, p. 694–697, doi:10.1126/science.aad3348.

Pierik, H.J., Stouthamer, E., Schuring, T., and Cohen, K.M., 2018, Human-caused avulsion in the Rhine-Meuse delta before historic embankment (The Netherlands): Geology, v. 46, p. 935–938, doi:10.1130/G45188.1.

Plink-Björklund, P., 2012, Effects of tides on deltaic deposition: Causes and responses: Sedimentary Geology, v. 279, p. 107–133, doi:10.1016/j.sedgeo.2011.07.006.

Plint, A.G., 2002, Paleovalley systems in the Upper Cretaceous Dunvegan Formation, Alberta and British Columbia: Bulletin of Canadian Petroleum Geology, v. 50, p. 277–296, doi:10.2113/50.2.277.

Plint, A.G., 2000, Sequence stratigraphy and paleogeography of a Cenomanian deltaic complex: the Dunvegan and lower Kaskapau formations in subsurface and outcrop, Alberta and British Columbia, Canada: Bulletin of Canadian Petroleum Geology, v. 48, p. 43–79, doi:10.2113/48.1.43.

Plint, A.G., and Wadsworth, J.A., 2003, Sedimentology and palaeogeomorphology of four large valley systems incising delta plains, western Canada Foreland Basin: implications for mid-Cretaceous sea-level changes: Sedimentology, v. 50, p. 1147–1186, doi:10.1111/J.1365-3091.2003.00599.X.

Prasojo, O.A., Hoey, T.B., Owen, A., and Williams, R.D., 2023, Down-delta hydraulic geometry and its application to the rock record: Sedimentology, doi:10.1111/SED.13062.

Prasojo, O.A., Hoey, T.B., Owen, A., and Williams, R.D., 2022, Slope break and avulsion locations scale consistently in global deltas: Geophysical Research Letters, p. e2021GL093656, doi:10.1029/2021GL093656.

Ratliff, K.M., Hutton, E.W.H., and Murray, A.B., 2021, Modeling long-term delta dynamics reveals persistent geometric river avulsion locations: Earth and Planetary Science Letters, v. 559, p. 116786, doi:10.1016/j.epsl.2021.116786.

Reitz, M.D., and Jerolmack, D.J., 2012, Experimental alluvial fan evolution: Channel dynamics, slope controls, and shoreline growth: Journal of Geophysical Research: Earth Surface, v. 117, p. 2021, doi:10.1029/2011JF002261.

Reitz, M.D., Jerolmack, D.J., and Swenson, J.B., 2010, Flooding and flow path selection on alluvial fans and deltas: Geophysical Research Letters, v. 37, p. n/a-n/a, doi:10.1029/2009GL041985.

Rhoads, B.L., 2020, River Dynamics: Cambridge University Press, doi:10.1017/9781108164108.

Rice, S., and Church, M., 1996, Sampling surficial fluvial gravels; the precision of size distribution percentile sediments: Journal of Sedimentary Research, v. 66, p. 654–665, doi:10.2110/JSR.66.654.

Riggs, R.M., Allen, G.H., David, C.H., Lin, P., Pan, M., Yang, X., and Gleason, C., 2022, RODEO: An algorithm and Google Earth Engine application for river discharge retrieval from Landsat: Environmental Modelling & Software, v. 148, p. 105254, doi:10.1016/J.ENVSOFT.2021.105254.

van Rijn, L.C., 1984, Sediment Transport, Part II: Suspended Load Transport: Journal of Hydraulic Engineering, v. 110, p. 1613–1641, doi:10.1061/(ASCE)0733-9429(1984)110:11(1613).

Rodier, J., and Roche, M., 1978, River Flow in Arid Regions, *in* Herschy, R. ed., Hydrometry : principles and practices, Wiley Blackwell, p. 453–472.

Rodríguez, E., Morris, C.S., and Eric Belz, J., 2006, A Global Assessment of the SRTM Performance: Photogrammetric Engineering & Remote Sensing, v. 72, p. 249–260, http://gipsy.jpl.nasa.gov (accessed August 2020).

de Rose, R.C., Stewardson, M.J., and Harman, C., 2008, Downstream hydraulic geometry of rivers in Victoria, Australia: Geomorphology, v. 99, p. 302–316, doi:10.1016/j.geomorph.2007.11.008.

Rossi, V.M., Kim, W., López, J.L., Edmonds, D., Geleynse, N., Olariu, C., Steel, R.J., Hiatt, M., and Passalacqua, P., 2016, Impact of tidal currents on delta-channel deepening, stratigraphic architecture, and sediment bypass beyond the shoreline: Geology, v. 44, p. 927–930, doi:10.1130/G38334.1.

Rossi, V.M., and Steel, R.J., 2016, The role of tidal, wave and river currents in the evolution of mixed-energy deltas: Example from the Lajas Formation (Argentina): Sedimentology, v. 63, p. 824–864, doi:10.1111/sed.12240.

Scott R.W., Holbrook J.M., Oboh-Ikuenobe F.E., Evetts M.J., Benson D.G., and Kues B.S., 2004, Middle Cretaceous Stratigraphy, Southern Western Interior Seaway, New Mexico and Oklahoma: The Mountain Geologist,.

Sageman, B.B., and Arthur, M.A., 1994, Early Turonian Paleogeographic/Paleobathymetric Map, Western Interior, U.S., *in* Caputo, M. v., Peterson, J.A., and Franczyk, K.J. eds., Mesozoic Systems of the Rocky Mountain Region, USA, SEPM (Society for Sedimentary Geology), p. 457–470, http://archives.datapages.com/data/rocky_sepm/data/032/032001/457_rocky_mount320457.htm (accessed December 2020).

Sassi, M.G., Hoitink, A.J.F., de Brye, B., and Deleersnijder, E., 2012, Downstream hydraulic geometry of a tidally influenced river delta: Journal of Geophysical Research: Earth Surface, v. 117, p. n/a-n/a, doi:10.1029/2012JF002448.

Scott, R.W., Oboh-Ikuenobe, F.E., Benson, D.G., Holbrook, J.M., and Alnahwi, A., 2018, Cenomanian-Turonian flooding cycles: U.S. Gulf Coast and Western Interior: Cretaceous Research, v. 89, p. 191–210, doi:10.1016/J.CRETRES.2018.03.027.

Seekell, D., Cael, B., Lindmark, E., and Byström, P., 2021, The Fractal Scaling Relationship for River Inlets to Lakes: Geophysical Research Letters, v. 48, p. e2021GL093366, doi:10.1029/2021GL093366.

Segura, C., and Pitlick, J., 2010, Scaling frequency of channel-forming flows in snowmelt-dominated streams: Water Resources Research, v. 46, doi:10.1029/2009WR008336.

Shamir, E., Ben-Moshe, L., Ronen, A., Grodek, T., Enzel, Y., Georgakakos, K., and Morin, E., 2012, Hydrology and Earth System Sciences Discussions Geomorphology-based index for detecting minimal flood stages in arid alluvial streams: Hydrol. Earth Syst. Sci. Discuss, v. 9, p. 12357–12394, doi:10.5194/hessd-9-12357-2012.

Sharma, S., Bhattacharya, J.P., and Richards, B., 2017, Source-to-sink sediment budget analysis of the Cretaceous Ferron Sandstone, Utah, U.S.A, using the fulcrum approach: Journal of Sedimentary Research, v. 87, p. 594–608, doi:10.2110/jsr.2017.23.

Sharman, G.R., Sylvester, Z., and Covault, J.A., 2019, Conversion of tectonic and climatic forcings into records of sediment supply and provenance: Scientific Reports 2019 9:1, v. 9, p. 1–7, doi:10.1038/s41598-019-39754-6.

Shields, M.R., Bianchi, T.S., Mohrig, D., Hutchings, J.A., Kenney, W.F., Kolker, A.S., and Curtis, J.H., 2017, Carbon storage in the Mississippi River delta enhanced by environmental engineering: Nature Geoscience 2017 10:11, v. 10, p. 846–851, doi:10.1038/ngeo3044.

Shiklomanov, A.I., Lammers, R.B., Rawlins, M.A., Smith, L.C., and Pavelsky, T.M., 2007, Temporal and spatial variations in maximum river discharge from a new Russian data set: Journal of Geophysical Research: Biogeosciences, v. 112, p. 4–53, doi:10.1029/2006JG000352.

Shinn, Y.J., Lee, H.S., Kwon, Y.K., and Kwak, W.J., 2014, Lithofacies distribution and depositional environment in the Lower Cretaceous McMurray Formation, BlackGold Lease, northern Alberta: implications for geometry and distribution of oil sand reservoirs: Geosciences Journal, v. 18, p. 325–337, doi:10.1007/s12303-014-0006-x.

Shuman, B.N., 2014, Approaches to Paleoclimate Reconstruction: Reference Module in Earth Systems and Environmental Sciences, doi:10.1016/B978-0-12-409548-9.09405-7.

Simpson, G., and Castelltort, S., 2012, Model shows that rivers transmit high-frequency climate cycles to the sedimentary record: Geology, v. 40, p. 1131–1134, doi:10.1130/G33451.1.

Sinha, R., 2009, The Great avulsion of Kosi on 18 August 2008: Current Science, p. 429–433, https://www.jstor.org/stable/pdf/24112012.pdf (accessed March 2022).

Slater, L., Villarini, G., Archfield, S., Faulkner, D., Lamb, R., Khouakhi, A., and Yin, J., 2021, Global Changes in 20-Year, 50-Year, and 100-Year River Floods: Geophysical Research Letters, v. 48, p. e2020GL091824, doi:10.1029/2020GL091824.

Slingerland, R., and Smith, N.D., 2004, River Avulsions and Their Deposits: Annual Review of Earth and Planetary Sciences, v. 32, p. 257–285, doi:10.1146/annurev.earth.32.101802.120201.

Sømme, T.O., Helland-hansen, W., Martinsen, O.J., and Thurmond, J.B., 2009a, Relationships between morphological and sedimentological parameters in source-to-sink systems: a basis for predicting semi-quantitative characteristics in subsurface systems: Basin Research, v. 21, p. 361–387, doi:10.1111/J.1365-2117.2009.00397.X.

Sømme, T.O., Martinsen, O.J., and Thurmond, J.B., 2009b, Reconstructing morphological and depositional characteristics in subsurface sedimentary systems: An example from the Maastrichtian–Danian Ormen Lange system, More Basin, Norwegian Sea: AAPG Bulletin, v. 93, p. 1347–1377, doi:10.1306/06010909038.

Sømme, T.O., Piper, D.J.W., Deptuck, M.E., and Helland-Hansen, W., 2011, Linking Onshore–Offshore Sediment Dispersal in the Golo Source-to-Sink System (Corsica,

France) During the Late Quaternary: Journal of Sedimentary Research, v. 81, p. 118–137, doi:10.2110/JSR.2011.11.

Stanley, D.J., and Warne, A.G., 1994, Worldwide initiation of Holocene marine deltas by deceleration of sea-level rise: Science, v. 265, p. 228–231, doi:10.1126/science.265.5169.228.

Stewart, I.T., Cayan, D.R., and Dettinger, M.D., 2005, Changes toward Earlier Streamflow Timing across Western North America: Journal of Climate, v. 18, p. 1136–1155, doi:10.1175/JCLI3321.1.

Stonevičius, E., Valiuškevičius, G., Rimkus, E., and Kažys, J., 2014, Climate induced changes of Lithuanian rivers runoff in 1960–2009: Water Resources 2014 41:5, v. 41, p. 592–603, doi:10.1134/S0097807814050133.

Stouthamer, E., Cohen, K.M., and Gouw, M.J.P., 2015, Avulsion and its Implications for Fluvial-Deltaic Architecture: Insights from the Holocene Rhine–Meuse Delta: From River to Rock Record, p. 215–231, doi:10.2110/sepmsp.097.215.

Strahler, A.N., 1952, Hypsometric (Area-Altitude) Analysis of Erosional Topography: Bulletin of The Geological Society of America, v. 63, p. 1117–1142, http://pubs.geoscienceworld.org/gsa/gsabulletin/article-pdf/63/11/1117/3426542/i0016-7606-63-11-1117.pdf (accessed February 2022).

Strahler, A.N., 1957, Quantitative analysis of watershed geomorphology: Eos, Transactions American Geophysical Union, v. 38, p. 913–920, doi:10.1029/TR038I006P00913.

Straub, K.M., Duller, R.A., Foreman, B.Z., and Hajek, E.A., 2020, Buffered, Incomplete, and Shredded: The Challenges of Reading an Imperfect Stratigraphic Record: Journal of Geophysical Research: Earth Surface, v. 125, p. e2019JF005079, doi:10.1029/2019JF005079.

Swenson, J.B., 2005, Relative importance of fluvial input and wave energy in controlling the timescale for distributary-channel avulsion: Geophysical Research Letters, v. 32, p. 1–5, doi:10.1029/2005GL024758.

Syvitski, J.P.M. et al., 2009, Sinking deltas due to human activities: Nature Geoscience, v. 2, p. 681–686, doi:10.1038/ngeo629.

Syvitski, J.P.M., and Milliman, J.D., 2007, Geology, Geography, and Humans Battle for Dominance over the Delivery of Fluvial Sediment to the Coastal Ocean: The Journal of Geology, v. 115, p. 1–19.

Syvitski, J.P.M., and Saito, Y., 2007, Morphodynamics of deltas under the influence of humans: Global and Planetary Change, v. 57, p. 261–282, doi:10.1016/j.gloplacha.2006.12.001.

Szabo, S. et al., 2016, Population dynamics, delta vulnerability and environmental change: comparison of the Mekong, Ganges–Brahmaputra and Amazon delta regions: Sustainability Science, v. 11, p. 539–554, doi:10.1007/s11625-016-0372-6.

Ta, T.K.O., Nguyen, V.L., Tateishi, M., Kobayashi, I., Saito, Y., and Nakamura, T., 2002, Sediment facies and Late Holocene progradation of the Mekong River Delta in Bentre Province, southern Vietnam: An example of evolution from a tide-dominated to a tide- and wave-dominated delta: Sedimentary Geology, v. 152, p. 313–325, doi:10.1016/S0037-0738(02)00098-2.

Tabata, K.K., and Hickin, E.J., 2003, Interchannel hydraulic geometry and hydraulic efficiency of the anastomosing Columbia River, southeastern British Columbia, Canada: Earth Surface Processes and Landforms, v. 28, p. 837–852, doi:10.1002/esp.497.

Tessler, Z.D., Vorosmarty, C.J., Grossberg, M., Gladkova, I., Aizenman, H., Syvitski, J.P.M., and Foufoula-Georgiou, E., 2015, Profiling risk and sustainability in coastal deltas of the world: Science, v. 349, p. 638–643, doi:10.1126/science.aab3574.

Thornthwaite, C.W., 1948, An Approach toward a Rational Classification of Climate: Geographical Review, v. 38, p. 55–94, https://www.jstor.org/stable/pdf/210739.pdf (accessed December 2020).

Toby, S.C., Duller, R.A., de Angelis, S., and Straub, K.M., 2019, A Stratigraphic Framework for the Preservation and Shredding of Environmental Signals: Geophysical Research Letters, v. 46, p. 5837–5845, doi:10.1029/2019GL082555.

Toby, S.C., Duller, R.A., de Angelis, S., and Straub, K.M., 2022, Morphodynamic limits to environmental signal propagation across landscapes and into strata: Nature Communications 2022 13:1, v. 13, p. 1–10, doi:10.1038/s41467-021-27776-6.

Trampush, S.M., Huzurbazar, S., and McElroy, B., 2014, Empirical assessment of theory for bankfull characteristics of alluvial channels: Water Resources Research, v. 50, p. 9211–9220, doi:10.1002/2014WR015597.

Tucker, C.J., Grant, D.M., and Dykstra, J.D., 2004, NASA's global orthorectified landsat data set: Photogrammetric Engineering and Remote Sensing, v. 70, p. 313–322, doi:10.14358/PERS.70.3.313.

Turner, R.E., Kearney, M.S., and Parkinson, R.W., 2017, Sea-Level Rise Tipping Point of Delta Survival: Journal of Coastal Research, v. 342, p. 470–474, doi:10.2112/jcoastres-d-17-00068.1.

Vakarelov, B.K., and Ainsworth, R.B., 2013, A hierarchical approach to architectural classification in marginal-marine systems: Bridging the gap between sedimentology and sequence stratigraphy: AAPG Bulletin, v. 97, p. 1121–1161, doi:10.1306/11011212024.

Valenza, J.M., Edmonds, D.A., Hwang, T., and Roy, S., 2020, Downstream changes in river avulsion style are related to channel morphology: Nature Communications, v. 11, doi:10.1038/s41467-020-15859-9.

Vörösmarty, C.J., Green, P., Salisbury, J., and Lammers, R.B., 2000, Global water resources: Vulnerability from climate change and population growth: Science, v. 289, p. 284–288, doi:10.1126/science.289.5477.284.

Wallace, D.J. et al., 2014, Shrinking and Sinking Deltas : Major role of Dams in delta subsidence and Effective Sea Level Rise: Nature Geoscience, v. 123, p. 1973–1984, doi:10.1038/ngeo129.

Wang, J. et al., 2022, GeoDAR: georeferenced global dams and reservoirs dataset for bridging attributes and geolocations: Earth System Science Data, v. 14, p. 1869–1899, doi:10.5194/ESSD-14-1869-2022.

Wang, H. et al., 2017, Impacts of the dam-orientated water-sediment regulation scheme on the lower reaches and delta of the Yellow River (Huanghe): A review: Global and Planetary Change, v. 157, p. 93–113, doi:10.1016/j.gloplacha.2017.08.005.

Wang, S., and Li, Y., 2011, Channel variations of the different channel pattern reaches in the lower Yellow River from 1950 to 1999: Quaternary International, v. 244, p. 238–247, doi:10.1016/J.QUAINT.2010.09.002.

Wang, Z., Wang, Z., and de Vriend, H.J., 2008, Impact of water diversion on the morphological development of the Lower Yellow River: International Journal of Sediment Research, v. 23, p. 13–27, doi:10.1016/S1001-6279(08)60002-5.

Warrick, J.A., Stevens, A.W., Miller, I.M., Harrison, S.R., Ritchie, A.C., and Gelfenbaum, G., 2019, World's largest dam removal reverses coastal erosion: Scientific Reports, v. 9, p. 1–12, doi:10.1038/s41598-019-50387-7.

Watkins, S.E., Whittaker, A.C., Bell, R.E., McNeill, L.C., Gawthorpe, R.L., Brooke, S.A.S., and Nixon, C.W., 2019, Are landscapes buffered to high-frequency climate change? A comparison of sediment fluxes and depositional volumes in the Corinth Rift, central Greece, over the past 130 k.y.: GSA Bulletin, v. 131, p. 372–388, doi:10.1130/B31953.1.

Whittaker, A.C., 2012, How do landscapes record tectonics and climate? Lithosphere, v. 4, p. 160–164, doi:10.1130/RF.L003.1.

Whittaker, A.C., Duller, R.A., Springett, J., Smithells, R.A., Whitchurch, A.L., and Allen, P.A., 2011, Decoding downstream trends in stratigraphic grain size as a function of tectonic subsidence and sediment supply: Bulletin of the Geological Society of America, v. 123, p. 1363–1382, doi:10.1130/B30351.1.

Williams, R.D., Measures, R., Hicks, D.M., and Brasington, J., 2016, Assessment of a numerical model to reproduce event-scale erosion and deposition distributions in a braided river: Water Resources Research, v. 52, p. 6621–6642, doi:10.1002/2015WR018491.

Wohl, E., and David, G.C.L., 2008, Consistency of scaling relations among bedrock and alluvial channels: Journal of Geophysical Research, v. 113, p. F04013, doi:10.1029/2008JF000989.

Wolman, M.G., and Miller, J.P., 1960, Magnitude and Frequency of Forces in Geomorphic Processes: The Journal of Geology, v. 68, p. 54–74, doi:10.1086/626637.

Wright, L.D., 1977, Sediment transport and deposition at river mouths: A synthesis: Bulletin of the Geological Society of America, v. 88, p. 857–868, doi:10.1130/0016-7606(1977)88<857:STADAR>2.0.CO;2.

Wu, X., Bi, N., Syvitski, J., Saito, Y., Xu, J., Nittrouer, J.A., Bianchi, T.S., Yang, Z., and Wang, H., 2020, Can Reservoir Regulation Along the Yellow River Be a Sustainable Way to Save a Sinking Delta? Earth's Future, v. 8, p. e2020EF001587, doi:10.1029/2020EF001587.

Yang, S.L., 2005, Impact of dams on Yangtze River sediment supply to the sea and delta intertidal wetland response: Journal of Geophysical Research, v. 110, p. F03006, doi:10.1029/2004JF000271.

Yang, S.L., Milliman, J.D., Li, P., and Xu, K., 2011, 50,000 dams later: Erosion of the Yangtze River and its delta: Global and Planetary Change, v. 75, p. 14–20, doi:10.1016/j.gloplacha.2010.09.006.

van Yperen, A.E., Holbrook, J.M., Poyatos-Moré, M., and Midtkandal, I., 2019, Coalesced delta-front sheet-like sandstone bodies from highly avulsive distributary channels: The low-accommodation mesa rica sandstone (Dakota Group, New Mexico, USA): Journal of Sedimentary Research, v. 89, p. 654–678, doi:10.2110/jsr.2019.27.

van Yperen, A.E., Holbrook, J.M., Poyatos-Moré, M., Myers, C., and Midtkandal, I., 2020, Low-accommodation and backwater effects on sequence stratigraphic surfaces and depositional architecture of fluvio-deltaic settings (Cretaceous Mesa Rica Sandstone, Dakota Group, USA): Basin Research, v. 33, p. 513–543, doi:10.1111/bre.12483.

Zhu, Y., Bhattacharya, J.P., Li, W., Lapen, T.J., Jicha, B.R., and Singer, B.S., 2012, Milankovitch-Scale Sequence Stratigraphy and Stepped Forced Regressions of the Turonian Ferron Notom Deltaic Complex, South-Central Utah, U.S.A: Journal of Sedimentary Research, v. 82, p. 723–746, doi:10.2110/jsr.2012.63.

Appendix

A.1. Data mining code

This code is used in the Google Earth Engine (https://code.earthengine.google.com/) to extract satellite imageries (i.e. Landsat, ArcticDEM and SRTM) from the Google server to the local drive. The steps involved are:

1. Drawing the polygon of the studied river deltas that cover the shoreline of the delta up to the delta apex

2. Choosing the image collection (e.g. Landsat 5, ArcticDEM, SRTM) from the Google server

3. Define the oldest date possible from the available dataset

4. Sort the data based on the cloud cover

5. Stitch the image strips to be one composite image that cover the area of interest

6. Export the image with their dedicated bands to enhance the water representation from the Landsat 5 image to the personal Google Drive

7. Download the satellite image from the Google Drive and analyse in the ArcGIS

```
//choosing the image from the collection with no cloud cover for the
certain date range
var collection = ee.ImageCollection (Landsat5)
.filterDate('1990-01-01','1990-12-31')
.filterBounds(Orinoco)
.sort('CLOUD_COVER',false);
//mosaic the images
var min = collection.median();
//showing the images that satisfy the cloud cover and date
requirement
```

```
var result = min.select('B5','B4','B1');

//showing the result and SRTM on the map below
Map.addLayer(result,{},'Landsat');

Map.addLayer(SRTM, {min:-50, max:200},'SRTM');

//importing ArcticDEM and adding to the map below
var dataset = ee.Image('UMN/PGC/ArcticDEM/V3/2m_mosaic');
var ArcticDEM = dataset.select('elevation');
var ArcticDEMVis = {
  min: -50.0,

  max: 1000.0,

  palette: ['0d13d8', '60e1ff', 'ffffff'],

};

Map.addLayer(ArcticDEM, ArcticDEMVis, 'Arctic DEM');

//Get a list of all dates properties.

var dates = collection

    .map(function(image) {

      return ee.Feature(null, {'date': image.date().format('YYYY-MM-
dd')})

    })

    .distinct('date')

    .aggregate_array('date');

print (dates);

//Export the Landsat, specifying scale and region.

Export.image.toDrive({

  image: result.select("B5","B4","B1"),

  description: 'Orinoco_landsat_4',

  scale: 30,

  region: Orinoco,

  maxPixels: 1e12,

});
```

```
//Export the SRTM, specifying scale and region.
Export.image.toDrive({
  image: SRTM,
  description: 'Jequitinhonha_SRTM',
  scale: 30,
  region: Jequitinhonha,
  maxPixels: 1e12,
});
//Export the ArcticDEM, specifying scale and region
Export.image.toDrive({
  image: ArcticDEM,
  description: 'Copper_SRTM',
  scale: 30,
  region: Copper,
  maxPixels: 1e12,
});
//Export ROI as shp file
Export.table.toDrive({
  collection: ee.FeatureCollection(Orinoco),
  description: 'Orinoco_geometry',
  fileFormat:"SHP",
})
```

A.2. Island size measurement code

This code will use the images produced by Delft3D for each timestep and each running scenario to calculate the island size distribution. The language used is Python that was applied in the Google Colab environment (https://colab.research.google.com/) instead of in the local drive to accommodate faster computational time. The steps involved are:

1. Import all the library/packages necessary

2. Import and convert all images to be binary

3. Crop the image to exclude scale and upstream island

4. Calculate each island size in comparison to total delta size to get dimensionless island size

5. Plot probability density function to be compared with theoretical island size distribution dominated by bifurcation only using R

```
#Connect to Google Drive
from google.colab import drive
from google.colab import files
drive.mount('/content/drive')
#Install libraries
!pip install opencv-python
!pip install numpy
!pip install pandas
#Import the libraries needed
from google.colab.patches import cv2_imshow
from array import array
from numpy import savetxt
import numpy as np
import cv2 as cv2
import csv
import pandas as pd
#Upload the results in the folder 'Island_sizes' inside your Google D
rive
#Import the image 'USXX_TXX.png'
image = cv2.imread("/content/drive/MyDrive/Colab Notebooks/US8.1/US8.
1_T051.png")
#Crop the image
crop = image[70:360, 92:415]
#Show the cropped image
cv2_imshow(crop)
#convert the color space to gray
gray = cv2.cvtColor(crop, cv2.COLOR_BGR2GRAY)
```

```
#apply Otsu's thresholding: determines an optimal global threshold va
lue from the image histogram (bimodal if the image is binarised)
thresh = cv2.threshold(gray,0,255,cv2.THRESH_OTSU + cv2.THRESH_BINARY
)[1]
#count the number of pixels that are not black (>0) in an image
pixels = cv2.countNonZero(thresh)
#finding white object from black background
#cv2.RETR_EXTERNAL = contour retrieval mode; take only hierarchy-
0 level contour
#cv2.CHAIN_APPROX_SIMPLE = contour approximation method; removes all
redundant poins and compresses the contour (e.g. 4 points for rectang
ular)
cnts = cv2.findContours(thresh, cv2.RETR_EXTERNAL, cv2.CHAIN_APPROX_S
IMPLE)
#len() = returns the number of characters in the string or length;
#example mylist = "Hello", len(mylist) = 5
cnts = cnts[0] if len(cnts) == 2 else cnts[1]
total = 0
#cv2.boundingRect => to draw approximate rectangle to highlight the r
egion of interest after obtaining contour from an image
#np.zeros => return a new array of image size, filled with zeros (0.x
x)
#image.shape => acquire image size (width, height)
#cv2.fillPoly => to add polygon on an image (original image, addition
al image, colours)
#cv2.countNonZero => for counting the number of non=zero pixels in th
e image
#+= => to add another value with the variable's value and assigns the
 new value to the variable
for c in cnts:
    x,y,w,h = cv2.boundingRect(c)
    mask = np.zeros(image.shape, dtype=np.uint8)
    cv2.fillPoly(mask, [c], [255,255,255])
    mask = cv2.cvtColor(mask, cv2.COLOR_BGR2GRAY)
    pixels2 = cv2.countNonZero(mask)
    total += pixels2
    cv2.putText(image, '{}'.format(pixels2), (x+150,y+45), cv2.FONT_H
ERSHEY_SIMPLEX, 1, (255,255,255), 1)
    print (pixels2)
cv2_imshow(thresh)
```